Study of Pulsar Wind Nebulae in Very-High-Energy gamma-rays with H.E.S.S.

Michelle Tsirou

THÈSE POUR OBTENIR LE GRADE DE DOCTEUR DE L'UNIVERSITÉ DE MONTPELLIER

En Astrophysiques

École doctorale I2S

Unité de recherche UMR 5299

Study of Pulsar Wind Nebulae in Very-High-Energy gamma-rays with H.E.S.S.

Présentée par Michelle TSIROU

Le 17 octobre 2019

Sous la direction de Yves A. GALLANT

Devant le jury composé de

Elena AMATO,	Chercheur,	INAF - Acetri	Rapporteur
Arache DJANNATI-ATAÏ,	Directeur de recherche,	APC - Paris	Examinateur
Yves GALLANT,	Directeur de recherche,	LUPM - Montpellier	Directeur de thèse
Marianne LEMOINE-GOUMARD,	Chargée de recherche,	CENBG - Bordeaux	Rapporteur
Alexandre MARCOWITH,	Directeur de recherche,	LUPM - Montpellier	Président du jury

UNIVERSITÉ DE MONTPELLIER

Study of Pulsar Wind Nebulae in Very-High-Energy gamma-rays with H.E.S.S.[1]

Michelle Tsirou

[1]High Energy Stereoscopic System

To my former and subsequent selves,
may this wrenched duality amalgamate
ultimately.

«Me mettre en face de la métaphysique
que je me suis faite
en fonction de ce néant
que je porte.»

Antonin Artaud,
Fragments d'un Journal d'Enfer, *à André Gaillard*, 1929.

" Ό,τι δεν συνέβη ποτέ, είναι ό,τι δεν ποθήσαμε αρκετά."

Νίκος Καζαντζάκης

"Strummer's law : no input, no output."

Joe Strummer

Abstract

Pulsar wind nebulae consist of magnetised clouds of positrons and electrons accelerated to very high energies through the action of a central pulsar, often embedded within a host supernova remnant. They are the largest population of firmly identified sources of TeV gamma-rays within the Galaxy and are thought to be contributors to the leptonic Galactic cosmic-ray spectrum, and thus viable source candidates in the quest to interpret the origin of the cosmic-ray positron fraction excess. Their very-high-energy gamma-ray emission is of particular interest for spectral models, as their dominant radiation process is inverse Compton scattering on target photons present in interstellar radiation fields such as the visible, near and far infrared ambient photons in addition to the Cosmic Microwave Background.

In this thesis dissertation I present the scope of my research work, which lies on pulsar wind nebula morphology and understanding their very-high-energy radiation.

I report the latest morphological and spectral studies of the pulsar wind nebula within the MSH 15-52 composite supernova remnant through High Energy Stereoscopic System (H.E.S.S.) observations. In this phenomenological study I have conducted a fit of the very-high-energy emission morphology beyond $\gtrsim 0.3$ TeV detected in HESS-I data using a template X-ray synchrotron map in the 4–7 keV band based on archival *Chandra* observations. In the model of the emission, the gamma-ray emission produced by inverse Compton scattering is thought to ensue from the same leptonic population responsible for the observed synchrotron emission, and thus the X-ray template represents the spatial distribution of these electrons and positrons, convolved with the spatial dependence of the magnetic field. Our best-fit results yield an additional extended TeV component located on the south-eastern region of the nebula, centered at ~ 4 pc from the position of the associated pulsar PSR B1509-58, with an intrinsic radius of $\sim 7'$ (or 9 pc). We also detect a significant steepening in the spectral shape of the total emission from the pulsar wind nebula, occurring above ~ 10 TeV. This coincides with a shrinking of the emission observed in the sky map, as revealed by our energy-dependent morphological analyses. Several scenarii are presented so as to explain our morphological and spectral results concerning the emission originating from MSH 15-52 . Based on the Galactic radiation field characteristics derived from published models, the gamma-ray emission is well described by leptons scattering on the far infrared and cosmic microwave backgrounds, respectively at lower and higher energies than the detected spectral steepening energy, which suggests an interpretation of the energy dependence as a consequence of *Klein-Nishina* effects in the cross-section.

During the last year of my thesis I have worked with collaborators on a study of drivers behind the observed significant offsets of TeV-emitting pulsar wind nebulae with respect to their pulsar. We performed relativistic (magneto)-hydrodynamical numerical simulations and tested physical setups in one-dimensional studies and are pursuing an ongoing two-dimensional investigation to quantify the effect of the pulsar proper motion in comparison to ambient medium density gradients so as to derive constrains on these physical factors leading to asymmetrical evolution in pulsar wind nebulae.

Acknowledgments

In this brief and laconic section, I would like to acknowledge the people, the organisations and the events that shaped my career.

Firstly, I would like to thank my PhD advisor, Dr Yves Gallant for giving me the opportunity to start a PhD and for always considering my ideas without restricting me to a label. Over the last three years I have learnt a tremendous amount by working with him. He has introduced me to the fascinating landscape of pulsar wind nebulae physics and has pushed me several times out of my comfort zone so as to better myself. You have helped me conquer my fear of public speeches, by encouraging me, frankly a ridiculous amount of times, to present my ongoing work in numerous occasions, and you were right by doing so. You have as well been a very thoughtful and understanding supervisor and have nurture my scientific curiosity with lots of discussions, references and by allowing me to travel to several schools, conferences and workshops all around the world so as to broaden my horizons. Thank you.

I would like as well to thank all the members of my thesis jury, some whom I have met and known throughout these years : Dr Marianne Lemoine-Goumard and Dr Elena Amato for undertaking the task of reading and commenting on my dissertation despite your overbooked agendas, Dr Arache Djannati-Ataï and Dr Alexandre Marcowith for accepting to participate as well in the examination of my PhD work. I have had the chance to glance at your work thanks to various meetings during the past years and I am truly humble for the time you have allocated into my thesis.

I am very grateful for the help of Dr Zakaria Meliani and the one of a kind expertise he has brought to our numerical simulation study. He has taken a very active role into this project whilst sharing his knowledge in the simulation game, which has helped tremendously the progress we have made. I want to thank as well Dr Régis Terrier, Dr Roberta Zanin, Dr Emma de Oña Wilhelmi, Dr Manami Sasaki and Dr Jacco Vink for all the fruitful discussions on our H.E.S.S. studies. I would like to take the time to thank Dr Nukri Komin and all the H.E.S.S. Galactic group conveners and members that have given us guidance throughout the MSH 15-52 task group activities.

Another round of thanks ought to go to the members of the laboratory I have been hosted for three years : the LUPM director Denis Puy, for his kindness and good intentions. My compatriot Georges for his care and thoughtfulness during these three years. The amazing Carole and Amel for their help in saving me when drowning into administrative tempests (and for their low-key wicked sense of humour), Lydie, Stéphane, Nicolas, Christophe, Denis C. and Sylvianne for always helping me when being lost into the abyss of IT, mission and practical predicaments. I shall keep a sweet memory of the lunch breaks with Michèle S., Nicolas, Vincent, Fred, Mathieu, and all the members of the EMA team.

The reason why I have had such an impactful emotional memory of the Montpellier lab is the presence of amazing, non-permanent, folks. Ma.P, Ju.D, An.A, Au, Qu.R and L. with whom I have shared an office space and have seen them come and go... Thank you Ju.D, An.A and Qu.R for being close friends and for the support and care you have shown me. Thanks as well to the other fantastic PhD students and postdocs that have become more friends than colleagues, cited per order of office location : Gr.B, Ma.Y, Be.T, Du.B, Lo.B, St.G, St.M, Jo.G., Ro.R, Th.L, Ma.S, Ga.F, Sa.V, Th.D, Ju.M. From the dark side of the corridor : thank you Ru.C and Ro.C. Amongst these friendship shout-outs, I would like to add all the wonderful people I have met during collaboration meetings, conferences, seasonal schools and other. I could enumerate your names but I would not make justice to the nature of connection we have developed in these trips.

So let me cite the cities, to have them as a memory stimulus map for future readings : Meudon, Palaiseau, Les Houches, Heidelberg, South Korea, Johannesbourg, Windhoek, Amsterdam, La Londe-les-Maures, Montpellier, Dublin, Pasadena, Marseille, Krakow, Platja d'Aro and Madison. It has been a pleasure to have met you, to have interacted and to have shared nice moments with you as well as stimulating debates.

In a more personal note, I would like to thank my parents for the colossal sacrifices they have made during my upbringing so as to provide me with an education, by paying for my tuition fees up until I left for University. Besides our differences and our rocky relationship, I am grateful for conveying me the importance of prioritising education above all and imposing me a strict work ethic that I have kept until today and that undoubtedly will be intrinsic in my conductor in all future career opportunities.

Finally I would like to thank all my close friends that I consider as family, from Athens, Paris and Montpellier that have shown me their unconditional support over the years and have saved me repeatedly from myself : Da.B, At.K, Cl.P, J-M.K, Mo.S, Re.B, Ma.F, Me.M, An.M, J-G.V, An.P, Ni.Z, El.G, Yo.R, and as well A.K, N.M, My.A, My.D, Is.S, Is.D, Zi.A, Ni. S, Ji. L, Ro.R, Am.Ki, Li.E, Al.F, E. and all the other relationships that I am not mentioning here with cryptic initials.
I care deeply for you. I do not say it as often as I should but I do the best of my broken capabilities to show it, in my way. I cherish our friendship and admire you profoundly, each one for the different side that we have shown each other as the multi-dimensional polygones we are in this revolving and poorly lit space.

Σας ευχαριστώ εκ βάθους καρδίας.

Contents

Part I

Introduction

Chapter 1

The VHE emission morphology of PWNe

1.1 The very-high-energy domain

Ενέργεια: "εν - έργο".
Energy : in action, at play.

Energy is a fundamental concept at the core of the notion of existence. Yet it is not evident how to define it with a general and universal function. How to combine the philosophical, technical and material conceptualisation of it? Its etymology stipulates that it is linked to action, to an effect and a consequence. Would that mean that the lack of action implies lack of energy?

In Physics, energy can be movement or temperature, it can be the potential of an action, it may be as well a reaction. Energy can be matter, it can be light and it might be dark. What system has truly no energy? Is the absence of energy a possibility? The idea of energy seems to be difficult to fully comprehend despite of it, and quite intuitively, it has been quantified, since it may be transferred but it can be transformed nonetheless. Its conservation is the basis of physical processes, being one of the (mostly) irrefutable laws in this chaotic Universe. Since it is a quantity, it has been assigned units of measurement, based on the cause of the phenomenon (from the Greek word φαινόμενο, what is shown, may be perceived) and its repercussion, the subsequent event on a certain type of system. I cannot provide (yet?) a satisfactory generalisation and definition of "energy". Nevertheless, there is one important notion in regards of it, that has been the founding of my research : energy is information.

During my thesis, I studied energy budgets from particles of a given nature, in particular photons and leptons, originating from a specific type of sources : nebulae surrounding a rapidly rotating compact object, more precisely a neutron star, known as a "pulsar" because of how scientists first perceived its observed signal during its discovery. I shall focus this dissertation on limning these fascinating sources, known as "pulsar wind nebulae". I focused on their emission, and since I have stipulated that energy is equal to information, I would have to stay consistent with my statement and construe it based on made hypotheses, by testing them, assessing their significance and then interpreting the physical phenomena that are most likely at their origin.

In my studies, I endeavoured, through the guidance of my supervisor and with the help of my colleagues, on interpreting information from a distinct energy range : the very-high energy domain. In the last decades, technological progress has opened up to scientists a window to the highest energy astrophysical systems. One of the many wonderous and exciting components of this very-high energy (VHE) realm would be the photon particles dubbed as γ-rays, that have energies beyond $\sim 10^5$ - 10^6 electron-Volts and range in more than eight orders of magnitude.

The eV being one of the many, many, frankly perhaps too many, units of energy used, is of particular interest as a comparison to the energy from electrically charged particles (see Chapter 3). Nevertheless, the VHE Universe is not only consisting of photons but of charged particles such as electrons, positrons, pions but of nuclei as well, ranging from photons to heavier elements up to iron. In my thesis I mainly focused on leptonic processes that could explain the observed emission of the most numerous class of sources in the Galaxy manifesting gamma-ray emission : the aforementioned pulsar wind nebulae.

1.2 Pulsars and their surroundings

Pulsar wind nebulae (PWNe) are agglomerations of magnetised ultra-relativistic particles, mainly composed of lepton pairs $e^{\pm}$ with a dash of ions in the mix, just enough to remind us that in estimating an action and its effects all types of processes ought to be considered, but just not enough to remind us that one needs to assess and estimate the dominant contributions. One of the intriguing aspects of such sources would be that they are usually part, at least during a considerable span of time of their evolution, of a composite system of objects. Pulsar wind nebulae, as their not so imaginative name suggest, are clouds of electrons and positrons formed around a pulsar from its injected outflow deposited by its relativistic wind. Neutron stars are compact objects and are the remaining core of a massive star that ended its lifetime by exploding from gravitational collapsing onto its core, resulting to a rather resounding "boom" (energy of $\sim 10^{51}$ erg), known as a supernova. The stellar envelop of the "dead" star is ejected onto its circumstellar medium (CSM) forming a supernova remnant (SNR) that will interact with the interstellar medium (ISM) by the propagation of the produced supernova blast-wave. In turn, the particles in the ambient medium will push back such an invasive powerful shock-wave and will induce by doing so a reaction to the action they subsist and produce a reverse shock travelling inwards the composite system. Pulsars and their environments are excellent astrophysical laboratories to study several of nowadays "hot" topics of several scientific disciplines, from compact object mergers, gravitational waves and more in general multi-messenger astrophysics general relativity, magnetic field reconnection, topology and turbulence, particle transport and escape, radiation processes on a multi-wavelength study, acceleration mechanisms, interactions with nearby objects, such as molecular clouds, contact and streaming instabilities, cosmic-rays and the list can go on and on, both in experimental and theoretical approaches. It should be noted, that it is highly improbable that all composite pulsar-PWN-SNR systems feature all the listed centres of interest simultaneously. It is important to be able to distinguish between the different behaviours and physical properties between the pulsar, the remnant ejecta nebula and the PWN. Notwithstanding, in order to study a problem one needs to understand the tangled evolutions of such an intricate system (Chapter 2).

1.3 The plethora of shapes regarding pulsar wind nebulae

During my thesis studies, I took an interest on the morphology of pulsar wind nebulae and on the comparison of the observed emissions in the very-high energy TeV with theoretical expectations and vice-versa. Due to the angular resolution of instruments in high energies, admittedly the study of PWNe based on gamma-ray skymaps may seem to the untrained eye as a dreary "potatoe"-shaped emission "harvesting". Indeed, in comparison to the finely resolved X-ray morphologies and for some radio observations, the filamentary canvasing on the sky map, gamma-ray observations of extended sources may seem underwhelming aesthetically. However, my artistic

compulsions have been satisfied when undergoing the steps for morphological analyses with H.E.S.S. datasets, one of the most angularly sensitive gamma-ray ground-based experiments : the High Energy Stereoscopic System (more details in Chapter 4), that will be surpassed by the upcoming, not yet operational, Cherenkov Telescope Array (CTA) in just a few (hopefully) years. In particular, I focused my efforts on one bright and extended gamma-ray source seen in the Galactic plane with H.E.S.S. : the pulsar wind nebula within the composite SNR MSH 15-52 . The reader may find in Chapter 5 a summary of my, and my collaborators', efforts in dissecting its TeV morphology and interpreting it based on its spectral information.

Indeed, when spatially resolved, a considerable amount of pulsar wind nebulae do not exhibit a common morphology as a population with one another. Some are embedded in barrel-shape remnants and seem to have elongated morphologies, others have a more bubble plerionic shape, other show bow-shock features, others may have diffusive tails and such that it is difficult to pinpoint easily a typical PWN morphology besides the expected spherically isotropic extended within a radius emission shape ensued in a conventional symmetrical evolution. Multi-wave length observations have shown that this is not the case for all PWNe. In my thesis, I have been motivated in particular by a morphology feature seen in a significant number of pulsar wind nebulae : an offset between the thought "central" pulsar and the peak of the TeV emission, as presented in Chapter 6. In Chapter 7 I relay the basis for attempting to simulate successfully and realistically the multi-scale system where pulsar wind nebulae evolve in.

Part II

Pulsar Wind Nebulae

Chapter 2

Astrophysical context and theory

Contents

2.1 Progenitors and supernovae

In this section we shall introduce the ongoing research regarding the properties of the progenitor stars resulting to composite pulsar wind nebula systems and summarise the different types of supernova explosions by focusing on the ones leading to the creation of compact objects.

2.1.1 Progenitor stars and their deaths

According to stellar evolution scenarii, a star is born onto the main sequence of the Hertzsprung-Russell (HR) diagram[12]. The HR diagram is a scatter plot of stellar populations illustrating the classification of stars based on their brightness and their temperature. The main sequence is the most heavily populated region of the graph[110], gathering several groups of stars (in the considered space-parameter) sharing common characteristics such as their size (radii of $\sim$ 0.1 - 20 $R_\odot$) , mass (0.1 - 40 $M_\odot$), luminosity (10^{-3} - 5.10^5 $L_\odot$) and effective temperature (ranging from 2 600 up to 38 000 K). Such a range of physical characteristics is being understood to be the product of nested causes. The input dictated by the protostar and its collapsed progenitor, a cool and dense molecular cloud fragmenting into stellar cores, will determine the newborn star initial placement in the main sequence of the HR diagram[65], [66], [67]. This input is linked to the richness of the protostellar region for example, to the condensation process effectiveness that will determine the increase of temperature and therefore the ignition of the nuclear reactions and to the hydrogen H amount of the protostar that later on will be converted into helium He. The latter shall insure that throughout the star evolution, the star will remain in the main sequence up until all the core hydrogen is consumed.

For stellar core temperatures T $\lesssim 10^7$ K, the proton-proton (p-p) reaction, where the helium is generated from produced deuterium from two protons, will be the dominant process. On the other hand, for T $> 10^7 K$, the CNO cycle, where helium is created by α-particle decay from unstable nitrogen formed from recursive proton-heavy nuclei (carbon, nitrogen and oxygen) reaction series, shall be the main energy source. Once the astron has turned all its hydrogen reserves into helium, the energy generation by nuclear fusion will be inhibited. The star will no longer be in hydrostatic equilibrium because of strong pressure and temperature gradients and will start contracting. The core will reach temperatures high enough to start converting helium into carbon and when in turn helium is consumed, the carbon core will start contracting and increasing temperature once more.

In Figure 2.1, we consider two cases in stellar evolution depending on the mass M of the star. For stars with M < 8 $M_\odot$, we have to treat differently the low mass stars $< 1 M_\odot$ from the mid-sized ones because of the variation of temperature with pressure and density. If the temperature gradient is considerably different from the adiabatic gradient, meaning the criterion for expansion and contraction without any heat transfer, then energy transport will be rather convective for higher gradients from the otherwise radiative nature. For low mass stars, the core should be in radiative equilibrium in contrast to the high mass stars where convection is

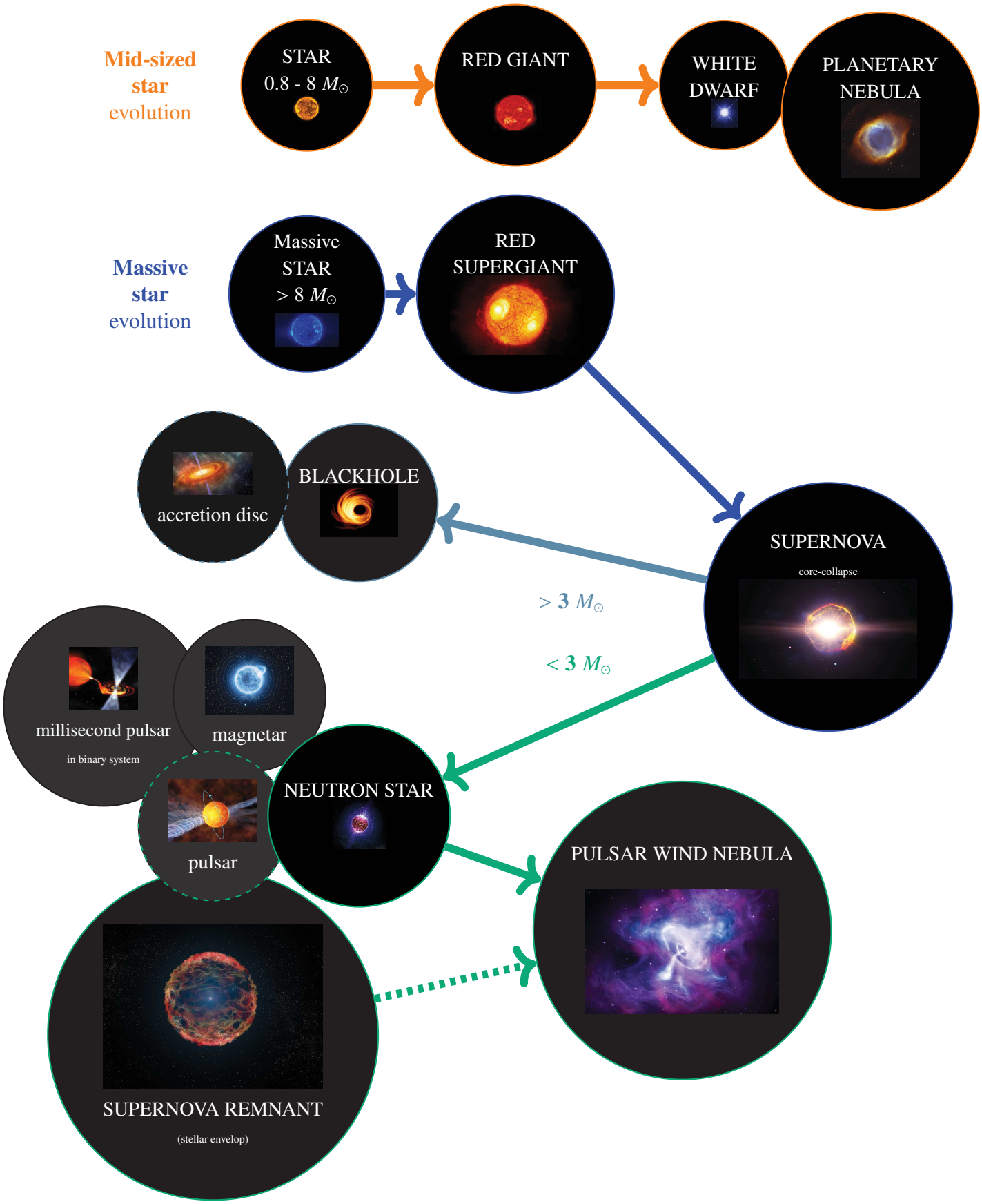

Figure 2.1 – Evolution of stars : resulting compact objects and their environments. A schematic simplified diagram for stellar afterlife illustration purposes. Progenitors with a core mass below $\sim 3\ M_\odot$ shall in time collapse onto their cores and form a neutron star that could also become a pulsar that may endow a pulsar wind nebula.

insuring the uniform consumption of hydrogen in the core. Stars with $M < 0.1M_{\odot}$ are called brown dwarfs because of their size and lack of nuclear reactions converting H to He.

For the mid-sized stars ($0.1M_{\odot} < M < 8M_{\odot}$)[64], after the H burns out, the CNO cycle has build up a carbon core that will continue contracting. Nevertheless it will not reach temperatures high enough to start consuming carbon because the contractions shall stop (electron degeneracy pressure at the core instead of gas pressure). : thus the carbon core will cool down and become a white dwarf with $M > 1.4M_{\odot}$ (Chandrasekhar limit, physical maximum mass allowed by fermion degeneracy pressure). The outer layers of the star will expand and at some point be expelled and ionised by the central white dwarf to form a planetary nebula.

Furthermore, the massive stars $> 8M_{\odot}$, will have initially a similar evolution as for the aforementioned lower mass case, burning the H and He, producing a contracting carbon core. Nevertheless, the massive stars will be able to contract to a radius that will increase the temperature to start the carbon ignition and will start consuming and producing successively heavier elements until an iron Fe core has been formed. Thus the core cannot be consumed into heavier nuclei and will begin its gravitational collapse. Depending on the stellar core mass, a compact object will ensue and will blast a powerful shock-wave : a progenitor, destructive and extremely energetic explosion, known as a supernova.

2.1.2 Types of supernovae and creation of a compact object

Supernovae (Sn) are amongst the most energetic and violent astrophysical phenomena of our local Universe. They are rapid and destructive explosions of a star, with either a thermonuclear or a core-collapse origin.

Thermonuclear supernovae are caused by the quick accumulation of hydrogen on the surface of a white dwarf by matter accretion from a companion star. The white dwarf will thus gain mass and exceed the Chandrasekhar limit, resulting to a thermonuclear explosion. This is the *single degenerate Chandrasekhar scenario*. There are other scenarii[136], like the *double degenerate* one, focusing on binary systems consisting of two closely separated white dwarfs. By losing energy via gravitational waves, both white dwarfs will grow closer and will implode after merging and exceeding the Chandrasekhar limit.

On the other hand, core-collapse supernovae are the outcome of a different explosion mechanism. They require massive progenitor stars as mentioned in Section 2.1.1 that will consume their core nuclei fueling the energy generation, ending in the gravitational collapse of the core and formation of a small and extremely overdense region : a compact object. As illustrated in Figure 2.1, depending on the mass of the stellar core, either a blackhole will be created for M > 3 $M_{\odot}$ [60] or a neutron star will be formed for a lower mass progenitor. In addition to the core remnant, the stellar envelope will be blasted away by the forward shock of the explosion and will consequently enrich the interstellar medium with the ejecta of the supernova remnant.

Supernovae are classified depending on their characteristic spectrum lines, their light curve shape and their maximum luminosity, mainly dichotomised as type I and type II and subsequently categorised in sub-types. Some observed cases have shown attributes from several predetermined supernova sub-classes and may not be allocated in any of them : they are labelled as peculiar supernovae. In Figure 2.2, a general diagram of supernova type sorting is given to emphasize the difference in composition of the stellar envelope of the progenitors shown in the spectra (element lines) and in the energetics of the explosion. Based on photometric and spectral supernova features observed, the general branching of the classification of supernovae [49] goes

as such :

- Sn type I : hydrogen lines are found on the spectrum
  - Sn sub-type Ia : hydrogen and silicon II lines, short duration of maximum peak indicating that the progenitor are low mass stars. These are thermonuclear very energetic bright events, used as "standard candles" in cosmology to track the evolution of the Universe up to high redshifts.
  - Sn sub-types Ib/c : Ib and Ic supernova types are thought to be led by similar mechanisms. Observed in active stellar formation regions of spiral galaxies, it is reckoned they have had high mass progenitors and that type Ib might have a greater hydrogen envelope than type Ic.
    - Sn sub-type Ib : hydrogen and helium I lines
    - Sn sub-type Ic : hydrogen but no helium I lines
- Sn type II : no hydrogen lines on the spectrum [115]
  - Sn sub-type IIb : no hydrogen nor silicon II lines, helium I are found. Spectrum shows similarities with the type Ib case. It is speculated that the progenitor had a relatively greater hydrogen envelope than the type I (b and c) progenitors and a less prominent one as the type II supernova paradigm.
  - Sn sub-type IIn : narrow spectral lines and slow intensity decrease. These features are regarded as an indication of interaction between the ejected stellar matter with the circumstellar medium.
  - Sn sub-type IIL : linear and continuous decrease of light intensity over time. It is thought that their progenitors' hydrogen envelope had a mass of $\sim$ 1- 2 $M_{\odot}$.
  - Sn sub-type IIP : rapid decline of light intensity over time up until a plateau is reached after a couple of months. In this case the progenitor's envelope mass is speculated to be of $\sim$ 10 $M_{\odot}$.

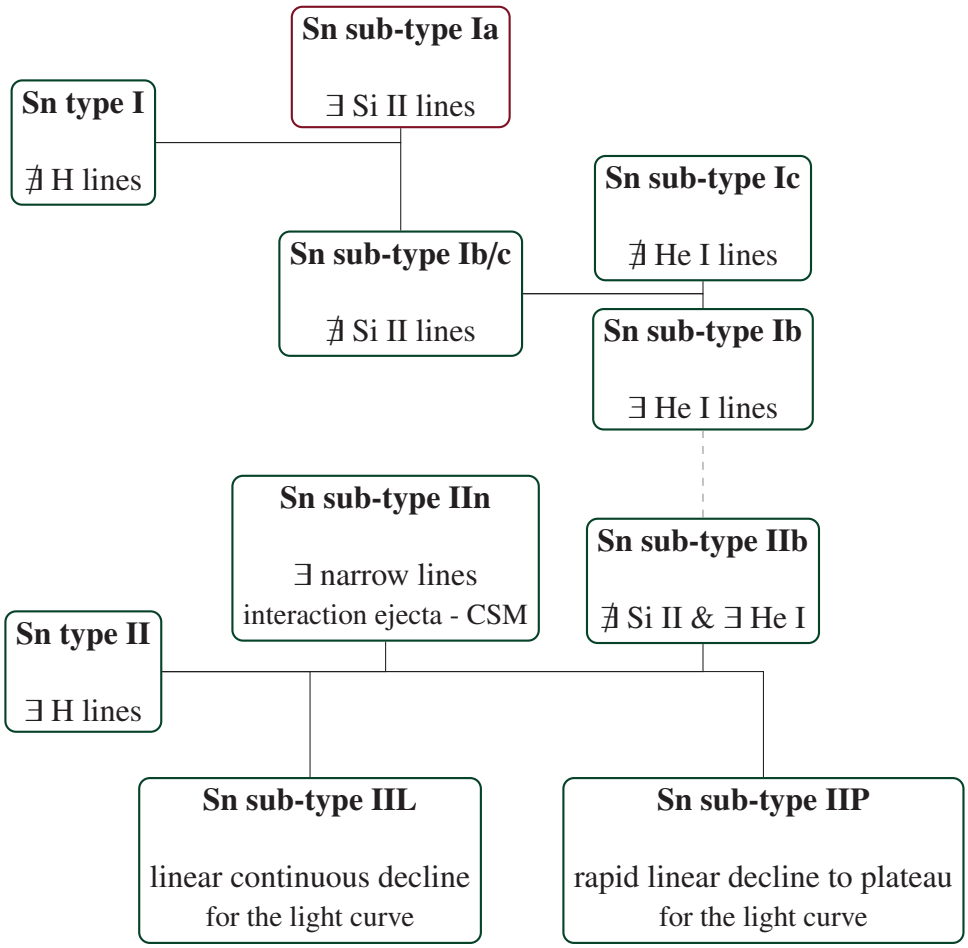

Figure 2.2 – Classification of supernovae (Sn) to types and sub-types. The red and green boxes indicate thermonuclear and core-collapse supernovae respectively. The following abbreviations for neutral and ionised elements are taken : hydrogen H, silicon Si II and helium He I.

2.2 Neutron stars

Neutron stars are the remains of the gravitationnally collapsed stellar core formed when a dying old massive star (mass ≤ 3 $M_\odot$) implodes. They are compact objects, retaining the stellar magnetic field and the rotational energy of their progenitors but applied in a considerably smaller radius ($\sim 10\ km$) and denser ($\sim 10^{17}$ kg.m^{-3}) system with mass of the order of a the solar mass ($\sim 1.35\ M_\odot$).

Pulsars (abbreviation of Pulsating Radio Sources) are rapidly rotating neutron stars, with a strong electromagnetic beamed emission emerging from the polar caps. The detected emission is therefore "pulsed", since an observer in the line of sight of the pulsar beam would detect a regularly oscillating signal with a short period.

2.2.1 Composition and characteristics of pulsars

Since the serendipitous discovery of the first radio pulsar in 1967, even though it was revealed not to be a "Little Green Man 1" [63], a tremendous number of pulsars varying in size, rotation period, surface magnetic field and rotational energy loss rates has been catalogued and studied. Examples of graphs illustrating these ranges of characteristics are given in Figure 2.4, 2.3 and 2.5.

Pulsars are powered through rotational energy to radiation energy conversion, resulting to an inevitable steady slow down of the object's spin and a gradual increase of their period. Their rotation period P_{pulsar} may be ranged from milliseconds, for the so-called *millisecond pulsars*, up to several seconds. Their period derivative $\dot{P}_{pulsar}$ can typically vary from $\sim 10^{-2}$ to 10^{-10} s.s^{-1}. The electromagnetic radiation from such a highly magnetised system is assumed to behave as if originating from low frequency magnetic dipole radiation. The rotational energy losses are estimated as follows:

$$\begin{aligned} -\left(\frac{dE_{rot}}{dt}\right)_{spin-down} = \dot{E}_{spin-down} = -\frac{d}{dt}\left(\frac{1}{2}I\Omega^2\right) &= -I\ \Omega\ \dot{\Omega} \\ &= -k_{inertia}MR^2\ \left(\frac{2\pi}{P}\right)\left(\frac{-2\pi\dot{P}}{P^2}\right) \\ &= 4\pi^2 k_{inertia}MR^2\left(P^{-3}\dot{P}\right) \end{aligned} \tag{2.1}$$

where Ω and $\dot{\Omega}$ are the rotation angular frequency (in $rad.s^{-1}$) and pulse derivative periodicity (in $rad.s^{-2}$), the momentum of inertia I is defined by the pulsar mass M, its radius R and an inertia constant equal to $k_{inertia} = \frac{2}{5}$ for a uniform rotating sphere [11]. The magnetic dipole will radiate at a rate of :

$$\begin{aligned} -\left(\frac{dE_{mag}}{dt}\right)_{spin-down} = \dot{E}_{dipole} = \frac{2}{3c^3}\left(|\ddot{m}|^2\right) \\ = \frac{2}{3c^3}\left(|\frac{d^2}{dt^2}(m_0 sin(\Omega t))|^2\right) \\ = \frac{2}{3c^3}\left(m_0^2\ sin^2\theta\ \Omega^4\right) \\ = \frac{2}{3c^3}\left(B^2\ R^6\ sin^2\theta\ \Omega^4\right) \end{aligned} \tag{2.2}$$

with $|m|^2$ the magnetic dipole moment of the pulsar, m_0 the magnetic dipole component perpendicular to the rotation axis (for a uniformly magnetised sphere with radius R, $m_0 = BR^3$) and θ the angle between the rotation and magnetic axes 2.11 [116].

By considering the magnetic dipole power as the main cause of rotational energy loss, when equating Equation 2.1 with Equation 2.2 one may find that :

$$\begin{aligned} \dot{E}_{spin-down} &\approx \dot{E}_{dipole} \\ \Omega\dot{\Omega} &\sim \Omega^4 \\ \dot{\Omega} &\propto \Omega^3 \end{aligned} \tag{2.3}$$

As a result of the pulsed nature of the detected signal, the period P is one of the most accessible pulsar parameters along with the rate at which this period fluctuates with time $\dot{P}$. In conventional pulsar evolution scenarii, neutron stars slow down at a given rate of rotational energy characterised by the braking index n :

$$\begin{aligned} \dot{\Omega} &= -\kappa\Omega^n \\ \ddot{\Omega} &= -n\,\kappa\,\dot{\Omega}\Omega^{(n-1)} = -n\frac{(\kappa\Omega^n)^2}{\Omega} \\ \text{yielding} \quad n &= \frac{\Omega\ddot{\Omega}}{\dot{\Omega}^2} \end{aligned} \tag{2.4}$$

with κ a quantity depending on the moment of inertia I, the magnetic field B, the radius R and the angle θ of inclination between the rotational and magnetic axes, considered constant if the above dependencies may be considered time-independent.

Using the dependence of the spin frequency found in Equation 2.3, the braking index for magnetic dipole radiation will be $n = 3$. This index is conveying the evolution of the pulsar spin-down.

$$\int_{P_0}^{P} P\,dP = \int_{t=0}^{t=\tau_{spin-down}} P\dot{P}\,dt \tag{2.5}$$

If one assumes that the period P and the period derivative $\dot{P}$ are not constant over time :

$$\begin{aligned} \left[\ \frac{P^2}{2}\ \right]_{P_0}^{P} &= P\dot{P}\ \left[\ t\ \right]_{t=0}^{t=\tau_{spin-down}} \\ \frac{P^2 - P_0^2}{2} &= P\dot{P}\,\tau_{spin-down} \end{aligned} \tag{2.6}$$

If the initial period of the pulsar is significantly shorter than the current observed period $P_0 \ll P$, then the characteristic age (or *spin-down age*) of the pulsar is :

$$\tau_{spin-down} = \frac{P}{2\dot{P}} \tag{2.7}$$

By assimilating the pulsar to an in-vacuum rotating magnetic dipole, the surface magnetic field will be :

$$\begin{aligned} B_{dipole} = \|\vec{B}\|^2 &= \frac{\sqrt{I\mu_0 c^3}}{4\pi^2 R^3}\left(P^{\frac{1}{2}}\dot{P}^{\frac{1}{2}}\right) \quad \text{(MKSA)} \\ &= \left(\frac{Ic^3}{8\pi^2 R^6}\ P\ \dot{P}\right)^{\frac{1}{2}} \quad \text{(CGS)} \end{aligned} \tag{2.8}$$

and the magnetic field at the light cylinder will be determined by the radius of the light cylinder R_{LC} which may be deduced in turn from the period P: $R_{LC} = \frac{P\,c}{2\,\pi}$. The light cylinder is the total virtual surface delimited by the azimuthal velocity of the co-rotating magnetic field reaching the speed of light. In Figure 2.3, the $P - \dot{P}$ diagrams shows the distribution of the pulsars based on the magnetic field strength in the given parameter space : strong surface dipole magnetic fields ($B_{dipole} > 10^{11}$ G) at the upper side of the diagram while the light cylinder magnetic field is stronger ($B_{LC} > 1000$ G) for pulsars with short and less variable spin periods at the left side of the diagram. The magnetic-field at the light cylinder is derived as :

$$B_{LC} = B_{dipole}\left(\frac{R}{R_{LC}}\right)^3 \tag{2.9}$$

In order to consider that the characteristic spin-down age is close to the age of the pulsar system, three strong assumptions have to be made :

- The initial spin period P_0 should be significantly shorter than the current rotational measured period P;
- The magnetic field emerging from the magnetosphere should be approximated as constant in time with insignificant variability;
- The spin-down of the pulsar should be accounted only from dipolar magnetic braking.

With the previous assumptions in mind, one may interpret populations shown on the diagram in Figure 2.4 by using their distribution in this parameter-space as a congregation delimiter. Old yet fairly energetic pulsars concentrate towards the lower left side of the graph, having rotational periods of few milliseconds, while energetic ones and with spin-down characteristic ages of less than a million years are clustered in the mid-upper right part of the figure. It is thought that based on the time-evolution independence of the magnetic field, one may expect newly formed pulsars to start their life at the upper left corner of the $P - \dot{P}$ diagram and to gradually move to the right and bottom side along lines of constant dipolar B-field (Figure 2.3), crossing lines of constant characteristic spin-down age (Figure 2.4). It is expected that pulsars thought to be young, based on their characteristic age, shall be in the vicinity of the explosion locii (sites of birth) and therefore will be found within a supernova remnant. However, older pulsars are more prone to be observed as isolated pulsars. This may be explained in part by long age systems where the supernova shocked ejecta have expanded and the radiation coming from the shocked medium is fading. An additional plausible explanation is the possibility of energetic kicks occurring during the supernova and propelling the pulsars with strong proper motion that eventually allow them to escape their parent supernova remnant. Nevertheless the observed distribution of the pulsars in the $P - \dot{P}$ shows that the evolution of pulsars as their age increases is not fully described by the expected braking effect as supported by the study of Johnston et al. (2019)[16]

The $P - \dot{P}$ diagram has been often used as an evolutionary tool to highlight trends of populations in the parameter space. In Johnston and Karastergiou (2017)[69], observed neutron star parameters have been compared to simulated distributions of evolved pulsars with chosen initial parameters (period, period derivative, distance to Earth and angular separation α of the rotational and magnetic alignments) and with an initial braking index extracted from a normal distribution centered around $n = 2.8$, in order to diagnose the impact of such parameters on the evolution of pulsars. In this study it has been implied that either the inclination angle α varies with time significantly or that the magnetic field decays thus implying that the braking index n cannot be considered as time-independent, raising the urgence of not always granting the

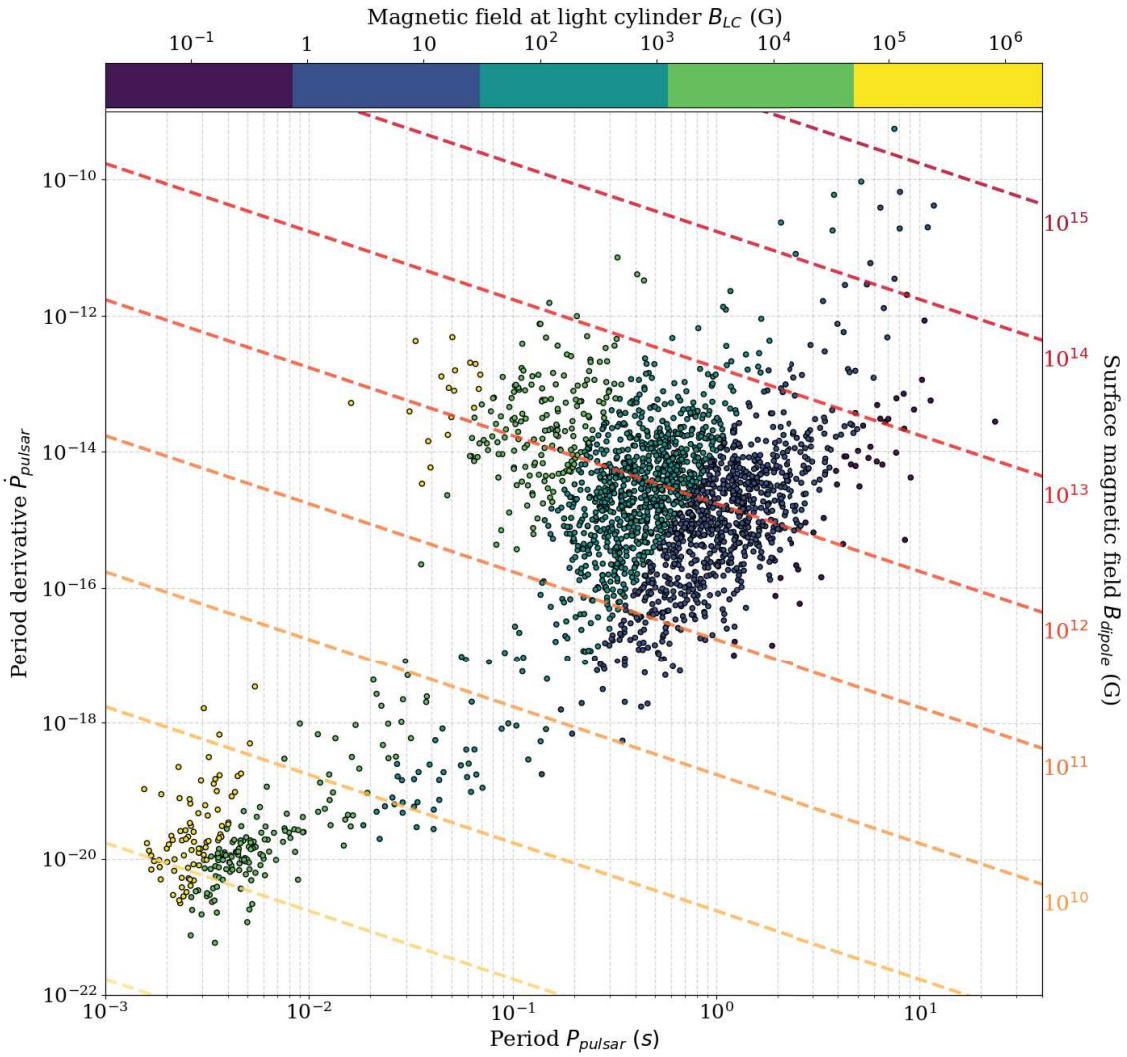

Figure 2.3 – $P-\dot{P}$ diagram showing (ATNF) catalogued (v1.6)[84] pulsars with measured periods P and period derivatives $\dot{P}$, without proper motion corrections. The dashed warm colour-gradient lines represent the parameter space for constant surface magnetic-field strength from a dipole assumption B_{dipole} ranging from 10^7 to 10^{15} G. The colourmap shown on top of the graph codes the value of the magnetic-field B_{LC} at the light-cylinder for each pulsar, ranging from 0.05 to 2.10^6 G.

conventional $n = 3$ value of evolution scenarii. In Figure 2.4, the mature pulsars are expected to move vertically in the parameter space and should yield larger braking indices. On the other hand, young pulsars with smaller angular axis separations α ought to have more important braking effects. In the aforementioned study the characteristic spin-down age $\tau_{spin-down}$ is significantly and consistently greater than the age of the middle-aged pulsars.

Millisecond pulsars are extremely rapidly rotating pulsars with very short time periods and particularly low spin-down rates. Combined with their high probability of having a companion object as part of binary systems, the *millisecond* pulsar population is distinct to the non-millisecond

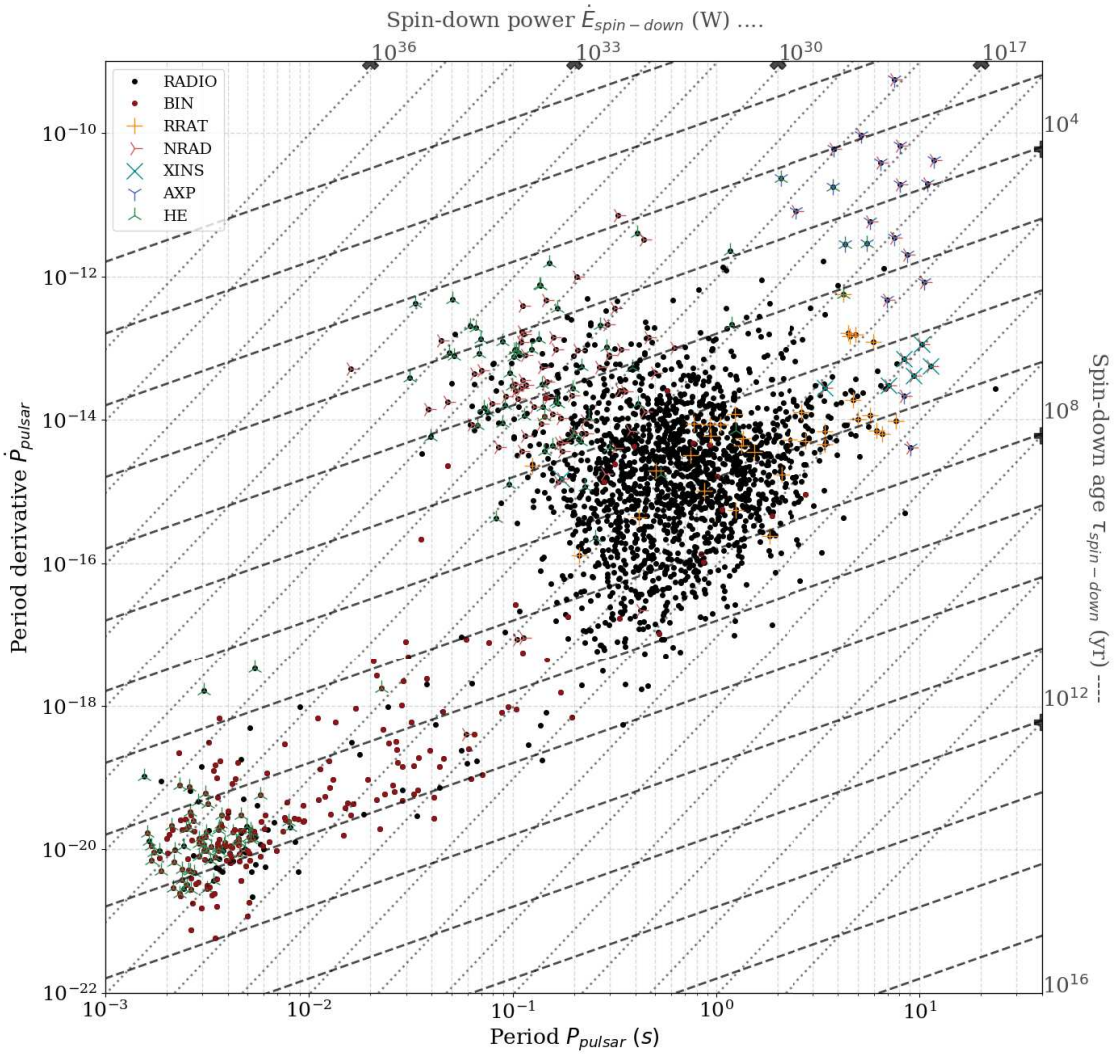

Figure 2.4 – $P - \dot{P}$ diagram showing 2 259 pulsars from the *Australian Telescope National Facility* (ATNF) catalogue [84] with measured periods P and period derivatives $\dot{P}$, without proper motion corrections. The *AXP* label stands for anomalous X-ray emitting pulsars with detected pulsations, which consist of magnetars, *HE* stands for the spin-powered pulsed emission pulsars with emission from radio up to to infra-red or higher energies, whereas the *NRAD* ones represent pulsars emitting on infra-red or higher energies. The *RRAT* marked pulsars are the ones with intermittent detected emission and the *XINS* are the isolated neutron stars with detected pulsed X-ray emission but with no radio counterpart observed. The *RADIO* labeled neutron stars are the isolated radio pulsars and the *BIN* ones are the ones with at least one detected stellar companion star part of a binary (or multiple) system. The dashed lines represent the parameter space for constant characteristic ages $\tau_{spin-down}$ ranging from 10 to 10^{16} years and the dotted lines represent the ones for a constant spin-down power $\dot{E}_{spin-down}$, ranging from 10^{17} to $10^{37} erg.s^{-1}$.

ones as having undergone a different evolution such as accretion from their binary companion for example. Thus they are consider by mosts as unrelated in evolutionary traits to young and middle aged pulsars.

Pulsars are created after core-collapsed supernovae and tend to be born nearby star formation regions in proximity of the galactic plane. They will progressively wander off towards higher galactic latitudes and lose energy up to a threshold dubbed as the "graveyard" zone limit on the graph; therefore there is an observational bias towards a younger thus more energetic neutron star population, located in the inner parts of the Milky way, along the galactic plane. Measurements of the so-called dispersion measure DM, i.e. the electron column density along the line of sight $DM = \int_0^d n_e dl$, provide an estimation of the pulsar location when it comes to its distance d from Earth. The distance may also be constrained thanks to HI absorption of the associated radio { PWN-SNR } by studying the optical depth of the in sight interstellar medium. The distance is derived by column densities, which requires to have a good estimation of the interstellar medium density distribution along the galaxy or a Galactic rotation curve.

Neutron stars have an extremely dense composition and the state of the matter within it, is still not completely understood and debatable, constituting an interest of research among the particle physics and compact object scientific communities studying different unified equations of state. For example, one composition model would delimit a greatly dense quark or pion core ($10^{15} g.cm^3$ in a radius of 1 km) surrounded by a neutron, superfluid proton and electron medium ($10^{14} g.cm^{-3}$ in $80 - 90\%$ of the star radius), covered by a thinner and less dense coat ($10^{11} g.cm^{-3}$) of the same medium and outer-layered by an ionised iron crust. Depending on the composition of the crust and on its viscosity, the, in principal, stable rotation velocity of the pulsar may suddenly increase and then exponentially recover its previous rate. This pulsar glitch phenomenon has been observed in several cases for both radio and X-ray pulsars and showcases rotational irregularities.

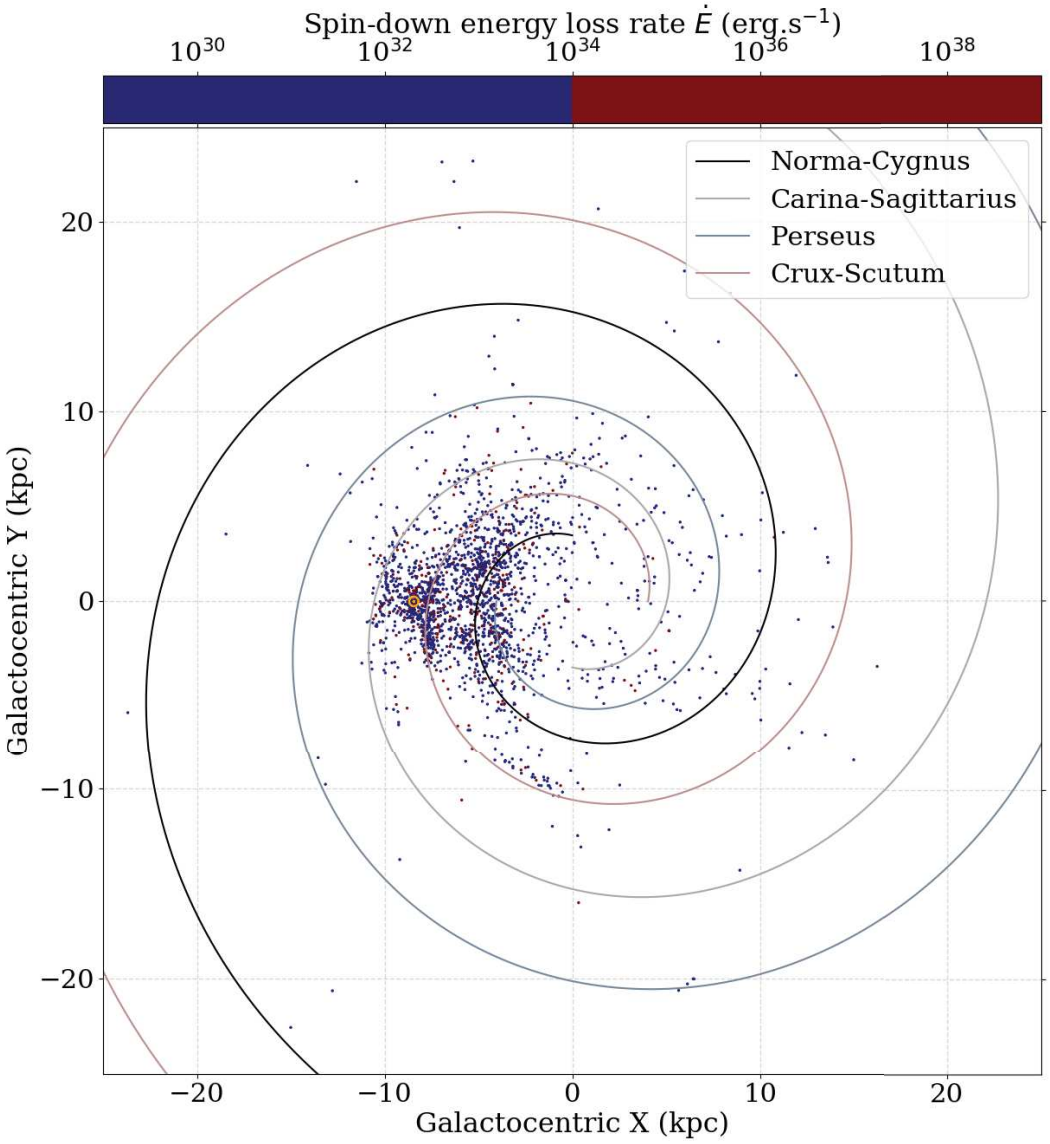

Figure 2.5 – Distribution of *ATNF* catalogued pulsars[84] overlaid on the Milky way spiral arm model from Faucher, Kaspi et al. (2006)[47], colour-coded by their energy loss rate. The orange ⊙ sign, represents the location of the Sun, which in the chosen model is set at $R = 8.5$ kpc

Another still not well understood conundrum would be the origin of electromagnetic collimated beams along the polar caps of the neutron star. It is thought that in the polar caps, at the regions nearby the magnetic field axis, the electric field is extremely strong and can be more important than the gravitational pull of the object thus "peeling-off" the ionised iron crust and conducting charged particles. If those particles are electrons, then they will form a negatively charged swarm called a "magnetosphere" in opposition of a rendered positively charged crustal surface. The magnetosphere will be composed of very energetic charged particles that may radiate synchrotron emission (Section 3.1).

Figure 2.6 – Schematic representation of a rotating pulsar. In this model, the rotation axis is separated by an angle α from the magnetic-field axis, the latter being a simple dipole approximation with, represented solely for illustration purposes, closed and "open" field lines (the latter ones are mis-represented and not based on analytical expressions). Several models conjecture that the twin collimated electromagnetic radio beam is emerging from the polar caps of the neutron star (*polar-cap model*) or that the light cylinder delimits an acceleration zone via electric potential gaps (*outer-gap model*) prone to induce only high-energy emission [131] .

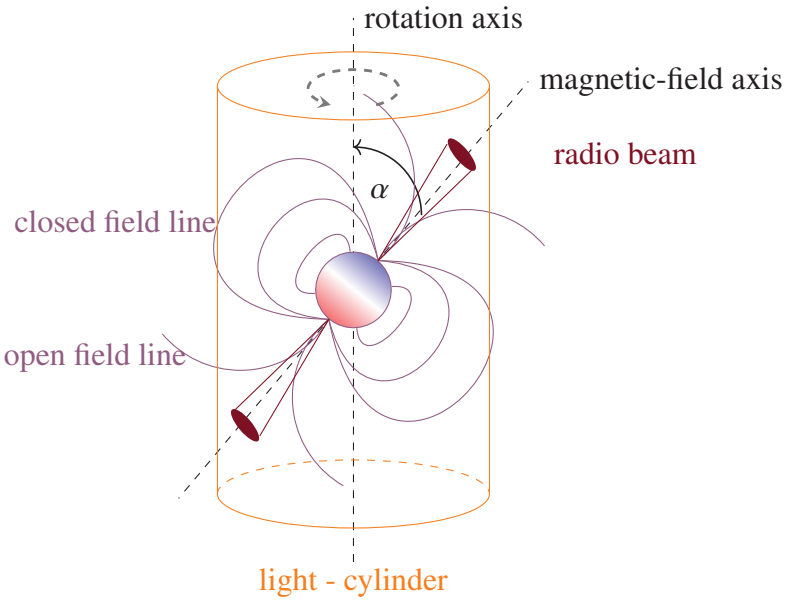

Pulsars and pulsar candidates (neutron stars with no confirmed detected pulsation) are the central engines that create and maintain the highly magnetised winds of electron and positrons, originating from their magnetospheres. They are characterised by their very rapid spin, which is the result from angular momentum conservation over the pulsar size ($\Omega \times R \sim constant$), and by their intense magnetic field, due to magnetic flux conservation over the pulsar surface ($B \times 4\pi R^2 \sim constant$).

2.2.2 Pulsars as leptonic cosmic-ray sources

Cosmic-rays are highly accelerated particles propagating in the Universe, with high (MeV-GeV) to ultra-high (ZeV) energy ranges. Even though the majority of cosmic-rays (up to 98%) are thought to be hadrons, a small fraction are expected to be positron and electrons. The cosmic-ray spectrum has been globally described as a power-law distribution over several energy orders, despite having two major features such as a steepening at 10^{15} eV (the PeV "knee"), a leveling at 10^{18} eV (the EeV "ankle"). A superficial overview of the all-particle spectrum is discussed in Section 3.3.

Conventionally, primary cosmic-rays, mainly protons, are produced and accelerated within supernovae remnants. Secondary cosmic-rays are produced through spallation of the primary ones onto the interstellar medium or by confinement nearby in situ molecular cloud regions. Pulsar systems are the main candidates as cosmic-ray engines below the knee and in recent years[57], the young and energetic pulsar population has been considered along with its generated

winds, as ultra-high cosmic-ray contributors. It is thought that the "knee" at PeV energies is the result of the shock acceleration of protons in supernova remnants in the Galaxy. Pulsars, along with their winds and nebular regions may also accelerate leptons up to high-energies ($\sim$ 10 GeV). Pulsar winds may show as well signatures of injection and acceleration of high-energy cosmic rays, through loading of heavy nuclei stripped from the neutron star surface.

2.2.3 The positron excess conundrum

Measurements from several experiments such as *AMS-02*[41], *PAMELA*[3], at $< 10^{15}$ eV have reported that the fraction of positrons (flux ratio $\frac{\Phi_{e^+}}{\Phi_{e^+ \& e^-}}$) compared to the electron one, increases from 10 to 200 GeV. The flux of the antimatter component of leptons cannot be explained by the amount of positrons produced by spallation reactions of primary cosmic-rays with the interstellar medium. This has been contradictory with most cosmic-ray origin and propagation models thus raising the importance of understanding the reason behind such a positron "excess", which has been attempted with millisecond pulsar models and with dark matter theoretical models as primary positron sources. A still very debatable topic would be to establish which of all the proposed mechanisms has a dominant contribution in the observed e^+ fraction.

Pulsar systems can provide valuable constraints in the search of explaining this excess, since their spectral energy distribution range from the radio band up to TeV gamma-rays. A key part in these studies is to model realistically the acceleration of the leptons within the confinement of the nebulae, understand the particle transport and then estimate the amount of released positron-electron pairs into the interstellar medium.

Recently, gamma-ray observatories amongst HAWC[55], Milagro, MAGIC[43] + VERITAS[106] and Fermi[43]) have reported the detection of extended VHE gamma-ray emission from the region of the *Geminga* and *Monogem* PWNe. These nebulae are spatially correlated with two bright ($\dot{E} \sim 1034$ erg.s^{-1}) and close to Earth ($\sim$ 0.25 - 0.30 kpc) pulsars, PSR 0633+1746 and PSR B0656+14 respectively. Based on the pulsar characteristic ages, which are of 342 kyr and 111 kyr *Geminga* and *Monogem* respectively, these two systems are old PWNe that are most likely relic PWN (see Section 2.4.3) while their once host supernova remnant has transitioned into a radiative stage and is fading away. Based on conventional pulsar-PWN-SNR evolution theory, that is presented in the following sections, these PWNe have escaped the SNR, given the kick velocity of the pulsar. At this stage the pulsar shall inject into its surrounding medium leptons that may form a "TeV halo" due to diffusion in the surrounding turbulent interstellar magnetic fields. Several studies are currently made so as to quantify the contribution originating from the PWNe and from the diffuse halo in regards to the electron-positron pairs consistent with the TeV spectrum.

When taking into account the number of reported detected pulsars, a cumulative positron emission originating from their pulsar winds and pulsar wind nebulae could be a plausible explanation of the positron fraction excess observed in the Galactic cosmic-ray spectrum. In Section 3.3.1 I discuss a little bit more in detail the leptonic cosmic-ray spectrum.

2.3 Pulsar wind

2.3.1 Pulsar particle outflow

The pulsar wind is thought to be predominantly composed by leptons (electron-positron pairs) with a possible small fraction of ions as well. It is an ultra-relativistic unshocked flow originating from the pulsar (Lorentz-factor $\gamma > 10$) characterised by a cold and highly magnetised upstream plasma (magnetisation $\sigma \gg 1$, see Equation 2.10), meaning that most of the energy transfer occurs as a Poynting flux ($\mu_0 \vec{\Pi} \propto \vec{E} \times \vec{B}$). This unshocked anisotropic wind as defined in the works of Spitkovski, Tchekhovskoy (2013)[119] ends in a defined spatial boundary, called the *termination shock* (TS), where the ram pressure of the pulsar unshocked wind is equalised by the pressure in the shocked wind of the pulsar wind nebula.

Pulsar wind nebulae are expanding bubbles filled by relativistic leptons in a relatively weak ambient magnetic field ($\sim 10\,\mu$G), inflated through the action of the pulsar via its generated wind pumping the circumstellar medium and depositing energy in the form of relativistic magnetised particles. It is considered that within this bubble, the B-field is coupled to the relativistic pairs, which could imply equipartition. However these nebulae show a weakly magnetised ($\sigma \sim 0.01$) and non-thermal plasma in opposition to the pulsar wind thus raising the question of how to reconcile the magnetisation of the termination shock upstream and downstream wind components. This would imply that there must be an extremely efficient magnetic-to-kinetic energy transfer in the pulsar wind, requiring strong magnetic dissipation in the upstream region or in the shock itself. This issue has been a long term conundrum in the relativistic magnetised outflow (PWNe, AGNi, GRBs) scientific community dubbed the "σ problem"[82] :

$$\sigma = \frac{||B||^2}{\mu_0\, n_{plasma}\, \gamma\, m\, c^2} \tag{2.10}$$

It has been speculated that a dissipation mechanism able to explain the σ-problem[92] could be related to the "striped" structure of the pulsar wind[19]. In *striped wind* models, there is a change of the magnetic field direction that induces the formation of corrugated current sheets that outside of the light cylinder separates opposite magnetic polarity plasma regions[80][42]. The current sheet would be prone to magnetic reconnection[114], which could explain powerful particle acceleration in the relativistic regime. Recent studies have shown that the striped component of the wind is annihilated before reaching the nebula yet large scale current sheets remain at the equatorial regions and could be broke into several magnetic islands (plasmoids) separated by secondary short current sheets. Large plasmoids may confine more energetic particles and they tend to merge with each other multiple times, as long as adiabatic expansion is not overpowering the magnetic island formation.

The pulsar wind determines spatially the region of the pulsar wind nebula formation. In Spitkovski (2006)[116], using magneto-hydrodynamic simulations, the author expresses the pulsar spin-down power from the force-free magnetosphere, of a neutron star with a magnetic dipole assumption, depending on the obliquity α, the angle between the rotation and magnetic-field axes. Equation 2.11 shows this dependency, where from $\alpha = 0°$ (aligned rotator) to $\alpha = 90°$ (perpendicular rotator) the spin-down power fluctuates by a factor of two, illustrated in Figure 2.7.

$$\dot{E}_{spin-down} = \frac{1}{4c^3}\, B^2_{dipole}\, R^6_{PSR}\, \Omega^4\, (1 + sin^2\alpha) \tag{2.11}$$

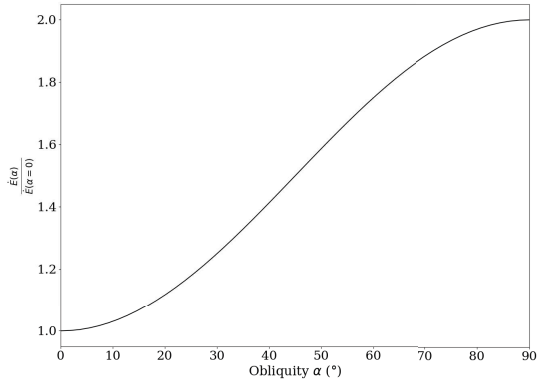

Figure 2.7 – Energy spin-down $\dot{E}(\alpha)$ compared to an aligned rotator $\alpha = 0°$ depending on obliquity based on Equation 2.11.

2.3.2 Pulsar wind termination shock

As mentioned in Section 2.3.1, the termination shock separates the upstream pulsar wind, which is unshocked highly magnetised plasma, and its downstream region, which is the beginning of the pulsar wind nebula bubble. In order to compute the termination shock position radius, from now on referred to as the *termination shock* (TS or R_{PW}), we use its definition as the balance of the wind ram pressure P_{PW} with the nebula pressure P_{PWN} 2.12 and then derive as follows afterwards the analytical form of the pulsar wind radius evolution.

$$\begin{aligned} p_{PWN} &\approx p_{PW} \\ \frac{1}{3}\frac{\frac{5}{11}\dot{E}\ t_{PWN}}{\frac{4\pi}{3}R_{PWN}^3} &\approx \frac{\dot{E}}{6\pi c R_{PW}^2} \end{aligned} \tag{2.12}$$

Using the Equation 2.12 equality, the radius of the pulsar wind R_{PW} may be defined as a function of the velocity of the pulsar wind nebula expansion $v_{PSR} = \frac{R_{PWN}}{t_{PWN}}$:

$$\begin{aligned} R_{PW} &= R_{PWN}\ \sqrt{\frac{22}{15c}}\ \sqrt{v_{pwn}} \\ R_{PW} &\approx R_{PWN}\ \left(\frac{22}{15\ c}\right)^{\frac{1}{2}} \left(\frac{k_{inertia}}{\Xi\Psi}\frac{M_{PSR}}{M_{ej}}\right)^{\frac{1}{4}} \left(R_{PSR}\ \frac{2\pi}{P}\right)^{\frac{1}{2}} \\ R_{PW} &\sim R_{PWN}\ \left(\frac{44\pi}{15\ c}\right)^{\frac{1}{2}}\ \left(\frac{4}{5}\right)^{\frac{1}{4}}\ \left(\frac{M_{PSR}}{M_{ej}}\right)^{\frac{1}{4}} \left(R_{PSR}\ \frac{1}{P}\right)^{\frac{1}{2}} \end{aligned} \tag{2.13}$$

with

$$\begin{aligned} \Xi\ E_{kin} &\approx E_{rot} \\ \Xi\ \frac{1}{2}\ \Psi M_{ej}\ v_{PWN}^2 &\approx \frac{1}{2}\ I\ (\Omega_0 - \Omega)^2 \\ v_{PWN} &\approx 2\pi\ \sqrt{\frac{k_{inertia}}{\Xi\Psi}\ \frac{M_{PSR}}{M_{ej}}}\ R_{PSR}\left(\frac{1}{P}\right) \end{aligned} \tag{2.14}$$

where we consider that the spin period $P_0 \ll P$ based on a conventional pulsar spin-down rate, that the pulsar inertia moment is the one assumed with spherical symmetry ($k_{inertia} = \frac{2}{5}$)

and that the rotational energy provided by the pulsar is converted to a fraction of $\Xi \sim 0.5$ of the kinetic pulsar wind nebula energy, with $M_{PWN} = \Psi M_{ej}$, where $\Psi \leq 1$.

This computation allows us to be able to estimate the termination shock of the pulsar wind, provided that we know the size of the pulsar wind nebula and its evolution with time.

2.3.3 Contact discontinuity and fluid instabilities

When shocks propagate in different density and proper velocity media, one may expect that the shocked fronts may leave behind contact discontinuities at the interface of two adjacent media. In the pulsar wind paradigm, there are two contact discontinuity shock-produced boundaries : one separating the shocked pulsar wind material from the shocked ejecta and another occurring at the shocked ejecta - shocked interstellar medium interface.

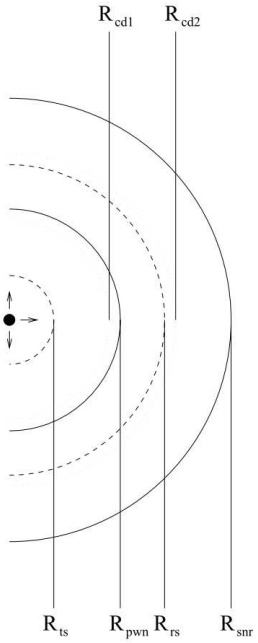

Figure 2.8 – Here is a schematic representation of the termination shock R_{ts}, pulsar wind nebula size R_{pwn} and the reverse R_{rs},forward shock of the supernova remnant R_{snr}. The contact discontinuities discussed above, are marked as R_{cd1} and R_{cd2}. Figure taken from van der Swaluw, Gallant et al. (2001)[129]

If one assumes a fluid-like behaviour for the pulsar wind, it should be confined within the contact discontinuity bounding the non-thermal pulsar wind component. At this contact discontinuity, the two local media can be approximated as two superimposed fluids. Thus *Kelvin-Helmholtz* and shear instabilities generated by the two fluids relative velocity between the unshocked wind and its shocked tail shall occur during small time scales however they shall be negligible compared to the *Rayleigh-Taylor* instabilities[101] generated by the difference of density (lighter medium pushing through the heavier one) between the media. Stream instabilities shall create local small-scale mixtures, that may produce filamentary structures within the shell of the shocked medium[100], [118].

Figure 2.9 – Illustration of a formed *Rayleigh-Taylor* instability at the contact discontinuity of a forward shock-wave propagating in a different density medium. This image is one of our discarded simulation sanity tests that we have produced with a hydrodynamic code that as mentioned on Chapter 7.

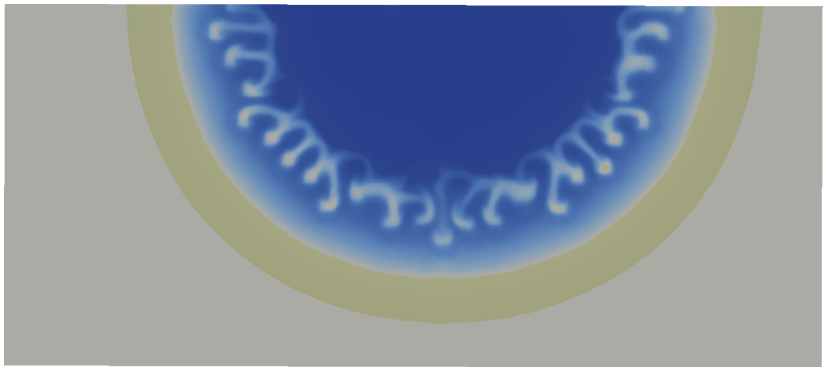

2.4 Pulsar wind nebula evolution within a supernova remnant

Pulsar wind nebulae (PWNe) are initiated by the termination shock (TS) created by the pulsar wind (PW) and are usually embedded within the supernova remnant (SNR), constituting a so-called *composite* system. Shell-type supernova remnants are the result of the progenitor star envelope ejecta interacting with the interstellar medium. They are characterised by their dynamical evolution and by the expectation that radiative losses are not affecting significantly their development until late phases. The SNR dynamics are defined by a free expansion (FE) initial stage where the ejecta dominate the growth of the nebula and by an adiabatic evolution phase named the *Sedov-Taylor* stage (ST) occurring later on. In this section we shall not focus on the later evolution of the system.

2.4.1 Free expansion phase : ejecta dominated stage

The free expansion (FE) stage begins with the supernova and the ejection of stellar matter onto the ambient medium. The ejecta will be supersonic, travelling with velocities greater than the speed of sound c_s in the given medium, thus a shockwave propagating outwards shall precede the propulsed ejecta into the surrounding medium. This shockwave is called the forward shock (FS) of the supernova remnant, determining the extent of the latter, by compressing and accelerating the interstellar medium through the physical excitation caused by the blast-wave.

2.4.1.1 Supernova remnant shock propagation

During this ejecta-dominated phase, the unshocked matter within the supernova remnant will freely expand and may be approximated to a spherical fluid confined in a pressurised bubble. The central pulsar will keep on injecting power and leptons into the system through its wind and the swept-up interstellar medium shall be accelerated. In order to model the expansion of the supernova remnant, we shall use the parametrisation of Truelove and McKee (1999)[124]. Based on the Euler equations of hydrodynamics (see Equation 2.24, 2.25, 2.26) and an ideal monoatomic gas equation of state ($\Gamma = \frac{5}{3}$) , dictating the expected evolution of size, velocity, pressure and density, we will consider the following parametrisation for an assumed uniform ambient medium obtained in their paper :

$$\begin{aligned} R_{SNR,\,FS\,|FE} &= R_{ch}\left[2.01\left(\frac{t}{t_{ch}}\right)\left(1+1.72\left(\frac{t}{t_{ch}}\right)^{\frac{3}{2}}\right)^{-\frac{2}{3}}\right] \\ R_{SNR,\,RS\,|FE} &= R_{ch}\left[1.83\left(\frac{t}{t_{ch}}\right)\left(1+3.26\left(\frac{t}{t_{ch}}\right)^{\frac{3}{2}}\right)^{-\frac{2}{3}}\right] \end{aligned} \tag{2.15}$$

where the authors of [124] have defined the characteristic scales for the time and radius dimensions as :

$$\begin{aligned} R_{ch} &\equiv \left(\frac{M_{ej}}{\mu_H\, n_0}\right)^{\frac{1}{3}} \\ t_{ch} &\equiv E_{SN}^{-\frac{1}{2}}\, M_{ej}^{\frac{5}{6}}\, (\mu_H n_0)^{-\frac{1}{3}} \end{aligned} \tag{2.16}$$

with $\mu_H = 1.4 \times 1.6 \times 10^{-24}$ g, the ambient density number n_0, the ejecta mass M_{ej} and energy the energy explosion E_{SN}.

The reverse shock of the supernova remnant shall follows the same progression as the forward shock and during the free expansion stage they co-evolve, as illustrated in Equation 2.15 where the radii of the blast-wave and the reverse shock have a dominant linear dependence with time $R \sim t$.

2.4.1.2 Pulsar wind nebula expansion

While the supernova remnant is expanding, the central pulsar engine will create a powerful wind that shall shock the circumstellar ejecta and form a nebula of electron and positron pairs. The pulsar wind nebula is defined starting from the termination shock of the pulsar wind, determined in Section 2.3.2 and approximated in Equation 2.13. It will expand freely and form a bubble of shocked material. To estimate the evolution of the pulsar wind nebula radius R_{PWN} we follow the model of the evolution of this bubble within the supernova remnants by Chevalier and Fransson (1992)[21]. We use the typical values of their model parameters $n_{in} = 0$ and $n_{out} = 9$ (which approximately corresponds to the case of $n_{out} \to \infty$) of power-law density profile. approximations for the inner ρ_{in} and outer ρ_{out} sections of the nebula respectively defined[20] as :

$$\rho_{in|out} = C(n_{in}, n_{out})\, R^{-n_{in|out}}\, t^{n_{in|out}-3} \tag{2.17}$$

Using their proposed solution of the dynamical equations in the phase where the pulsar energy input $\dot{E}$ may be considered approximately constant, the radius R_{PWN} is equal to :

$$\begin{aligned} R_{PWN} &= \left[\frac{(5-n_{in})^3\,(3-n_{in})}{(11-2n_{in})\,(9-2n_{in})} \frac{\dot{E}}{4\pi C(n_{in}, n_{out})} \right]^{\frac{1}{(5-n_{in})}} t^{\frac{6-n_{in}}{5-n_{in}}} \\ &\textit{with} \\ C(n_{in}, n_{out}) &= \left(\frac{n_{out}-3}{n_{out}-n_{in}} \right) \left[\frac{(3-n_{in})(n_{out}-3)}{2(5-n_{in})(n_{out}-5)} \frac{M_{ej}}{E_{SN}} \right]^{\frac{(3-n_{in})}{2}} \frac{(3-n_{in})}{4\pi} M_{ej} \end{aligned} \tag{2.18}$$

The radius of the pulsar wind nebula in the ejecta-dominated stage is then reduced to :

$$R_{PWN} \approx 1.44 \times \dot{E}^{\frac{1}{5}}\, E_{SN}^{\frac{3}{10}}\, M_{ej}^{-\frac{1}{2}}\, t^{\frac{6}{5}} \tag{2.19}$$

2.4.2 Sedov-Taylor phase : adiabatic evolution

The *Sedov-Taylor* (ST) stage commences when the reverse shock resulting from the outward blast-wave being impeded by the ambient interstellar medium starts shocking inner region ejecta thus gradually accelerates its movement towards the centre. The reverse shock shall reach the shell of the pulsar wind bubble and will interact with it.

2.4.2.1 Supernova remnant reverse shock interaction

The opposition caused by the interstellar medium barrier onto the shocked ejecta at the blast-wave front will induce a reverse shockwave back through the interior of the system. While propagating onto the centre, this shock will reverse its direction of motion of at a finite time causing an implosion until it reaches the pulsar wind nebula shell. Then the accumulated hot material behind the reverse shock will start compressing. Thus the kinetic energy of the compressed ejecta will start converting into thermal energy producing a hot shell of gas. In turn it will inflate and its expansion will hereafter become supersonic, producing a second forward shock travelling outwardly. This will have as a result the eventual generation of a second reverse

shock once the secondary forward shock has reached the interface of the shocked ejecta with the interstellar medium. This forward and reverse shockwave subsequent creations will occur until the expansion of the shocked matter barriers stops being supersonic. This compressions and reverberations will be transited by an oscillation of the contact discontinuity of the nebula until the PWN bound relaxes its adiabatic phase evolution [40].

At the discontinuity contact interface (Section 2.3.3), *Rayleigh-Taylor* instabilities will greatly grow and create turbulent flow. The heavy mixing between the two different density media will at some point fade the frontier defined by the contact discontinuity.

The continuity of motion and of the shock and the non-radiative evolution assumption, allows to use the general *Sedov-Taylor* solution for spherical, self-similar blast-waves in a uniform ambient medium, where the shockwave will have a non-linear time dependence : $R \sim t^{\frac{2}{5}}$. This is derived from the continuity Euler equations of hydrodynamics (Equation 2.21 for matter conservation, Equation 2.22 for velocity conservation and Equation 2.23 for energy conservation) set up in a spherical symmetry framework, in space ($\vec{g} = \vec{0}$) and with a barotropic relation $p = P(\rho)$ for an isentropic case where $P(\rho) = \rho^{\Gamma}\, c_s^2$ with $\Gamma = \frac{5}{3}$ for an ideal monatomic gas, which yield the conservation equations 2.24, 2.25 and 2.26. The energy conservation equation has been altered based on the first law of thermodynamics, stating that the exchange of heat of a system is the sum of the difference in its internal energy and its pressure per change of volume, which allows to express the total energy of the system E per unit volume (or mass) as the sum of its internal energy E_{int}, its kinetic energy ($\frac{1}{2}v^2$ and its pressure (p) per unit of mass or volume.

Following the *Sedov* similarity solution[15] to simplify this set of equations by assuming that the fluid density, motion and energy may be reduced to depend only on time and radius as illustrated by Equation 2.20, showing the shockwave radius R_{sh} and velocity v_{sh}, where ξ_0 is a dimensionless quantity depending on the adiabatic index Γ. We will adopt the same value of $\xi_0 \approx 2.026$ as [124].

$$\begin{aligned} R_{sh} &= \left(\xi_0 \frac{E_0}{\rho_0}\right)^{\frac{1}{5}} t^{\frac{2}{5}} \\ v_{sh} &= \frac{2}{5}\frac{R_{sh}}{t} = \frac{2}{5}\left(\xi_0 \frac{E_0}{\rho_0}\right)^{\frac{1}{5}} t^{-\frac{3}{5}} \end{aligned} \tag{2.20}$$

General expression of continuity Euler equations of hydrodynamics:

$$equation\ of\ density\ :\ \frac{\partial \rho}{\partial t} + div(\rho \vec{v}) = 0, \tag{2.21}$$

$$equation\ of\ motion\ :\ \rho\left[\frac{\partial \vec{v}}{\partial t} + (\vec{v}.\nabla)\vec{v})\right] = -\nabla p + \rho \vec{g}, \tag{2.22}$$

$$equation\ of\ energy\ :\ \frac{\partial E}{\partial t} + \nabla(E + p)\vec{v} = \rho \vec{v}.\vec{g} \tag{2.23}$$

Spherical symmetry expression of hydrodynamics equations for blast-wave shock:

$$\frac{\partial \rho}{\partial t} + \frac{1}{r^2}\frac{\partial}{\partial r}(r^2 \rho v) = 0, \tag{2.24}$$

$$\frac{\partial v}{\partial t} + v\frac{\partial v}{\partial r} + \frac{1}{\rho}\frac{\partial p}{\partial r} = 0, \tag{2.25}$$

$$\frac{\partial}{\partial t}\left[\rho\left(E_{int} + \frac{1}{2}v^2\right)\right] + \frac{1}{r^2}\frac{\partial}{\partial r}\left[r^2 \rho v\left(E_{int} + \frac{p}{\rho} + \frac{1}{2}v^2\right)\right] = 0 \tag{2.26}$$

The reverse shock will have a more complex evolution standing apart from its initial co-evolution with the forward shock, accelerating towards the centre of the remnant and reaching the pulsar wind nebula where it shall merge with the shocked ejecta in the PWN. We can estimate using Truelove and McKee' parametrisation (for $n_{in} = 0$, based on their Equation 71) that the Sedov-Taylor phase will start at approximately an age t_{ST} :

$$\begin{aligned} t_{ST} &= 0.495 \times E_{SN}^{-\frac{1}{2}}\, M_{ej}^{\frac{5}{6}}\, (\mu_H n_0)^{-\frac{1}{3}} \\ &\approx \frac{1}{2} \times t_{ch} \\ &\sim \frac{1}{2} \times 1.65 \left[\left(\frac{E_{SN}}{10^{51}\, erg}\right)^{-\frac{1}{2}} \left(\frac{M_{ej}}{5\, M_\odot}\right)^{\frac{5}{6}} \left(\frac{n_0}{1\, cm^{-3}}\right)^{-\frac{1}{3}}\right] kyr \end{aligned} \tag{2.27}$$

Following the same model of [124] cited in Section 2.4.1.1, the forward and reverse shocks in the adiabatic evolution stage occurring in a uniform density environment at starting at t_{ST} (Equation 2.27) are positioned from the centre of the supernova remnant as (table 5 from [124]):

$$\begin{aligned} R_{SNR,\, FS\, |ST} &= R_{ch}\, \left(1.42\left(\frac{t}{t_{ch}}\right) - 0.254\right)^{\frac{2}{5}} \\ R_{SNR,\, RS\, |ST} &= R_{ch}\, \left(\frac{t}{t_{ch}}\right)\left[0.779 - 0.106\left(\frac{t}{t_{ch}}\right) - 0.533\, ln\left(\frac{t}{t_{ch}}\right)\right] \end{aligned} \tag{2.28}$$

Table 2.1 – Sedov-Taylor (ST) regime timescale for different explosion energy E_{SN}, ejected mass M_{ej} and ambient density numbers n_0 combinations. The beginning of the ST evolution phase is of the order of the characteristic time scale t_{ch} (Equation 2.16), its end is of the order of the transition to radiative stage t_{tr} timescale (Equation 2.31). The bold values depict the extrema for these sets of input parameters : earliest ST transition, latest ST transition, shortest ST phase and longest ST phase. Systems with massive ejecta propagating into low density environments without an extreme energy input will transition to the ST stage in timescales of the order of $\sim$ 10 kyr, while the less massive yet energetic ejecta in dense media will transition to the ST phase in a few hundred year lifetime. The longest adiabatic phases depend on fairly energetic explosions whilst the shortest ones happen for massive ejecta in dense media. The transition from *Sedov-Taylor* to *snow-plough* stage occurs at $\sim 10 - 500$ kyr.

t_{ch} (kyr)	t_{tr} (kyr)	ST duration (kyr)	E_{SN} (10^{51} erg)	M_{ej} ($M_\odot$)	n_0 (cm^{-3})
0.2	18.1	17.9	5.0	2.0	5.0
0.3	42.4	42.0	5.0	2.0	1.0
0.4	12.4	11.9	1.0	2.0	5.0
0.5	18.1	17.6	5.0	6.0	5.0
0.6	10.5	9.9	0.5	2.0	5.0
0.7	143.3	142.6	5.0	2.0	0.1
0.8	29.0	28.2	1.0	2.0	1.0
0.8	18.1	17.3	5.0	10.0	5.0
0.9	42.4	41.5	5.0	6.0	1.0
1.1	24.6	23.6	0.5	2.0	1.0
1.1	12.4	11.3	1.0	6.0	5.0
1.3	42.4	41.0	5.0	10.0	1.0
1.6	10.5	8.9	0.5	6.0	5.0
1.6	98.1	96.5	1.0	2.0	0.1
1.6	484.9	**483.3**	5.0	2.0	0.01
1.7	12.4	10.7	1.0	10.0	5.0
1.8	143.3	141.5	5.0	6.0	0.1
1.9	29.0	27.1	1.0	6.0	1.0
2.3	83.4	81.0	0.5	2.0	0.1
2.4	10.5	**8.1**	0.5	10.0	5.0
2.7	24.6	21.9	0.5	6.0	1.0
2.8	143.3	140.5	5.0	10.0	0.1
2.9	29.0	26.1	1.0	10.0	1.0
3.6	332.1	328.5	1.0	2.0	0.01
4.0	484.9	481.0	5.0	6.0	0.01
4.1	24.6	20.5	0.5	10.0	1.0
4.1	98.1	94.0	1.0	6.0	0.1
5.0	282.1	277.1	0.5	2.0	0.01
5.8	83.4	77.5	0.5	6.0	0.1
6.1	484.9	478.9	5.0	10.0	0.01
6.3	98.1	91.8	1.0	10.0	0.1
8.9	83.4	74.4	0.5	10.0	0.1
8.9	332.1	323.2	1.0	6.0	0.01
12.6	282.1	269.5	0.5	6.0	0.01
13.6	332.1	318.5	1.0	10.0	0.01
19.2	282.1	262.9	0.5	10.0	0.01

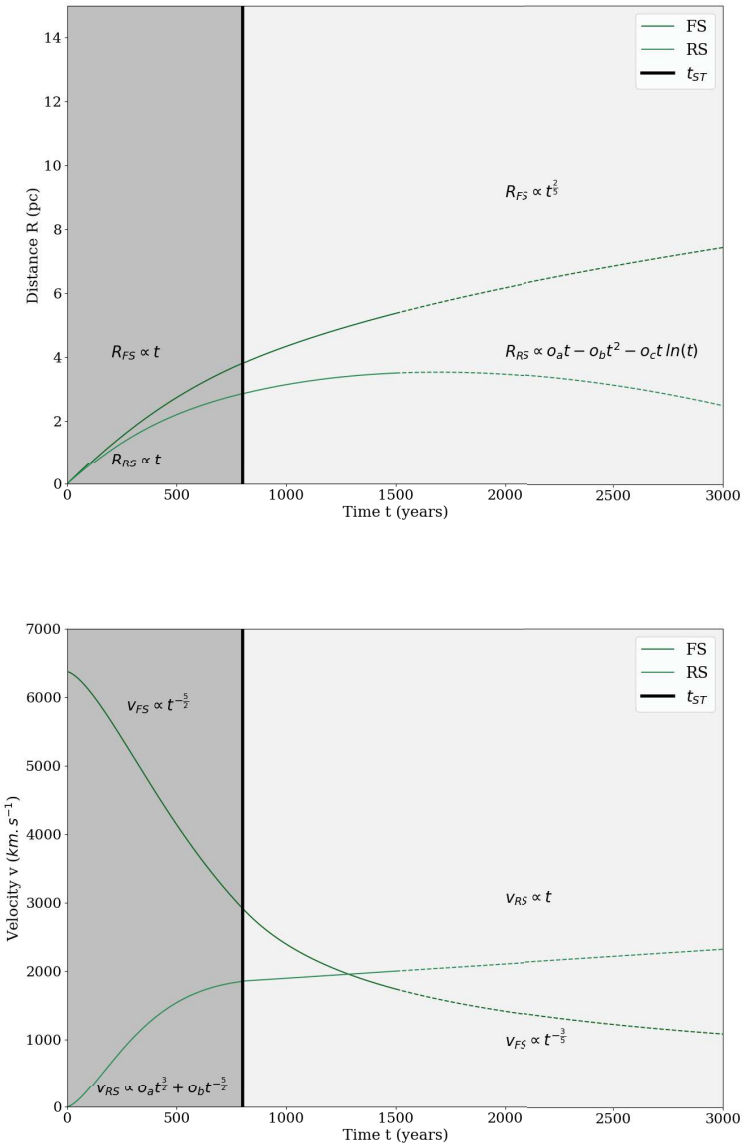

Figure 2.10 – Evolution of the forward (FS) and reverse (RS) shocks propagation after a supernova explosion. The solid thick black line delimits the start of the *Sedov-Taylor* stage (light grey area) at t_{ST} and the end of the free expansion regime (darker grey area). Distance to the centre of the explosion up to the shock front evolution with time on the bottom panel and evolution of the shock velocity on the top panel. In this example, the influence of the central pulsar and its environments have been omitted, the dotted lines trace the evolution beyond the hypothetical time when the reverse shock reaches the pulsar wind nebula. The parameters for the supernova remnant have been chosen as such : $E_{SN} = 10^{51}\ erg$, $M_{ej} = 5M_{\odot}$ and $n_0 = 1.0\ cm^{-3}$, for a uniform ejecta case ($n_{in} = 0$ [124]).

2.4.2.2 Pulsar wind nebula confinement and compression

The reverse shock of the supernova remnant will collide with the pulsar wind nebula after a few kyr (Table 2.1) have passed since the birth of the system. The reverse shock will compress the nebula which will yield a pressure increase and a subsequent expansion of the PWN. This will

result into several successive interactions of the shock with the nebula leading to oscillations of the PWN size over a few thousand of years and the development of more *Rayleigh-Taylor* instabilities at the contact discontinuity interface at the pulsar wind nebula bubble limit[70].

Once the reverberations of the reverse supernova remnant shock and the pulsar wind nebula have ceased, the pulsar wind nebula will continue to expand through the action of the pulsar injecting wind power to the system. Nevertheless, this steady subsonic expansion will happen in hot shocked ejecta and two cases will ensue depending on the timescales compared to the braking of the pulsar. If the pulsar has significantly slowed down and its current energy input is negligible for evolution purposes, the pressure equilibrium with the Sedov blast-wave behaviour will occur : the PWN is no longer freely expanding but its pressure evolves as that of an adiabatic relativistic fluid of index $\Gamma = \frac{4}{3}$. Thus the pressure P of the bubble will follow $P \propto R^{-4}$ meaning that it shall expand with time as $R \propto t^{\frac{3}{10}}$ based on the Sedov blast wave time dependence $R \sim t^{\frac{2}{5}}$ [111] (Section 2.4.2.1). On the other hand, if the pulsar has not significantly slowed down in the beginning of the adiabatic evolution phase of the nebula, then its size should expand with time as $R \propto t^{\frac{11}{15}}$, deduced by considering the contact discontinuity condition where the pressure of the pulsar wind nebula P_{PWN} should be equal to the supernova remnant interior pressure P_{SNR}, as expressed in Equation 2.29. [129].

Since most cases with conventional astrophysical input parameters yield characteristic timescales t_{char} of a few thousand years (Table 2.1) and the beginning of the *Sedov-Taylor* phase t_{ST} is of the same order as t_{ch} it is most likely that the pulsar has started braking considerably enough to decrease the expansion rate of the pulsar wind nebula.

$$
\begin{aligned}
p_{PWN} &\approx p_{SNR} \\
\dot{E}\ t\ R_{PWN}^{-3} &\approx E_{SN}\ R_{SNR\ FS\ |ED}^{-3} \\
&\textit{which yields} \\
R_{PWN} &\approx \left(\frac{\dot{E}\ t}{E_{SN}}\right)^{\frac{1}{3}}\ R_{SNR\ FS\ |ST} \\
&\approx \left(\frac{\xi_0}{\mu_H}\right)^{\frac{1}{5}}\ \dot{E}^{\frac{1}{3}}\ E_{SN}^{-\frac{2}{15}}\ n_0^{-\frac{1}{5}}\ t^{\frac{11}{15}}
\end{aligned}
\tag{2.29}
$$

At the same stage, the termination shock (TS), which consists the inner bound of the PWN may be found by equating the pressure of the pulsar wind with the pressure of the pulsar wind nebula. The PWN is in pressure equilibrium with the supernova remnant thus :

$$
\begin{aligned}
p_{PW} &\approx p_{PWN} \approx p_{SNR} \\
\frac{\dot{E}}{4\pi c R_{PW,\,TS}^2} &\approx \frac{E_{SN}}{\frac{4}{3}\pi R_{SNR}^3} \\
&\textit{which yields} \\
R_{PW,\,TS} &\approx \left(\frac{1}{3c}\right)^{\frac{1}{2}}\ \left(\frac{\xi_0}{\mu_H}\right)^{\frac{3}{10}}\ \dot{E}^{\frac{1}{2}}\ E_{SN}^{-\frac{1}{5}}\ n_0^{-\frac{3}{10}}\ t^{\frac{3}{5}}
\end{aligned}
\tag{2.30}
$$

2.4.3 Snow-plough phase

The *Sedov-Taylor* stage will alter either if the pulsar exits the system or if the latter is no longer adiabatic. In Chapter 6, we shall consider the configuration of a pulsar with proper motion leaving the confinement of the supernova remnant. The pulsar wind nebula inside the supernova

remnant will become a *relic PWN* because it will no longer be pulsar power-driven and the supernova remnant will transition to a radiative state.

The adiabatic phase ends when the cooling time of the hot gas bubble is comparable or shorter than the age of the system. In Blondin et al. (1998)[14] they model the supernova remnant during this radiative late evolution stage, considering it as a thin high density spherical shell of cooled gas confined by a radiative shock. This stage is called the *pressure-driven snow-plough* (PDS) phase, because of the pressure applied by the interior of the supernova remnant, still expanding adiabatically, to the thin shell, pushing it into the interstellar medium.

To estimate the age of transition t_{tr} from the adiabatic to the radiative phase, assuming that radiation losses are no longer negligible within the swept-up ejecta shell, the authors set the age of the system t found from the *Sedov-Taylor* blast-wave solution (velocity of the shock $v_{sh} = R_{sh}t^{-1}$, see Equation 2.20) equal to the cooling time t_{cool} depending on a temperature T volume cooling function $\Lambda(T) \sim (10^{16}\ T)^{-1}$ (in $erg.cm^3.s^{-1}$) and use the adiabatic shock relation of temperature and velocity : $T \propto v^2$.

$$\begin{aligned} t_{tr} = t &= t_{cool} \\ &\propto T^2\ n_0^{-1} \\ &\propto v^4\ n_0^{-1} \\ &\propto \left(\frac{R_{sh}}{t}\right)^4 n_0^{-1} \\ &\propto \left(E_{SN}^{\frac{1}{5}}\ n_0^{-\frac{1}{5}}\ t^{-\frac{3}{5}}\right)^4 n_0^{-1} \\ t &\propto E_{SN}^{\frac{4}{5}}\ n_0^{-\frac{9}{5}}\ t^{-\frac{12}{5}} \\ t &\propto E_{SN}^{\frac{4}{17}}\ n_0^{-\frac{9}{17}} \end{aligned} \tag{2.31}$$

which approximately yields :

$$t_{tr} = 2.9 \times 10^4 \left(\frac{E_{SN}}{10^{51}\ erg}\right)^{\frac{4}{17}} \left(\frac{n_0}{cm^{-3}}\right)^{-\frac{9}{17}}\ yr$$

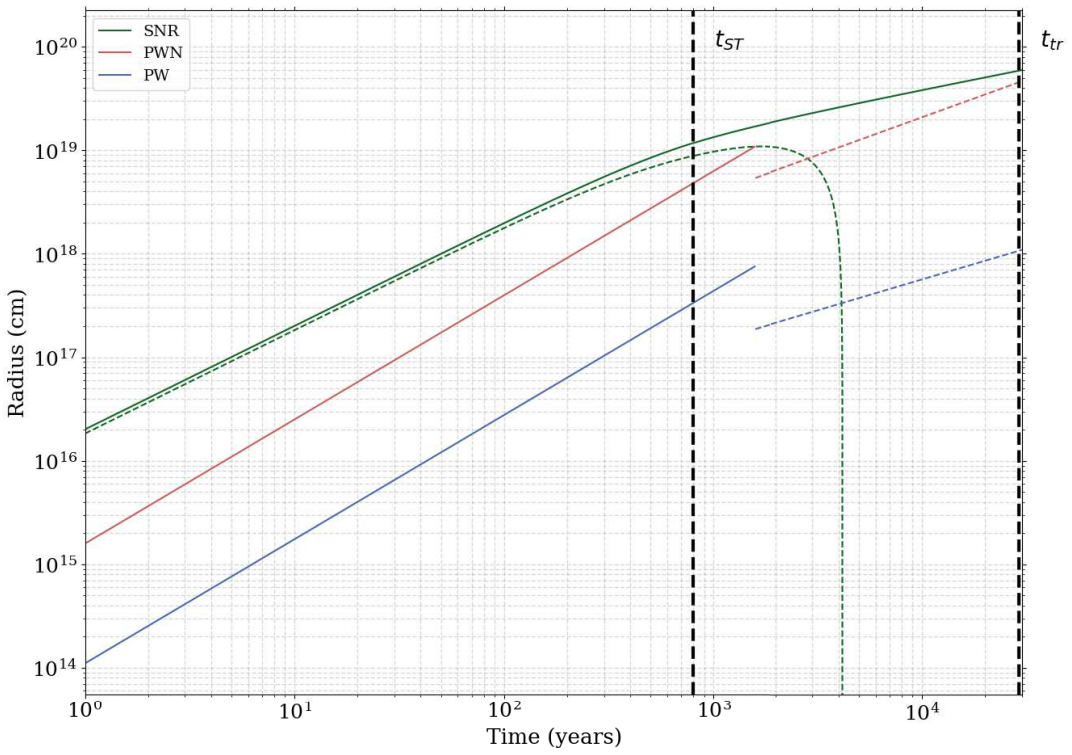

Figure 2.11 – Evolution of the supernova remnant forward shock and reverse shock radii (solid and dashed green lines), of the pulsar wind nebula outer radius (red lines) and the termination shock of the pulsar wind (blue lines). The free expansion stage dominated by the supernova ejecta begins from the earliest ages up to t_{ST}, where the adiabatic evolution shall start up to a t_{tr} time, when it shall transition to a radiative evolution, not depicted in this graph. In the *Sedov-Taylor* phase, the PWN and PW radii are considered for the constant spin-down power case (pulsar braking is omitted).

Chapter 3

Multi-wavelength astronomy as a probe of radiation processes

Contents

During the last few decades, astronomy has been a catalyst for challenging Humanity's understanding and conceptualisation of astrophysical systems. Leaps in technology and in thought have led to an astonishing progress with regard to multi-wavelength observations and modelling. In order to interpret the emitted photon energy spectrum of a given source, one has to account accelerated particle spectra occurring in various astrophysical environments and understand the radiation processes involved when light exudes.

3.1 Synchrotron radiation

In the following section, I shall define the characteristics of the radio waveband, being a window to the astronomer onto the submillimeter landscape, reflecting relativistic gyroradiation(Section 3.1). Additionally, I will mention the non-thermal X-ray emission coming from the same radiation process but for more energetic particle populations. Moreover I will discuss about the insight brought from radio and X-ray observations to the energy transfer and particle transport panorama of systems such as PWNe (Section 3.1.3 and Section 3.1.4), focusing on the leptonic contributions, that may originate from the sub-mm, the infra-red and even from the optical like the famous Crab nebula, and well discussed PWN such as G21.5-0.9, G54.1+0.3 and 3C58.

3.1.1 Synchrotron emissivity

The synchrotron radiation of ultra-relativistic leptons is one of the best probes of magnetic field distribution in astrophysical environments, since it is the signature of charged particles moving in spiral paths along magnetic field lines. First observed in particle physics experiments (the early *betatron* experiments[34]), it results from high energy electrons or positrons gyrating in magnetic fields, scattered in pitch angle because of small-scale B-field irregularities. We shall consider that they shall follow a regular orbit by considering that such small scale deviations would be negligible for energetic particles. The velocity of the particle is constant along the magnetic field direction and circular in the perpendicular direction with a radius called "gyroradius". In respect to this radius, the relativistic gyrofrequency $\nu_{g,rel}$ is defined for a high energy electron spiralling in a uniform B-field with a constant pitch angle α and accelerated towards the guiding centre of its orbit such as :

$$\nu_{g,rel} = \frac{qB}{2\pi\gamma m_e c} = 2.8\ \gamma^{-1}\ MHz\ G^{-1} \tag{3.1}$$

with q as the charge and m_e the mass of an electron, B the magnetic-field stregth value, γ the Lorentz factor and c the celerity.

The total synchrotron radiation loss rate for a charged particle where its acceleration is perpendicular to its velocity vector, which is the case for the synchrotron process, and in the laboratory framework is as :

$$-\frac{\mathrm{d}E}{\mathrm{d}t} = 2\sigma_T c U_{mag} \gamma^2 \beta^2 \sin^2\alpha \tag{3.2}$$

with c as the celerity, γ as the Lorentz factor of the charged particle, $\sigma_T = \frac{q^4}{6\pi\epsilon_0^2 c^4 m_e^2} = \frac{8\pi\, q^4}{3\, m_e^2 c^4}$ as the Thomson scattering cross-section, valid as long as the mass energy of the scattering charged

particle is significantly greater than the energy of the photon $\gamma h\nu \ll m_e c^2$ in the lab-frame, with $U_{mag} = \frac{B^2}{2\mu_0} = \frac{B^2}{8\pi}$ as the magnetic energy density and the velocity-to-celerity ratio $\beta = \frac{v}{c}$ tending to unity in the ultra-relativistic regime when $v \longmapsto c$.

When averaged over an isotropic distribution of pitch angles, the ultra-relativistic ($\gamma \ll 1$) gyroradiation loss rate is simplified as :

$$-\frac{\mathrm{d}E}{\mathrm{d}t} = \frac{4}{3}\sigma_T c U_{mag} \gamma^2 \tag{3.3}$$

The synchrotron spectrum has a broadly defined peak near the critical ν_c frequency such as :

$$\nu_{syn} = 0.29\nu_c = 0.29\ \frac{3}{2}\ \sin\alpha\ \nu_{g,\,non\ rel}\ \gamma^2 \tag{3.4}$$

where the gyrofrequency in the non-relativistic case is $\nu_{g,\,non\ rel} = \frac{qB}{2\pi m_e c}$. It may be assumed that almost the entirety of the energy radiated by a relativistic charged particle is emitted at 0.29 times the critical frequency, meaning that the radiation in the $[\nu\ ;\nu + d\nu]$ range is assigned to a leptonic population with energies ranging in $[E\ ; E + dE]$. This approximation leads to link the synchrotron emissivity to the distribution of electrons:

$$\epsilon(\nu)\ d\nu = N(E)\ dE\ (-\frac{dE}{dt}) \tag{3.5}$$

where $N(E)\ dE$ is the electron number density and $-(\frac{dE}{dt})$ is the radiation loss rate defined in Equation 3.3. Moreover an other common assumption, based on the fact that both the energy spectra of cosmic-rays and in general from emission by non-thermal sources may be modelled as a simple power-law distribution, would be to consider a power-law trend followed by the leptons :

$$N(E)\ dE = \kappa\ E^{-p}\ dE \tag{3.6}$$

with κ and the electron index p being the amplitude and the slope of the power-law electron energy spectrum, respectively. By using the approximation of Equation 3.4 where $\nu_{syn} \approx \nu_{g,\,non\ rel}\ \gamma^2$, also known as a δ-function approximation, one may simplify the synchrotron emissivity expression of Equation 3.5 as :

$$\epsilon(\nu) \propto \kappa\ B^{\frac{(p+1)}{2}}\ \nu^{\frac{-(p-1)}{2}} \tag{3.7}$$

The quadratic dependence of the synchrotron flux with the magnetic field and the Lorentz factor underlined from Equation 3.2, is intrinsically connected to the dependence between the magnetic component and the emitted frequency shown in Equation 3.7. The synchrotron emissivity is directly linked to the so called spectral index s, which is the differential energy flux index, defined as $s = \frac{(p-1)}{2}$, that is derived from the following expression and the one found on Equation 3.7 : $\epsilon(\nu) \propto \nu^{-s}$.

3.1.2 Synchrotron cooling

As stated in Section (3.1), a charged particle emitting synchrotron radiation will lose energy at a rate of $-\frac{dE}{dt}$ from its initial energy E. The synchrotron characteristic cooling time $t_{syn,\,cool}$ is defined as :

$$t_{syn,\,cool} = E\ \left(-\frac{dE}{dt}\right)^{-1} = \frac{3}{4}\frac{m_e^2 c^3}{\sigma_T}\ \frac{8\pi}{B^2}\ \frac{1}{E} \propto B^{-2}\ E^{-1} \propto B^{-2}\ \gamma^{-1} \tag{3.8}$$

As illustrated by Equation 3.8, the synchrotron cooling time $t_{syn,\,cool}$ will be shorter for high energy particles and shall decrease in strong magnetic fields. This relation with the B-field

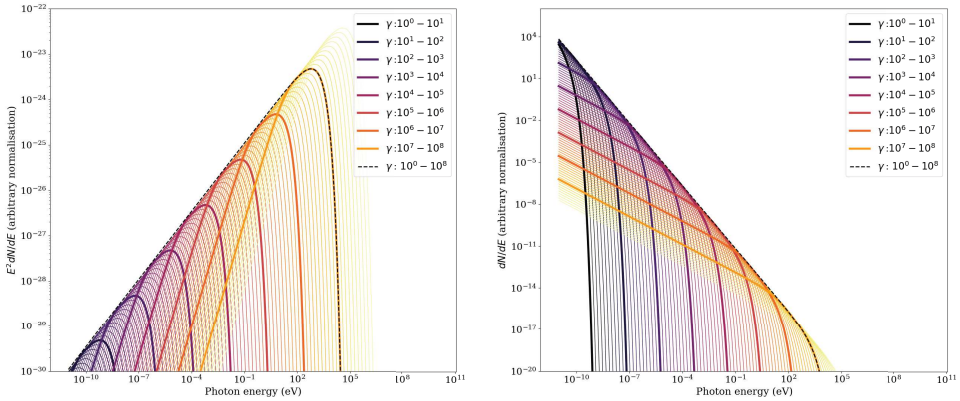

(a) Spectral energy distributions. (b) Photon energy fluxes.

Figure 3.1 – Spectra for leptonic populations with Lorentz factors γ ranging from 1 to 10^8, following the same power-law electron spectrum distribution, with $p = 2$ and the same decorrelation energy and an arbitrary amplitude, computed with the *naima* python package [140]. These illustrations correspond to intrinsic luminosities for Figure 3.1a and intrinsic differential luminosities for Figure 3.1b.

highlights that in strong magnetic field astrophysical environments, the synchrotron cooling time can be significantly shorter than the age of the observed system.

Furthermore the difference of time scales between the electron cooling lifetime and the age of the system, leads to think that there must be a steady injection of continuously accelerated energetic leptons in order to explain the observed synchrotron spectra, spatially integrated over the size of the given source. This is important as for the determination of the spectral break in the synchrotron electron spectrum, occurring at the synchrotron cooling break frequency $\nu_{syn,\,break}$. Let us consider an example of a continuous power-law injected spectrum of a relativistic leptonic population, as the likes of the one introduced in Equation 3.6. Let us choose a system with a uniform, constant and isotropic magnetic field, which shall remain fixed for the rest of this explanation. If no synchrotron cooling occurs, the electrons injected at a constant rate shall follow the initial power-law trend with an electron index of p, such as $N(E) \propto E^{-p}$ and therefore will emit as $\epsilon(\nu) \propto \nu^{-\frac{(p-1)}{2}}$ (Equation 3.7). Indeed this ought to represent the part with no cooling, low energy synchrotron spectrum up to the the synchrotron cooling break. Let us reckon with particles injected with higher energies than a given break energy $E_{syn,\,break}$. This would imply that they would cool shortly after their injection, meaning that the electron density shall drop with regard to the cooling rate onto the population without cooling such as $N(E_{syn,\,break} \ll E) \propto N(E_{e,\,no\,cool})\, t_{syn,\,cool}$. This may be summarized in the following :

$$N(E) \propto \begin{cases} E^{-p}, & E \ll E_{syn,\,break} \\ E^{-p-1}, & E \gg E_{syn,\,break} \end{cases} \quad thus \quad \epsilon(\nu) \propto \begin{cases} \nu^{-\frac{(p-1)}{2}}, & \nu \ll \nu_{syn,\,break} \\ \nu^{-\frac{p}{2}}, & \nu \gg \nu_{syn,\,break} \end{cases} \tag{3.9}$$

The cooling break characteristics provide information on both the strength of the ambient magnetic field enclosing the emitting source and the age of such a system, as long as there is no outward evidence of particle propagation away from the acceleration site as they are losing energy via synchrotron cooling. As illustrated in Figure 3.1b, the synchrotron spectrum of a population of electrons is the sum of several single electron energy contributions within the considered energy range. The synchrotron cooling may be one of several explanation behind the distortion of injection electron spectra, such as ionisation and radiative losses.

3.1.3 Radio properties of PWNe

Synchrotron radiation is commonly the process behind the continuum radio emission observed in the Milky Way, radio emission coming from supernova remnants and radio-loud active galactic nuclei. It is thought to be the mechanism at the origin of X-ray continuum emission from quasars as well as an explanation for the non-thermal optical continuum of the Crab nebula. Over the last decades, several pulsars and their environments have been detected in the radio band, consisting of a wide sample of "joined" systems, pulsar wind nebulae (PWNe) and different types of SNRs. Their morphology is a reflection of the central engine, usually a fast rotating compact object, and the observed radio continuum is associated with the injected relativistic particle spectrum.

Pulsar wind nebulae show typically flat (spectral index $0.0 \leq s \leq 0.3$) radio continuum spectra, with the exception of a handful observed more extreme examples such as G141.2+5.0 [104] and the northern wing of the *Kookaburra* complex [122] (Figure 6.7). Such values of steeper spectral indices are usually the case for evolved systems, such as shell-type supernova remnants and aged PWNe. This spectrum characteristics are compatible with Bremsstrahlung emission originating from interstellar ionised regions of HII. Nonetheless these regions are known sources of thermal emission. The non-thermal radio emission emerging from PWNe (steaming from linear polarisation perpendicular to the magnetic field) indicates where the aged injected particles lie, clearly showing a dependence with distance from the central object. If there are no freshly high energy particles injected in the nebula, then a spectral index jump of almost 0.5 is expected occurring at the synchrotron cooling break. For PWNe where there is such a particle injection, the synchrotron break frequency will dependent on the locii within the system. The radio emission of PWNe is created by lower energy particles, meaning that they will have longer lifetimes, as displayed on Equation 3.8 and discussed in Section 3.1.2. This implies that observations in the radio band will reflect the time-integrated energy budget of the pulsar wind nebula.

From a morphological aspect, the radio emission of pulsar wind nebulae may be intertwined and confounded with other components within and outside the system : the possible emission of the central object often identified as a pulsar and the supernova remnant interaction with the interstellar medium or a nearby object such as a molecular cloud. In addition to the complexity introduced by the components of such a structure, observational binds of radio detection, such as calibration challenges to obtain high-resolution imagery, unaccounted projection effects in the line of sight and confusion of contiguous bright sources, render PWN morphology studies tricky. To overcome these challenges, a feasible solution when possible, would be to compare the radio emission to X-ray emission,

3.1.4 Non-thermal X-ray emission

In high energy astrophysics, the terms of non-thermal and thermal emission are used to distinguish between the continuum radiation of a particle distribution with a non-Maxwellian energy spectrum with one that may be approximated by blackbody radiation or a thermal Bremsstrahlung spectrum.

Just like the radio emission of PWNe, the X-ray non-thermal emission of such systems are attributed to synchrotron radiation and are an indirect depiction of the magnetic field and particles within the nebula. Spectral information in the X-ray domain, reflects the "cooled" by synchrotron losses young particles injected in the system in contrast to the older particles probed by the radio emission.

Let us estimate, based on Equation 3.8, the synchrotron cooling lifetime of two sets of leptons that we shall name R and X, one of with $5\ .10^{-4}$ TeV $< E_{e,R} < 5\ .10^{-2}$ TeV and another with $10 <$

$E_{e,X} < 700$ TeV. In Figure 3.2, one may read the synchrotron cooling loss lifetime for each said set. The energy ranges for population R is the computed electron energy leading to synchrotron radiation in the [4 .10^{-8} - 4 .10^{-4}] eV range, which corresponds to the radio band for a magnetic field of 10 μG. The population X is the energy of electrons leading to synchrotron radiation in the [10^2 - 10^5] eV range, which corresponds to the X-ray band. These electron values for set R, $t_{syn,\,cool}$ may reach up to "infinite" time values (the age of the Universe is estimated to be at (13.78 ± 0.02) 10^9 yr !) for a an extremely low magnetic field value (which is not a physical case for PWN media) and low electron energies and may drop up at a scale of ~ tens of thousands of years for a very high magnetic field value with significantly more energetic electrons (tens to hundreds GeV). For the lower energy electrons of set X, the lower B-field value configuration yields lifetimes of the order of million of years while higher in energy electrons above $E_{e,X} \sim 0.1$ PeV, will have a synchrotron cooling time of time scales of just a few years.

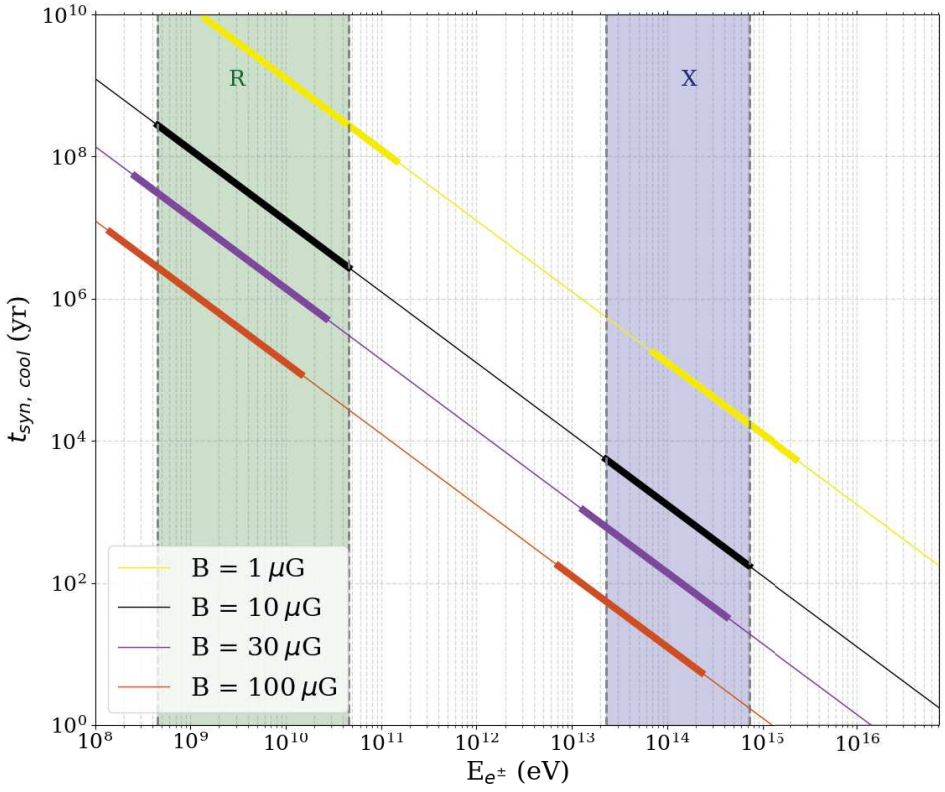

Figure 3.2 – Graph showing the synchrotron cooling time $t_{syn,\,cool}$ as a function of the electron energy E for different magnetic field B values. In Section 3.1.4 the two depicted sets R and X of electron populations are mentioned in the text. The wider in width lines correspond to the energy ranges in the radio [4 .10^{-8} - 4 .10^4] eV and soft and hard X-ray [10^2 - 10^5] eV bands.

3.2 Inverse Compton scattering and other leptonic processes

The wave-particle duality of light is a key ingredient in the understanding of radiation processes, especially the ones defined by scattering. Electromagnetic radiation may be perceived both as moving perturbations in space (waves) and as particles with no mass. Thus light gathers particle-like properties, and may therefore collide with other particles, and likewise possesses wave-like characteristics such as emissivity.

3.2.1 Photon - lepton scattering : process and regimes

There are several cases of scattering of the system { photon - charged particle}, depending on the energy transfer during an elastic collision.

3.2.1.1 Thomson scattering

The so-called *Thomson scattering* occurs when electromagnetic waves are scattered with a given angle θ by stationary free electrons (see Figure 3.3). This results to a symmetric scattering compared to the θ angle, suggesting that the radiation in the forward and backward motion directions of the wandering photon is similar. Photons will not gain or lose energy during the process but rather decrease in number density when energy is scattered out of the electromagnetic beam, thus it will determine an optical depth in a medium for Thomson scattering. The cross-section during this process, named the *Thomson cross- section* σ_T, bears a great importance as it is the physical limitation of the spreading of the electromagnetic radiation (see Equation 3.10). Provided that the photon energy is lower than the energy of the stationary electron in its frame of reference or that the electron velocity is sub-relativistic, the scattered light beam shall not experience a significant change in radiation frequency.

$$\sigma_T = \frac{8\pi}{3} r_e^2 = \frac{q^4}{6\pi\epsilon_0^2 c^2 m_e^2} \approx 6.7\ 10^{-29} m^2 \tag{3.10}$$

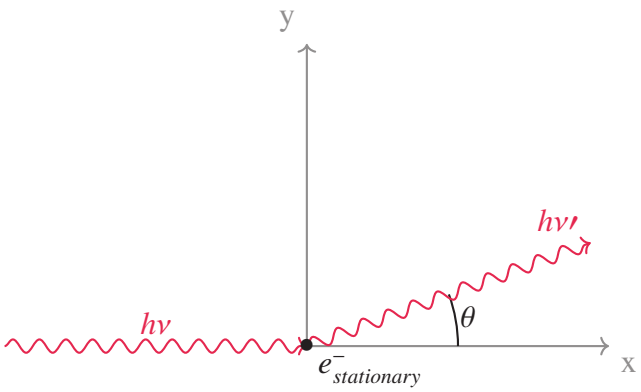

Figure 3.3 – Schematic diagram illustrating the Thomson scattering of a single photon $h\nu$ on a stationary electron e^-. In this case, the photon frequency before and after the scattering remains unchanged ($\nu = \nu\prime$) and the electron does not recoil. The photon is scattered with a θ angle as shown in the diagram.

3.2.1.2 Compton scattering

The *Compton scattering* is equivalent to the Thomson scattering process as to the collision elements but holds a major difference : during the collision there is an inflection in light frequency, due to the electron recoil energy effect (see Figure 3.4). The electron shall gain energy and the photon will lose energy. The Thomson cross-section mentioned in Equation 3.10 is a valid approximation for non-relativistic movement of the electron and if the energy of the photon is much lower than the mass energy of the electron : $h\nu \ll m_e c^2$. These are the conditions required of scattering in the Thomson regime, since the centre of momentum frame of the system { stationary electron + colliding photon} is moving at velocities that allow the electron to "see" the photon, therefore for the photon to collide with it and to be scattered.

Nevertheless, this is no longer the valid for highly energetic photons where $h\nu \sim m_e c^2$ or if the charged particles are ultra-relativistic. This latter would imply that the centre of momentum frame has the same velocity as the relativistic particle thus it would require to take into account the quantum relativistic cross-section to rigorously compute the amount of scattered photons. In this regime, one ought to use the Klein-Nishina formula for the cross-section. In Equation 3.11, one may find the quantum relativistic cross-section in the ultra-relativistic limit where $\gamma \gg 1$ or in the electron rest-frame, when $h\nu \gtrsim m_e c^2$. As illustrated on Figure 3.5, the difference of approximations for the cross-section may yield up to five orders of magnitude of misestimation, which is crucial for interpreting the radiation coming from very-high energy sources.

$$\sigma_{K-N} \approx \pi \left(\frac{q^2}{4\pi\epsilon_0 m_e c^2} \right)^2 \left(\frac{m_e c^2}{h\nu} \right) \left(ln\left(\frac{2h\nu}{m_e c^2} \right) + \frac{1}{2} \right) \tag{3.11}$$

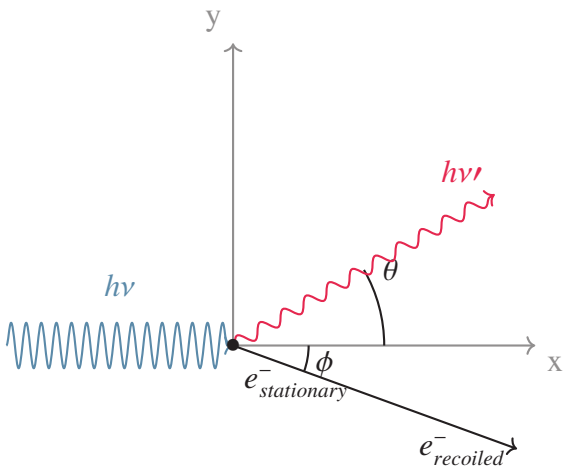

Figure 3.4 – Schematic diagram illustrating the Compton scattering of a single photon $h\nu$ on an electron e^-. In this case, the photon frequency before and after the scattering alters ($\nu \neq \nu'$), the radiation shall be "cooled" $\nu' < \nu$ by the transfer of energy onto the electron. The electron and photon are scattered with a ϕ and θ angle respectively, as depicted in the above diagram.

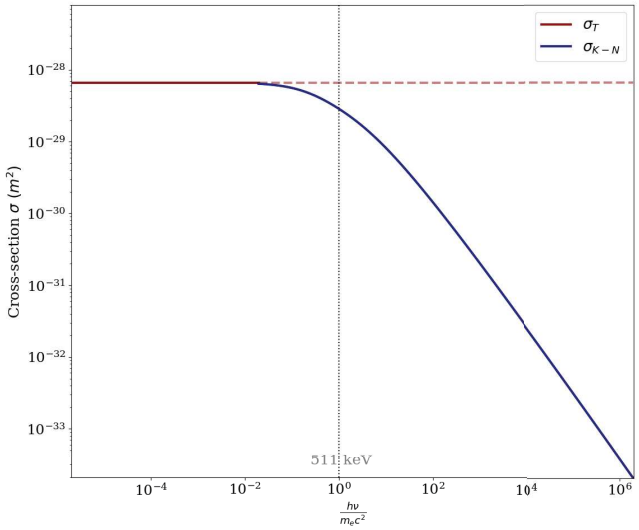

Figure 3.5 – Graph of the cross-section in the Thomson (red line) and Klein-Nishina (blue line) approximations depending on the photon energy, ranging from 1 eV to 1 TeV. For $h\nu \ll m_e c^2$, the particle cross-section is matching the Thomson cross-section estimation for the non-relativistic and low photon energy cases (see Equation 3.10); for $h\nu \geq m_e c^2$ the relativistic quantum cross-section based on the Klein-Nishina formula is computed and for ultra-relativistic regimes, the Klein-Nishina cross section of Equation 3.11 shows a $\propto (h\nu)^{-1}$ decline.

3.2.1.3 Inverse Compton scattering

Inverse Compton (IC) scattering is one of the dominant leptonic processes behind high energy radiation from astrophysical sources. It is akin as a process to the Compton scattering (Section 3.2.1.2), however it consists of the scattering of ambient photons from ultra-relativistic electrons. Low energy photons shall "harness" the kinetic energy of electrons thus after the collision electrons will lose energy and be slowed whereas photons will gain energy.

In the Thomson regime (see Section 3.2.1.2) the inverse Compton scattering cross-section is equal to the Thomson cross-section (Equation 3.10) for low photon energies and mildly relativistic populations. Notwithstanding, at higher energies and for ultra-relativistic cases, on each interaction, the electron will be significantly "cooled" and thus the energy transfer of the kinetic electron energy to the photon energy should be considerably more abrupt. The fact that at high energies the cross-section drops due to relativistic effects, as illustrated in Figure 3.5, introduces a spectral steepening of the IC spectral energy distribution in the very-high energy range. Nevertheless, very-high leptons may reach even higher energies since they should be less prone to cooling because of their smaller cross-sections.

The energy loss via inverse Compton scattering, integrated over solid angle (isotropic distribution is assumed), is computed as such :

$$-\frac{\mathrm{d}E}{\mathrm{d}t} = \frac{4}{3}\sigma_T c U_{rad} \gamma^2 \beta^2 \tag{3.12}$$

with U_{rad} being the energy density of radiation coming from a target photon population.

By using the same assumption as the one used for the synchrotron spectrum in Section 3.1, regarding the power-law electron distribution of Equation 3.6, one may find that the spectral emissivity $\epsilon(E)$ is dependent on the frequency of the scattered radiation with :

$$\epsilon(\nu) \propto \nu^{-\frac{(p-1)}{2}} \propto \nu^{-s} \tag{3.13}$$

thus yielding similar results to the synchrotron spectral index. The spectral index for scattered radiation is $s = \frac{(p-1)}{2}$, with p being the electron spectral index.

Given the similarities of the radiated powers in the synchrotron and inverse Compton processes, let us discuss how they compare. Both average energy loss equations for synchrotron (Equation 3.3) and inverse Compton (Equation 3.12) have a similar constant component and dependencies with the Lorentz factor as $\propto \gamma^2$ and with a linear growth in respect of an energy density contribution coming from the ambient environment of the source, from the magnetic field for synchrotron radiation and from radiation fields for the IC scattering.

$$\frac{\left(-\frac{dE}{dt}\right)_{IC}}{\left(-\frac{dE}{dt}\right)_{syn}} = \frac{U_{rad}}{U_{mag}} \tag{3.14}$$

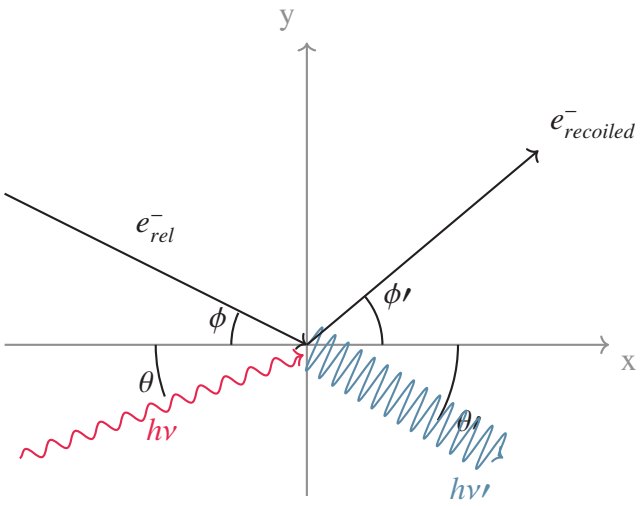

Figure 3.6 – Schematic diagram illustrating the inverse Compton scattering of a single photon $h\nu$ on a highly energetic ultra-relativistic electron e^-. In this case, the photon frequency before and after the scattering alters ($\nu \neq \nu\prime$), the radiation shall be "heated" ($\nu\prime > \nu$) by the transfer of energy from the recoiled electron, that will lose energy. The electron and photon have incoming ϕ and θ angles respectively and are scattered with a $\phi\prime$ and $\theta\prime$ angle, as depicted in the above diagram.

3.2.2 Target photon populations

In very-high energy astronomy, the inverse Compton spectra are the sum of several lepton scatterings on different photon targets. In order to estimate the total spectral distribution from IC radiation, one has to take into account several photon field contributions to be used as seeds for the modelling. We shall assume these photon distributions are isotropic in the rest frame of the observer. So as to compare the different radiation fields apt to be targets for scattering, we will focus on their estimated temperature and energy densities as a function of the galactic position of the emitting source.

We shall focus on the cases where the dominant contributions to the inverse Compton scattering are derived from blackbody radiations described by the Planck radiation law, based

on a Bose-Einstein distribution. For example, the spectral radiance per frequency S_ν, meaning the radiated power emitted per solid angle, per surface area and per spectral variable, here the frequency, is given as :

$$S_\nu(\nu, T) = \frac{2h\nu^3}{c^2}\left(\frac{1}{(e^{\frac{h\nu}{k_B T}} - 1)}\right) \tag{3.15}$$

3.2.2.1 Cosmic Microwave Background

The *Big Bang* theory, one of the most established theses aiming to decipher our observable Universe, may explain the cosmic microwave background (CMB) as a relic radiation coming from the earliest, ~ 13.7 billion years ago, and most explosive, dense, primeval hot phenomenon interpreting the evolution of said Universe. This radiation has been first detected serendipitiously in the sixties by Penzias and Wilson[91] and has since been an important project for various experiments throughout the years, studying the dynamics of the primordial Universe and testing cosmological models, by measuring temperature anisotropies linked to fluctuations of matter density at the origin of large scale structure formation.

In 2018, the *Planck* collaboration, published the latest measurements resulting from their scientific program studying the early Universe and its evolution[93]. They consisted of deep field, high resolution maps produced by a continuous scanning of the microwave and submillimeter sky for almost four years. These results are the latest-to-date constraints and limits on parameters of the standard cosmological model. All measurements are still in general agreement with previous published results of *Planck*, *WMAP* (Wilkinson Microwave Anisotropy Probe) and *COBE* (COsmic Background Explorer) missions, all favouring the ΛCDM model, known as the standard cosmological model based on a parametrisation with a dark energy constant Λ, a cosmological dark matter (CDM) type and a baryonic matter component.

Despite the CMB map anisotropies, that have been very useful for probing cosmological models, the CMB may be roughly assumed as an isotropic background radiation. As the name suggests, it is seen in the radio band, in the sub-millimeter and microwave windows, named after the peak of radiated energy in this band following Wien's displacement law, where the wavelength of a blackbody radiation curve peak λ_{peak} is linked to the temperature T linearly as $\lambda_{peak} T \approx 2.9 \,.\, 10^{-3} m.K$. It is speculated to be the relic emitted radiation of the moment when the expanding Universe became optically thin, being approximated to a blackbody radiator at ~ 3K (redshifted). The COBE satellite results have given a more precise estimation of this temperature, setting it at 2.725 ± 0.002 K. Based on the Stefan-Boltzmann law, underlining the relation between the total thermal energy radiated from a hot surface and the absolute temperature T, one may estimate the radiation energy density U_{rad} computed as :

$$U_{rad} = \frac{4}{c}\,\sigma_{SB}\,T^4 \tag{3.16}$$

Using the cosmic microwave background measured averaged temperature of ~ 2.72 K, we may deduce a value of $U_{rad} = 0.26 eV.cm^{-3}$ for the energy density of the CMB target photon population.

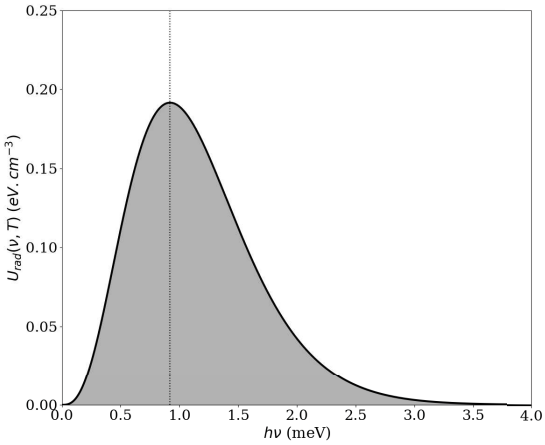

Figure 3.7 – Graph of the radiation energy density U_{rad} as a function of photon energy $h\nu$, computed based on a blackbody approximation using the Planck radiation formula for the spectral radiance per frequency (Equation 3.15). When integrating over the energy range, one may find a radiation energy density of $\sim 0.26\ eV.cm^{-3}$, corresponding to the estimated value found using Equation 3.16

3.2.2.2 IR backgrounds and stellar dust

While the comsic microwave background is an important contributor of target photons susceptible to IC scattering, another major input of seed photons in the Galactic scale are the radiation backgrounds in the mid-infrared, far-infrared (FIR) and submillimeter bands, coming from dust emission. They account for a substantial part of the high energy and very-high energy gamma-ray observed spectra as well as prompting the gamma-ray propagation through the interstellar medium. Examples of temperature and photon densities for different positions in the modelled radiation fields may be found on Table 6.2.

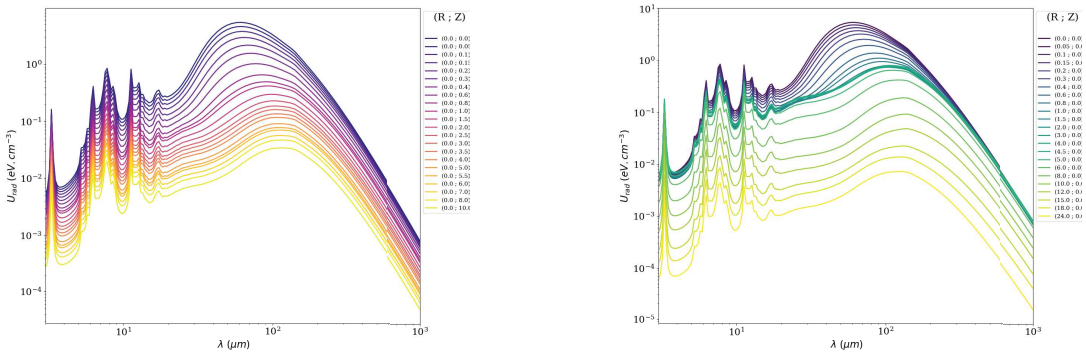

(a) Radial position R set at the galactic centre and vertical position Z varying from 0 to 10 kpc.

(b) Vertical position Z set at the galactic centre and radial position R varying from 0 to 24 kpc along the galactic plane.

Figure 3.8 – Radiation field energy densities U_{rad} in the [0.1 – 1000] μm band originating by dust emission based on the model by Popescu et al. (2017)[95] for a galactocentric radial position R and a galactocentric vertical position Z.

Another radiation background to consider is the emission associated to stellar sources. This emission seen in ultraviolet-visible (> 0.1 μm) is an important factor to account for when modeling extra-galactic emission. Moreover star light shall have a considerable input in optical and near-infrared (NIR, $\sim 0.1\mu m$), which should affect the gamma-ray spectra at lower energy, in the MeV range.

The NIR emission can be approximated with a blackbody radiation, characterised by a temperature $T \sim 3000K$ and an energy density of $U_{rad} \sim 0.5\ eV.cm^{-3}$ that is increasing towards the galactic centre region. This may be explained partially due to a high amount of diffuse dust from the Milky Way disk, that will inevitably absorb stellar light. Both models and observations have shown that there is an increase of energy density of infrared radiation fields.

The Popescu et al. (2017)[95] model (Figure 3.8a,3.8b) is based on an axisymmetric radiative transfer model for galaxies like the Milky Way, using a separate disk geometry for the old and young stellar populations, constrained by submillimeter, UV-optical and IR observations. The stellar radiation components are seen through a common distribution of diffuse dust, with properties assumed to follow Weingartner and Draine (2001) dust-grain size distribution and extinction within the Milky Way [133] (grain emissivity is not well constraint in the submillimeter regime though). One main caveat of this galactic radiation model cited by the authors is the axial symmetry assumption, that does not predict the variations of diffuse radiation in-between the arms and inner arms of the Milky Way.

The models of the interstellar radiation field used in the model by Porter at al. (2017) [96] attempt to take into account the spatial complexity of the Galaxy by including asymmetric elements. The authors use a 3D modelling by Robitaille et al. (2012)[108] that they call the "R2" model and that encodes an axisymmetric bulge, a smooth disk, four major and two minor local spiral arms. They as well use the "F98" model by Freudenreich (1998)[51] modelling a non-axisymmetric bulge and warped stellar and dust smooth discs. This latter model does not include the spiral arm asymmetry element in comparison to model R12, as seen in 3.9.

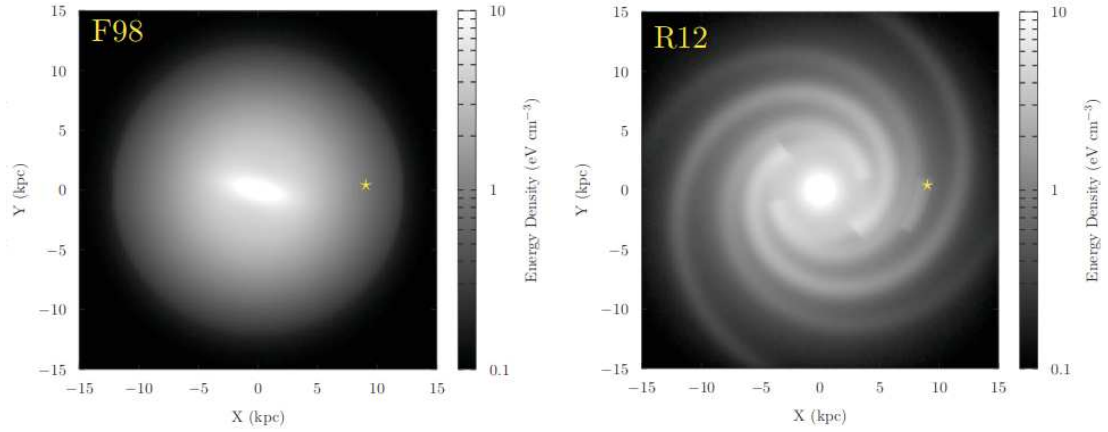

Figure 3.9 – Integrated radiation field energy densities for the models F98 and R12 used in Porter et al. (2017). The yellow star marks the position of the Sun in the galactocentric coordinate system. Figures taken from the corresponding paper[96].

3.2.3 Free-free interaction and thermal Bremsstrahlung

Leptons may interact with other free particles, such as free electrons or ions present in the interstellar medium. Since both particles are unbound before and after the scattering process, the resulting interaction product is called the *free - free* emission. The mechanism behind this

radiation process, is the interaction of the electron with the Coulomb field of other free particles, leading to a change in their momentum. The accelerated charged particles will emit photons so as to conserve the energy before and after the scattering and thus be decelerated. The resulting radiation is also called *Bremsstrahlung* radiation, from the German word for "braking radiation".

This process may occur in a dense, hot non-relativistic plasma. Thermal *Bremsstrahlung* may be observed in Hα regions, or ionised regions like galaxy clusters or diffuse nebulae like star clusters (such as the *Orion* nebula). This thermal process is a signature of leptons following a Maxwell-Boltzmann distribution. Within other astrophysical sources where electrons are accelerated, id est in shock waves, the particles follow a power law distribution, yielding non-thermal *Bremsstrahlung* radiation, which may be observed in systems such as supernovae remnants[22] contributing to the diffuse Galactic emission.

3.2.4 Pair-production and pair annihilation

When the energy of a photon is greater than the combined mass energies of a particle and its anti-particle in their rest frame, then two paired particles can be produced. During this process, the conservation laws are obeyed which entails that the sum of the charge and lepton number of the children particles will be null to match the parent photon characteristics. Electron-positron pairs may be produced, such as muons and anti-muons. To achieve the lowest mass pair production, the process requires a high energy photon with an energy E > 2 $m_e c^2$ ~ 511 + 511 keV.

$$\gamma + e^{\pm} \longrightarrow e^{\pm} + e^{+} + e^{-} \tag{3.17}$$

Another pair-production mechanism would be a photon-photon interaction, which is the quantum mechanical inverse process of the pair annihilation process. For high energies photon-photon interactions may produce an electron-positron pair, depending on the relative direction of the photon propagation. This pair-production would occur the most efficiently when there is a head-on collision, meaning that the relative angle between two photon tends to $\frac{\pi}{2}$ and naturally is impossible when the photons travel in parallel directions. An important aspect of the photon-photon pair creation would be that their cross section is a function of energy. In this case, the maximum cross section occurs when the product of the energies of the two parent photons is ~ (1 MeV × 1 MeV). This implies that a high energy gamma-ray photon of the order of a GeV will "see" a keV X-ray photon and that a very-high energy gamma-ray TeV photon may scatter with an extremely low energy photon of 1 eV (visible-near infrared).

3.3 Radiation from hadrons

In this section I will consider examples of radiation with a hadronic origin that are of interest in cosmic-ray gamma-ray astronomy.

3.3.1 Cosmic-ray fluxes

The measured cosmic-ray spectrum covers a wide range of energies, a range of $\sim$ 13 orders of magnitude, from below 10^8 eV up to almost 10^{21} eV. The overall spectrum is described as a piece-wise power-law and has been interpreted as having a mainly hadronic contribution, mostly from light ionised nuclei such as protons, helium and a remaining portion composed of heavier nuclei, with a secondary particle small contribution of charged particles as well, mainly electrons and positrons ($\sim$ 1 %). Some of the big questions that taunts yet excites scientists since their discovery regarding cosmic-rays, would be their origin, their abundance in elements and interpreting the "knees" (steepening) and "ankles" (flattening) of their spectral energy distribution : what are the acceleration mechanisms, where do they happen and how?

In Figure 3.10 the cosmic-ray spectra derived for the proton (p), the lepton ($e^- + e^+$ and e^+ flux), the antiproton ($\bar{p}$), the diffuse gamma-ray flux (γ), the isotropic gamma-ray background radiation (γ *IRGB*) and the neutrino ($\nu + \bar{\nu}$) upper limits are shown from top to bottom on the left side of the plot. The all-particle combined spectrum is presented in this figure with notations as to the estimated cosmic-ray flux rate detected on a given surface area for 100 GeV ($\sim$ one particle per square centimeter per second), 3 PeV (one particle per square meter per year), 5 EeV (one per square kilometer per year) and 10 ZeV (one per square kilometer per century). Fortunately for life on Earth, its atmosphere provides a natural protection shield from incoming cosmic-rays. Lower energy cosmic-rays may be detected directly with instruments on satellites or with high-altitude flown balloons but higher energy cosmic-ray detections on such experiments are restricted by their small collection area that allows only scarce amount of such high energy particles to encounter them and depth of detector so as to measure them. On the other hand, even thought the terrestrial atmosphere does not permit direct observations of cosmic-ray fluxes from the ground, it provides a calorimeter for secondary particle detections. Thanks to the last decades technological advancement, ground based detectors can provide a unique view by detecting secondary particles produced by hadronic cascades in Earth's atmosphere, when produced by very high energy cosmic-rays.

As depicted in Figure 3.10, the differential cosmic-ray spectrum is steeply decreasing as a function of energy, as a power-law with an index of $\xi \sim -2.7$ up to $\sim 3 - 5.10^{15}$ eV. The subsequent spectral variation is dubbed the "knee" since the spectrum steepens to higher energies. At energies above this knee, the spectrum follows a power-law with an index $\xi \sim$ -3.1 up to energies of $\sim 3 - 6.10^{18}$ eV where a flattening of the spectrum occurs, that is dubbed as an "ankle". More recent studies argue the presence of other deviations (an ankle at $\sim$ 10 PeV and a second knee at $\sim$ 100 PeV) [5], [89], [18].

Measured cosmic-rays above the Earth's atmosphere are dominated by $<$ 10 GeV. For cosmic-rays with $\gg$ 1 GeV, their origin is correlate to the solar activity. For higher energies, their provenance is from outside the solar system, with a general consensus based on theoretical models for estimated confinement radii based on the accelerated particle energy, that the bulk of cosmic rays from $\sim$ 1 GeV up to $\sim$ 4 PeV (the first knee of the spectrum) are from within the Galaxy. Above the ankle, ultra-high energy cosmic-rays are less likely to come from the Milky way and ought to have an extra-galactic origin. For the energy gap between the knee and the

ankle, both galactic and extra-galactic cosmic-rays may contribute. The ultra-high energy regime is a good discriminator since based on these energy scales, the galactic magnetic fields would be less prone to confine them, thus explaining the global isotropy from their reconstructed skymap origin position. For the extra-galactic particles different type of sources are studied as possible accelerators, such as Active Galactic Nuclei and starburst galaxies.

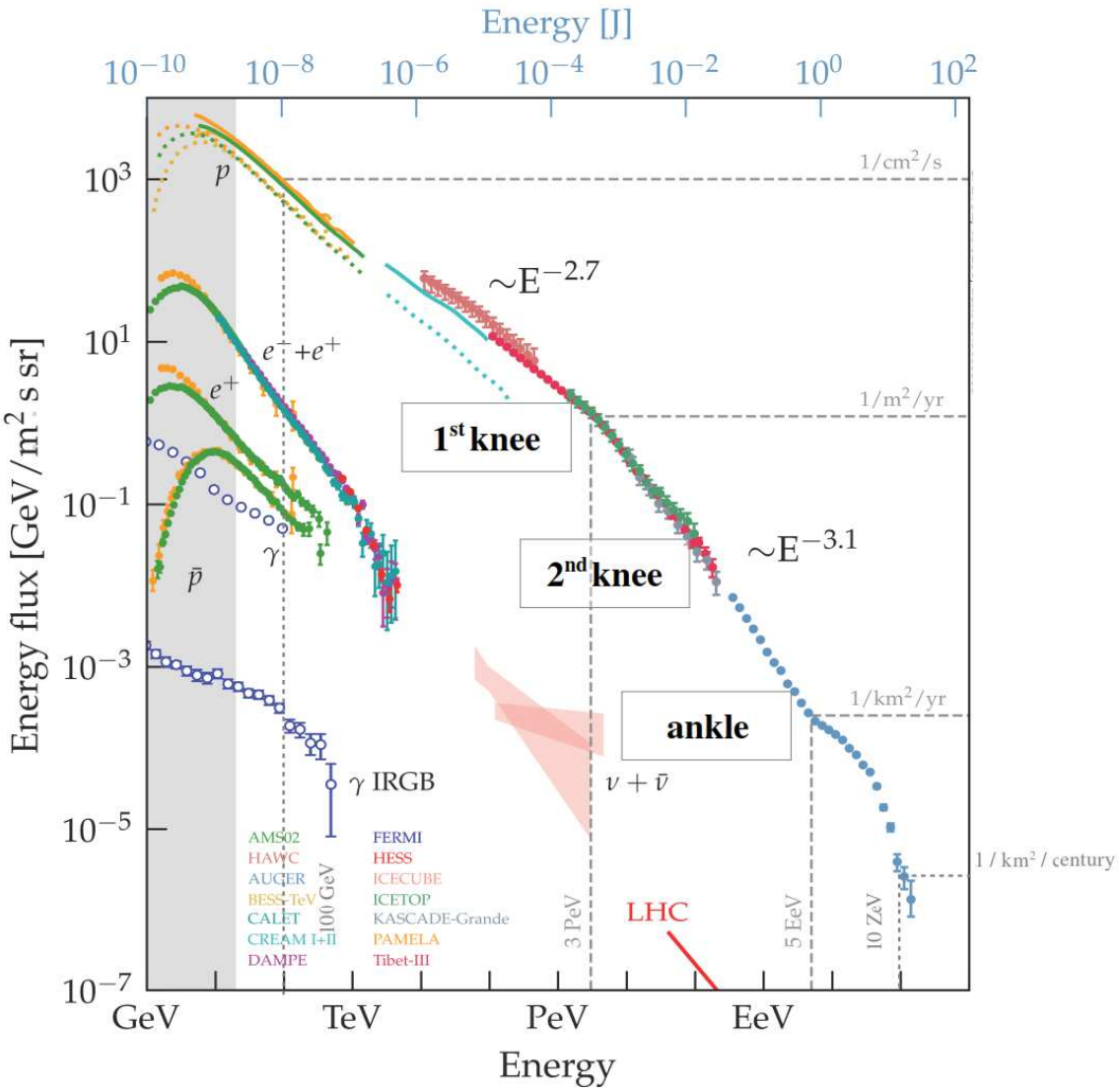

Figure 3.10 – All-particle cosmic-ray spectrum measured by the listed in the key gamma-ray experiments for direct, indirect and collider measurements. Figure taken from Carlo Evoli (slightly modified). See Appendix 9 for references.

Cosmic-rays are relativistic particles, with an acquired very high kinetic energy thanks to acceleration mechanisms, that may permit cosmic-rays to escape their acceleration site. Such a mechanism for example would be the diffusive shock acceleration, which is a random scattering of particles in between dense zones, often described with a "tennis table" allegory for the particles bouncing back and forth across the discontinuity of the upstream region with the interaction site. Studies of acceleration mechanisms along with theoretical and phenomenological investigations on the diffusion and turbulence of astrophysical objects and their surrounding

media are fascinating and very elaborated disciplines that unfortunately I will not include in this dissertation as they are beyond the scope of the study of pulsar wind nebulae, where leptonic processes are the most dominant contributions.

Based on the type of the particle, its energetics and the environment in which it propagates, regarding the turbulence of the ambient magnetic-field, the medium density and its ionisation for example, cosmic-rays below the ultra-high energy range (order of EeV) would be susceptible to stochastic trajectories induced by deviations at characteristic scales. In the total cosmic-ray flux, the fraction of electrons is rather small however gamma-ray electrons are of particular interest in cosmic-ray astronomy. Due to their smaller mass in comparison to protons, the radiative energy losses of leptons are stronger than the ones for nuclei. In a diffusion approximation, high energy (MeV - GeV) electrons would be confined within a $\sim$ 1 kpc radius, thus making them more prone in nearby galactic sources. One of the prime candidates to explain the contribution of cosmic-rays originating from the Milky Way, are supernova remnants (SNRs), considered as efficient accelerators of such cosmic-rays.

3.3.2 Pion decay

When accelerated protons p encounter ambient target protons of the interstellar medium, they collide and produce secondary particles such as protons, neutrons and pions π as shown in Equation 3.18. The charged mesons have very short lifetimes ($\sim$ 10 - 100 ns) thus the pion produced population shall decay once more. The charged pions $\pi^{\pm}$ shall decay into muonic (anti)neutrinos ν_{μ} and charged muons $\mu^{\pm}$, which will decay later on as secondary particles : leptons $e^{\pm}$ and muonic/electronic (anti)neutrinos ν_{μ}/ν_{e}. As for the neutral pions, they will eventually decay into photons.

$$\begin{cases} p + p & \longrightarrow p + n + \pi^{+} \\ p + p & \longrightarrow p + p + \pi^{+} + \pi^{-} \\ p + p & \longrightarrow p + p + \pi^{0} \end{cases} \quad \text{that shall decay as :} \quad \begin{cases} \pi^{+} & \longrightarrow \mu^{+} + \nu_{\mu} \\ \pi^{-} & \longrightarrow \mu^{-} + \bar{\nu_{\mu}} \\ \pi^{0} & \longrightarrow \gamma + \gamma \end{cases} \tag{3.18}$$

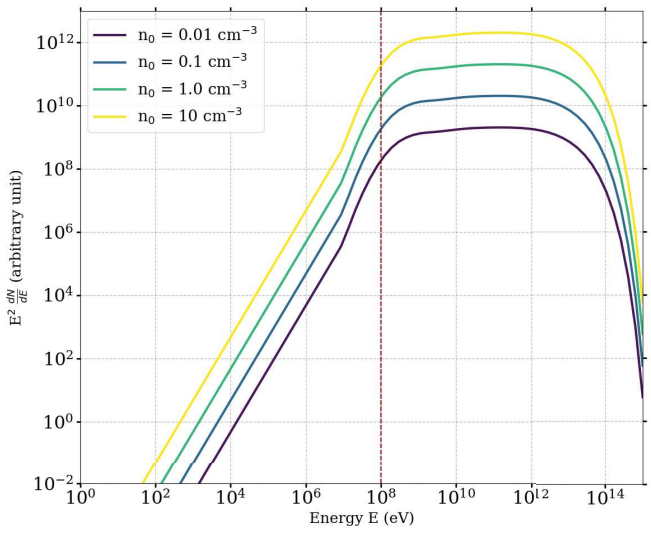

Figure 3.11 – Spectral energy distributions for radiation produced by the pion-decay process on different density ambient media of protons.

This process of radiation is of particular interest for astronomers, since the photon energy spectrum will show a pion "bump" at ~ 0.1 GeV (as depicted in Figure 3.11), providing that the ambient medium is dense enough, so that this neutral pion decay produces enough gamma-rays for this spectral bump to be discernible on a observationally constructed spectrum. This phenomenon is linked to a pile-up at a threshold energy due to the mass of pions. For three orders of magnitude density gradient, an approximate three order of magnitudes on the energy distribution can be expected as depicted on the example in Figure fig:pion-decay.

The local environment of a supernova remnant is a possible site of both proton-proton interactions and inverse Compton scattering. Thus gamma-ray observations of such systems can provide insight on the radiation mechanism by considering hadronic and leptonic models to interpret the spectral distribution. In a purely hadronic model, the spectral index s of the gamma-ray emission would be comparable to the spectral index of the accelerated hadron (if the photon flux exhibits the characteristic "pion bump"). In a purely leptonic model, the emitted spectrum will be flatter than that of the accelerated particle. Most likely, emission from supernova remnants may combine both processes, with cases where one is more dominant than the other. Realistically modelling the emission requires more complex hybrid models applied on observational datasets acquired with high sensitivity instruments. Indeed, the discrimination between the dominant processes may depend on the region of the extracted spectra, since they could reflect the emission of a different source component or the interaction with a closeby system thus raising the urgency to achieve higher angular resolution observations.

Part III

Very-high-energy gamma-rays

Chapter 4

High Energy Stereoscopic System

Contents

The H.E.S.S. experiment

The High Energy Stereoscopic System (H.E.S.S.) is a ground-based experiment situated at the Khomas Highland of Namibia located at 1800 m above sea level. It is a very-high-energy gamma-ray astronomy instrument able to detect and reconstruct signals originating from photons with energies ranging from about hundreds of GeV (≈ 0.05 - 0.28 TeV) to about a hundred TeV (≈ 100 - 125 TeV). The H.E.S.S. project has been fully operational since 2004 and its scientific activity has been prolonged at least until 2022. Its position in the southern hemisphere provides an ideal viewing for observations along the Galactic plane. Moreover its remote yet accessible by car location in the Namibian desert (∼ 100 km from the capital, Windhoek) is optimal for all year long observations due to favourable meteorological conditions: mild climate, low winds and low humidity.

Figure 4.1 – H.E.S.S. site in Namibia with four medium-sized Cherenkov telescopes CT1-CT4, layed in a square configuration from right to left and with one large-sized Cherenkov telescope CT5 in the middle of the array.

In this section, one will find a brief explanation of the Cherenkov imaging technique (Section 4.1) focusing on the data acquisition and the air-shower reconstruction (Section 4.3.0.3), prompting well-resolved spectral and spatial mapping of sources generating non-thermal emission. Furthermore the H.E.S.S. observatory configuration eras up to the present, (HESS-I, HESS-II and HESS-IU) will be summarised in Section 4.2. Finally I will present in Section 4.3.0.2 my short monitoring study of the calibration flat-fielding for the large sized Cherenkov telescope *CT5*.

4.1 Imaging Atmospheric Cherenkov Telescopes

So as to reconstruct the atmospheric shower resulting after the chain-reaction originated by an incoming high energy photon, it is required to have a good representation of the molecules and aerosols in the atmosphere. Depending on its composition, the propagation of the Cherenkov light as well as the dispersion of secondary particles may differ. Earth's atmospheric opacity renders the observation of X and gamma-rays from ground based experiments very difficult in energies below the very-high energy gamma-ray regime. This is not an issue encountered by satellites however it is practically and financially difficult to build large detector areas and detectors of sufficient depth in radiation lengths, so as to be able to collect the higher range of energy photon. Thus, Imaging Atmospheric Cherenkov Techniques (IACTs) have been developed over the last decades to harness, indirectly, very-high energy photons.

4.1.1 Ground-based gamma-ray astronomy : air showers

When penetrating Earth's atmosphere, high energy particles ($\gtrsim GeV$) generate extensive air showers of electromagnetic (electrons, positrons or photons) and hadronic (mainly protons) cascades. Hadronic cosmic-rays arrive nearly isotropically in space due to the spatial deflection from their origin by magnetic fields whereas VHE neutral photons are spatially correlated with the source at their origin since they are not prone to such deviations. The main objective in ground-based gamma-ray astronomy is to identify whether the incident particle is a nucleus (hadronic cosmic-rays) or a photon (gamma-rays) by classifying the detected event, to locate its provenance and to measure its incoming energy.

The interaction of an incident VHE gamma-ray photon in the upper atmosphere with ambient nuclei produces electron-positron pairs. The electric field of such leptonic pairings shall interact in turn with the electrostatic field of atmospheric nuclei and shall initiate braking radiation, known as *Bremsstrahlung* emission (Section 3.2.3). This free-free emission process will produce slightly lower energy gamma-ray photons, which will interact with the nuclei of the atmosphere and result into new pair-creations that will drive again Bremsstrahlung emission and so on : this is a simplified scheme of the chain-reactions occurring in electromagnetic cascades during the first stages of secondary particle production in the upper atmosphere. The energy lost by each lepton after *Bremsstrahlung* or pair-creation radiation processes while propagating in the atmosphere onto the ground is characterised by a length scale, the radiation length $X_0 \sim 37$ g.cm^{-3}. This is underlined in the following average energy expression E and the particle density N as a function of transverse depth X :

$$\begin{aligned} E(X) &= E_0 \, e^{-\frac{X}{X_0}} \\ N(X) &= e^{\frac{X}{X_0}} \end{aligned} \tag{4.1}$$

In the *Heitler* model[87], the *Bremsstrahlung* and pair-creation processes are assumed to be the only dominant radiation mechanisms, both equally probable to occur in a cascade. This model assumes that for the secondary particles of the shower, the lost energy from the parent particle at each step of the cascade will be distributed evenly among its produced child particles (leptons and photons) (Figure 4.2). The maximum depth X_{max} of the cascade would be in this case :

$$X_{max} = \frac{ln(\frac{E_0}{E_{critical}})}{ln(2)} \, X_0 \tag{4.2}$$

with $E_{critical}$ being the energy below which ionisation losses dominate the *Bremsstrahlung* energy losses (see Chapter 3).

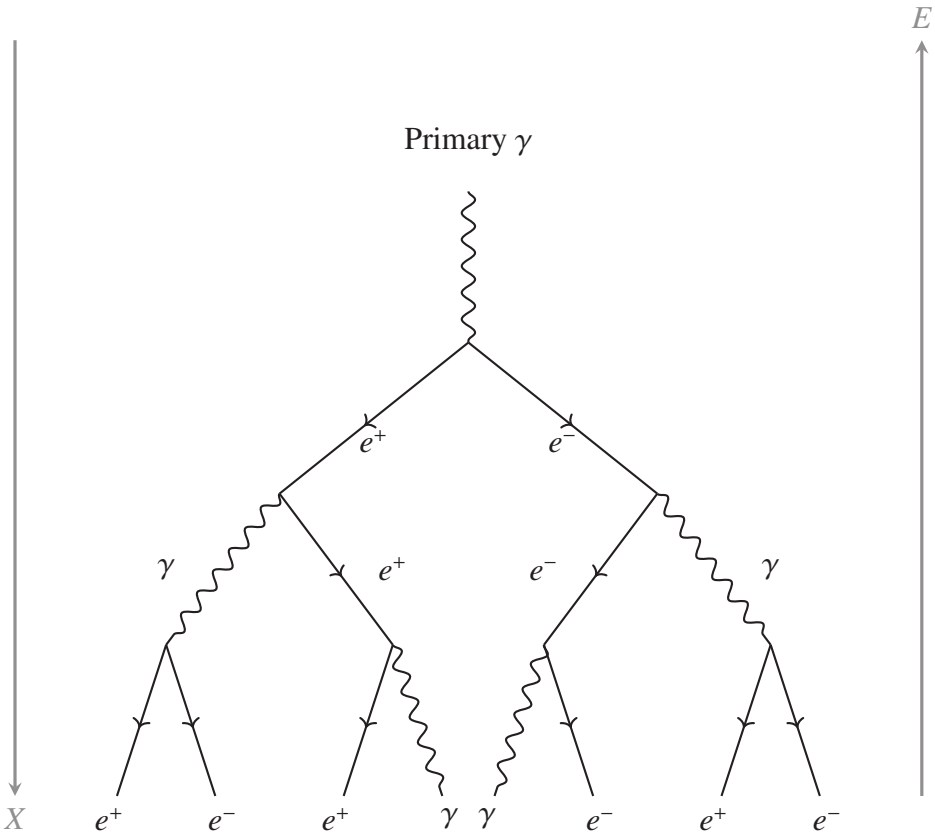

Figure 4.2 – Diagram of the first interaction steps of an electromagnetic cascade triggered by a primary photon penetrating Earth's atmosphere, based on the *Heitler* model. Left axis represents the depth X and the right axis the average energy E of the electromagnetic primary and secondary particles of the cascade. Based on Equation 4.2, an incident primary gamma-ray with an energy E_0 will lose half its energy at a depth $X = X_0 ln(2)$, three quarters of its initial energy at a depth $X = 2X_0 ln(2)$, and so on.

Cascades originating from an incident hadron will have endured additional interactions, including nuclei spallation from the impact, that will produce pions and mesons. The neutral pions π^0 may decay into gamma-ray photons whereas charged pions π^+ and π^- will decay to charged muons μ^+ and μ^-, and will have a longer combined parent then child particle livetime and reach the ground and therefore the detector. Hadronic showers may generate muonic components from the charged pion decay and a neutrino component generated from the pion, meson and muon decay. The different secondary particle sub-showers generated in the induced hadronic cascade render the reconstruction of the shower complex.

The growth of the cascade ceases when energy losses from ionisation become dominant in regard of the low energy created particles. This extinction occurs at a critical energy $E_{critical}$ defined when the ionisation losses equal the *Bremsstrahlung*. In air it has been estimated at $\sim$ 85 MeV for cascade particle average energy when the maximum shower development has been achieved[76] [109]. At the ground level, one may observe shower spreads[107], generated by gamma-ray photons, of a few meters. The size and structure of an extended air-shower depends on the characteristics of the primary particle i.e. the incident photon or hadron, such as its initial energy, the zenith angle when penetrating the atmosphere and the height of the first interaction with the atmospheric nuclei. Various studies via Monte-Carlo (MC) simulations[79] have underlined the difference between the intrinsic variability of hadron generated atmospheric showers with ones generated of gamma-rays of the same energy. Hadron showers are prone

to larger fluctuations. Due to transverse momentum transfer, the lateral extent of the shower increases, therefore the larger the transverse momentum component is, the larger the fluctuations shall be. This is used as a criterion to distinguish between electromagnetic and hadronic cascades.

4.1.2 Cherenkov radiation

High energy cascade particles produce *Cherenkov* radiation[130] when their velocity v in the Earth's atmosphere is greater than the phase velocity of light $c_{medium} = \frac{c}{n}$, where c is the celerity and n the refractive index in the given dielectric medium, which would be $n > 1$. This emission is the product of a varying electric dipole momentum originating from an asymmetric polarisation of the medium where the charged high velocity relativistic particles travel, giving rise to photon radiation as a result of the energy conservation principle. Thus, this effect will generate a wave front moving at velocity v and at a Cherenkov angle $\Theta_c = \frac{c}{n\,v}$, as illustrated in Figure 4.3. A particle of mass m may produce Cherenkov radiation if its relativistic energy is higher than the following energy threshold $E_{c,thresh}$ (energy for $v = c_{medium}$) :

$$\begin{aligned} E_{c,thresh} &= \gamma\, m\, c^2 \\ &= \left(\frac{1}{\sqrt{1 - \left(\frac{c_{medium}}{c}\right)^2}} \right) m\, c^2 \\ &= \left(\frac{1}{\sqrt{1 - (n)^{-2}}} \right) m\, c^2 \end{aligned} \tag{4.3}$$

Based on this energy threshold, particles with low mass will require a lower minimal energy to produce Cherenkov radiation that may be detected on the ground, as long as the atmosphere is transparent to the Cherenkov light wavelength, occurring usually in optical wavelengths at the blue range down to the ultra-violet domain, above ~ 300 nm.

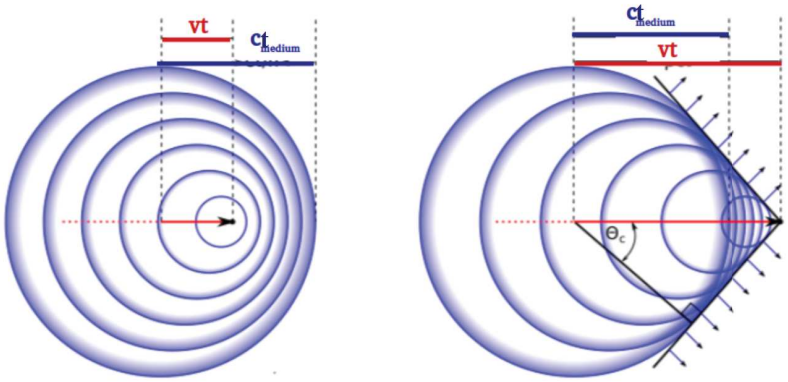

Figure 4.3 – Diagram illustrating the electromagnetic waves emitted along the propagation direction of a charged particle. On the left panel : case when the velocity v of the particle is less than the phase velocity of light in a transparent medium c_{medium}. On the right : case when $v > c_{medium}$. A Cherenkov light cone with an angle Θ_c forms along the axis of propagation. Figure taken (and slightly modified) from [99].

For cascades produced by high energy particles forming a Cherenkov angle $\Theta_c \sim 1°$, the Cherenkov light shed on the ground, called the *Cherenkov light pool*, would be greater than 0.1 km^2. This implies that the effective area where the primary gamma-ray photon of the air shower may be detected by ground-based experiments is rather large. Therefore, in order to detect a very-high energy primary particle, the widespread covered by the detectors on the ground has to be broad so as to be able to collect observe one of the following observables :

- the Cherenkov light generated in a transparent medium
- charged secondary particles such as leptons or muons reaching ground-levels
- fluorescence light generated in the atmosphere by very energetic cascades

These are all observables that allow the indirect detection of very-high energy gamma-rays, able to be observed via various ground-based techniques for detecting electromagnetic cascades : the Imaging Atmospheric Cherenkov Technique (Image Atmospheric Cherenkov Telescopes : H.E.S.S. , MAGIC, VERITAS, CANGAROO) based on the detection of Cherenkov photons emitted in extensive air showers by UV-sensible photomultipliers and the Air Shower Array one (HAWC, MILAGRO, Tibet-AS γ, Auger), detecting the secondary particles that reach the ground level at high altitudes thanks to a wide array of scintillators or water tanks. These two techniques are complementary, since IACTs have a smaller field of view ($< 2°$) compared to the Air Shower arrays ($< 45°$), however are able to reach energy thresholds of $\sim$ 0.05 - 0.2 TeV compared to 5-10 TeV for the latter. Another complementarity between these two very-high energy gamma-ray techniques would be the observation duty cycle which is constrained for IACTs by the ambient light : observations happen during the night time, limited by the moonlight contamination. By contrast, air shower arrays are not limited by optical light contamination and are able to operate both during the day and the night, allowing to have a considerably larger duty cycle but more prone to background contamination from charged cosmic rays.

4.2 H.E.S.S. phases and configuration

The High Energy Stereoscopic System experiment is an currently array of five imaging Cherenkov telescopes. These instruments allow to detect signals from cosmic gamma-ray radiation originating from galactic and extra-galactic gamma-ray sources emitting in the $\sim [0.1 - 100]$ TeV band through imaging of the Cherenkov light from atmospheric showers. All of the telescopes consist of a large single reflector dish of mirror facets, used to focus the incoming light onto the detector, which is a fast-imaging camera (Figure 4.4).

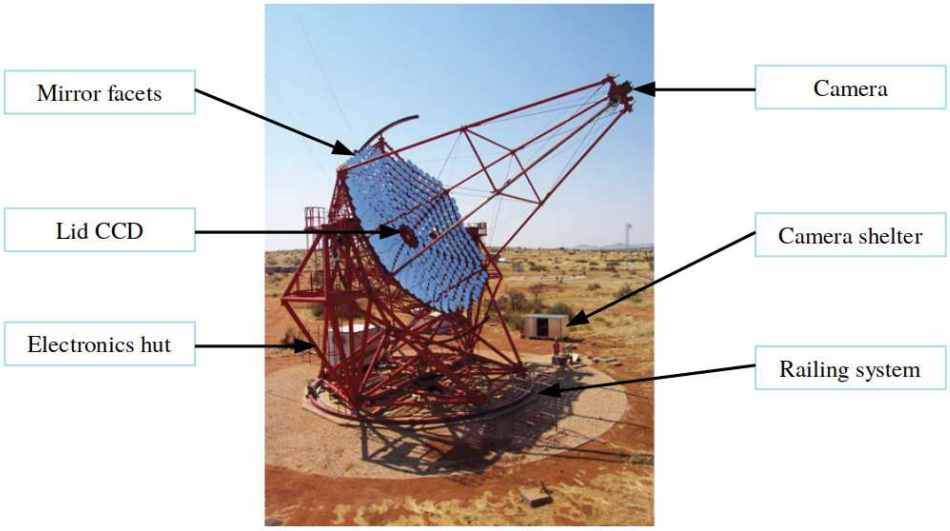

Figure 4.4 – Imaging Cherenkov Telescope on the H.E.S.S. site. This is the CT4 medium-sized telescope in side view, which is composed of a a hexagonal shaped reflector dish of mirror facets that focuses the light signal onto the Cherenkov camera. The H.E.S.S. Cherenkov camera is focused on a height of 10 km approximately corresponding to the typical shower maximum location. The focus of stars in the sky is on the camera lid which is imaged by a charged couple device (CCD camera) located in the plane of the reflector dish.

Four telescopes are medium-sized (see Section 4.2.3) and placed in a square formation while the fifth one is a large Cherenkov telescope in the middle of the array (see Section 4.2.4). The array configuration may be seen in Figure 4.5.

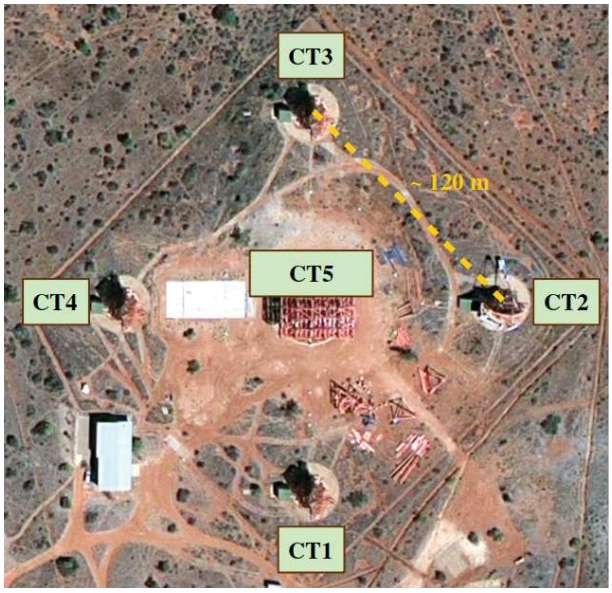

Figure 4.5 – H.E.S.S. site, view from above. The medium-sized telescopes CT1-CT4 are placed in a square array and the large-sized telescope CT5 is at the middle.

4.2.1 Event triggering

The camera of the H.E.S.S. telescopes has photosensors divided into drawers with 16 photomultipliers pixels. Each drawer is divided into two cards of 8 pixels. The light photons are collected by Winston cones at each camera pixel, and amplified by a photomultiplier tube. So as to be able to detect the signal generated by an observed shower, photomultiplier tubes (PMTs) record the charge of input photo-electrons (p.e.) and amplify the resulting current.

H.E.S.S. is nominally operating in a trigger charge mode, meaning that data are read out only when specific criteria of coincidence and luminosity are met. The camera is triggered by an incoming cascade when there is a coincident signal, above a threshold charge within a time span of a few nanoseconds (3 pixels with > 4 photo-electron (p.e) in a time window of 1.3 ns), for a number of pixels within a group of 64 neighbouring camera pixels. In nominal data acquisition mode, when the camera is triggered, the signal is integrated over the previous 16 ns, centered on the trigger time since the trigger occurred. This time integration window of several ns is essential in order to make sure to 1) integrate the maximum duration in the time window of the Cherenkov light wave front passage and 2) not drown the Cherenkov light signal in Night Sky Background noise fluctuations (see Figure 4.6).

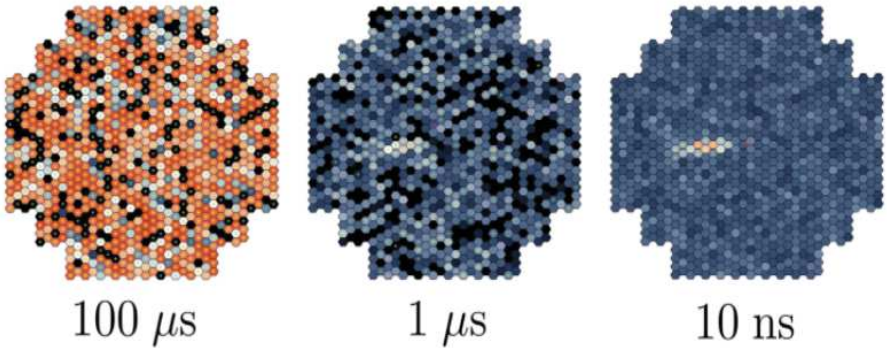

Figure 4.6 – Simulated camera type HESS-I images of a gamma-ray event. Each image has been produced with a different time window signal integration : from left to right 100 μs, 1 μs and 10 ns. The colorscale indicates the intensity received by each camera pixel. For longer time integration duration, the signal produced by the gamma-ray event is contaminated by background noise. Figure taken from [74], produced by K. Bernlohr.

After the time integration of the signal from the moment of the trigger, the recorded charge is converted to ADC steps (Analogic to Digitel Converter). Besides this individual camera trigger, another trigger for coincident events detected in the other telescopes is applied with an coincidence time of 80 ns that will lead to the data transfer onto the central system, so as to reduce the contamination caused from isolated muon events. When there is no telescope multiplicity, the telescope data acquisition is re-launched. The trigger rate for each observation depends on the hardware state, the atmospheric conditions and on the zenith angle at the time of the observation run. The trigger rate increases with decreasing zenith angle as a source will rise in the night sky because of the depth of first interaction in the incoming air shower. The cascade reaches its maximum at a $\sim$ 10 km altitude. When observing at large zenith angles, the air shower shall be more inclined and will illuminate a larger area on the ground with a scarcer photon density. Thus this effect with zenith angle will lead to a weaker signal detected on the ground level and will require a lower trigger rate.

4.2.2 Data acquisition

The duty cycle of H.E.S.S. occurs at night when the position of the Sun on the sky is at a $\gtrsim 18$ ° angle under the horizon. Officially the *darktime* observations occur while the moon is as well positioned under the horizon. Recently, twilight and *moonlight* observation tests have started after the revival of previous studies in the H.E.S.S. collaboration by decreasing the PMT gain; however it is still in a preliminary stage where further studies on the telescope performances are required. Based on the darktime good-weather observations, the annual H.E.S.S. observation time amounts to $\sim$ 1000 hours. A nominal observation run has a duration of 28 minutes, so as to homogenise observation conditions for each run and limit the data store volume.

In H.E.S.S. , the observational periods are delimited by the close-to-full and full moon, which are nights where no observations are made. Each shift of observation period requires two to three H.E.S.S. collaboration members to be present on site during night time to conduct the observations by parking the telescopes, supervising the loading/unloading CT5 camera from the shelters and deal with any kind of issue or warning message from any step of each observation run. The runs set automatically from an official scheduler based on observation proposals made by collaboration members and approved by the Observations committee. In case of targets of opportunity (ToOs) such as transient sources like gamma-ray bursts (GRBs), gravitational wave and potential neutrino events, it is essential to have an operational group of shifters ready to launch smoothly the additional observations triggered by the alert. In addition to problem solving, being contacts on site and overall conductors of the observation program, the shifters schedule manually *calibration* runs at the end or beginning of several night times so as to permit the ongoing monitoring of hardware performances. I have had the opportunity to experience the above shifters' duties by being on the P201710 shift.

After triggering the data recording, the output analogue signal is digitised in the drawers and then sent to the central data acquisition crate via an optical fibre.There are three channels: the trigger channel and two acquisition channels with different gains: the high-gain (HG) channel, used to detect signals with charges < 200 p.e. and the low-gain (LG) channel used to cover the range from 15 to 1600 p.e.

4.2.3 HESS-I and HESS-IU : medium-sized Cherenkov telescope array

Optics

The four medium-sized Cherenkov telescopes CT1-CT4 have a dish diameter of 12 m. The reflectors have a *Davies-Cotton* optical design[88] with 382 circular identical mirror facets with 60 cm diameter, which allow easy alignment and better image quality up to $\sim$ degrees from the optic axis before off-axis aberrations become significant. The total reflector dish area is $\sim$ 110 m^2. The Davies-Cotton design introduces a time-spread of a few nanoseconds into the light pulse due to the inherit asynchronous total reflector surface of the optical design. The light reflected off the dish is focused onto a Cherenkov camera at a 15 m distance, which is the focal length of the reflector. The CT1-CT4 telescope cameras have 960 pixels of 0.16° each which yield a field of view of ~ 20 $^{\circ 2}$. The buffer memory is set to 128 ns, where the 16 ns signal integration window is used when the cameras are triggered. The coincident trigger event rate for one camera is typically greater or equal to 1 kHz while it is reduced to 200-400 Hz for the entirety of the array. The estimated time of data recording is of $\sim$ 450 μs, which is added to the dead time since no other data may be acquired before its end. For the HESS-I array, the central trigger is

stereoscopic, requiring a multiplicity above two array telescopes.

From late 2016 to mid 2017, the four HESS-I cameras CT1-CT4 have been upgraded so as to improve their performance. In particular, one of the main goals behind this upgrade, was to reduce the camera dead time to a comparable value to CT5, in an effort to improve stereoscopic mode observations with all five telescopes of the array. This camera hardware and software modification change, including replacements of mechanical systems such as the trigger, read-out, power and cooling components but excluding the photomultipliers, will be referenced as the HESS-IU era. Along with the hardware and software changes, a second data acquisition mode called "sample mode" has been made possible in parallel of the nominal "charge mode". This additional acquisition mode has been implemented so as to allow more flexibility on the time window integration of the signal in order to prevent image truncation of high energy events, which have higher impact distances and therefore require longer image time gradient. During sampler mode, individual signals of the order of a few $\sim$ ns are taken in a 9 and 16 ns time window, permitting a more efficient time integration for very high energy events [141].

4.2.4 HESS-II : adding a large-sized Cherenkov telescope to the array

Camera and trigger

In 2014, the HESS-II phase started with the inauguration of a fifth, large-sized Cherenkov telescope CT5 added to the centre of the array. Its effective dish diameter is $\sim$ 28 m (23 m $\times$ 33 m) composed by 875 hexagonal mirror facets with a 90 cm "diameter". The reflectors have a parabolic shape optical design and the hexagonal shape of the mirror facets had been chosen for close packing purposes, to form a total reflector area of $\sim$ 610 m^2, with a focal length of 36 m. The parabolic shape design has been preferred over the *Davies-Cotton* optics because the former does not introduce significant asynchronous reflector surface as the latter, which would be enhanced by the larger dimensions of this Cherenkov telescope compared to the other ones in the array. The camera of CT5 has 2048 pixels of 0.07° each, yielding a $\sim$ 10 $^{\circ 2}$ field of view. The buffer memory is set to 256 ns, in which a nominal 10 ns signal integration window time is used when the camera is triggered. In HESS-II, CT5 can trigger the central system on its own and therefore observe in monoscopic mode, with a 15 μs dead time due to electronics. Thanks to its large collective area, CT5 has a lower air shower energy threshold of [0.02 – 0.1] TeV that is scientifically motivated so as to bridge the observational energy gap between satellite and ground-based experiments. However its central trigger rate is of a few kHz which makes it more prone to background noise contamination. Despite its 580 tonnes of weight, CT5 has a powerful motorised system which allows a 100° rotation in one minute, making it a great tool for transient source observations which require fast and impromptu pointings.

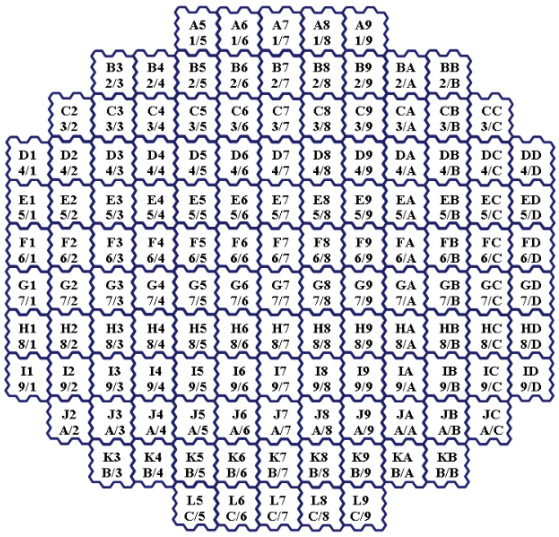

Figure 4.7 – Decomposition of the CT5 camera into drawers with the coding based on the hardware (H/H) and software (SS) conventions, where H and S range from A to L and from 1 to 9. CT5 has 128 drawers of 16 PMTs each, rendering an image of 2048 pixels.

4.3 Calibration

The output of the telescope cameras is converted to a charge value per pixel, in ADC steps, which are raw data depending on the camera electronics, the performances of the photo-multipliers and the mirror reflectivity and alignment. In addition to simulated instrument response functions (IRFs), it is essential to track the evolution with time of the hardware and to calibrate it.

For example, the calibration of the telescope pointing precision is usually made by comparing the position of well-known stars in dedicated pointing runs. This is achieved during the beginning and the end of an observational period by turning on a set of LEDs mounted on the lid of the camera and using them as reference points in comparison to catalogued background stars.

The information acquired both by regular calibration is used as well to convert the ADC steps of the recorded data to photo-electrons. The calibration is used to deduce the conversion coefficients during the digitisation of the signal and to account and correct pixel-to-pixel variations in performance. For each event, the signal amplitude of each pixel in the camera is measured in ADC steps $A_{ADC}^{channel}$ and is derived in photoelectrons $A_{p.e}^{channel}$ in the high (HG) and low (LG) gain channels as :

$$\begin{aligned} A_{p.e}^{HG} &= \frac{A_{ADC}^{HG} - P_{ADC}^{HG}}{G_{ADC/p.e}^{HG}} \times FF \\ A_{p.e}^{LG} &= \frac{A_{ADC}^{LG} - P_{ADC}^{LG}}{G_{ADC/p.e}^{HG}} \times FF \times \frac{HG}{LG} \end{aligned} \tag{4.4}$$

where

- $P_{ADC}^{channel}$ is the position of the baseline, the pedestal, for each acquisition channel measured in ADC steps
- $G_{ADC/p.e}^{HG}$ is the gain measured in the high-gain channel measured in ADC steps per photo-electron

- $\frac{HG}{LG}$ is the amplification ratio between the high and low gain channels
- FF characterises the relative efficiency of a pixel compared to the mean value over the camera, the flat-field coefficient

For both acquisition channels of each camera pixel, the calibration of the electronics provides the pedestal (which is evaluated in a sliding time window from the data), the high gain and the ratio of the two gain channels. The flat-field coefficient is a corrector factor to account variation in camera inhomogeneity.

4.3.0.1 Pedestal and Gains

In the calibration process, in order to determine the Cherenkov signal, it is required to estimate a baseline of the system response when zero Cherenkov photons are "detected". The pedestal of a pixel is defined as the mean average of ADC steps when there is no signal emitted nor detected. In the dark, meaning in the absence of Cherenkov light, electronic noise will have a narrow Gaussian distribution in ADC steps that provides the position of the dark pedestal, In order to obtain the electronic pedestal for each camera pixel, dedicate runs are made with the lid of the camera kept closed, securing almost no ambient light contamination. Pedestals depend on the temperature of the hardware, which may vary from ~ 20° C up to ~ 40° C and as experience through the years has taught us, sometimes by more, depending on the weather conditions and on the absence of light signal and therefore of any kind of luminous contamination.

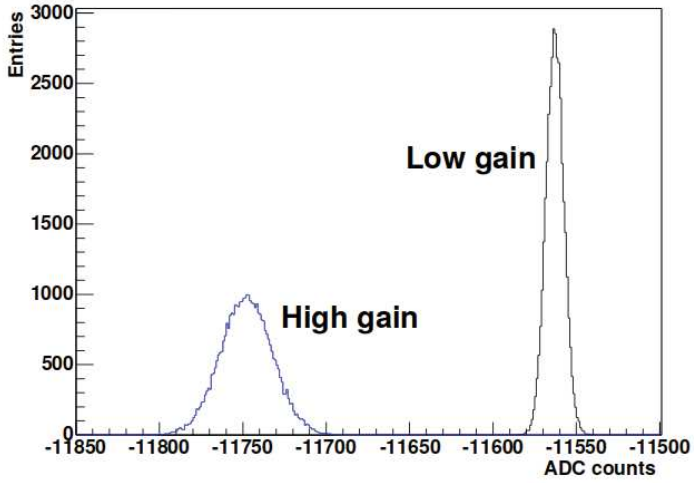

Figure 4.8 – Distribution of the pedestal in ADC steps for the high (HG) and low (LG) gains of a camera pixel in HESS-I. Figure taken from H.E.S.S. calibration paper (2004)[29].

So as to convert the electric signal from ADC steps to p.e, the gain has to be estimated. This is achieved by measuring single photo-electrons emitted from a dedicated and pre-calibrated pulsating LED (light emitting diode) source, that provides a flash with an average 1 p.e. The value of the gain for each pixel is obtained by fitting the distribution of pixel values (in ADC steps) after a single p.e calibration run, which is the convolution of the instrument response with a Poisson distribution from the LED signal. This fitted distribution is approximated with two Gaussian components : the electronic pedestal and the single p.e. The high-gain channel is sensitive to the single p.e because it has enough resolution in comparison to the low-gain channel. The number of ADC steps between the pedestal and the single p.e. signal is set to ~ 80 ADC

steps, for a PMT gain of $2{\times}10^5$, so that the peak of the single p.e signal may be distinguishable. The charge distribution of the signal of $n_{p.e}$ photoelectrons in ADC steps X_{ADC} is fitted as[37] :

$$\begin{aligned} Q(X_{ADC}) = N_{tot} \times \frac{e^{-\mu_{spe}}}{\sqrt{2\pi}\,\sigma_P}\, e^{\left(\frac{\left(X_{ADC}-P^{HG}_{ADC}\right)^2}{2\sigma_P^2}\right)} \\ + N_{tot} \times \mathcal{N}_{Poisson} \sum_{n=1}^{n>>1} \frac{e^{-\mu_{spe}}}{\sqrt{2\pi n}\,\sigma_{spe}} \frac{\mu_{spe}^n}{n!}\, e^{\left(\frac{\left(X_{ADC}-\left(P^{HG}_{ADC}+nG^{HG}_{ADC/p.e}\right)\right)^2}{2n\sigma_{spe}^2}\right)} \end{aligned} \tag{4.5}$$

where

- N_{tot} is the total number of events
- μ_{spe} is the average number of photoelectrons per event, known as the single p.e fraction
- P^{HG}_{ADC} is the position of the pedestal in ADC steps through the high-gain channel
- σ_P is the width of the pedestal Gaussian
- σ_{spe} is the width of the single p.e Gaussian
- $G^{HG}_{ADC/p.e}$ is the gain of the photomultiplier in the high-gain channel
- $\mathcal{N}_{Poisson}$ is a normalisation constant depending on how close to a Poisson distribution is the fitted distribution. If it is a true Poisson distribution, $\mathcal{N}_{Poisson}$ should be equal to unity.

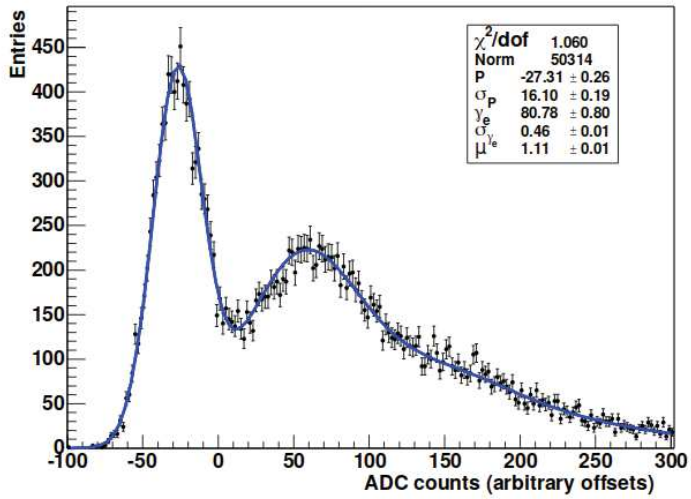

Figure 4.9 – Distribution in ADC steps for a single photoelectron run in the high-gain channel (HESS-I). The lower charge peak corresponds to the pedestal position and the second one to the single p.e signal. The blue line indicates the two Gaussian fit, where the parameters are shown in the upper-right corner of the plot. Figure taken from [29].

4.3.0.2 Flat-field

The photocathodes and Winston cone light collectors, as well as atmospheric conditions during observation time and the quantic efficiency of the photomultipliers may introduce some variation

in the homogeneity of the pixel charge distribution seen by a Cherenkov camera. This quality alteration is due to the optical transparency of the atmosphere varying with time and with a global hardware evolution as the years go by. Therefore the efficiency of the light collection must be calibrated regularly. This optical efficiency is measured as the relative response of each camera pixel when detecting the light coming from a well-know source homogeneously shedding light onto the camera. This is achieved by conducting flat-field runs, where a source composed of 13 LEDs is shedding a stable light at a well defined wavelength.

For HESS-II, the LUPM group has been in charge of building and providing a calibration source for the flat-field runs and possible outdoor single photoelectron runs. The calibration source is mounted at the centre of the CT5 dish. The calibration source is emitting a flat-field light pattern at 400 nm with 3 - 4 ns pulses full width at half maximum between 0.1 p.e and 1000 p.e at a 1 Hz to ~ 8 kHz repetition rate. The design has 13 LED pulsers that may be activated individually. The global pulser voltage is adjustable and is set from -8 V (with a total of 9 selected LEDs) to -12 V (all 13 LEDs activated). The concept utilised by the instrument LUPM team is shown in Figure 4.10 with an example of stability test using one of the LEDs firing continuously for 24 hours at a 1kHZ repetition rate and recording every 15 minutes the output signal. The flatness of the source light is estimated at ~ 10 % from laboratory measurements. The LUPM team is as well involved in the Cherenkov Telescope Array calibration studies.

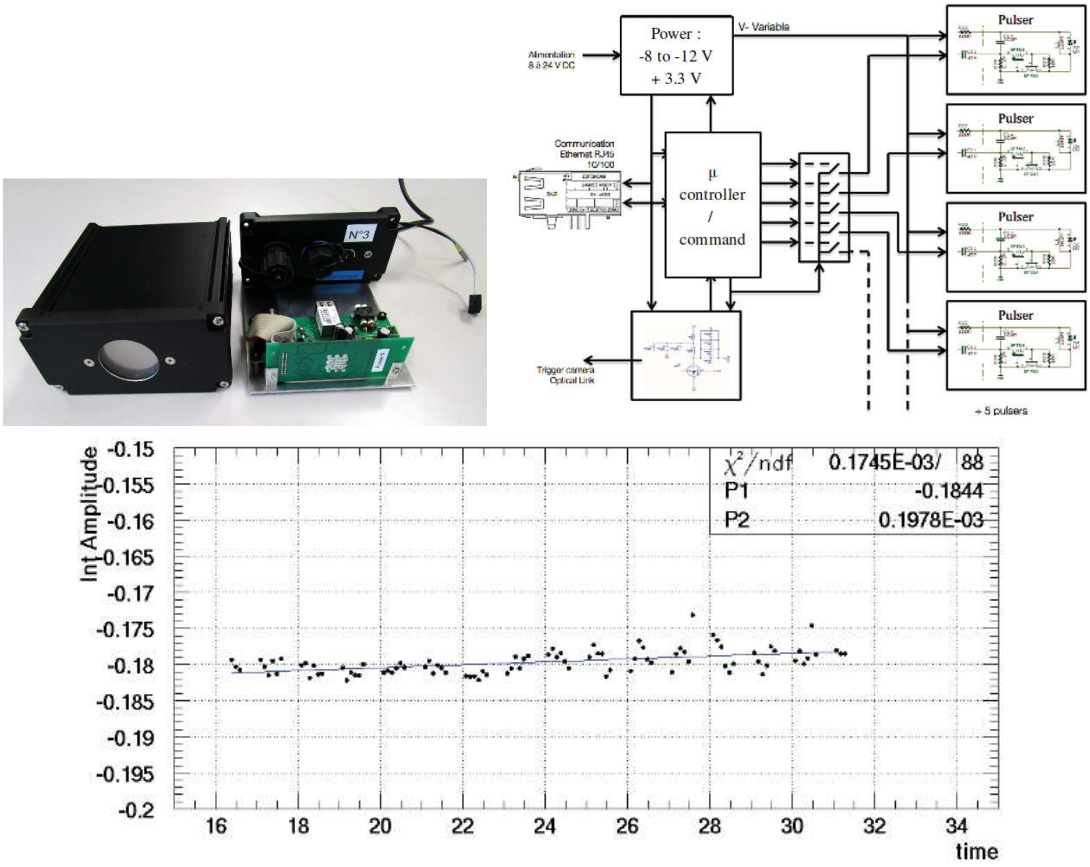

Figure 4.10 – Prototype developed by the LUPM instrument group of the flat-field pattern calibration source at 400 nm. On the bottom panel, an example of calibration source stability test conducted in the laboratory is shown, as described in Section 4.3.0.2.

During my thesis, I have been assigned the task of monitoring regularly the flat-field runs taken during the observation shifts so as to alert if there is an issue. So as to do so, I have

used and altered a code developed by Dr Diane Fernandez Gangoso during her PhD thesis at LUPM, several years ago. This code permits to read a flat-field run, to compute the fitted signal distribution charge in ADC steps in the high and low gain channels and to obtain the intensity seen by the CT5 camera for each pixel.

I will present briefly some examples of studies conducted in the spirit of monitoring the flat-field runs taken from 2017 up to the beginning of 2019. For each flat-field run, I tried to conduct a fast analysis as quick as possible following the days after it had been taken so as to make sure to notify the H.E.S.S. instrument experts if there were any inconsistencies that could underline an issue either with the data acquisition software (erroneous read out or source control) or with the source stability. I have worked on accumulating the measurements of the mean charge (Figure 4.11) in the high-gain channel and on checking the camera image for each taken run. An example is shown in Figure 4.12, where in 2017 an accumulation of runs showed a slight offset illumination from the center of the camera. After alerting the flat-field source experts, a manual correction had been made on-site during autumn 2017 so as to re-align the source mounting.

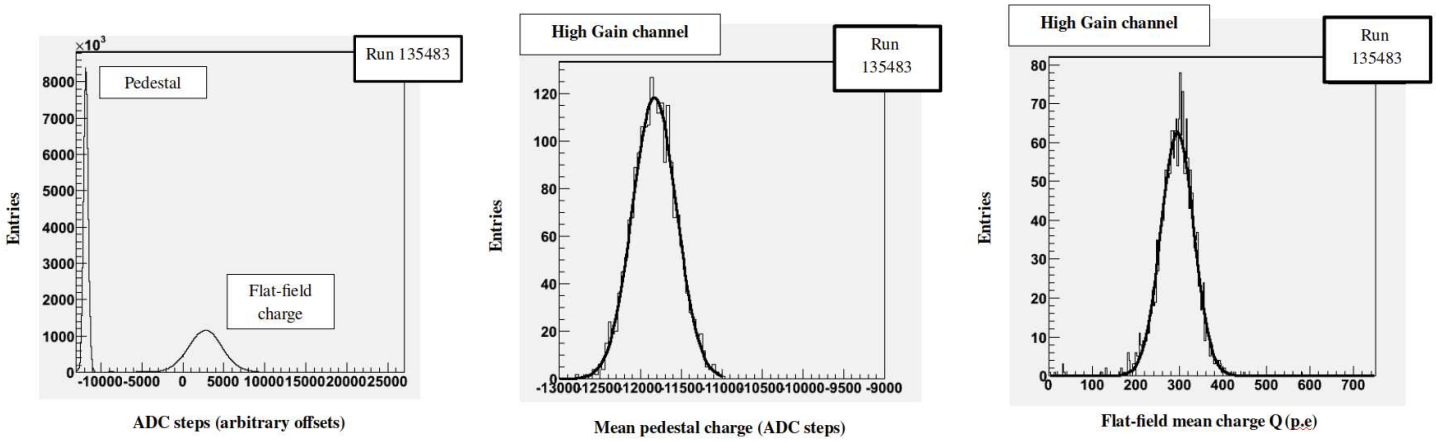

Figure 4.11 – Charge distributions from reading a CT5 flat-field run. On the left : global charge distribution in ADC steps for the high-gain channel. In the middle : pedestal charge averaged over all entries, fitted with a Gaussian distribution yielding an average charge of -11830 ± 275 ADC steps. On the left : flat-field mean charge in photoelectrons fitted with a Gaussian distribution yielding a mean charge $Q_{mean} \pm \sigma_Q$ of 240 ± 43 p.e with a ∼ 15 % dispersion from its mean value.

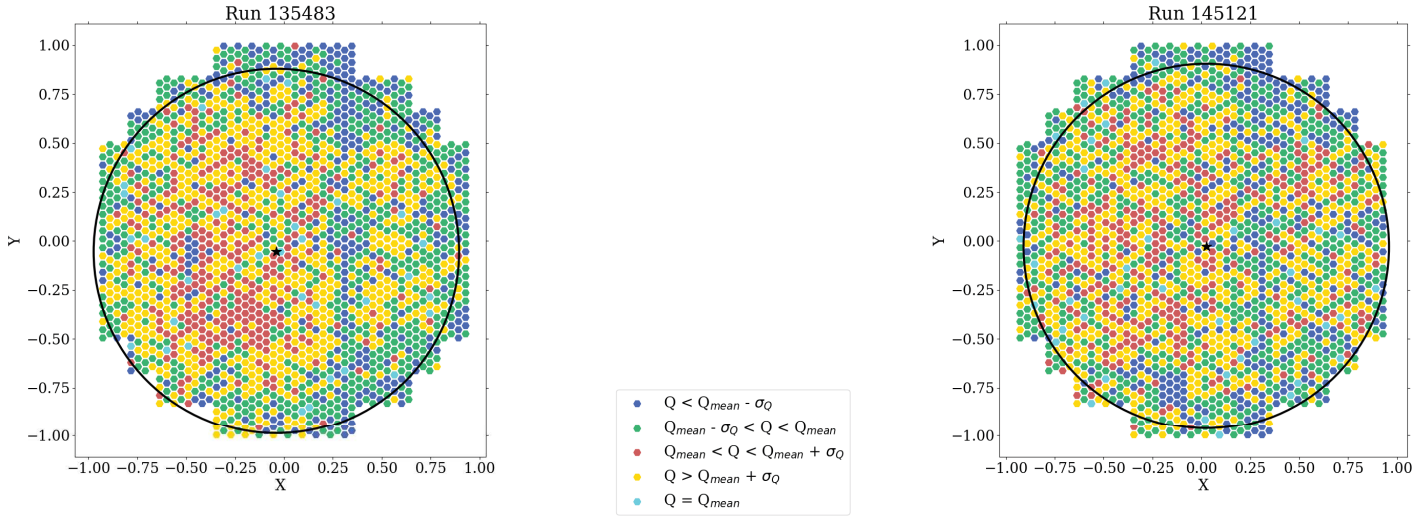

Figure 4.12 – Images of camera pixels and their charge Q from the high-gain channel in photoelectrons. On the left a run from 2017 and on the right a run from 2019. The colours represent the pixel charge value in comparison to the fitted mean Q_{mean} and standard deviation σ_Q values extracted from distributions as illustrated in Figure 4.11. The black circle and star represent a two-dimensional Gaussian fit applied on the image so as to determine if there is an apparent offset (right panel).

By keeping track of any encountered problems during the shifts by reading the shifter's logs, I have been able to omit from my studies the runs that were incomplete (stopped due to the end of darktime) or that occurred when there were errors with the CT5 hardware and/or software, such as pixel saturation or other technical issues. From the resulting sub-sample, where the criterion was that there where no technical nor practical issues during the data acquisition, I have been able to produce a preliminary stability curve for the derived mean pixel charges during 2017, 2018 and the beginning of 2019 as shown in Figure 4.13, for all runs where all drawer responses were as expected (no discarded drawers). Two methods were employed for such derivations : A) direct measurement on the data histogram of the mean value and of its quadratic mean and B) the Gaussian fit of the distribution yielding the mean and standard deviation values. In the beginning of 2018, a manual intervention has been made by the H.E.S.S. CT5 camera team by raising the voltage of the power of the photomultipliers, making its average Q_{mean} value to jump from 306 ± 40 p.e to 352 ± 43 p.e. On Table 4.1, the parameter values of the linear regression fit depicted in the graphs of Figure 4.13 show that for the observation periods in 2017 and 2018, there has been a steady decrease of the mean charge value due to the expected deterioration of the hardware with time. The values regarding the difference between the two methods of derivation confirms that both methods are equivalent within their estimated error intervals, even though the Gaussian fit method B seems to estimate systematically over $\gtrsim$ 20 p.e than method A. An important point that should be stressed is that I do not use the computed most recent values of the photomultiplier gain $G^{HG}_{ADC/p.e}$. So as to derive at the earliest convenience the charge distributions and not having to wait for the single photoelectron runs to be processed and to be stored in the H.E.S.S. calibration database, I use the same read-from an old SPE run mean distribution of the gain for each individual pixel of the camera. This consistent gain value, which is not realistic and its value should be the closest estimation made around the run date during

the observational period, can explain the apparent decrease of the mean charge with time. The average intensity of the signal declines with time due to the degradation of the photomultiplier gains. To counter-effect with this, their voltage is raised, which was the case in the beginning of 2018. However, this does not affect the quality tests regarding the flat-field shown in Figure 4.12 since they are scaled to the mean signal of the corresponding run.

Table 4.1 – Table with the fit values of linear regression ($Q_{mean} = a\times$ run + b) on the samples of the derived mean charge value Q_{mean} from the flat-field runs over 2017 and 2018. The study of the runs taken in 2019 are still in progress. The method index convention is as presented in Figure 4.13. The linear correlation coefficient r, measures the strength and the direction of a linear relationship of the mean charge value over the time.

Method	Year	Slope a (p.e per run)	Intercept b (p.e)	Correlation coefficient r
A	2017	-5.8 10^{-3}	1086.54	-0.85
B	2017	-6.0 10^{-3}	1112.40	-0.87
A - B	2017	1.8 10^{-4}	-25.86	0.38
A	2018	-7.6 10^{-3}	1421.57	-0.96
B	2018	-7.8 10^{-3}	1442.64	-0.97
A - B	2018	1.4 10^{-4}	-21.07	0.29

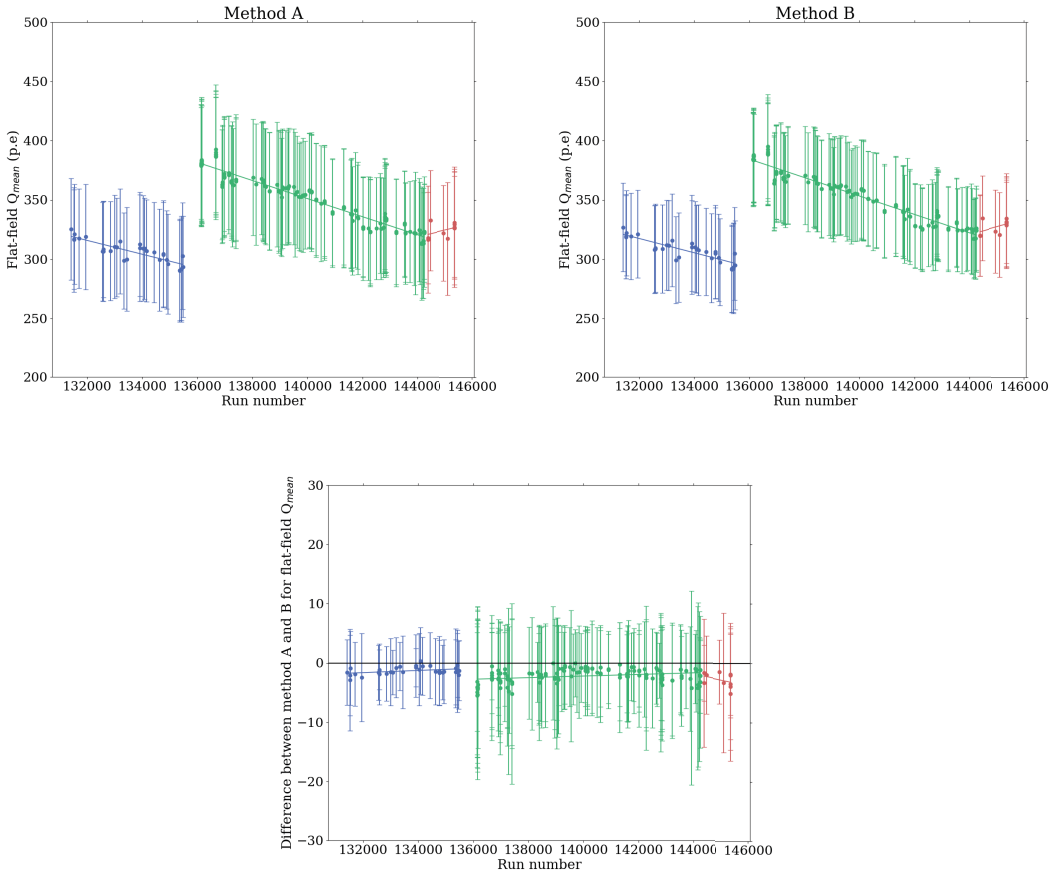

Figure 4.13 – Values of the flat-field mean charge Q_{mean} derived for runs in 2017 (blue), 2018 (green) and beginning of 2019 (red). Top panel : values derived directly from the histogram data (method A) and those derived after fitting the distribution with a Gaussian function (method B). Bottom panel : difference between the values found with method A and method B. The parameters of the fitted linear regression shown with solid lines on the graphs can be found in Table 4.1.

In regards of the calibration flat-field monitoring during my thesis work, I plan to automate the procedure so as to keep the same uniform study tool up until the camera of CT5 is replaced with the *FlashCam* prototype[134], in autumn 2019.

4.3.0.3 Reconstruction and image analysis

Once the calibration of the instruments is made, the analysis of the incoming signal, or lack of it, originating from a cascade triggered by an incident cosmic-ray photon or hadron will allow to reconstruct its origin in direction, its provenance as which primary parent particle has triggered the chain of atmospheric reactions and thus its energy. This requires to clean the taken images by applying cuts on the Cherenkov signal, as signal charge thresholds. The images can be parametrised in the so-called *Hillas* reconstruction, by fitting an ellipse using its position, its width, its length, its amplitude and its distance from the camera. The parameters are scaled per telescope and averaged depending on the multiplicity (number of triggered telescopes within the array). The details of such reconstruction are presented in [38].

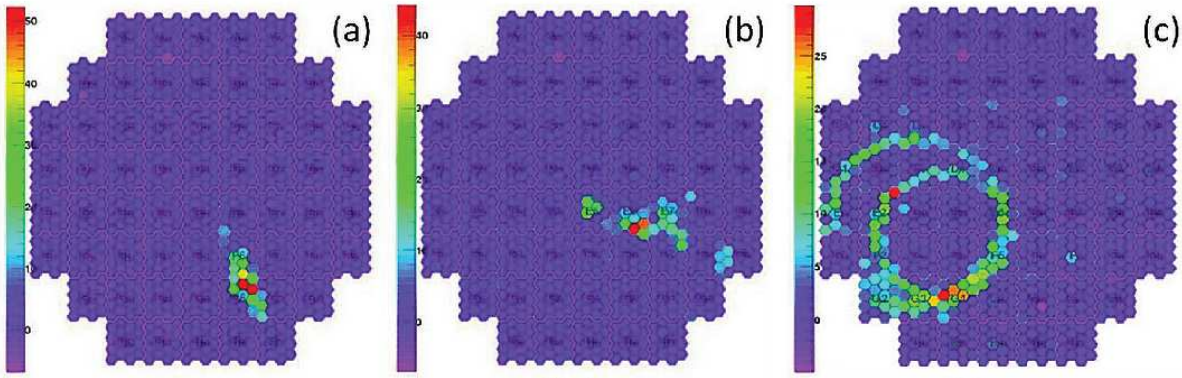

Figure 4.14 – Examples of the HESS-I telescope camera images when detecting a gamma-ray photon (a), a hadron (b) and a muon (c). The muon gives a distinctive ring feature but in case of large impact it may be mistaken for a gamma-ray event because of its segmented shape. Hadron and gamma-ray discrimination can be made on the spread of the ellipse, which is more regular in the gamma-like events. All parametrisation require to be compared with accurately simulated events so as to classify the events and minimise spurious detections.

The image ellipse parameters are compared to MC generated parameter tables so as to separate the photon and hadron events (example of camera images shown in Figure 4.14), to reconstruct the direction of provenance and to estimate the energy of the primary particle. The width and length of the ellipsoid are compared with expected values and may provide, when combined based on multiplicity, a multiple point-of-view (from telescopes in different spatial position) reconstruction of the spread of the shower and thus provide a robust gamma-ray/hadron discrimination. The event classification is therefore made on the basis of discriminating parameters so as to separate the gamma-ray candidate events with the background events.

By extrapolating the major axes of the ellipses present in multiple telescope images, the intersection point will provide the direction of the incoming shower. Consequently the monoscopic direction reconstructions will be less rigorous than the stereoscopic ones with high multiplicity. In order to reconstruct the energy of the incident photon, the image amplitude and distance to the camera centre (that is linked to the impact parameter of the shower) may be used by taking into account the zenith angle of the observation. At a given impact, the amplitude is proportional to the energy of the cascade given both the simulated and measured optical efficiencies.

In H.E.S.S. , two reconstruction template-based methods are generally used : the *Model ++* analysis chain tool [37] and the *ImPACT* (Image Pixel-wise fit for Atmospheric Cherenkov Telescopes) [90]. In these procedures, the cleaned image is fitted with a model prediction derived from MCMC simulations where the reconstruction on energy and direction is simultaneous.

In Chapter 5, examples of background estimation, source morphological and spectral analyses will be given concerning a particular source of interest.

Chapter 5

The VHE gamma-ray morphology of the PWN MSH 15-52 limned with H.E.S.S

Contents

5.1 Astrophysical context

Within the composite SNR MSH 15-52 (G 320.4-1.2 [126]), the central compact object has been identified as the pulsar PSR B1509-58 (pulsations first detected in [85]). Both have been observed in radio wavelengths [46], in X-rays [45], [6] and in high-energy gamma-rays [23], whilst the asymmetrical and irregular shape of the PWN, slightly reminiscing of the silhouette of a hand, has been brought to light. In 2005, VHE gamma-ray emission was reported by H.E.S.S. , coincident with the X-ray PWN. Its morphology based on 22.1 hours of observations was best described by an elliptical Gaussian component [30]. Over the years, in later studies, slightly more complex models with additional components have been used for the fitting procedure of the shape of the VHE emission and have been proven to statistically better describe the distribution of the emission than the single Gaussian component model [59].

The morphology of this object seen in X-rays is linked to synchrotron radiation thus it is strongly depending on the magnetic field assumptions. Inverse Compton (IC) scattering on seed photons of either the Cosmic Microwave Background (CMB), the Far Infrared radiation from dust (FIR) and/or the Near Infrared and visible radiation from stellar absorption (NIR) are likely be the dominant leptonic mechanism that may accelerate photons up to TeV energies [23].

In this chapter, I will present the dedicated study I have conducted alongside Dr Y. Gallant, and other members of the H.E.S.S. collaboration (in particular Drs R. Terrier, E. de Oña-Wilhelmi, R. Zanin, M. Sasaki and J. Vink) regarding this pulsar wind nebula system. I compare the VHE gamma-ray morphology of the composite system linked to the IC scattering, to the synchrotron radiation via available non-thermal X-ray data Section 5.2.2. Moreover, I present the results of an energy-dependent morphological analysis (Section 5.3.1.4) and report on the spectral shape of the emission (Section 5.3.2). Finally, I discuss the implications of our results (Section 5.4) on the modelling of the spectral energy distribution when considering realistic photon target populations for the VHE spectrum derived from our latest study.

5.2 Observations

In this analysis, HESS-I data are used for the morphological study as the instrument response functions (IRFs) are better understood since they have been extensively studied. A HESS-II dataset has been considered for the spectrum computation, as to allow a lower energy threshold that may be achieved when including CT5. However the spectral analyses with HESS-II data we have conducted, did not have the appropriated simulated IRFs for the HESS-IU observations due to production delay. We performed a HESS-I spectral analysis, to be consistent with the HESS-I analysis.

5.2.1 Gamma-ray dataset

In order to disentangle the morphology of the composite SNR MSH 15-52 , we use a larger H.E.S.S. dataset of observations of the HESS-I era than the previous publication. We use gamma-ray count maps generated with the *ParisAnalysis* (version 0-8-24 Prod 6)[37] using a Model ++ standard (*Std*) and high resolution (*HiRes*) cut method. The results have been cross-checked using the *HAP* chain as well, being an independent reconstruction and calibration analysis chain in H.E.S.S.

The main analysis, Model ++, uses a gamma-ray all-pixel log-likelihood minimisation reconstruction technique developed for IACTs, based on the comparison of the raw telescope

images with simulated expected images from semi-analytical models. The event classification is made based on discriminating parameters that separate the data into :

- gamma-ray candidates ("gamma-like" events). Their signal peak is within the chosen discriminating variable value.
- background (cosmic-ray events). Their signal can be clearly decorrelated based on the value of the discriminating variable.
- un-categorised events. Their contribution falls in between the expected gamma and hadronic components of the signal in respects to the discriminating variable.

This classification of the signal events based on a given discriminating variable is illustrated in Figure 5.1.

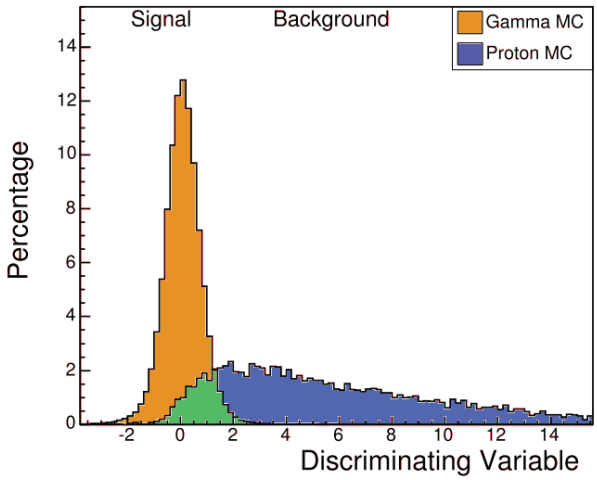

Figure 5.1 – Signal and background event classification based on a given discriminating variable derived from Monte-Carlo (MC) simulations of gamma-ray and proton induced air showers detected at the ground level from Cherenkov cameras. In this example, if the discriminating parameter value is chosen at 1.5, this would imply that most of the gamma-ray signal (yellow shade area) would be attributed however there would be a $\gtrsim 2$ % contamination per bin of the data sample from cosmic-ray background events. If the discriminating variable is set to 0 for example, the background contamination would be very low but it would imply that half of the gamma-like events would be rejected as well. This underlines the importance of finding a suitable balance between the background rejection and the signal statistics based on the chosen discriminating variable values.

In these analyses, runs have been selected within a radius of 2.0° from the central position of MSH 15-52 withstanding the criteria for adequate environmental conditions whilst the acquisition occurred. The dataset consists of 49.6 hours of live time. Several analyses sets have been studied so as to investigate the energy range of the detected emission by setting different energy thresholds (see Section 5.3.1.4). The model-based reconstruction technique has proven that it derives a more precise direction and energy reconstruction of the primary particle of the air shower while using a robust background rejection. Based on H.E.S.S. data, this model reconstruction method yields a factor of ~ 2 better sensitivity than the *Hillas* reconstruction technique.

Standard cuts consist on an event selection based on the noise-to-signal likelihood associated with the night sky background, the primary interaction depth range and the background associated

pixel grouping associated to hadron clusters. The cut on the energy is set by assigning a default threshold of 60 p.e. which roughly corresponds to $\gtrsim 0.3$ TeV. When these criteria apply, the total exposure is amounting to 37.7 exposure-corrected hours. As for the high resolution cuts, all the above selections apply in addition to a given criterion on the direction error of the reconstructed particle shower. The resulting exposure-corrected time is 45.2 hours, as a radius of 2.5° of run selection has been applied. Although the data sample is statistically reduced with the above additional measure, it remains less contaminated by non-related lepton-induced showers thus ensuring a higher quality reconstructed event selection.

Moreover, for the energy-dependent analyses, the energy bin choice has been made after ensuring an optimal statistical equipartition of the excess within each bin after numerous tests. The investigation occurred within the [0.3 – 0.6], [0.6 – 1.2], [1.2 – 2.4], [2.4 – 4.8], [4.8 – 9.6] and > 9.6 TeV photon energy ranges (see Section 5.3.1.4).

To extract the signal from the HESS-I latest dataset, we used a comparison method between the number of events within a region of interest ("on" region) and a region used as a background estimator, assuming there are no gamma-ray events but only background ones in said selection ("off" region). To account for region size difference and IRFs variation within the two types of "ON" and "OFF" regions, a factor $\alpha_{ON/OFF}$ is introduced in the data analysis that allows to estimate on the expected background events that should be found within the targeted region of interest, accumulated for each number of selected run. The excess signal Σ_{excess} deduced from the average number of events in the respective "ON" and "OFF" regions is :

$$< \Sigma_{excess} >= < N_{ON} > - \alpha_{ON/OFF} \times < N_{OFF} > \tag{5.1}$$

In order to estimate the background, we subtracted any significant known gamma-ray emitting region present in the field of view of our analysis by applying a mask on the selected excluded regions. We based our choice of exclusion on the H.E.S.S. Galactic Plane Survey catalogued sources, resulting to the following circular excluded regions. We exclude a radius of 0.3° around the published position of HESS J1503-5820 [102], [59]. It is a source for which its very-high energy gamma-ray emission has not been firmly identified with an origin, thought to be associated with a high-energy point-like source detected by the *Fermi-LAT* 2FHL catalogue[24]. We exclude as well a radius of 0.5° around the reported position of HESS J1458-608, a spatially associated source with the pulsar PSR J1459-6053 and with a in source in the 3FGL high-energy catalogue[48]. We have not excluded the source HESS J1457-593, since there is a very small fraction of its emission that lies within our chosen field of view. Finally, we impose a target mask around our source of interest, HESS J1514-591 with a 0.4° radius. A schematic mapping of the excluded regions may be found in Figure 5.2.

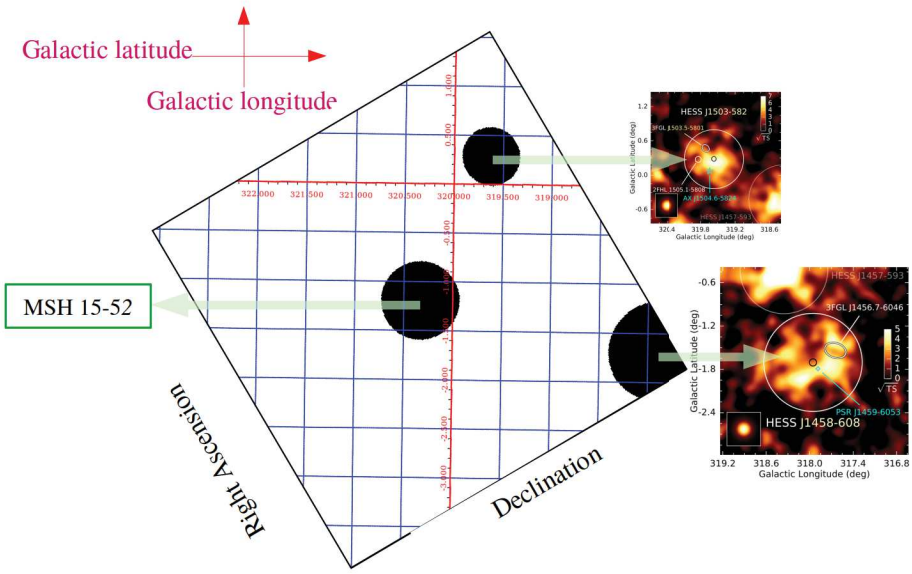

Figure 5.2 – Schematic illustration of the field of view of our analyses (black square of 16 $^{\circ 2}$) for the source MSH 15-52 with the excluded region selection (black discs) in a Galactic coordinates framework. The additional panels on the right are excerpts from the HGPS published results, used to determine the exclusion region, showing the spatial associations for these objects. The legend for these panels may be found in [59].

Since the source of interest is an extended source, in a relatively low contamination field of view that permits to spatially resolve the emission from the targeted object in respects to the other detected very-high energy sources and not heavily affected by the diffuse large scale galactic plane emission due to its Galactic latitude, two methods of background estimation would be suited and will be discussed here : the *Ring Background* and *Template Background* techniques. The two methods differ in their philosophies.

The *Ring Background* one consists of estimating the significance of the events classified as gamma-ray candidates in a shell region around a test position. It requires to determine the camera acceptance to gamma-like events and to compute sky maps either by assuming that the acceptance depends on the distance to the centre of the camera (radial acceptance) or by using a two-dimensional approach (2D acceptance) where the camera acceptance is projected using the pointing of each run. The *Template Background* method estimates the significance of both gamma candidate and background events in the same region as opposed to the annular method. We opted in our analyses for H.E.S.S. to use the *Template background* method as it is more suited for extended sources, as the resulted hadronic estimations with the *Ring background* method showed some unorthodox structures at the borders of the field of view, linked to the acceptance calculation for this method in comparison to the positioning of the chosen excluded regions at the borders of the field of view.

The study is conducted via image analysis on 4° x 4° images with a bin-size of 0.01°.pix^{-1} in the J2000 equatorial coordinate frame, centered on RA = 228.5290° and DEC = -59.1575°. The fitting procedure was made with the Sherpa package[50] using the raw count map of the gamma-like events, the Point Spread Function (PSF), a smoothed background and an integrated exposure map assuming a spectral index of gamma = 2.27[44]. We based our conclusions on the resulting *Cash* statistic[81] found after a Nelder-Mead simplex optimization method[77], which is a likelihood $\mathcal{L}$ function such as *Cash* = -2log($\mathcal{L}$).

5.2.2 X-ray template

In our analysis, we are focusing on tracing the lepton distribution of the PWN in MSH 15-52. In order to construct an X-ray template map, I have examined the extent of the energy range correspondence of the gamma-ray IC emission to the synchrotron radiation in X-rays.

At the north-western (NW) part of the source, the Hα nebula RCW 89 composed of irregular filaments, is spawning thermal emission. According to the spectrum of the brightest region in RCW 89, the thermal emission can be fitted with a non-equilibrium ionisation model (VNEI)[8] up until 3.8 keV and the non-thermal emission beyond with a power-law, as shown in Figure 5.3. The RCW 89 region is a knotted complex region with different estimated abundances, ionisation ages and temperatures as highlighted by the study of Yatsu et al. (2005)[139] suggesting that spectroscopic imaging hints that the thermally-emitting clumps in RCW 89, may be due to the encounter of the pulsar jet with the SNR shell boundary, but do not show detectable emission above $\sim$ 4 keV.

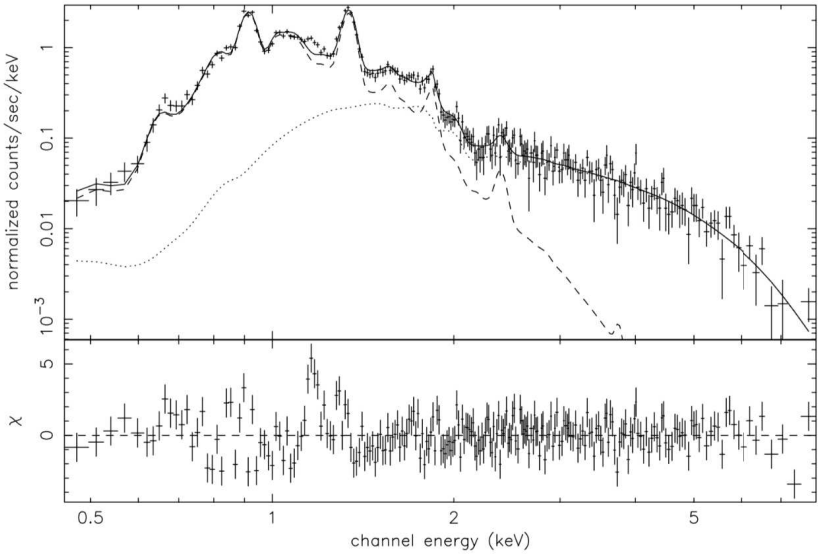

Figure 5.3 – Total spectrum of the RCW 89 region detected by the *Chandra* X-ray satellite[113]. The data are fitted with a non-equilibrium ionisation model (VNEI)[8] (dashed line) that corresponds to the thermal emission of the Hα region. The non-thermal component of the spectrum is fitted with a power-law (solid line depicting the global model) [139].

The X-ray template used in this analysis has been established using available *Chandra* [113] data (PI : P. Slane) of four archival observations amounting to $\sim$ 200 ks of exposure. We have chosen a threshold of 4 keV for the X-ray emission map so as to omit the thermal component at lower energy emanating from the SNR and in particular from the RCW 89 region. We use a modified version of the exposure-corrected X-ray map with an average estimate of the background, based on four regions in the image, subtracted from the template (Figure 5.4). The emission coming from the pulsar has been replaced by an average of its immediate surroundings so as to discard the emission from the X-ray emitting pulsar. Furthermore, a mask has been applied in order to keep only the significant X-ray emission from the PWN and to prevent noise at the outskirts of the image from influencing the fit.

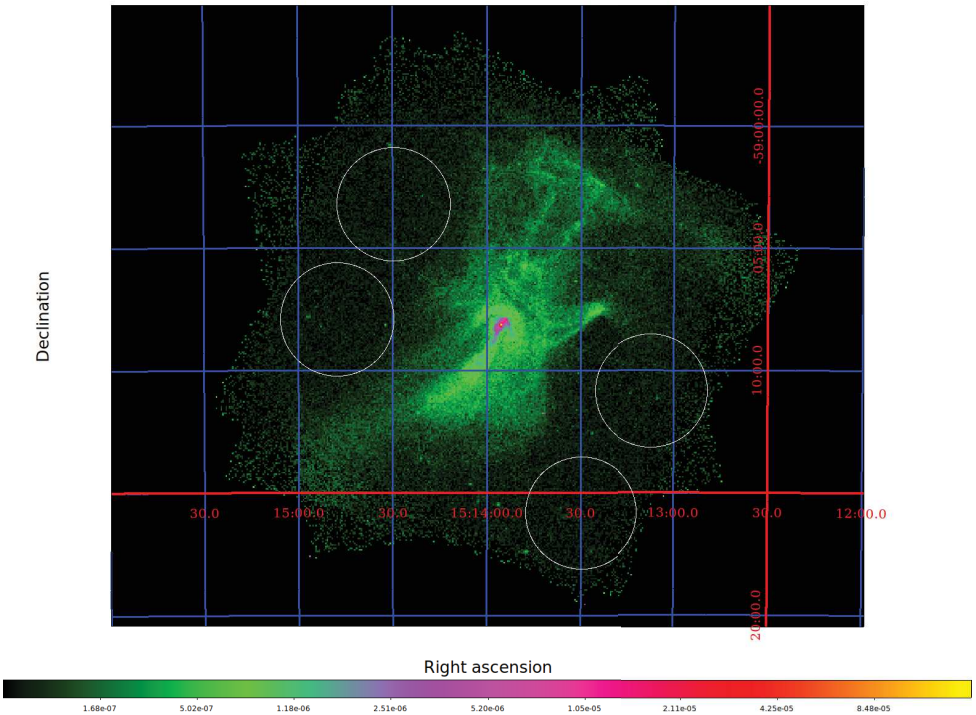

Figure 5.4 – Original X-ray template from *Chandra* archival observations in the [4 - 7] keV band. The white circles delimit the background estimation regions as discussed in 5.2.2. The peak of the emission is concentrated around the position of the pulsar.

One-zone model fits of the synchrotron and IC emission results to a magnetic field value $B \approx 17\,\mu$G[30] in the nebula. Electrons with a peaking synchrotron spectrum at $h\nu_{\rm synch} > 4$ keV will range at $E_e \gtrsim 100$ TeV. Same models for the gamma-ray IC emission suggest that the Galactic FIR background is the dominant target photon population [2] and shall be discussed in Section 5.4. For a blackbody temperature of 45 K, gamma-rays with $E_\gamma \gtrsim 0.3$ TeV are scattered by electrons with $E_e \gtrsim 2$ TeV. For synchrotron radiation in the [4 -7] keV, photons in the [40 - 60] TeV range will be produced by the acceleration of leptons alongside the magnetic field line. For the [0.3 - 20] TeV emission by IC on the CMB (where T $\sim$ 2.7 K),leptons have energies ranging from 9 to 80 TeV. When considering the infrared background from dust (T $\sim$ 45 K), the energy ranges from 2 to 20 TeV.

Despite the discrepancy regarding the outline of somewhat lower energy leptons prompted by the VHE gamma-ray map, given the compatible spectral indices [1], the distribution of the electrons and positrons can be hypothesised to be consistent between the gamma-ray morphology and the synchrotron map emission seen in soft X-rays.

5.3 Analyses

In this section I will summarise some of the methods and procedures used in our analysis regarding the source morphology (Section 5.3.1) and its derived spectrum (Section 5.3.2). The flux map of our analysis ranging from [0.3 - 100] TeV is shown in Figure 5.5, along with the contours of the X-ray template used for the morphology study.

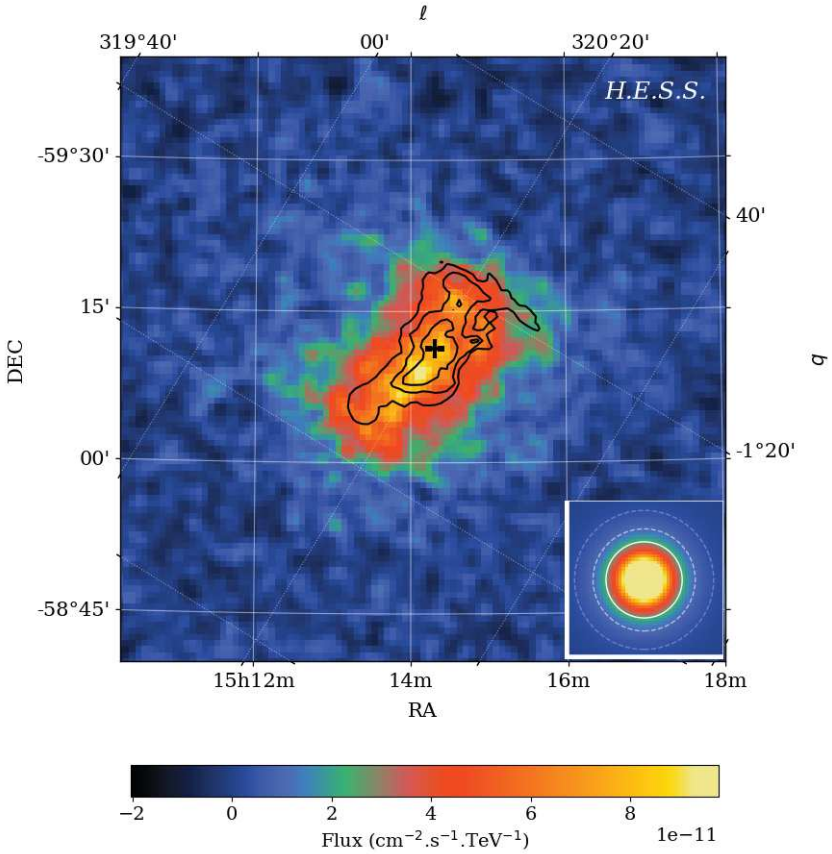

Figure 5.5 – H.E.S.S. Gaussian smoothed (at 1σ) flux map of the emission of MSH 15-52 . The black cross points to the position of the central pulsar PSR B1509-58. The black contours represent the X-ray emission seen with *Chandra*, used as a template in our analysis. At the bottom right, the instrument PSF is shown, with the 68%, 80% and 95% levels in white dashed lines.

5.3.1 Morphology

5.3.1.1 Emission fit

I fitted the emission maps, using different models consisting of first fixing the background, then convolving the X-ray template (and the additional components) with the H.E.S.S. point spread function (PSF) and multiplying the result by the exposure map (Equation 5.3.1.1). These models for the morphology fit of the very-high energy gamma-ray emission of MSH 15-52 may be summarised with the following equations :

$$\mathcal{M}_G = I_{BKG} + I_{EXP} \times (I_{PSF} \circledast \left[\mathcal{G}_{comp}\right]) \tag{5.2}$$

$$\mathcal{M}_X = I_{BKG} + I_{EXP} \times (I_{PSF} \circledast \left[T_{X-ray}\right]) \tag{5.3}$$

$$\mathcal{M}_{XG} = I_{BKG} + I_{EXP} \times (I_{PSF} \circledast \left[\left(T_X + \mathcal{G}_{comp}\right)\right]) \tag{5.4}$$

$$\mathcal{M}_{\alpha X} = I_{BKG} + I_{EXP} \times (I_{PSF} \circledast [(T_X \times R^{\alpha}_{PSR})]) \tag{5.5}$$

$$\mathcal{M}_{\alpha XG} = I_{BKG} + I_{EXP} \times (I_{PSF} \circledast \left[\left(T_X \times R^{\alpha}_{PSR} + \mathcal{G}_{comp}\right)\right]) \tag{5.6}$$

where the $\mathcal{M}_?$ notation corresponds to the model and its major components besides the instrument response functions $I_{???}$ (background, point spread function and exposure) : G for the geometrical component, X for the X-ray template and α for the distance dependence of the magnetic field assumption index (refer to description in Section 5.3.1).

The influence of the PSF has been explored by testing our procedure using a PSF broadened with a standard deviation of $\sigma = 0.022°$, which is representative of the PSF uncertainty based on a systematic study (H.E.S.S. collaboration paper on resolving the kpc jet morphology of the active galactic nucleus Centaurus A, paper submitted). Systematic errors have been derived by fluctuating the amplitude of the fixed background ± 20 %.

In order to discriminate on the best-fit model, I used a statistical tool from the literature, that compares the likelihood of each different model based on the made hypotheses so as to efficiently compare all the models (nested or not). This statistical test is known as the Akaike Information Criterion (AIC) [4]. It comprises a likelihood function and considers the number k of independently adjusted parameters in the given model thus enabling the comparison between models with different number of parameters : $\mathrm{AIC} = -2\log(L) + 2k$. The AIC may be as well defined based on the *Cash* statistic as $\mathrm{AIC} = Cash + 2k$ (see Section 5.2.1). The difference between the criteria $\Delta\mathrm{AIC} = \mathrm{AIC}_{\mathrm{model\,1}} - \mathrm{AIC}_{\mathrm{model\,2}}$ is used to determine the best model.

Here is a description of all the model components we introduced in our tested hypotheses in all the morphological analyses we have done for this pulsar wind nebula.

5.3.1.1.1 Geometrical components

We have used two-dimensional geometrical components, available in the *Sherpa* python package, as listed below :

- A symmetric Gaussian $\mathcal{G}_{G_{sym}}$ with four parameters : the position X and Y of its centre, its amplitude A and its intrinsic size σ defined from its full width at half maximum (FWHM).
- A disc $\mathcal{G}_{disc}$ with four parameters : the position X and Y of its centre, its amplitude A and R its radius.
- A projected 3D shell $\mathcal{G}_{shell}$ with five parameters : the position X and Y of its centre, its amplitude A, its inner radius R_{in} and its outer radius R_{out}.
- An asymmetric Gaussian $\mathcal{G}_{G_{asym}}$ with six parameters : the position X and Y of its centre, its amplitude A, its intrinsic size σ_{major} on its major axis, its eccentricity ϵ and the angle θ of its major axis.
- A Sersic profile[112] $\mathcal{G}_{Sersic}$ with seven parameters : the position X and Y of its centre, its maximum peak A, its core radius R, its eccentricity ϵ, the orientation angle θ of its major axis and the Sersic index n (if n = 0.5 it is a Gaussian distribution, if n=1 an exponential one, if n=4 a *de Vaucouleurs*[39] one, if n $\longrightarrow$ 0 it resembles a disk feature).

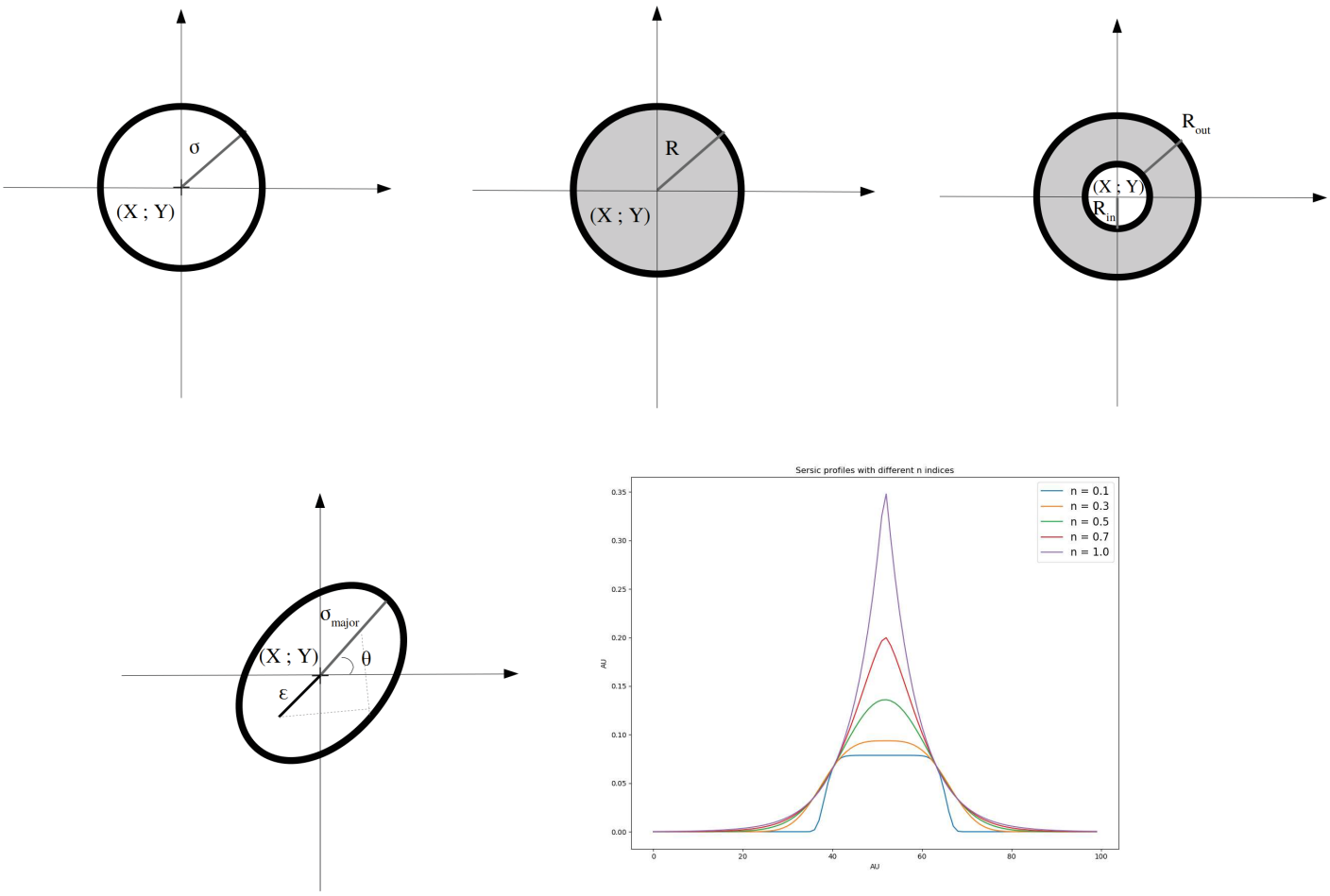

Figure 5.6 – Four cartoons illustrating the parametrisation of the geometrical model component (besides their amplitude). Top row, from left to right : symmetric Gaussian $\mathcal{G}_{G_{sym}}$, disc $\mathcal{G}_{disc}$ and shell $\mathcal{G}_{shell}$. Bottom row : asymmetric Gaussian $\mathcal{G}_{G_{asym}}$ and 2D Sersic distribution $\mathcal{G}_{Sersic}$. The graph depicts a 1D Sersic profile projection for different indices n ranging from 0.1 to 1.0.

5.3.1.1.2 The α parameter

Following the conclusions underlined in (de Jagger and Djannati-Ataï)[36] regarding a common trend shared by many pulsar wind nebulae seen with H.E.S.S. relying on the comparison of their energy fluxes produced by synchrotron and inverse Compton and being close to unity, we use this property to fit the gamma-ray morphology of MSH 15-52 with the spatial distribution of its X-ray emission. When using only the X-ray template for fitting the shape of the gamma candidates count map, the $\mathcal{M}_X$ model, the results indicated that the central region around the pulsar is dominating the fit procedure, even though the emission coming from the pulsar itself had been previously removed in the image analysis. This can be clearly seen in the residual map, where there is an apparent correlation between the position of the pulsar and the striking negative residuals (see model $\mathcal{M}_X$ shown in Table 5.2). Thus the actual longitudinal profile of MSH 15-52 is not fully reproduced, as in addition to the plunging negative residuals mentioned above, there are also positive residuals at larger distances from the central emission.

This strongly implies that the X-ray emission coming from the region around the pulsar is still too bright when compared to our gamma-ray data. Therefore, by assuming that the magnetic field **B** varies spatially, we impose a dependency of **B** with the projected distance R_{PSR} to the pulsar

position, by multiplying the X-ray template by R^{α}_{PSR} where α is a given index to be determined by the fit results (see Equation 5.5 and 5.6 for models $\mathcal{M}_{\alpha X}$ and $\mathcal{M}_{\alpha XG}$).

An example of the re-binned (to suit our gamma-ray map resolution and sky projection) X-ray template when applied this α-parameter magnetic field approximation is shown in Figure 5.7 for different values of the parameter.

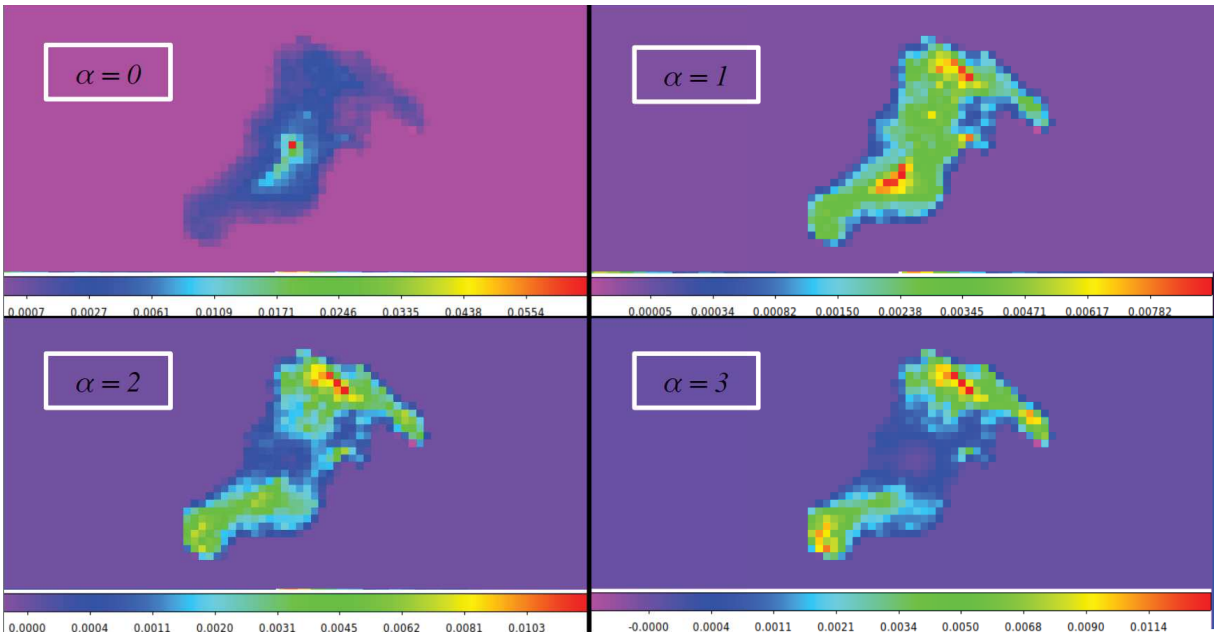

Figure 5.7 – Example of X-ray templates used in the fitting procedure for four values of the α parameter as described in the legend.

This parameter α, should hint at the actual dependence of **B** with the distance R. Thus based on this magnetic field component approximation, the Inverse Compton flux F_{IC} is approximated to the synchrotron flux F_{sync} times the distance R to a given power α : $F_{IC} \propto F_{synch} \times R^{\alpha}$.

I shall discuss further the interpretation of this introduced to our morphological model investigations α parameter in Section 5.4.1.

In the fitting procedure, the alpha parameter value ranges from 0 up to 3 with steps of 0.01. We have estimated its errors by considering the test statistic found for each value of α and by estimating the 1σ-error from its minimal value (which is set as $\alpha \sim 1.3 \pm 0.25$).

5.3.1.2 Elongated emission

When performing the fit with the model $\mathcal{M}_G$ (Equation 5.2), meaning by fitting the gamma-ray emission of the source with a geometrical component, the best fit-models based on the AIC, are the ones introducing an elongated shape. The most significant results for the *Std* cut wide energy range analysis are summarised in the following tables and figures. The Sersic profile fit (model $\mathcal{G}_{Sersic}$) confirms the assumption that a Gaussian-like distribution is the most preferred best on the Sersic index ($n = 0.58 \pm 0.06$ which is ~ 0.5) and yield same results as the asymmetrical Gaussian (model $\mathcal{G}_{G_{asym}}$) which is preferred to the symmetrical one (model $\mathcal{G}_{G_{sym}}$) with a ΔAIC of 109. This confirms the previously published H.E.S.S. results [30], stating that the emission of the MSH 15-52 PWN is elongated and asymmetrical in longitudinal profile comparison in the two directions axes.

Table 5.1 – Summary of the size characteristics of the fitted emission when applying a lone geometrical component : model $\mathcal{M}_G$ (see Equation 5.2).

$\mathcal{G}_{comp}$ name	Model map	Residuals map	Parameters	AIC
$\mathcal{G}_{G_{asym}}$	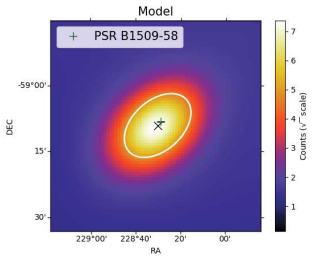	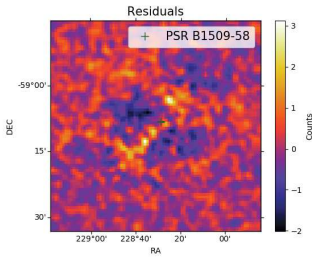	• σ_{major} : 7.49 ′ ± 0.17 ′ • σ_{minor} : 4.85 ′	**282 037**
$\mathcal{G}_{G_{sym}}$	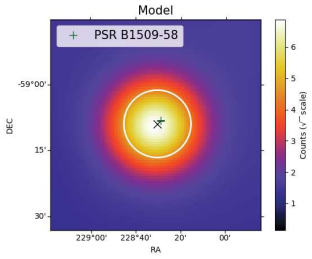	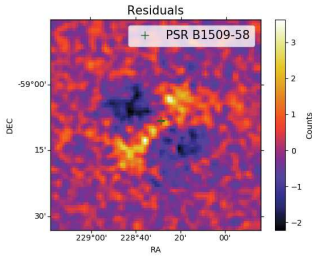	• σ : 6.51 ′ ± 0.13 ′	282 156

The shape of the residuals in the solely geometrical component models indicates that there is a underestimation of the emission along the direction axis of the source and a overestimation along its perpendicular direction.

5.3.1.3 X-ray template fit

The use of an X-ray template in the morphological fit of the MSH 15-52 emission is both motivated by the physics of the radiation processes, the synchrotron mapping of corresponding leptonic populations that shall be scattered via Inverse Compton on seed photons, and by the positive residuals shown in Table 5.1. The template is used in the fit procedure as a map whose amplitude A_{X-ray} (in counts) is a thawed parameter. We compare this derived amplitude with the amplitude of the added geometrical components in the model fit by considering the respective amplitude ratio $A_{G/X-ray}$. For the case of a symmetrical 2D Gaussian, we integrate the counts found for its amplitude parameter over its intrinsic size and compare it to the X-ray amplitude A_{X-ray} so as to deduce the portion of its contribution $P_{G/X-ray}$

The summary of the best-fit results with the morphological models encompassing the use of the X-ray template may be found in Table 5.2.

Table 5.2 – Summary of the size and amplitude components for the best-fit models incorporating an X-ray template (see Equation 5.3, 5.4, 5.5, 5.6).

Model name	Model map	Residuals map	Characteristics	AIC
$\mathcal{M}_X$	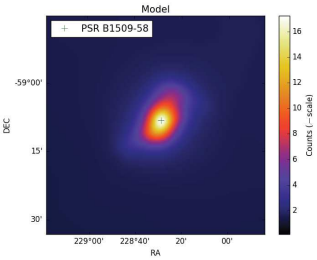	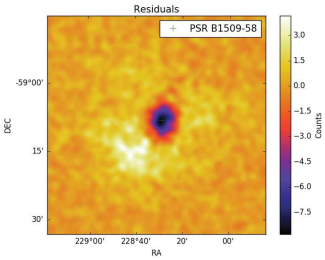	• A_{X-ray} : 1020 ± 25 counts	283 327
$\mathcal{M}_{XG_{Gsym}}$	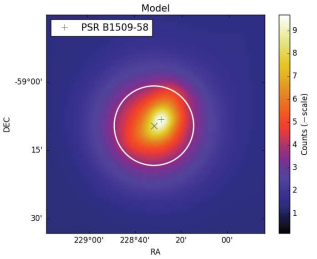	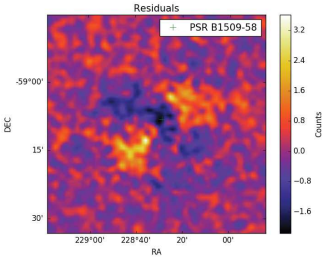	• $P_{G/X-ray}$: 82 % ± 6 % • σ : 7.41 ′ ± 0.20 ′	282 087
$\mathcal{M}_{XG_{Gasym}}$	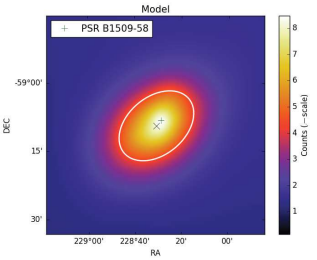	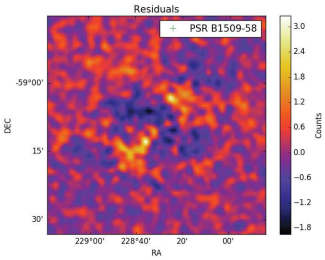	• $A_{G/X-ray}$: 0.014 ± 0.004 • σ_{major} : 7.88 ′ ± 0.23 ′ • σ_{minor} : 5.38 ′	282 029
$\mathcal{M}_{\alpha X}$	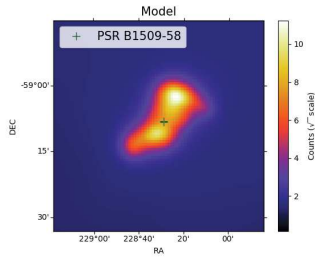	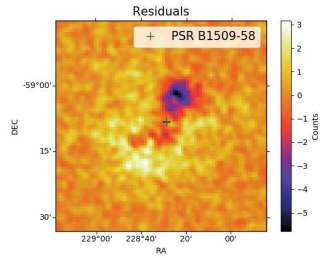	• A_{X-ray} : 1184 ± 26 counts	282 775
$\mathcal{M}_{\alpha XG_{Gsym}}$	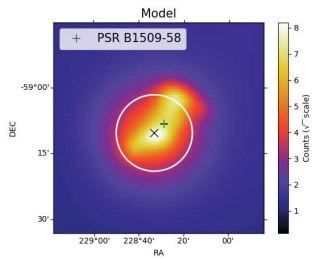	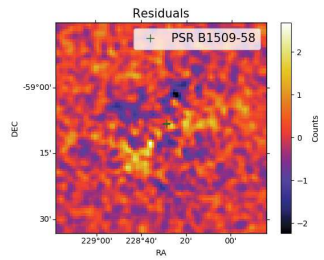	• α = 1.3 • $P_{G/X-ray}$: 69 % ± 6 % • σ : 7.38 ′ ± 0.24 ′ • RA : 15 h 14 min 17.0 sec ± 2.5 sec • DEC : -59 ° 10 ′ 55 ” ± 19 ”	**281 980**
$\mathcal{M}_{\alpha XG_{Gasym}}$	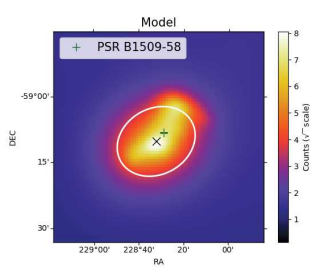	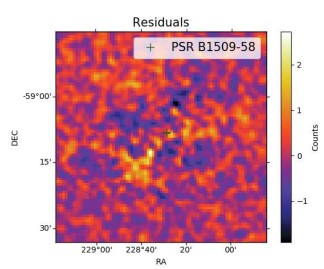	• α = 1.3 • $A_{G/X-ray}$: 0.003 ± 0.0005 • σ_{major} : 7.88 ′ ± 0.28 ′ • σ_{minor} : 6.37 ′ • RA : 15 h 14 min 13.6 sec ± 2.5 sec • DEC : -59 ° 10 ′ 47 ” ± 18 ”	**281 973**

5.3.1.4 Energy-dependence

Besides the analyses in the wide energy ranges of [0.3 – 100] TeV, I have investigated the possible energy dependence of the extended emission observed for the pulsar wind nebula within MSH 15-52 . After extensive investigation, I chose the following energy bins within the [0.3 – 0.6], [0.6 – 1.2], [1.2 – 2.4], [2.4 – 4.8], [4.8 – 9.6] and > 9.6 TeV photon energy ranges. We have used two different sets of cuts applied for the event reconstruction, the standard (*Std*) and high-resolution (*HiRes*) cuts as described in Section 5.2.1 and compared in Figure 5.8 based on the estimated excess (derived from Equation 5.1).

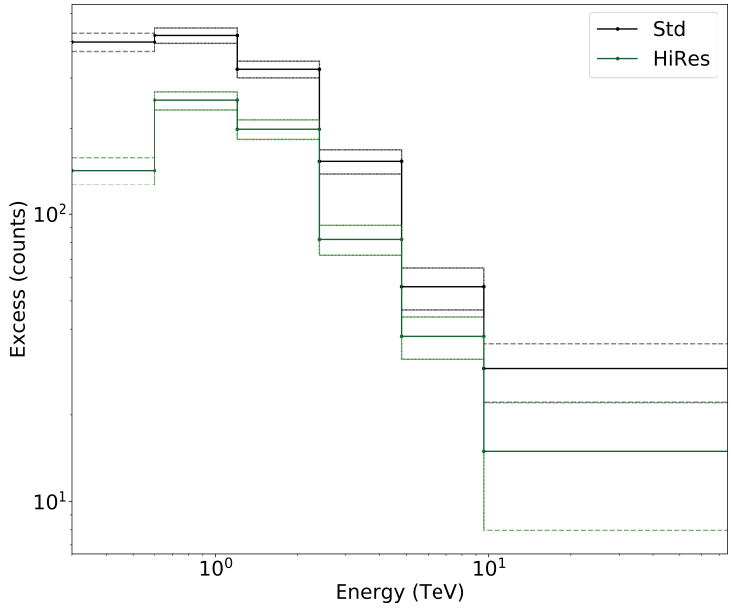

Figure 5.8 – Excess count distribution in the six energy band for the *Std* (black) and *HiRes* (green) cuts analyses, plotted in a logarithmic scale.

After further inspection on the data, we found that the excess beyond ~ 30 TeV becomes negative, due to a misrepresentation of the estimated background, as seen in Figure 5.10 for the *Std* cuts analysis. Therefore we performed the morphological analysis for the highest energy bin again and imposed an upper bound at 30 TeV. The results are still currently cross-checked with an independent analysis tool as the H.E.S.S. collaboration guidelines require and will not be shown in this dissertation. The latest results from the main analysis-side, all seem to be in agreement with the ones shown here and shall be published once the cross-check procedure is completed.

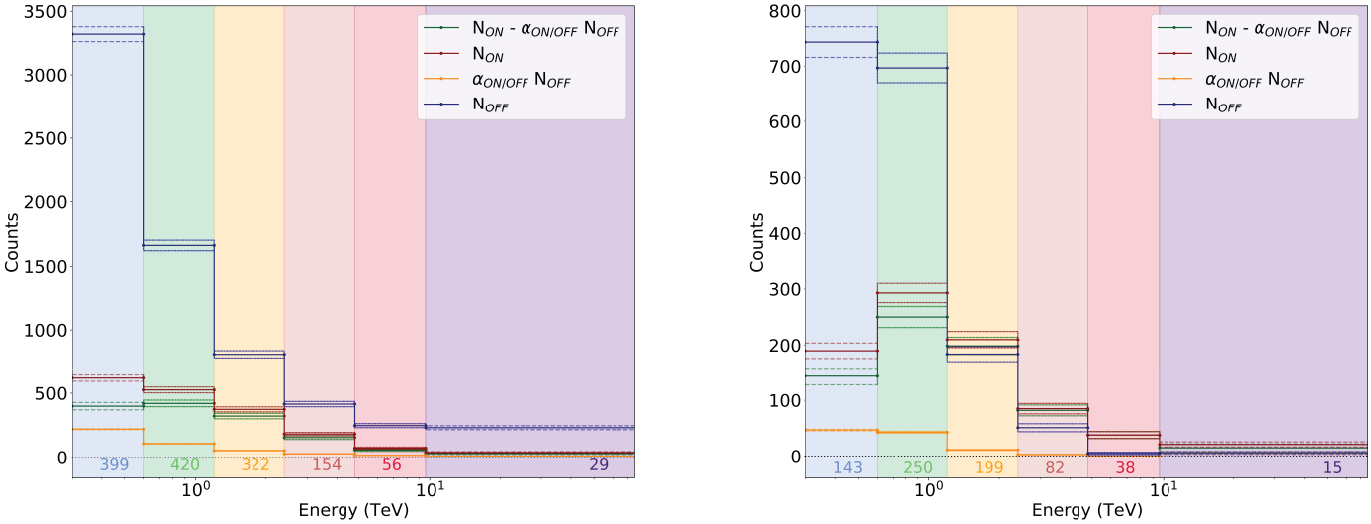

Figure 5.9 – Counts distribution in the six energy band for the *Std* cuts analyses (left) and *HiRes* cuts (right). The green line represents the estimated excess counts derived from the ON and OFF regions (see Equation 5.1). The coloured numbers indicate the total said excess in each colour-coded energy bin. The red line represent the counts within the ON region and the blue line within the OFF one. The orange line represents the background counts acceptance-corrected.

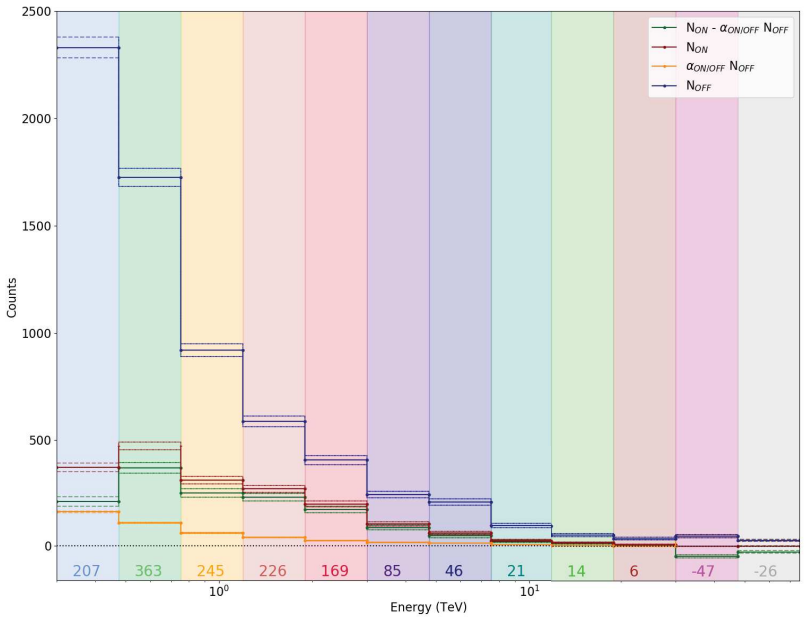

Figure 5.10 – Counts distribution in twelve logarithmically spaced energy bands for the *Std* cuts analyses. The green line represents the estimated excess counts derived from the ON and OFF regions (see Equation 5.1). The coloured numbers indicate the total said excess in each colour-coded energy bin. The red line represent the counts within the ON region and the blue line within the OFF one, The orange line represents the background counts acceptance-corrected.

The best-fit models when fitting the emission in each energy bin, have been systematically the ones including a Gaussian component (or a two-dimensional Sersic profile with an index ~

[0.4 - 0.6]). Our conclusions on the energy-dependence of the source are drawn from the lone asymmetrical Gaussian model (model $\mathcal{M}_{G_{G_{sym}}}$). In Figure 5.11 I show the extent of the fitted emission (its intrinsic size) as a function of energy. There is a overall tendency of the total emission shrinking and it is marginally significant at the highest energy bin : above $\sim$ 10 TeV. This energy range is as well the lowest one from the chosen bins in number of statistics but comprises a deviation at $\sim 3.0\sigma$ and 4.6σ from a constant extent hypothesis in the *HiRes* and *Std* cut analyses respectively. The morphological shrinking at the highest energy bands trend > 5 TeV is seen as well on the significance maps shown in Figure 5.12.

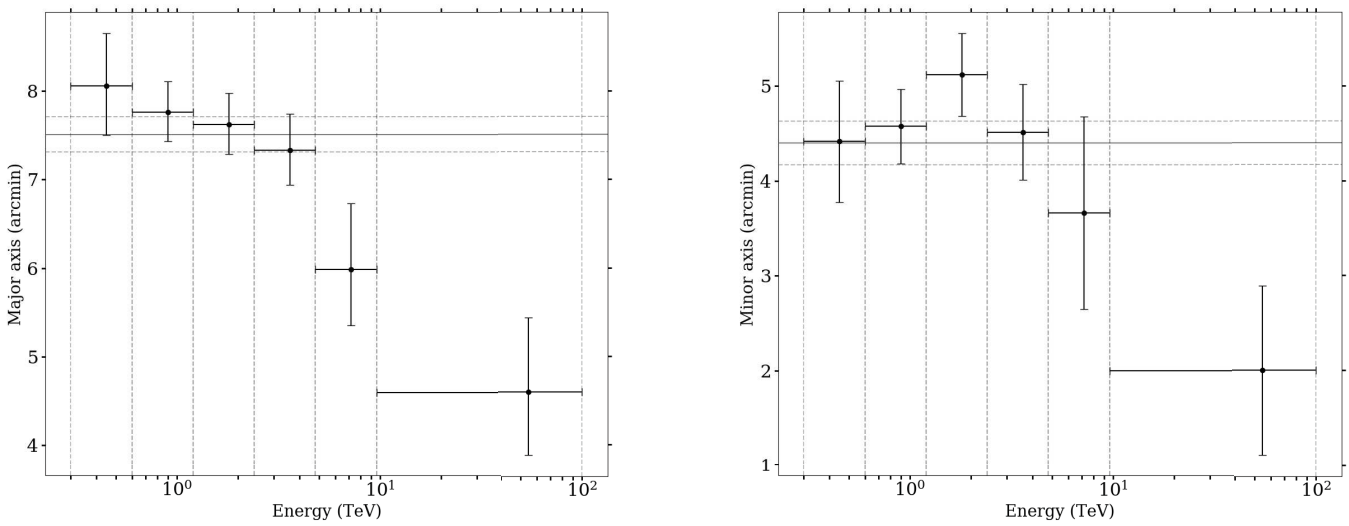

Figure 5.11 – Evolution of the major and minor axes of the best-fit model $\mathcal{M}_{G_{G_{asym}}}$ with energy. The dashed grey line represents the corresponding value found in the wide energy range analysis from 0.3 to 100 TeV with the *HiRes* cuts configuration.

In addition to the morphological shrinking, we derive as well the position of the peak of the VHE emission and find a $\sim 0.05°$ offset with the position of the pulsar PSR B1509-58, which yields a value of 3.8 pc. This result is consistent with the reported upper limit of 4 pc published in the H.E.S.S. Galactic plane Survey[59].

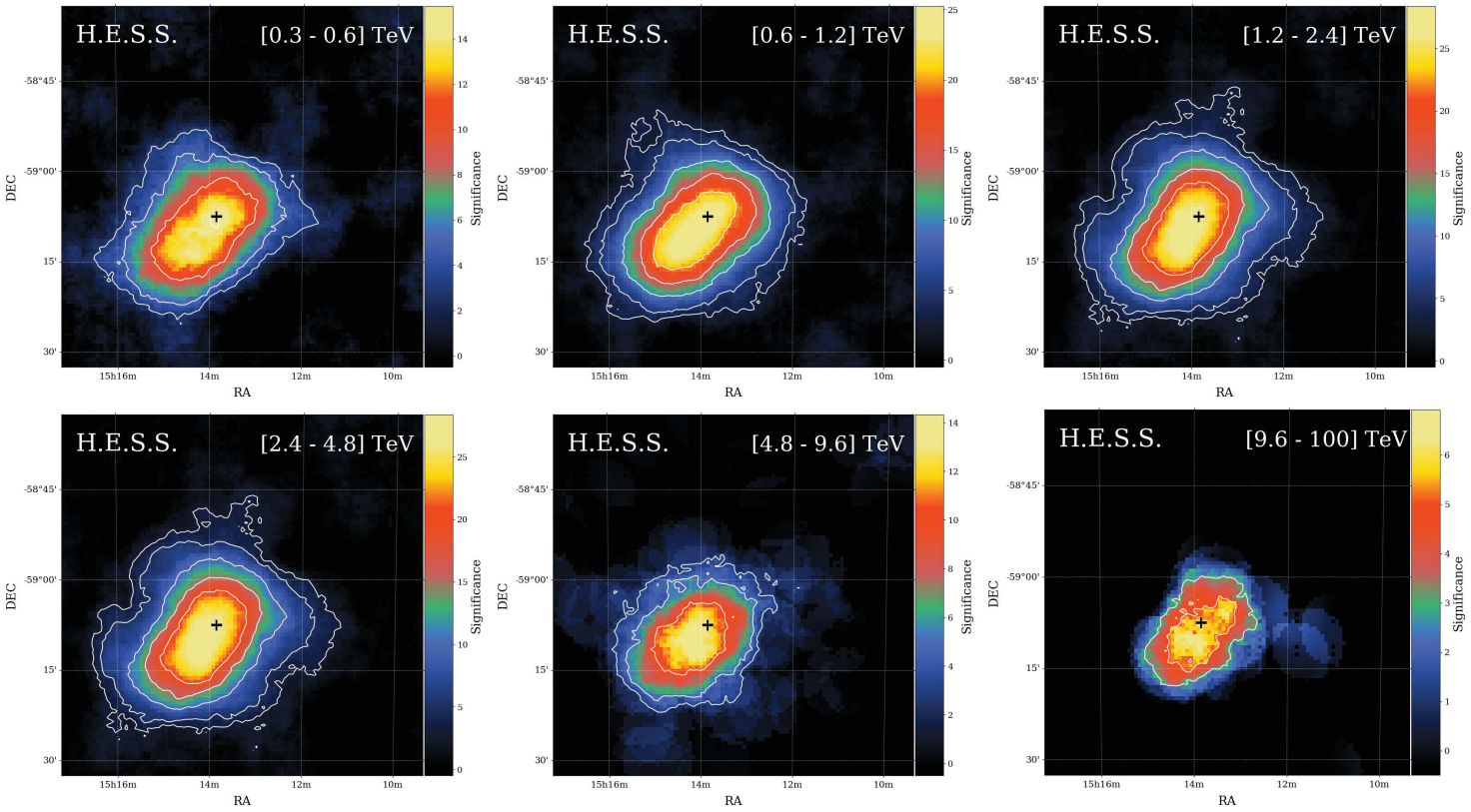

Figure 5.12 – Energy-dependent significance maps of the gamma-ray emission originating from the pulsar wind nebula within the composite supernova remnant MSH 15-52 seen with H.E.S.S.. The white contours represent the 3σ, 5σ, 10σ, 15σ, 20σ confidence levels. The energy-dependent morphological analysis confirms that there is a significant shrinking of the very-high energy emission beyond $\sim$ 10 TeV.

5.3.2 Spectrum

The differential energy spectrum measured for a given source seen by H.E.S.S. is the flux Φ defined as the number of gamma-ray photons N per unit of time and per unit of surface :

$$\Phi(E) = \frac{1}{dE\ \mathcal{A}} \frac{dN}{dt} \quad [TeV^{-1}.cm^{-2}.s^{-1}] \tag{5.7}$$

where $\mathcal{A}$ is the area of the surface, the analysis selection cuts and the energy of the measured excess events. The counts would be the product of the flux, the effective area which depends on the zenith angle of observation, and the duration of observation. This instrument response function is usually deduced from MCMC simulation tables. The flux is measured within an energy range separated in smaller energy bins. However the energy resolution of the telescope is not infinite and will induce an estimated probability that an event is reconstructed with a slightly different energy than its true energy. So as to estimate the gamma-ray flux as a function of its true energy, we usually opt by fitting the spectral data with a parametrised equation. The forward folding technique is based on the assumption of a given spectral shape such as a :

- power-law (PL) with 2 parameters

$$\frac{dN}{dE} = \Phi_0 \left(\frac{E}{E_0}\right)^{S_0} \tag{5.8}$$

- power-law with an exponential cut-off (ECPL) with 3 parameters

$$\frac{dN}{dE} = \Phi_0 \left(\frac{E}{E_0}\right)^{S_0} \times e^{-\left(\frac{E}{E_{cut-off}}\right)} \tag{5.9}$$

- broken power-law (BPL) with 4 parameters

$$\frac{dN}{dE} = \Phi_0 \times \begin{cases} \left(\frac{E}{E_0}\right)^{S_1}, & when\ E \leq E_{break} \\ \left(\frac{E}{E_0}\right)^{S_1} \times \left(\frac{E_{break}}{E_0}\right)^{S_2 - S_1}, & when\ E \geq E_{break} \end{cases} \tag{5.10}$$

- log-parabola or curved power-law spectrum (CPL) with 3 parameters

$$\frac{dN}{dE} = \Phi_0 \left(\frac{E}{E_0}\right)^{S_1 - S_2 log(\frac{E}{E_0})} \tag{5.11}$$

with Φ_0 the flux amplitude normalisation, E_0 the reference energy, $s_?$ spectral indices, $E_{cut-off}$ and E_{break} the energy where the exponential cut-off or the spectral break occur (respectively).

The expected number of gamma-ray photons in a bin of reconstructed energy is the integration over the reconstructed energy range of said bin and over the range of its true energy (which may be null up to infinite) of : the instrument energy resolution, the acceptance and the considered spectral shape. The computed spectrum shall be fitted with the assumed spectral shape used for the forward folding to derive the spectral points. The comparison between the different shape fits is made using the statistical tools to estimate the likelihood of a Poisson distribution and with chi-squared tests.

We have conducted several analysis configurations so as to compute the spectrum of the VHE gamma-ray emission of the MSH 15-52 PWN by considering stereocopic and monoscopic event reconstructions in both H.E.S.S. phases. Our HESS-II stereoscopic and combined (hybrid stereoscopic and monoscopic observations) analyses, as well as all analyses including runs taken after the HESS-IU intervention, have suffered in terms of adequate IRFs due to technical delays within the global production of simulation tables within the collaboration. In reflection of our morphological analysis, where our work focused on HESS-I datasets due to better understanding of the point spread function systematics, we opted to conduct a HESS-I data spectral analysis mainly. In this dissertation I will discuss the HESS-I spectrum and will briefly mention our HESS-II spectrum derived from only the CT5 monoscopic configuration.

In Figure 5.13 the resulted spectrum from our study is shown. We have integrated over an energy range of [0.3 - 30] TeV, using a 0.1 TeV energy bin size with a reference energy at 1 TeV.

We have chosen a minimum 20 % fraction of the maximum effective area to omit energy threshold features that tend to introduce a false flatness of the spectrum at the lowest energy ranges, after numerous trials in order to conclude on the fraction value. This threshold effect is illustrated in the HESS-II monoscopic spectrum with solely CT5 reconstruction shown in Figure 5.14. This chosen value corresponds to the fraction of the maximum energy where the maximum effective area is estimated, and all events above this energy are accepted in the energy reconstruction.

Based on the extended emission of the source, we set a maximal target size of the source θ^2_{max} of 0.09 $^{\circ 2}$ and use a full containment effective area and energy resolution method, consisting of generating simulated large square angular distances θ^2 to the source look-up tables. This approach is used to take into account the dependence on the point spread function for in a larger angular size target region than the one used by default for a point-like source. The efficiency

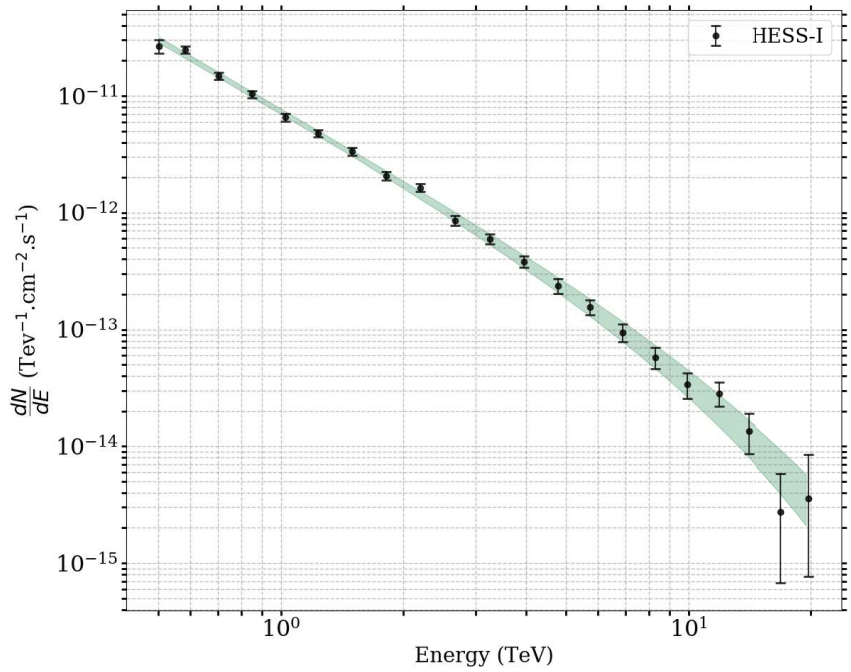

Figure 5.13 – Flux spectrum of the very-high energy emission of the MSH 15-52 pulsar wind nebula derived from HESS-I data, with a power-law following a spectral index of $s \sim 1.9$ exponentially cut (ECPL fit) at $E_{cut-off} \sim 10$ TeV. All derived parameters of a few spectral shape assumptions of interest are presented in Table 5.3

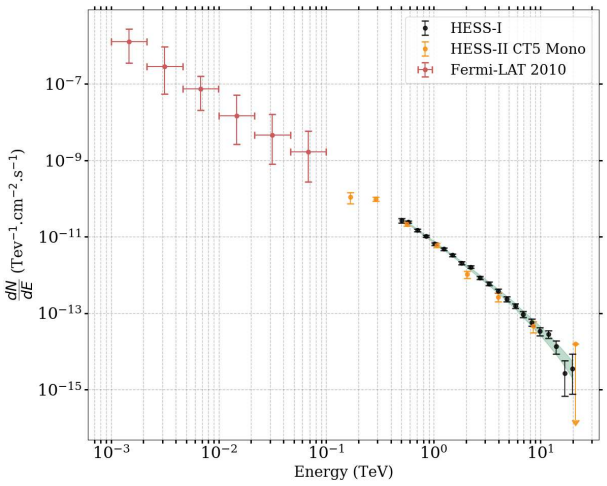

Figure 5.14 – Flux spectra of the gamma-ray emission originating from the MSH 15-52 PWN. The high energy emission seen with the *Fermi-LAT* satellite published in [2] (in red) is showing a power-law of a compatible index with the ones found in our latest H.E.S.S. spectral analyses : from a HESS-I stereoscopic configuration (shown in Figure 5.13) and from the HESS-II purely monoscopic reconstruction (in orange). The latter suffers from energy threshold effects due to our choice of the lowest energy range in the energy reconstruction and is shown here for illustration purposes. Erratum : the Fermi-LAT first and second spectrum points are upper limits.

of the θ^2 cut depends on the energy therefore this method comprises the application of several angular sizes on the extended source so as to estimate correctly the energy dependence of the acceptance. Opting for this cut applied on the data allows to include all photon counts from the extended size of the source into the spectrum derivation but is limited by the background

increasing the statistical error uncertainty. As long as the extent of the emission is larger than the full containment method is adapted. We have as well compared our resulted spectrum points by imposing 3σ, 5σ and 8σ significance per energy bin. In Table 5.3, I show several of the generated flux spectra for the very-high energy emission of MSH 15-52 considering several spectral assumptions as described above (Equation 5.8 - 5.11). All computed spectrum points have $>8\sigma$ significance from the expected event count within the given reconstructed energy bin and a 20% energy threshold has been applied.

The best-fit parameter values for each shape configuration are shown along with their significance in therms of the log likelihood Λ and χ^2 per degree of freedom values compared to the null hypothesis, which is the case of the data distribution not following the given fitted parametrised shape. Based on these statistical tests, we notice that all spectral shapes introducing a spectral alteration at higher energies are significantly preferred to the power-law hypothesis. Tables from the literature [98] have been used to convert the χ^2 difference [81] given the difference of degrees of freedom of each hypothesis, to confidence levels. In comparison to the PL hypothesis, the ECPL, BPL and CPL at a 4.45σ, 4.25σ and 4.30σ significance respectively, and are all preferred. We as well compare the ECPL with the BPL hypotheses, finding only a $\sim 1.3\sigma$ preference for the latter, which does not permit to discriminate between these two assumptions. We conclude that the spectral alteration of the spectrum at $>$ TeV ranges is statistically significant and we present the flux spectrum showing an exponential cut-off at ~ 10 TeV in Figure 5.13.

Table 5.3 – Table of the computed flux spectra for the emission of MSH 15-52 with different spectral shape assumptions.

Spectral shape	Spectrum	Parameters	Statistics
PL (Eq.5.8)	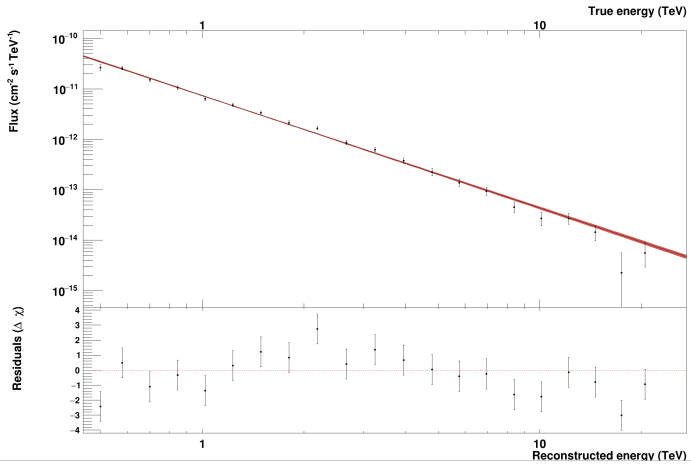	• E_0 : 1.40 TeV • Φ (1 TeV) : (7.35 ± 0.20) $.10^{-12}$ $TeV^{-1}.cm^{-2}.s^{-1}$ • s_0 : 2.23 ± 0.03	• Λ : -26.9 • χ^2/dof : 53.9/39
ECPL (Eq.5.9)	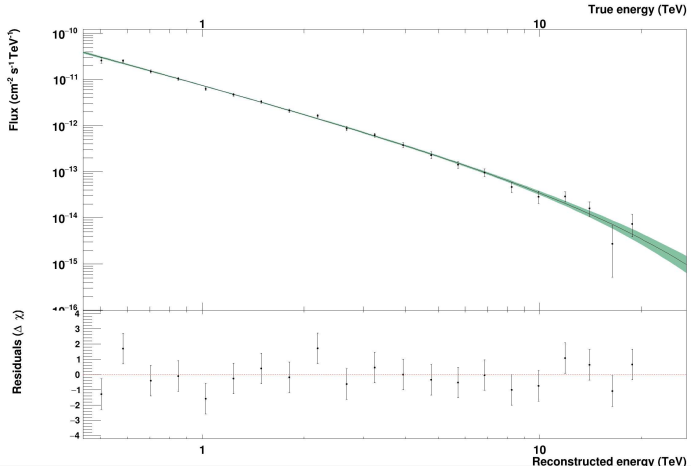	• E_0 : 1.13 TeV • Φ (1 TeV) : (7.46 ± 0.20) $.10^{-12}$ $TeV^{-1}.cm^{-2}.s^{-1}$ • s_0 : 1.97 ± 0.07 • $E_{cut-off}$: (10.78 ± 2.74) TeV	• Λ : -17.1 • χ^2/dof : 34.2/37
CPL (Eq.5.11)	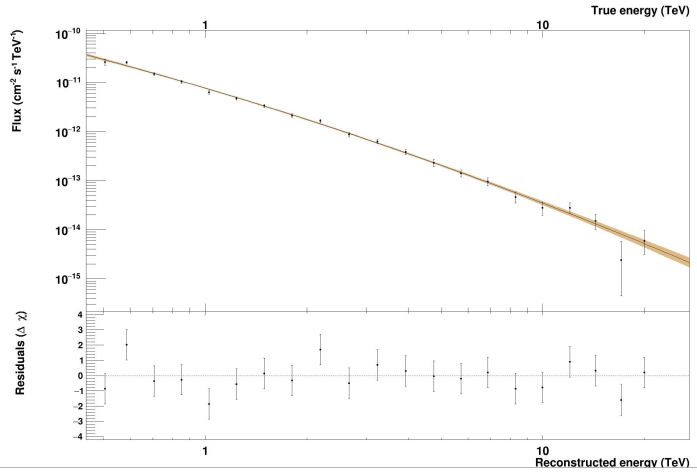	• E_0 : 1.00 TeV • Φ (1 TeV) : (7.63 ± 0.21) $.10^{-12}$ $TeV^{-1}.cm^{-2}.s^{-1}$ • s_1 : 2.04 ± 0.05 • s_2 : 0.13 ± 0.03	• Λ : -17.7 • χ^2/dof : 35.4/38
BPL (Eq.5.10)	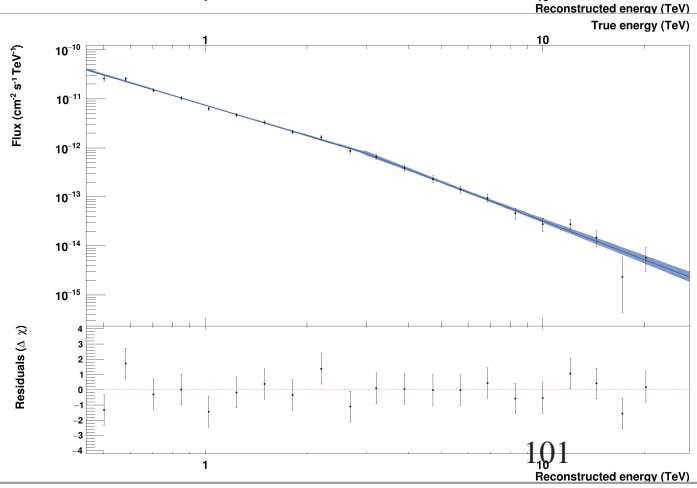	• E_0 : 5.45 TeV • Φ (1 TeV) : (7.38 ± 0.20) $.10^{-12}$ $TeV^{-1}.cm^{-2}.s^{-1}$ • s_1 : 2.06 ± 0.06 • s_2 : 2.63 ± 0.14 • E_{break} : (3.00 ± 0.70) TeV	• Λ : -16.2 • χ^2/dof : 32.4/37

5.4 Characterisation

In this section I shall discuss our analysis results. I attempt to draw conclusions from the morphological X-ray and TeV gamma-ray emission investigations, by interpreting the physical meaning that could lead to them and raising some limitations to the possible ascertainment (Section 5.4.1). Furthermore I focus on the asymmetrical shape of the MSH 15-52 pulsar wind nebula and on its implications on an asymmetrical evolution. In Section 5.4.2, I show a preliminary effort of modeling the spectral energy distribution derived from our latest H.E.S.S. spectral analysis.

5.4.1 X-ray and gamma-ray emission spatial correlation

In Section 5.3.1, I have described the morphological analyses I made for characterising the shape of the very-high energy gamma-ray emission of the PWN within the composite SNR MSH 15-52 seen with H.E.S.S. We found, in agreement with the previously published H.E.S.S. collaboration papers (dedicated analysis H.E.S.S. collaboration (2005)[30] and in the Galactic plane survey [59]) that the source is extended (Section 5.3.1.2), with an emission spreading up to ~ 9 pc on one direction (from north-west to south-east) and up to ~ 5 pc on the other (from north-east to south-west). The north region of the gamma-ray emission is delimited by the supernova remnant shell partially seen [46] in the radio band (ATCA, Molonglo)[78]. The southern part is confined within the radio SNR shell but seems to be only partially spatially coincident with it. The observed X-ray emission of the pulsar wind nebula seen by various experiments (*Chandra[54], XMM-Newton[68], Suzaku[33], INTEGRAL[135], NuSTAR[32]*) has shown an elongated hard X-ray emission coincident with the high-energy and very-high energy gamma-ray emission of the nebula, comprised within the radio SNR shell. A bright soft X-ray thermal component is seen at the north-west region of the source, coincident with the RCW 89 Hα emitting region. This multi-wavelength emission of the composite system comprising the radio supernova remnant, the pulsar wind nebula within it and the bright energetic pulsar is mapped in the sketch shown in Figure 5.15.

Our analysis has yielded that when considering the non-thermal X-ray emission as a spatial tracer of the lepton population that corresponds to the one emitting the gamma-ray radiation via inverse Compton scattering on target photons (see Section 5.3.1.3), there is a non-linear correlation between the emission in these two energy bands. To quantify this non-linearity, we have introduced a parameter, that we have dubbed as the α-parameter in our model nomenclature (Section 5.3.1.1.2), that hints the distance R dependence of the magnetic-field **B**, when making the rather strong assumption of it being isotropic in a spherical symmetry. By assuming that the magnetic field **B** varies spatially, we imposed a dependence of **B** with the projected distance R to the pulsar position, by multiplying the X-ray template by R^{α} where α is a given index to be determined by the fit results (model $\mathcal{M}_{\alpha XG}$ Equation 5.6). Based on this magnetic field component approximation, the Inverse Compton flux Φ_{IC} is approximated to the synchrotron flux Φ_{sync} times the distance R to a given power α : $\Phi_{IC} \propto \Phi_{synch} \times R^{\alpha}$. As for the mentioned fluxes, Φ_{sync} is proportional to the lepton density $N_{e^{\pm}}$ and to the magnetic field B with a given index β : $\Phi_{synch}(\nu) \propto B^{\beta} \times N_{e^{\pm}}$. In turn, B is dependent to the distance with another given index δ as : $B \propto R^{\delta}$. On the other hand, Φ_{IC} is proportional to $N_{e^{\pm}}$ and the photon density U_{rad} which is assumed to be uniform. With these different approximations in hand, one finds that $\frac{\Phi_{IC}}{\Phi_{synch}} \propto R^{-\beta\delta}$ $\propto R^{\alpha}$ thus giving the following simple relation between those indices : $\delta = -\frac{\alpha}{\beta}$.

The distribution of the leptonic population can be described as a power law such as $N(E)\mathrm{d}E \propto \kappa E^{-p}\mathrm{d}E$ Section 3.1. The dependence of the flux with the frequency ν and the magnetic field is then such as $\Phi_{\nu} \propto \nu^{\frac{1}{2}(1-p)} B^{\frac{1}{2}(1+p)}$. Thus we can link the previously mentioned index β with p the

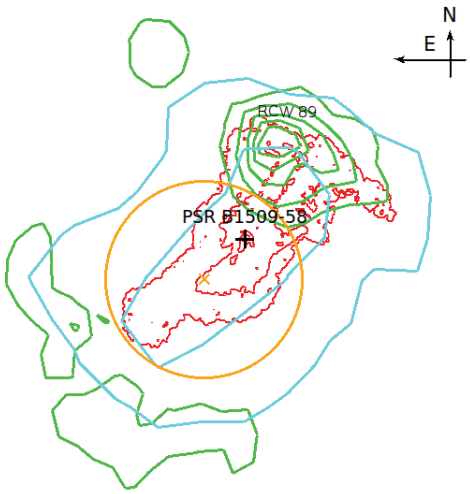

Figure 5.15 – Cartoon spatial mapping of multi-wavelength emission coming from the composite system MSH 15-52 , based on arbitrary level emission contours made on : radio observations (in green - Molonglo Galactic Plane Survey (MGPS) using the Molonglo Observatory Synthesis Telescope (MOST) at 843 MHz with a resolution of $43'' \times 43''$ cosec |dec|), the X-ray template used in our analysis Section 5.4.1 (in red - Chandra archival observations ($\sim$ 200 ks) in the 4 to 7 keV band), and the γ-ray emission (in cyan - $\gtrsim$ 0.3 TeV detected with HESS-I). The orange circle represents the extent of the symmetrical added Gaussian component found in one of our best-fit morphological models, model $\mathcal{M}_{\alpha XG}$ (Equation 5.6). The position of the bright energetic pulsar PSR B1509-58 seen in radio, X-rays and HE gamma-rays, is noted with a black cross. We as well note the RCW 89 Hα region.

electron index and s the synchrotron index such as $\beta = \frac{1}{2}(1 + p) = s + 1$. Thanks to this relation, when using our fitted estimations of the α index $\sim$ 1.3 then for a spectral index of $\beta \approx 2.2$, one finds that the dependency between the magnetic field and the distance is $B \propto R^{\delta}$ with $\delta \sim$ -0.5, that at first glance could be interpreted as the magnetic-field being roughly proportional to the inverse of the square root of the distance.

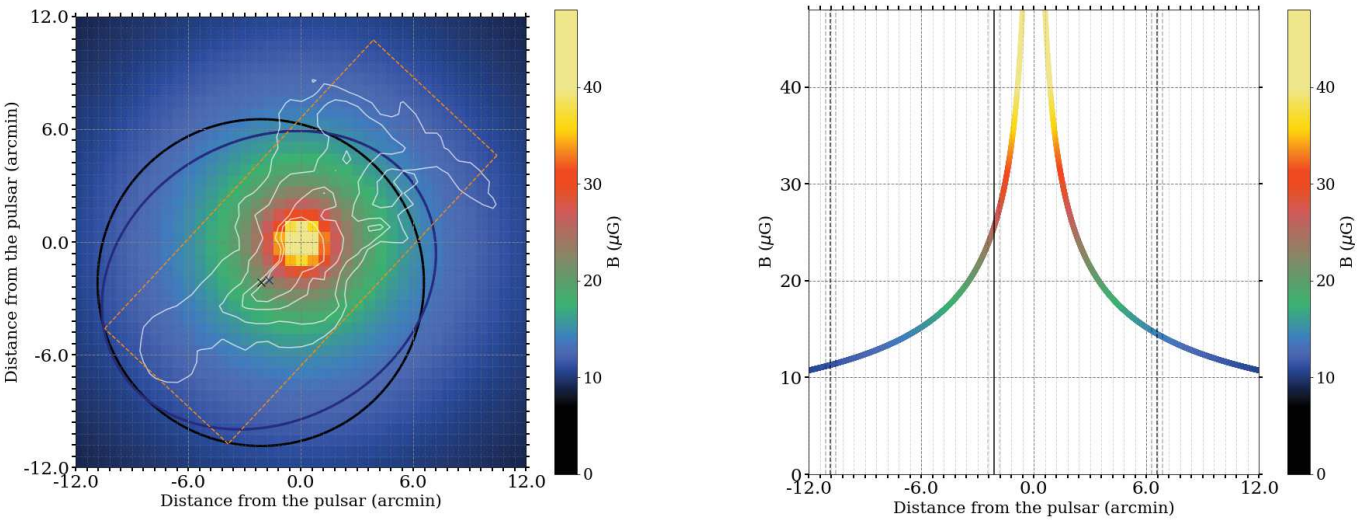

Figure 5.16 – Inferred hypothetical magnetic field profile from our modelling of the morphology of the gamma-ray emission of MSH 15-52 compared to the extent of its X-ray radiation. On the left : inferred 2D map of the magnetic field dependence with the distance as $B \propto R^{-\frac{1}{2}}$, a very rough approximation yielded by the α parameter of our model Section 5.3.1.1.2. The white contours represent the X-ray template we used in the fit of the VHE gamma-ray emission, along with the position and the extent of the additional Gaussian component that we find in our best-fit results. The orange box represents the area in which we integrated the value of the 2D magnetic field map so as to find a mean value of ~ 17 μG from previous publications [30]. On the right : 1D projection of the inferred profile so as to show the chosen spatial dependence with R. The black vertical lines represent the extent of the uncorrelated spatially VHE gamma-ray emission in comparison to the X-ray one.

However we cannot affirm that we have measured indirectly the spatial dependence of the ambient PWN magnetic-field for two important reasons. First, we have a wide statistical error on the α-parameter, where its 1σ confidence interval is set between $\alpha \in [1.1 - 1.4]$. Additionally, our spectral analysis has shown as well that the inverse Compton spectral index, given the spectral shape assumption, may lie approximately within $s_{IC} \in [1.8 - 2.3]$, which raises the possibility of having same order fluctuation for the synchrotron index value. Secondly, a very strong limitation on this result would be the approximation of the magnetic-field varying spatially with the R the *same way* in every region of space. The irregular features seen in the X-ray emission of the nebula Figure 5.4 surrounding the possible electromagnetic beam axis of the central pulsar (the "fingers" and the "wrist", following the "hand"-shape analogy), along with the difference between the lateral extent of the emission between the northern and southern regions could be an indication of stronger magnetic field lines on one part of the nebula. Moreover, the spatial variation of electrons may not be identical in synchrotron and inverse Compton distributions after all, due to the different electron energies being observed. The mapping of the magnetic-field component is beyond the scope of our study and therefore we limit our conclusions on the quantification of the spatial non-linearity between the X-ray and the gamma-ray emission. We remind that we have limned an extended additional gamma-ray emission, which comprises about 70% of the total flux, with an intrinsic radius of $\sim 7.4'$, implying that the γ-ray emission extends farther than the PWN observed in X-rays. This Gaussian component is offset from the position of the pulsar by ~ 4 pc, which is in agreement with the value of the upper limit reported in the

HGPS and confirms that MSH 15-52 is one of several PWN that show an offset of their VHE gamma-ray peak emission in respects to the position of its central pulsar.

An additional result we have found in our analyses is that the X-ray extent of the PWN is smaller than the one observed in gamma-rays. One could ponder if that smaller synchrotron radiation extent points to more severe losses of high-energy particles that correspond to the X-ray emission, compared to the VHE gamma-rays. Radiative cooling is the predominant effect but let us consider what we could infer based on our magnetic-field approximation parameter in our morphological model. Assuming the suggested magnetic field B dependence as $\propto R^{-\frac{1}{2}}$, we estimate the magnetic field at the outskirts of the extended gamma-ray emission and find a value of $\sim 10\ \mu$G with this heavily biased B-field profile shown in Figure 5.16. For this magnetic field value, we find an energy of leptons $E_{e^{\pm}}$ = [144 - 190] TeV for synchrotron radiation in the [4 - 7] keV range.

By assuming an outflow velocity profile from the calculations of Reynolds(2009)[103], we estimate a steepening of the electron energy at ~ 70 TeV. This means that this synchrotron cut-off would occur at two to three factors of electron energy below the ones in the X-ray radiation band of the used map template. We conclude in this case, that the effect would probably not be sufficient to explain the larger gamma-ray extent compared to that in X-rays. In this hypothesis, we would expect to have a possible contribution to the shrinking morphology of the nebula at higher energies, due to a possible relatively low magnetic field medium around the pulsar wind nebula, possibly the supernova ejecta, but this conjecture heavily relies on our estimation of the magnetic field.

Following our statement that the morphology of the PWN in the X-ray band appears somewhat irregular we stipulate another conjectural scenario, of leptons escaping their confinement. The nebula is thought to be aligned with the rotation axis of the pulsar, however there is a strong asymmetry between the north-west and south-east regions, alongside the jets of the pulsar. If the halo and the other component share the same spectral behaviour, then one could have an estimation of the magnetic field. The fact that the synchrotron radiation does not match the extent of the γ-ray emission may suggest a relatively low magnetic field medium surrounding the PWN, such as the SN ejecta. In order to fully study this hypothesis, we would need to take into account the somewhat complex geometry of the system resulting by the reverse shock interacting with the ejecta. This also implies a strongly diffusive medium, with an energy-dependent diffusion coefficient κ at $\sim 10^{28}$ cm^{2}s^{-1}, meaning that the leptons would be escaping their confinement propagating into the ejecta.

We assume a diffusion coefficient such as $\kappa \sim \frac{R^2}{2t_{age}}$ with R the size of the gamma-ray "halo" (not to be confused with the TeV haloes in the PWN literature that might be observed at late evolution stages of the system [56] when leptons diffuse in the interstellar medium) and t_{age} the estimated age of the system based on the age of the pulsar. Our energy-dependent results a shrinking of said halo component at higher energies, which would not be in favour of a strong diffusion region depending with energy at the south-west region of MSH 15-52 . This scenario could be further explored by estimating upper limits for the magnetic field amplitude and speculating on the degree of turbulence of this system, however given the complexity of the assumptions that should be made, we are not taking in consideration besides accounting for a not dominant contribution to the extent of the MSH 15-52 gamma-ray emission not correlated to the X-ray one.

The offset of the highest gamma-ray energy locus compared to the position of the pulsar, along with the reported interstellar medium densities at the north-west (up to ~ 10 cm^{-3}) and south part (~ 0.5 cm^{-3}) of the nebula [46] are possible explanations of the asymmetric shape of

the pulsar wind nebula. The medium inhomogeneity is implying that the system has reached the *Sedov-Taylor* stage and has begun its adiabatic evolution after the reverse shock of the supernova remnant has reached the northern boundaries of the nebula and has begun interacting with it because of the forward shock encountering a denser medium. On the contrary, based on the less dense southern region of the system, the system ought to be still at its ejecta-dominated phase, continuing its free expansion within the supernova remnant. This tilted morphology due to an uneven crush of the pulsar wind nebula bubble by the reverse shock crashing on its outskirts on only one side, is being favoured in light of our energy-dependent analysis.

5.4.2 Spectral cut-off and energy-dependence

Our results indicate that there is a significant spectral alteration (Figure 5.13) concurring with a VHE gamma-ray morphological shrinking of the emission (Figure 5.12) at energies $\sim$ 10 TeV. Our energy-dependent morphological analyses could be prone to a statistical bias introduced by lower statistics at the higher energy bins, but they have been checked in two different event selection cut configurations, where the excess signal up to 30 TeV is $\gtrsim 3\sigma$ and the background mis-estimation contamination is contained to assure the completeness of our highest energy samples.

We append our energy-dependent spatial compression of the emission deduction to the exponential cut-off occurring at the same energy range. We have compared our generated spectra with the expected energy distribution of events that could be detected by the HESS-I telescope array in compliance with the obtained event rate used in the reconstruction of the spectra. We as well have studied the influence of energy threshold effects, selection run cuts and IRFs configuration conjectures in the derived spectral parameters. We find that the cut-off hypothesis is at $\sim 4.5\sigma$ significance preferred to the previously published power-law assumption.

A spectral change ensues to discard as a hypothesis a constant uniform propagation of an on-going lepton injection at the site of the pulsar, within the integrity of the pulsar wind nebula interpretation and to consider scenarii that could explain the spectral steepening at very high energies in correlation to the morphological energy dependence. Our results do not permit to discriminate between a broken power-law (BPL) and an exponential cut-off power-law (ECPL) assumption. This could have been very helpful in our considered interpretation scenarii including the relic nebula assumption (see Chapter 2 and Chapter 6) supported by the smooth curvature of the spectrum (from the ECPL shape) and the continuous injection of fresh particles within the system allegated by a steeper component extending to higher energies (BPL shape).

We proceed with the modelling the VHE gamma-ray spectral energy distribution (SED) with the reported dominant leptonic radiation process of inverse Compton scattering on infra-red emitting radiation fields. We do not use UV radiation field densities because of *Klein-Nishina* regime dominance affecting the contribution of such high energy photons in the photon-lepton scattering process. We use target photon field densities and estimated temperatures obtained by the published interstellar radiation field models of Popescu et al.(2017)[95] and Porter et al. (2017)[96] (see Section 3.2 and Table 6.2). We do not include in this preliminary modelling of the SED the effects of magnetic field fluctuations, adiabatic losses or escaping leptons from their confinement because of the fairly young age of the system based on the reported characteristic age of the pulsar PSR B1509-58, which is at $\tau_{ch} \sim$ 1500 - 1600 yr. If the pulsar had a a conventional spin-down history, then this upper limit on its age, in combination to the HI absorption measurements (Gaensler et al. (1999)[52] concluding that the distance to the

supernova remnant G320.4-01.2 lies in the range of 3.8 kpc $< D <$ 6.6 kpc, while the dispersion measure of the pulsar suggests a distance $D \approx 4.4$ kpc with the most recent Galactic free electron density model[84]. In our modelling we place the system at a 4.4 kpc distance.

The lack of measured pulsar proper motion suggests that the explosion centre was near the current position of PSR B1509–58. It should be noted that teams working in the observational radio pulsar domain are currently studying this pulsar so as to measure or at least quantify possible significant proper motion from the compact object. As discussed in earlier sections, given the multi-wavelength observations of the emission from the MSH 15-52 system, one may conclude that the SNR blast wave must then have expanded asymmetrically, with a large radius of $R = (20 \pm 2)\, d_4$ pc being reached to the south-eastern region, [52]. To reconcile this large size with the relatively young age implied by the characteristic age of the pulsar, a fairly energetic explosion and a low medium density on the SE side are required. Gaensler et al.[52] suggest that the progenitor of this SNR was a helium star, combining an ejecta mass $M_{\rm ej} \approx 1.5 M_{\odot}$ and an explosion energy $E \sim 3 \times 10^{51}$ erg. The circumstellar medium density to the SE is $n_{\rm H} \sim 0.01$ cm^{-3} while the northern part has a number of filamentary ionised structures that vary in density but can yield a ~ 5 cm^{-3} average density in the wider scale north region[138]. These studies confirm the a hint of inhomogeneity in the vicinity of the pulsar wind nebula.

The leptons responsible for the gamma-ray emission are of slightly lower energy than those traced by the synchrotron [4 - 7] keV X-ray template we have used in our morphological fits. When considering a mean magnetic-field of $\sim 20\, \mu$G, the leptons shall have an energy $E_e \gtrsim 100$ TeV with synchrotron radiative lifetimes < 300 yr which are shorter than the estimated age of the system. This would lead us to expect that the freshly injected particles in the system are traced by the morphology seen in non-thermal X-rays. The fact that we detect a gamma-ray extended emission beyond this X-ray PWN size could be interpreted as the relic nebula. This would be highlighted by a a cut-off at the synchrotron spectrum due to cooling occurring at lower energy ranges. We notice that the energy-dependent morphology shows such a shrinking of the additional Gaussian component. We underline that to derive our estimates of lepton energies in the different discussion section, we are using the Thompson approximation which would not be a good approximation at energies above $\gtrsim 10$ TeV.

Our preliminary spectral energy model is shown in Figure 5.17. In our modelling of the emission originating from the pulsar wind nebula, we fit our analysis H.E.S.S. dataset and the published dataset from the *Fermi-LAT* collaboration. We overlay our best-fit model with available 1) soft and hard X-ray power-law parameters presented in [7] and 2) the latest available *Fermi-LAT* spectral derivations. We do not use these spectral points in our fit for the X-ray data would dominate the fit procedure due to their small statistical uncertainties in comparison to the gamma-ray observations thus the precision on the modelling of the synchrotron radiation would weight more in the fit than the inverse Compton scattering, which would not provide us with the best description of the VHE emission. We prefer to use the 2010 HE gamma-ray dataset over the Fermi Extended Sources Catalogue (2017) published data as the former one is based on a dedicated analysis in contrast to the latter one which is the result of a uniform method applied across the survey.

We have fitted the spectral energy distribution using the *naima* python package[140], using for the electron spectrum a broken power-law exponentially cut-off (ECBPL) spectral shape parametrised as following (see Section 5.3.2 for parameter conventions) :

$$\mathcal{S}(E) = \mathcal{A} e^{-\left(\frac{E}{E_{cut-off}}\right)} \times \begin{cases} \left(\frac{E}{E_0}\right)^{-S_1}, & when\ E \leq E_{break} \\ \left(\frac{E}{E_0}\right)^{-S_2} \times \left(\frac{E_{break}}{E_0}\right)^{S_2 - S_1}, & when\ E \geq E_{break} \end{cases} \tag{5.12}$$

We introduce in our model several degrees of freedom :

- the ECBPL spectral parameters (normalisation, two spectral indices, energy break, cut-off energy)
- the mean magnetic-field B for the synchrotron radiation
- the number density of target protons for the pion-decay process (from accelerator data on proton-proton interaction from [71], nominal value in the *naima* routines)
- the photon densities and temperature for the Far infrared (FIR) and Near infrared (NIR) radiations fields

For the inverse Compton scattering, we set the radiation field values to be comprised within a range centered around the derived values from the models of Popescu et al, 2017 and Porter et al, 2017 shown in Table 6.2c and 6.2b. For the magnetic field we set an initial value of 17 μG, as reported in [30]. We opted to first fit manually the distribution so as to have a better estimation for the initial parameter values and to ensure that the minimisation of the logarithmic likelihood is not converging towards local minima.

Our best-fit model yields the parameters for the electron spectrum and the characteristics of the targeted populations of interest for each considered radiation process shown in Table 5.4 :

Table 5.4 – .

Parameter	Unit	Median value	Allowed interval
Normalisation $\mathcal{A}$	10^{35} eV^{-1}	$2.58\ ^{+0.06}_{-0.09}$	$[0, +\infty]$
Index s_1	-	$2.52\ ^{+0.48}_{-0.42}$	$[-\infty, +\infty]$
Index s_2	-	$3.18\ ^{+0.20}_{-0.11}$	$[-\infty, +\infty]$
Energy break E_{break}	TeV	$11.4\ ^{+2.12}_{-2.9}$	$[0, +\infty]$
Cut-off energy $E_{cut-off}$	TeV	$933\ ^{+182}_{-258}$	$[0, +\infty]$
Mean magnetic-field B_0	μG	$11.9\ ^{+3.3}_{-3.1}$	$[0, +\infty]$
Proton number density n_H	cm^{-3}	$0.99\ ^{+0.16}_{-0.28}$	$[0, +\infty]$
FIR temperature T_{FIR}	K	$38.2\ ^{+4.1}_{-6.0}$	[30, 45]
FIR photon density U_{FIR}	cm^{-3}	$0.59\ ^{+0.16}_{-0.12}$	[0.4, 0.8]
NIR temperature T_{NIR}	K	$3017\ ^{+404}_{-390}$	[2500, 3500]
NIR photon density U_{NIR}	cm^{-3}	$1.46\ ^{+0.20}_{-0.38}$	[0.8, 1.6]

We find a compatible magnetic field with the one reported from one-zone model in H.E.S.S. collaboration 2005. Our model of the emission of MSH 15-52 indicates that there is a break of the spectral shape at $\sim$ 10 TeV and that the ECPBL shape is comparable to a simpler broken power-law, with an index of $\sim$ 2.5 at energies below the break and a slope of $\sim$ 3.2. We note that for the cut-off energy and the proton number densities, the values and statistical errors point to them not being constrained by the data. The fit procedure provides the certainty that several spectral deviations are not observed and that one steepening feature occurs in the very-high energy spectrum. The hadronic process is rather negligible in comparison to the leptonic contributions and the self-synchrotron Compton is completely negligible. An interesting result of our model

would be that the inverse Compton scattering occurring on CMB photons and on Far infrared radiation fields seem to have dominant contribution in the TeV range, while at energies beyond $\sim$ 10 TeV the CMB becomes more dominant over the FIR. In comparison to our result from our morphological analysis where we observe the shrinking of the gamma-ray emission at these energy ranges could be an effect of tracing higher energy leptons and it could also be the reason behind our detected spectral cut-off, simply due to *Klein-Nishina* effects.

One underlined indirect hypothesis that we have introduced from the early stages of our morphological studies, has been that our selected energy ranges covered by the used X-ray template for tracing the synchrotron component of the total PWN emission, map slightly lower energy leptons than the ones behind the gamma-ray radiation we investigate. In order to establish if this could explain the electron energy cut-off we find at $\sim$ 10 TeV, we estimate the radiative losses regarding synchrotron cooling.

In Figure 5.18, we show the computed synchrotron cooling timescales for electron energy ranges determined from synchrotron radiation in the photon energy ranges of the radio and X-ray domains. We have chosen values for the magnetic field from 10 μG (which is the best-fit value from our SED adjustments) up to 20μG. We have as well considered the energy ranges of the observed X-ray emission with the *Chandra X-ray observatory* in [3 - 7] keV range and the *NuSTAR* mission in the [15 - 30] keV range. We find that for the mapped synchrotron photons with the X-ray template we have used in our morphological analyses, the corresponding traced electron energies lying between 100 TeV and 200 TeV will yield synchrotron cooling times of the $\sim$ 600 yr to $\sim$ 1000 yr for B = 10 μG, which are relatively comparable to the age of the system based on its pulsar characteristic age of 1560 yr. Even for a higher mean magnetic field value and with electrons producing the X-ray synchrotron emission seen with NuSTAR, the cooling scales would be of the order of a a century. The synchrotron cooling losses are prone to have an effect by steepening the spectral distribution, but do not explain the electron energy break at $\sim$ 10 TeV we obtain from the the spectral energy distribution fitted based on the data from the gamma-ray photon spectra.

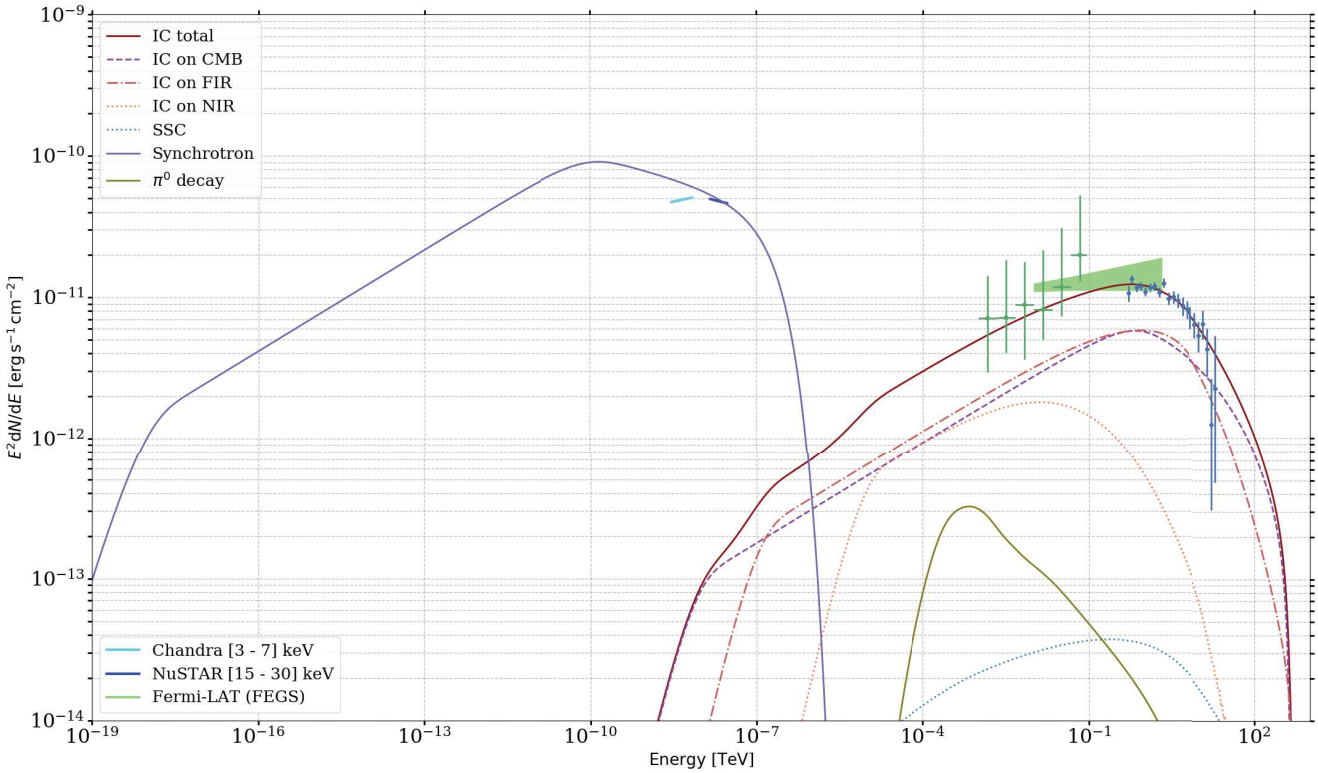

Figure 5.17 – Spectral energy distribution for the emission of the MSH 15-52 pulsar wind nebula seen with H.E.S.S.. The blue dataset corresponds to our latest HESS-I spectral analysis. The green data correspond to the published *Fermi-LAT* spectral points derived from a dedicated analysis [23]. In this graph, the following derived spectra are overlaid : in light green the butterfly error corresponding to the derived spectrum points from the Fermi Extended Sources Catalogue (2017) [25], in cyan the *Chandra* power-law best-fit model in the [3 - 7] keV range, in dark blue the *NuSTAR* spectral model in the [15 - 30] keV band [7]. We use in our SED fit the H.E.S.S. and Fermi-LAT dataset. We indicate in the key legend the leptonic (synchrotron, self synchrotron Compton, inverse Compton on various radiation fields) and the hadronic process (proton-proton interactions) that we have used in the modelling and show their contribution based on our resulting best-fit parameters for each one of them.

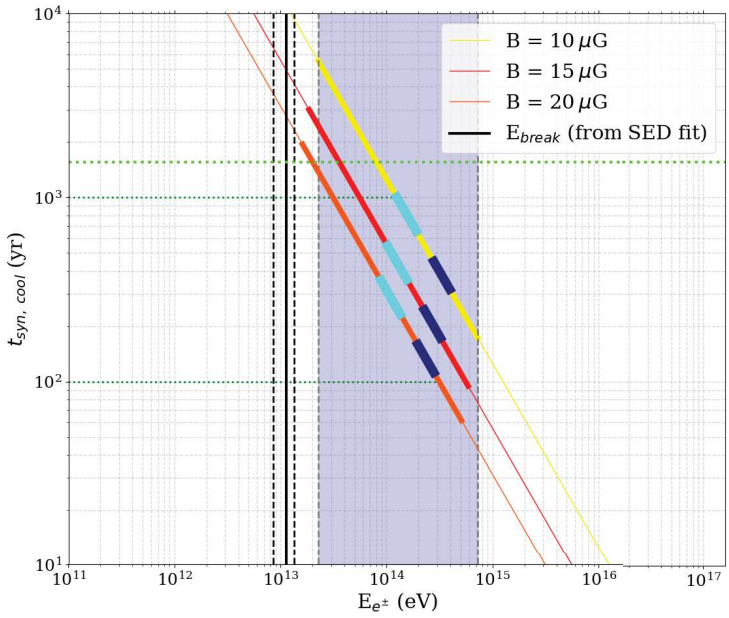

Figure 5.18 – Synchrotron cooling time $t_{syn,\,cool}$ for magnetic field strength values B of 10 μG, 15 μG and 20 μG as a function of electron energy. We show the electron energy values corresponding to a given photon energy. The wider in width lines soft and hard X-ray [10^2 - 10^5] eV bands, where we shade in dark blue the corresponding electron energy band for B = 10μG for each radiation band respectively. The wider cyan and dark blue lines, correspond to the [3 - 7] keV (*Chandra*) and [15 - 30] keV (*NuSTAR*) X-ray ranges that we overlay in our SED in Figure 5.17. We show the synchrotron cooling time possible range (in dotted dark green lines) based on the mean magnetic field strength and the synchrotron electron energy corresponding to the photon energy ranges of MSH 15-52 X-ray emission observed with *Chandra* and *NuSTAR*. We have plotted in black the electron energy break found from fitting the MSH 15-52 SED, which is around $\sim 10^{13}$ eV (Table 5.4) and in lime green dotted line the characteristic age of the pulsar, assumed to be the age of MSH 15-52 .

Part IV

Asymmetric pulsar wind nebulae

Chapter 6

Offset TeV population

Contents

6.1 H.E.S.S. observations of offset systems

To this day, the online inventory for registered very-high energy (TeV domain) gamma-ray astrophysical sources *TeVCat*[132], includes 35 pulsar wind nebulae (29 firmly confirmed PWNe and six newly announced confirmed systems) with four additional source candidates, all findings of several gamma-ray observatories such as H.E.S.S, MAGIC, HAWC, VERITAS, MILAGRO, CANGAROO, other ground-based IACTs, Air Shower experiments and space satellite Fermi-LAT.

Thanks to its location to the South hemisphere and to its high sensitivity ($\sim$ 0.7% of the Crab flux), the H.E.S.S. experiment has been in a very adequate position to observe the Galactic plane and has been able to detect numerous galactic and extragalactic sources in this domain. In this section we shall focus on the results of the several year long observation survey of the Galactic plane from H.E.S.S. , inventorying uniform morphological and spectral features for all detected sources. We shall discuss the population study made for the pulsar wind nebulae findings and examine the PWNe showing a significant offset between the centre of gamma-ray emission and the position of the injecting pulsar.

6.1.1 The H.E.S.S. Galactic Plane Survey

Using data from over almost a decade of observation of the night sky, from 2004 to 2013, the H.E.S.S. collaboration published in 2018 [59] the H.E.S.S. Galactic Plane Survey (HGPS). It depicts the Milky way galaxy in the very-high energy domain, using datasets from the HESS-I phase, with gamma-ray emission from 0.1 to 100 TeV within a spatial skymap coverage of longitude ℓ, from 70 to 250 °, and of latitude b from -5.0 to +5.0 °. The survey consists of a source catalogue of 78 objects in total, extracted from two-dimensional fits of significant excess on spatial maps coupled with spectral analyses to derive information for the emitting radiation of the source.

In order to scan and extract significant emission along the Galactic plane, the Galactic centre region and other complex morphology regions (shell-like supernova remnants) with overlapping components have been masked from the skymaps of the survey so as to model the large-scale diffuse galactic emission. Afterwards the skymaps have been splitted into regions of interest (ROIs), based on significant ($> 5\sigma$) emission present in at least one ROI and chosen so as to make sure to not marginally position significant emission within it. A maximum size of $\Delta\ell \sim 10°$ has been chosen for the ROIs width and a full length ranging in latitude $|b| = 5°$. The emission has been modelled with multiple symmetric 2D Gaussian components added successively, taking into account the H.E.S.S. instrument response functions (IRFs) such as the estimated counts originating from the background, the point spread function and the exposure in each chosen region.

To alleviate the component extraction in the HGPS from eventual contamination of false-detections emerging from the multi-component fit approach, several globally defined measures had to be taken. Systematic break down into several less extended components of very bright extended gamma-ray sources has been counter-effected by merging into one source all multiple not clearly spatially resolved components. The very large yet faint Gaussian components resulting from the local excesses of galactic diffuse emission omitted in the large-scale modelling, are discussed as artifacts and have been excluded from the HGPS catalogue.

The identification and association of sources has been conducted following a spatial correlation criterion between the detected VHE gamma-ray centre position and a plausible counterpart

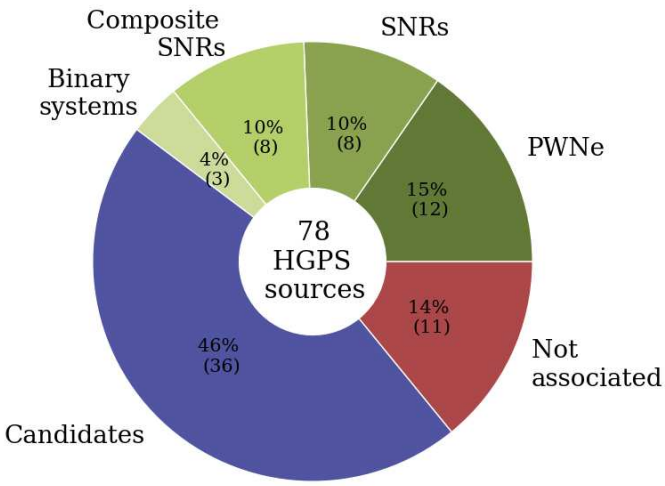

Figure 6.1 – Pie chart of the total 78 extracted sources in the HGPS. The green shades represent the confirmed identified. The blue shade corresponds to the not firmly identified sources based on the survey criteria but possibly candidate sources with possible associations. The red shade represents the sources with no found associations.

from another catalogued galactic object. All objects positioned within an angular distance smaller than the spectral extraction radius used for each candidate source, are labelled as associated with the detection. This association criterion has been intentionally inclusive in order to make sure not to miss any possible association, motivated by plausible offsets and size differences in astrophysical systems. Nevertheless it is as well subject to spurious correlations. The associations have been made with catalogued and archived high-energy emission (Fermi-LAT 2FHL[24], 3FGL[48]) detections, shell-like supernova remnants, composite supernova remnants, pulsar wind nebulae and pulsar wind nebulae candidates and energetic pulsars.

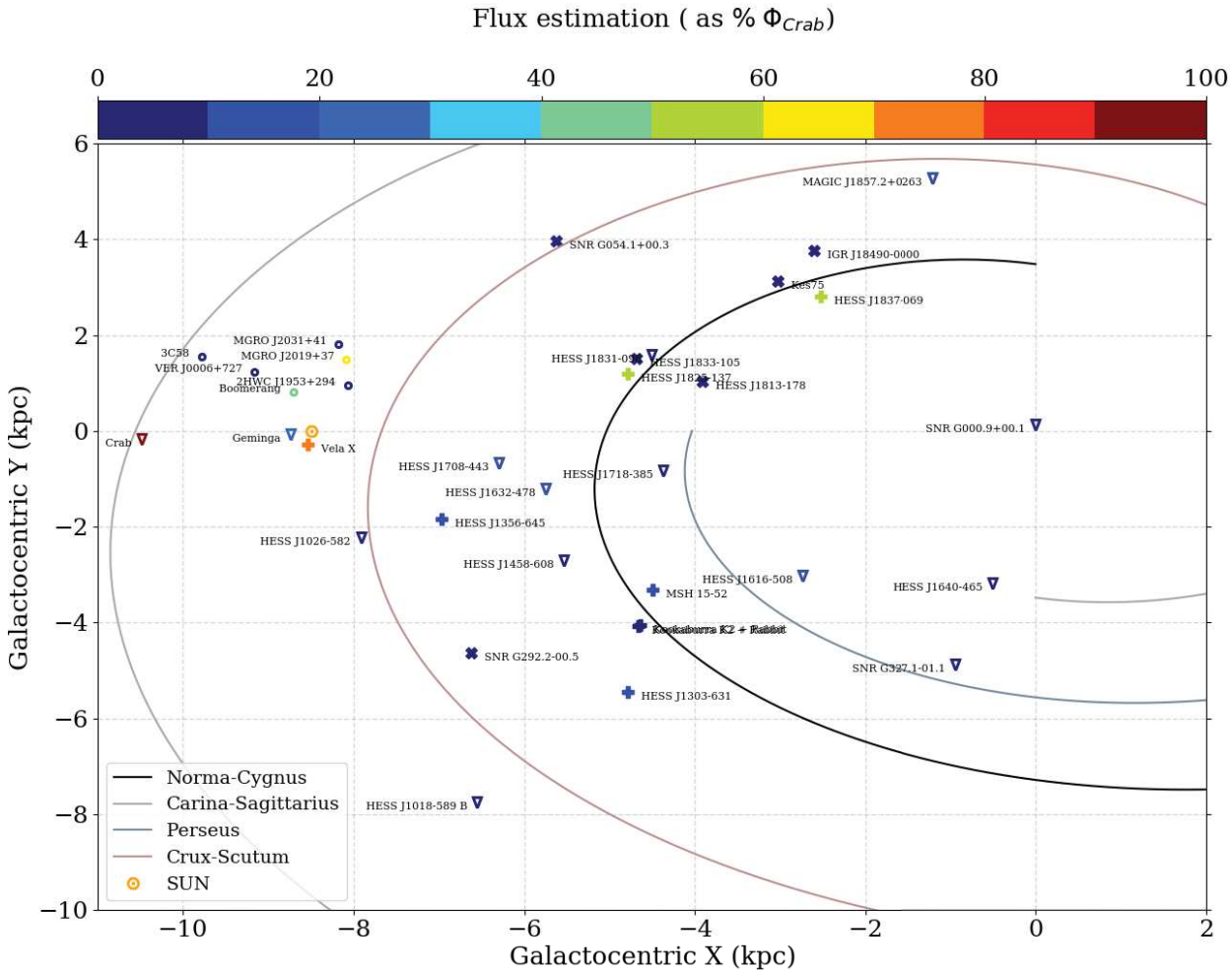

Figure 6.2 – Galactocentric mapping of the *TeVCat*[132] registered pulsar wind nebulae. The color code corresponds to the published flux of the source compared to the Crab. The crosses correspond to the H.E.S.S. PWNe that show a significant offset between the pulsar and the centre of TeV emission (sample mentioned in Table table:offset). The triangles are other PWN detected and identified by H.E.S.S.. The circles correspond to other published PWN candidates from other experiments and also seen by H.E.S.S.. The remaining ones are depicted with x's.

6.1.2 TeV population of pulsar wind nebulae

Using the detected TeV pulsar wind nebulae found in the HGPS, a companion paper has been published [94] where a population study has been conducted on the considered firmly identified pulsar wind nebulae sample. In this section, we shall focus on the confirmed pulsar wind nebulae publish in the population study paper [94] and in particular on the position of the detected very-high energy gamma-ray emission centroid compared to the position of the pulsar within the nebula.

In the fourteen PWNe published sample, nine of them are the firmly confirmed nebulae and five additional sources labelled as composite SNRs with confirmed embedded PWNe based on the HGPS. One may refer to Table 6.1 where the characteristics of this population study based on the HGPS and the measured pulsar physical properties catalogued in the ATNF PSRcat [84] are listed. It is worth mentioning that half of the VHE sources in the sample show a significant and large offset (larger than a couple of parsecs) between the position of the pulsar and the peak of the gamma-ray emission based on the uniform morphological study of the HGPS. Such uniformity in the data analyses and quality cuts provides a consistent approach for deriving model parameter values and allows a better understanding of the sampled population completeness. Nevertheless specific source-dedicated analyses bring to the table an more rigorous and adjusted to the nature of the observed system studies, requiring to conform the data selection to the faintness or brightness, extent and/or background fluctuation noise contamination of the emission.

Table 6.1 – Table of HGPS sources labeled as firmly identified pulsar wind nebulae from [94] and characteristics of their embedded pulsar based on the *ATNF* pulsar catalogue. The sorting has been made by increasing offset d_{offset} between the pulsar position and the peak of VHE gamma-ray emission, D is the distance of the pulsar to the observer, t_{ch} is the pulsar characteristic age derived from its measured period P, v_{PM} is the pulsar proper motion, when available measurement exist in the literature, $\dot{E}_{sd}$ is the spin-down energy loss rate, B_{surf} is the surface magnetic field derived from a dipole configuration, B_{LC} is the magnetic field at the light-cylinder and R_{PWN} is the size of the VHE gamma-ray emission based on a multi-Gaussian component model catalogued in the HGPS.

d_{offset} (pc)	*HGPS* source name	*ATNF* source name	D (kpc)	t_{ch} (kyr)	v_{PM} ($km.s^{-1}$)	$\dot{E}_{sd}$ ($10^{36} erg.s^{-1}$)	B_{surf} ($10^{12} G$)	B_{LC} ($10^{4} G$)	P (ms)	R_{PWN} (pc)
33.0 ± 6	**J1825-137**	B1823-13	3.61	21.4	399	2.8	2.8	2.5	101.5	32.0 ± 2.0
20.5 ± 1.8	**J1303-631**	J1301-6305	10.72	11.0	-	1.7	7.1	1.1	184.5	20.6 ± 1.7
17.0 ± 3	**J1837-069**	J1838-0655	6.6	22.7	-	5.6	1.9	5.0	70.5	41.0 ± 4.0
7.3 ± 1.5	**J1418-609**	J1418-6058	1.89	10.3	-	4.9	4.4	3.0	110.6	9.4 ± 0.9
5.5 ± 1.14	**J1356-645**	J1357-6429	3.1	7.3	-	3.1	7.8	1.6	166.1	10.1 ± 0.9
5.1 ± 1.2	**J1420-607**	J1420-6048	5.63	13.0	-	10.4	2.4	7.1	68.2	7.9 ± 0.6
2.37 ± 0.18	**J0835-455**	B0833-45	0.28	11.3	77	6.9	3.4	4.4	89.3	2.9 ± 0.3
< 11.0	J1119-614	J1119-6127	8.4	1.6	-	2.3	41.0	0.6	408.0	14.0 ± 2.0
< 10.0	J1930+188	J1930+1852	7.0	2.9	-	11.6	10.3	3.8	136.9	< 9.0
< 10.0	J1849-000	J1849-0001	7.0	42.9	-	9.8	0.7	12.3	38.5	11.0 ± 1.9
< 4.0	**J1514-591**	B1509-58	4.4	1.6	-	17.5	15.4	4.2	151.3	11.1 ± 2.0
< 2.0	J1813-178	J1813-1749	4.7	5.6	-	55.9	2.4	25.3	44.7	4.0 ± 0.3
< 2.0	J1833-105	J1833-1034	4.1	4.9	-	33.7	3.6	14.2	61.9	< 4.0
< 2.0	J1846-029	J1846-0258	5.8	0.7	-	8.1	48.8	1.3	326.6	< 3.0

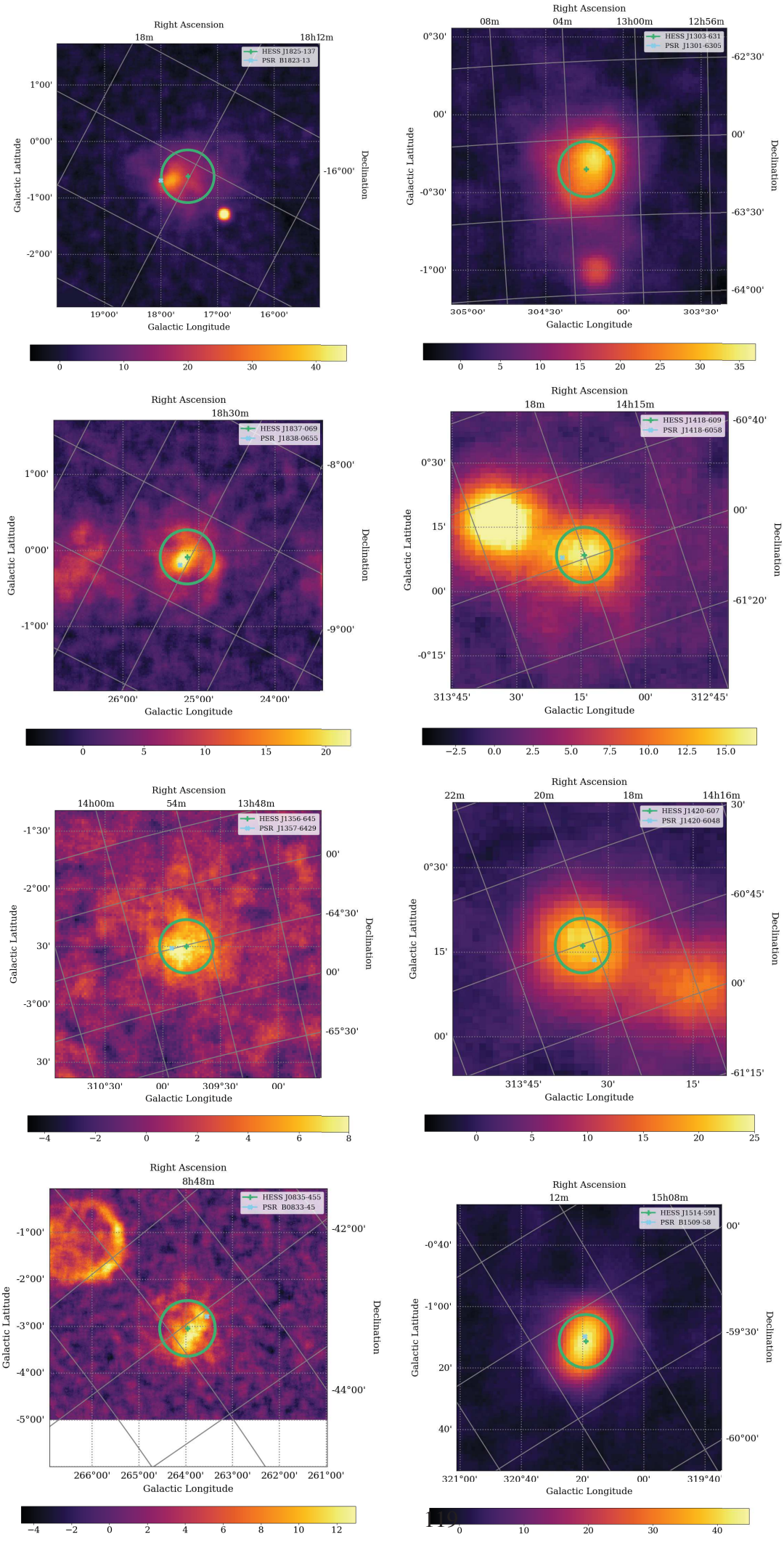

Figure 6.3 – Significantly offset PWNe seen by H.E.S.S. .

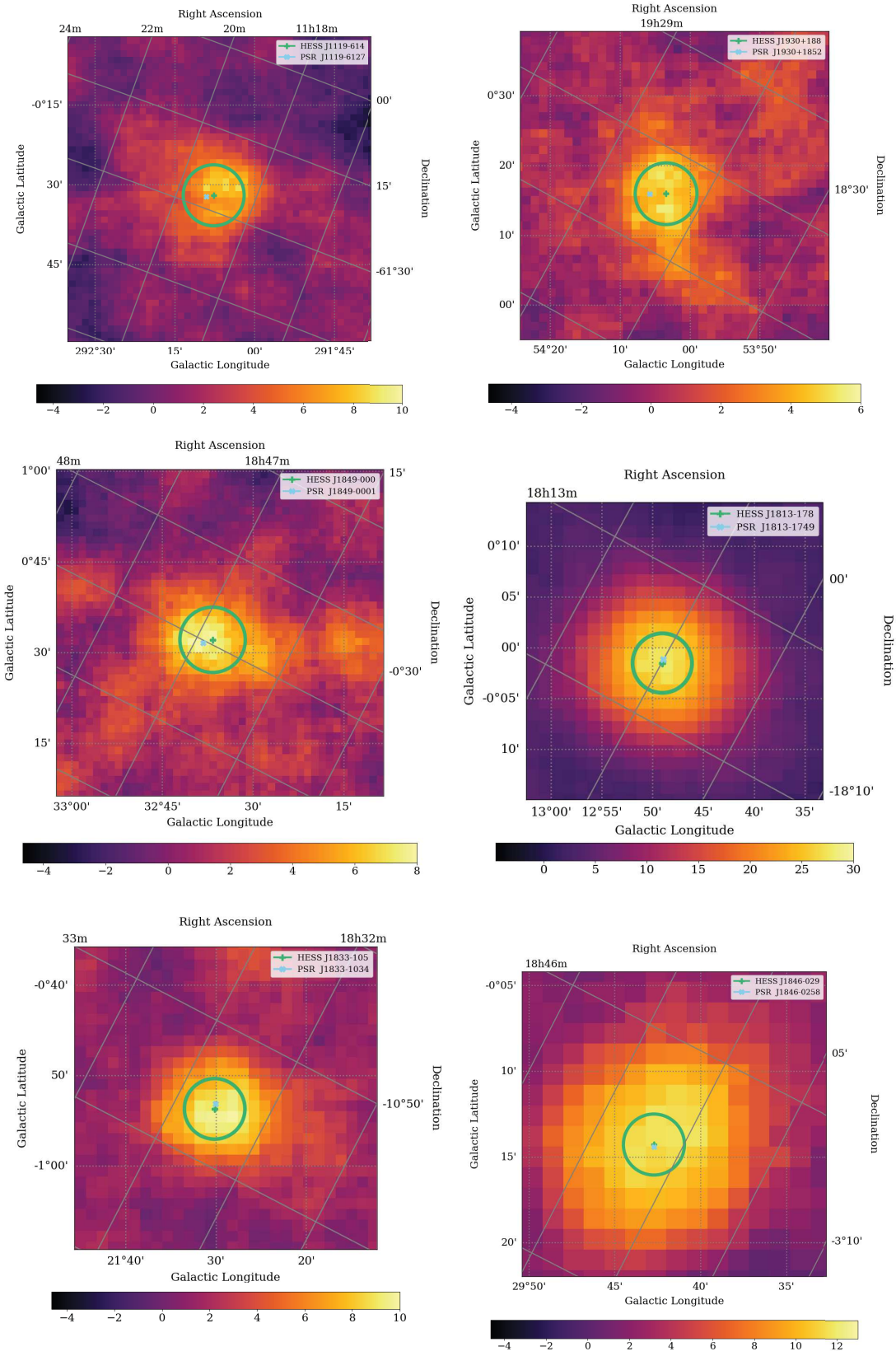

Figure 6.4 – Pulsar wind nebulae studied in the [94] that do not show a statistically significant offset. The size of the PWN depicted by the green circle depicts the upper limit/size from the HGPS catalogued morphological values. The green "X" mark points to the published coordinates of the centre of emission based on the multi-Gaussian component model of the gamma-ray emission and the cyan cross represents the position of the pulsar reported in the *ATNF* pulsar catalogue. In Figure 6.3 and in this set of skymaps, the map size has been adjusted for each source as five times its reported HGPS size. The significance colourbar has been adjusted for each case accordingly to the brightness and extent of the source.

In the discussion below, we shall consider the seven significantly offset pulsar wind nebulae shown in bold letters in Table 6.1 and we will add to this sub-sample the HGPS source J1514-591 (MSH 15-52). The dedicated more in-depth morphological analysis discussed in Section 5.3.1 has shown an extended asymmetric gamma-ray emission that re-enforces the hypothesis of a significant offset with the current pulsar position.

6.1.3 Pulsar wind nebulae with significant offset pulsars

In this section we summarise the latest reported status for each of the significantly offset-TeV sources concerning their detected and interpreted emission (for the PWN HESS J1514-519, see Chapter 5). We as well provide the values of the target photon populations in the field of each source based on the interstellar radiation field models of Popescu et al. (2017)[95] and Porter et al. (2017)[96] that we have fitted with a diluted blackbody emission. We derive the temperature and energy density for the near (Table 6.2b) and far (Table 6.2c) infrared radiation fields, that are of interest for modelling the inverse Compton scattering radiation.

Table 6.2 – Temperature, wavelength peak and photon energy density values derived by a diluted blackbody fit for the radiation field models of Popescu et al (2017) and Porter at al. (2017), extracted for the location of each significantly offset pulsar wind nebula.

(a) ISRFs : Ultra-violet - visible domain (UV-Vis) : ~ [0.1 - 0.8] μm

HGPS source name	Popescu+17 (T, λ_{peak}, U_{rad}) (K, μm, eV.cm^{-3})	Porter+17 F98 (T, λ_{peak}, U_{rad}) (K, μm, eV.cm^{-3})	Porter+17 R12 (T, λ_{peak}, U_{rad}) (K, μm, eV.cm^{-3})
HESS J1825-137	(4985 , 0.74 , 0.972)	(5291 , 0.69 , 1.459)	(5830 , 0.63 , 1.670)
HESS J1303-631	(5633 , 0.65 , 0.278)	(5763 , 0.64 , 0.589)	(6464 , 0.57 , 0.879)
HESS J1837-069	(5105 , 0.72 , 0.956)	(5375 , 0.68 , 1.449)	(5355 , 0.69 , 2.207)
HESS J1418-609	(5323 , 0.69 , 0.541)	(5597 , 0.66 , 0.791)	(5944 , 0.62 , 1.002)
HESS J1356-645	(5083 , 0.72 , 0.507)	(5486 , 0.67 , 0.629)	(5879 , 0.62 , 0.800)
HESS J1420-607	(5323 , 0.69 , 0.541)	(5563 , 0.66 , 0.785)	(5647 , 0.65 , 0.954)
HESS J0835-455	(5757 , 0.64 , 0.283)	(5664 , 0.65 , 0.440)	(5712 , 0.64 , 0.527)
HESS J1514-591	(4815 , 0.76 , 0.744)	(5465 , 0.67 , 0.896)	(5554 , 0.66 , 1.098)

(b) ISRFs : Near infra-red (NIR) : ~ [0.8 - 5.0] μm

HGPS source name	Popescu+17 (T, λ_{peak}, U_{rad}) (K, μm, eV.cm^{-3})	Porter+17 F98 (T, λ_{peak}, U_{rad}) (K, μm, eV.cm^{-3})	Porter+17 R12 (T, λ_{peak}, U_{rad}) (K, μm, eV.cm^{-3})
HESS J1825-137	(2849 , 1.29 , 2.102)	(3210 , 1.14 , 1.471)	(3333 , 1.1 , 1.555)
HESS J1303-631	(3048 , 1.20 , 0.504)	(3180 , 1.15 , 0.577)	(3296 , 1.11 , 0.748)
HESS J1837-069	(2841 , 1.29 , 2.145)	(3219 , 1.14 , 1.543)	(3430 , 1.07 , 2.121)
HESS J1418-609	(2899 , 1.27 , 1.128)	(3164 , 1.16 , 0.791)	(3268 , 1.12 , 0.950)
HESS J1356-645	(2828 , 1.30 , 1.069)	(3188 , 1.15 , 0.636)	(3288 , 1.12 , 0.766)
HESS J1420-607	(2899 , 1.27 , 1.128)	(3158 , 1.16 , 0.790)	(3280 , 1.12 , 0.943)
HESS J0835-455	(3088 , 1.19 , 0.511)	(3196 , 1.15 , 0.435)	(3286 , 1.12 , 0.523)
HESS J1514-591	(2789 , 1.32 , 1.608)	(3217 , 1.14 , 0.908)	(3344 , 1.1 , 1.082)

(c) ISRFs : Far infra-red (FIR : ~ [25 - 350] μm.

HGPS source name	Popescu+17 (T, λ_{peak}, U_{rad}) (K, μm, eV.cm^{-3})	Porter+17 F98 (T, λ_{peak}, U_{rad}) (K, μm, eV.cm^{-3})	Porter+17 R12 (T, λ_{peak}, U_{rad}) (K, μm, eV.cm^{-3})
HESS J1825-137	(37 , 97.07 , 0.973)	(38 , 95.90 , 1.043)	(41 , 88.28 , 0.830)
HESS J1303-631	(31 , 115.9 , 0.237)	(35 , 102.10 , 0.339)	(39 , 92.29 , 0.381)
HESS J1837-069	(38 , 95.20 , 1.032)	(38 , 95.33 , 1.226)	(40 , 89.62 , 0.552)
HESS J1418-609	(34 , 106.71 , 0.526)	(36 , 100.58 , 0.546)	(39 , 93.09 , 0.497)
HESS J1356-645	(34 , 106.72 , 0.498)	(35 , 103.04 , 0.380)	(38 , 94.12 , 0.331)
HESS J1420-607	(34 , 106.71 , 0.526)	(36 , 100.60 , 0.549)	(38 , 94.54 , 0.447)
HESS J0835-455	(31 , 116.29 , 0.245)	(35 , 102.51 , 0.230)	(37 , 98.54 , 0.182)
HESS J1514-591	(36 , 100.54 , 0.756)	(36 , 99.46 , 0.621)	(39 , 92.74 , 0.498)

6.1.3.1 HESS J1825-137

The detected pulsar wind nebula identified with the source HESS J1825-137 is one of the most extended systems seen in the TeV domain. Its intrinsic size has been estimated to be $\sim$ 100 pc assuming a 4 kpc distance, encompassing an energy dependent morphology depending on the location within the large extent. Based on the latest H.E.S.S. analysis [28], the emission of the nebula appears to shrink at lower energies, while for > 10 TeV energies the VHE emission centres progressively around the pulsar PSR B1823-13, illustrated by Figure 6.5. Figures taken from the corresponding publication [28].

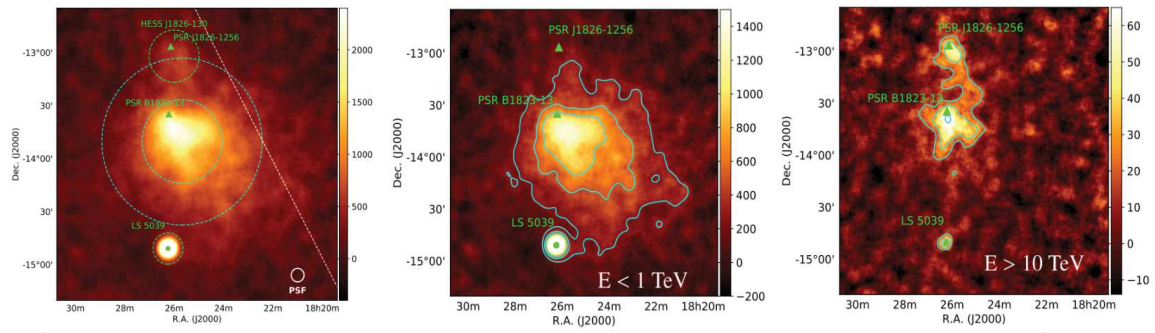

Figure 6.5 – Excess count maps from H.E.S.S. Collaboration 2018 (Mitchell et al.) of the HESS J1825-137 region. Left panel : HESS-I analysis with energy threshold at $\sim$ 0.2 TeV. The white dashed line indicates the Galactic plane, positions of pulsar present in the filled of view are represented with green triangles and the dashed light blue circles show the spectral extraction regions used. Middle and right panels: Energy-dependent excess count maps in the < 1 TeV and > 10 TeV bands. The significance contours for the lower energy map are at 5, 10 and 15 σ while for the higher energy skymap they are shown at 3, 5 and 10 σ. Figures taken from Mitchell et al, HESS Collaboration (2018).

In the field of view of the PWN HESS J1825-137, two other sources are present : the binary system *LS* 5039 with a point-like very bright emission and the PWN candidate HESS J1826-130 speculated to be associated with the pulsar PSR J1826-1256. In the HGPS uniform analysis, the energy dependence had not been investigated however the distance dependence of the emission had been underlined by the three extended Gaussian best-fit model result. This source provides an exceptional insight in particle transport studies thanks to its high flux and large extent in comparison with the H.E.S.S. instrument angular resolution. Nevertheless this as well makes its morphological analysis more complex because of other source contamination in the field of view while making the emission prone to projection effects along the line of sight.

6.1.3.2 HESS J1303-631, a not so dark source

The source HESS J1303-631 had been initially classified as a dark source because of early analyses that showed no multi-wavelength counterpart emission. Eventually it has been identified by associating it to a pulsar thanks to evidence of energy-dependent morphology[58]. As illustrated in Figure 6.6, the high energy > 10 TeV emission spatially concentrates around the pulsar PSR J1301-6305 whereas the lower energy emission < 2 TeV extends at the South-East region. This has made it possible to associate it to an X-ray PWN counterpart.

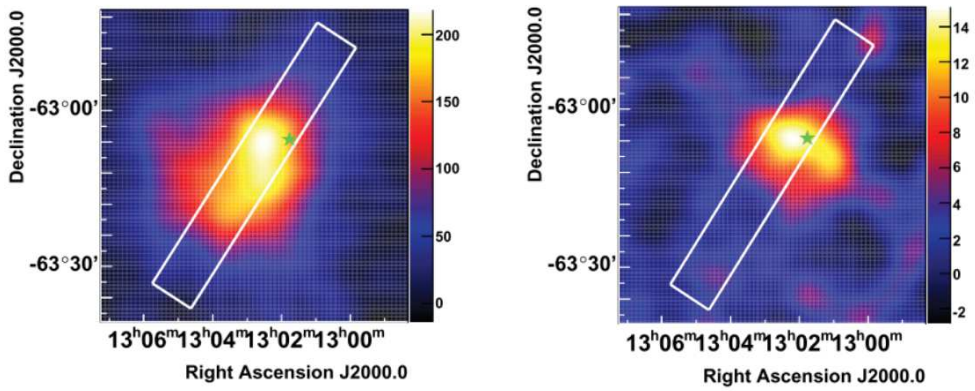

Figure 6.6 – Excess maps in the < 2 TeV (left) and > 10 TeV (right) energy bands for HESS J1303-631. The green star denotes the position of the pulsar J1301-6305. The white rectangle delimits the region in which the authors [58] estimated the offset from the pulsar by extracting count profiles along the chosen axis. Figures taken from H.E.S.S. Collaboration et al, (2012)[58]

6.1.3.3 HESS J1837-069 and HESS J1356-645

HESS J1837-069 has an elongated VHE gamma-ray emission more extended than the X-ray pulsar wind nebula, coinciding with the southern part of the non-thermal X-ray *G25.5+0.0* complex. Its TeV emission had been discovered by H.E.S.S. in the first survey of the inner Galaxy in very-high energy gamma-rays [26], the precursor of the HGPS. After its discovery, it has been associated with the X-ray emitting pulsar PSR J1836-0655 [86].

The source HESS J1356-645 has been discovered in the continuation of the HGPS as well, associated to the pulsar PSR J1357-6429, it has radio and X-ray counterparts showing an extended faint feature of non-thermal diffuse spatially coincident emission with the pulsar wind nebula [27].

6.1.3.4 HESS J1418-609 and HESS J1420-607, Kookaburra region : the Rabbit and K2

HESS J1418-069 is one resolved and confirmed pulsar wind nebula lying in the *Kookaburra* region also known by the canonical name : the *Rabbit*. It is less bright than its neighbour PWN in HESS J1420-607, the *K2* component of the complex and is located at the western part of the region. Both PWNe coincide each with a radio "wing" of non-thermal emission, being the reason behind the region name (*Kookaburra* : type of bird prominent in the Oceanic continent). In Figure 6.7, the VHE emission does not spatially correlate with the centre of the extended radio emission neither with the HII region seen in the North-West part. The presence of such thermal emission from higher density areas in the vicinity of both sources suggests that, if no projection effects are behind the complexity of the region, the ambient medium where these two nebulae are evolving is heterogeneous.

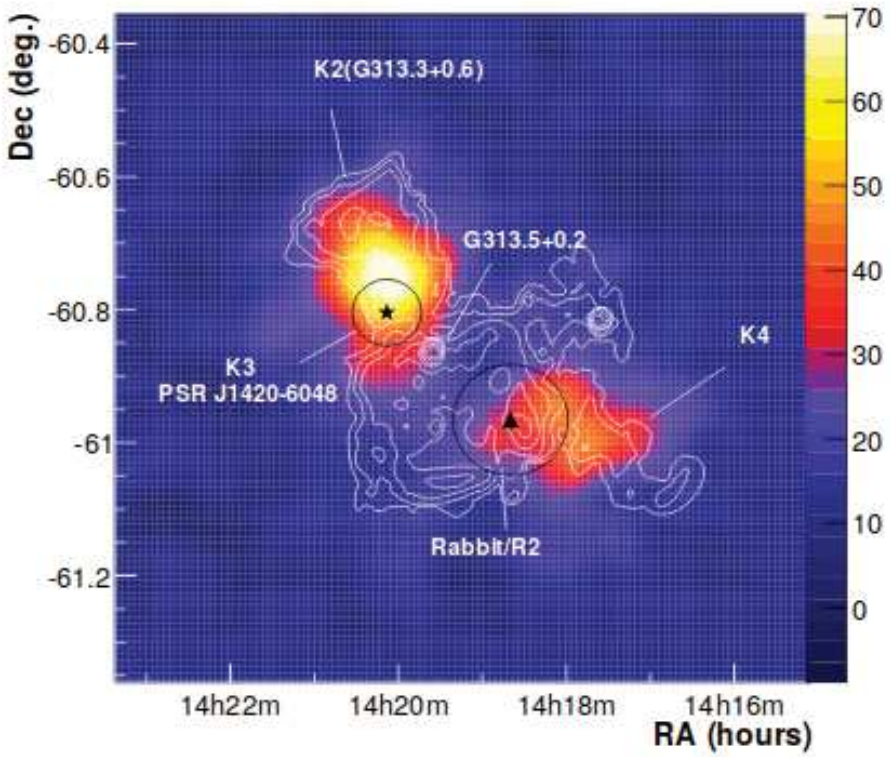

Figure 6.7 – Excess smoothed map of the resolved VHE gamma-ray emission in the *Kookaburra* region. The black markers show the position of the energetic pulsars associated with the PWNe HESS J1418-609 and HESS J1420-607 energetic pulsars. The white contours shown the radio emission from *ATCA* 20 cm high resolution images. Figure taken by the corresponding discovery publication [26].

6.1.3.5 HESS J0835-455, Vela X

HESS J0835-455, matching the radio source known as *Vela X*, is a very bright pulsar wind nebula with an elongated emission around the *Vela* pulsar PSR B0833-45, all being sources of the *Vela* constellation from where they are named after. It has an additional X-ray counterpart with a filamentary structure seemingly originating from the pulsar, called the "Vela cocoon". In Tibaldo et al, for the H.E.S.S. Collaboration (2019)[31], the origin of this X-ray-TeV cocoon feature has been studied by considering two scnenarii : an advective particle transport coming from an asymmetric evolution of the PWN and a particle diffusion within a complex ambient magnetic-field structure.

6.1.4 How analogous is the morphology of the offset TeV-pulsar PWNe?

Let us recap the attributes through dedicated morphological analyses of the significantly offset pulsar wind nebulae :

- Extended very-high energy gamma-ray bright emission spatially associated with a young(ish)/middle-aged $t_{ch} < 30$ kyr and energetic $\dot{E} > 10^{36}$ erg.s^{-1} pulsar.

- Multi-wavelength counterparts of non-thermal emission that :
  - provide the location of older and different in energy (than the ones producing TeV radiation) particle populations,
  - show potential magnetic-field structure peculiarities and strong diffusion regions.

- Mean magnetic-field values derived from one-zone models of the order of a few ($\sim$ 5 - 30 μG)

- Energy-dependent morphology that allows to allocate the site acceleration and the lepton injection locus compared to a developing relic pulsar wind nebula

6.2 Plausible drivers behind morphological asymmetry

The offset between the position of the pulsar and the fresh lepton injection location has been interpreted as a possible result of different physical factors. We shall discuss in the following some of the most widely considered drivers behind asymmetrical VHE gamma-ray PWNe morphologies, focusing on their spatial extent related to their pulsar. We consider them as parameters to be varied in our simulation studies (Section 7.1).

6.2.1 Pulsar initial kick

In the event of an asymmetrical explosion, supernovae may yield an uneven kick-back of the remaining progenitor core that forms the neutron star and thus convey to the newly born compact object a given velocity. The pulsar, having a typical $\sim 1.5 M_{\odot}$ mass in a $\sim 4 \cdot 10^3$ km^3 volume shall travel its surroundings within the ballistic limit after the acquired propulsion for a considerable dynamic system evolution age. One plausible cited explanation for the pulsar and VHE emission offset in evolved, “middle-aged" pulsar wind nebulae would be the proper motion of the pulsar, since the pulsar will continuously inject particles into the system but the initial pulsar wind nebula formed at its birth locus will not be replenished and will become a relic. However, as illustrated in Figure 6.9, in order to explain systematically the observed offset as the traveled distance by the pulsar based on its proper speed, one has to consider a wide range of velocities, differing from the typical measured ranges of $\sim$ 300 km.s^{-1} (Hobbs et al, 2005 [84]).

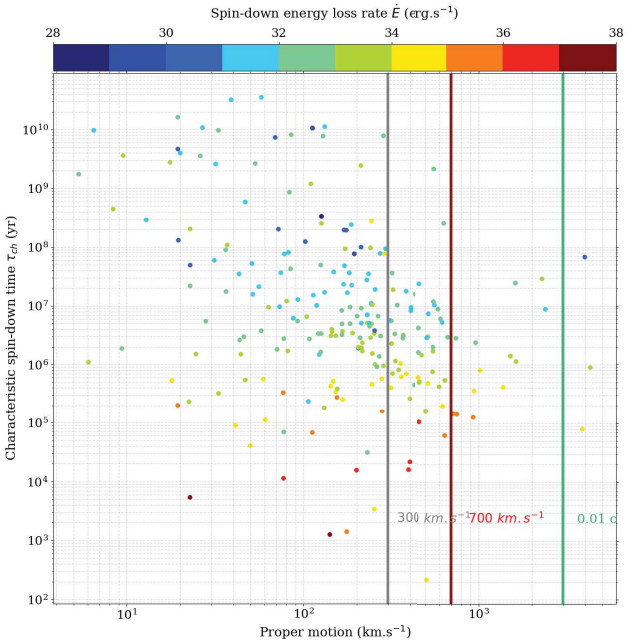

Figure 6.8 – Pulsar spin-down rate vs proper motion for the sample of pulsars in the *ATNF* catalogue [84] where a the proper velocity is measured. Population studies on the velocity distribution have been made by [84] and [9].

We note that based on the *ATNF* catalogue-provided proper motion velocities for PSR B1823-13 and PSR B0833-45 shown in Table 6.1, the first one is not sufficient to explain the reported offset seen by H.E.S.S. for the largely extended pulsar wind nebula J1825-137, by more than a

2.5 factor. As for the Vela system, the proper motion of the pulsar is not in the in the direction where its offset could be explained by the pulsar kick velocity.

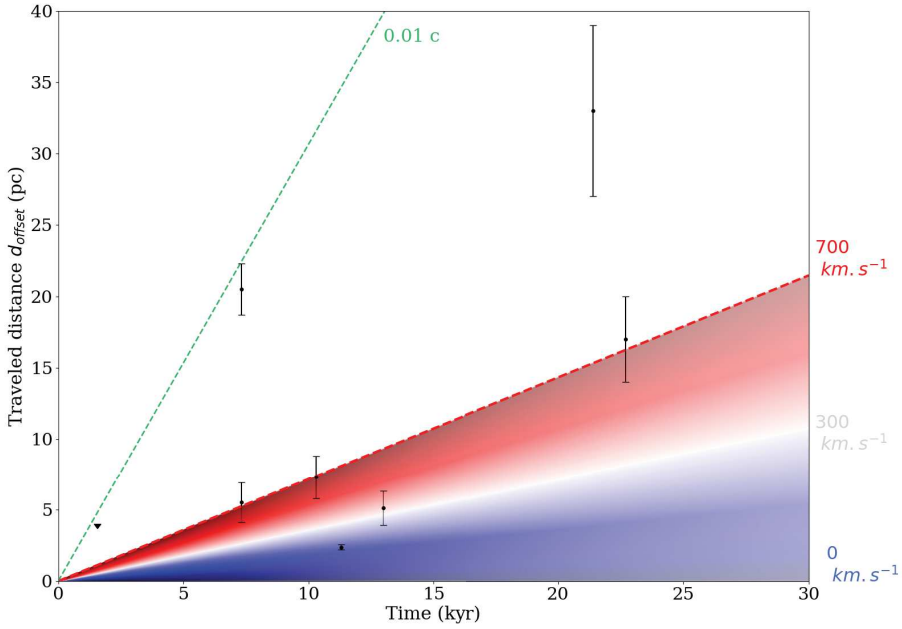

Figure 6.9 – Distance traveled by a kicked pulsar for different ballistic velocities ranging from 0 (dark blue) to 700 (dark red) km.s^{-1} and for one percent of the speed of light (orange dashed line). The lighter shaded and white zone between the low (blue) and high (red) velocities delimits the measured typical proper velocity range of pulsars (millisecond pulsars excluded) which is centred around $\sim$ 250 - 350 km.s^{-1}. The measured offsets d_{offset} of the firmly identified pulsar wind nebulae sample mentioned in Section 6.1.3 figure for each pulsar spin-down age. We notice that only a few PWNe seem to agree with the expected pulsar proper motion values and that the rest require high velocities ($> 500\ km.s^{-1}$) and for some improbable $\sim 10^3 km.s^{-1}$ to explain the several parsec offset [9].

Nevertheless, pulsar proper motion is one of the main physical justification evidenced by the overall offset seen for pulsar wind nebulae and PWN candidate sources. We use it as one of the two main parameters to investigate its influence in pulsar-PWN-SNR system evolution with time (Section 7.3.1).

6.2.2 Asymmetrical pulsar wind

Another cause for possible pulsar wind nebulae deformation would be an asymmetrical outflow of ions and leptons from the pulsar that would depend on the obliquity angle between the magnetic-field axis emerging from the polar caps of the pulsar and its rotational axis. In our simulations, we compute the energy flux of the pulsar wind based on the assumption that it reaches its maximum in the equatorial direction, thus coupling the Poynting flux to a pulsar wind initial particle flow asymmetry parameter (Komissarov and Lyubarsky, 2004 [75]). We do not wish in our study presented in Section 7.1 to examine its influence in deforming the termination shock shape oblongly because of the core power computation it would require to consistently

spatially resolve the pulsar wind with a great refinement while we simulate the pulsar wind bubble and the supernova remnant blast waves (forward and reverse) in scales greater by 3 to 5 orders of magnitude. This deformation would render the shape of the PWN elongated along one given axis but would not explain an offset of the position of the pulsar.

6.2.3 PWN magnetic-field topology

Pulsars are astrophysical objects with very high magnetic-field at their surface 10^7 (for millisecond pulsars) to 10^{15} G (for magnetars), strengths derived under the assumption of a dipolar magnetic field. For the significantly offset pulsar wind nebulae sample presented in Section 6.1, their associated pulsars have an estimated surfacic B-field of $> 10^{12}$ G (see Table 6.1) and typically experience an energy rate loss of rotational energy of the order of 10^{36} - 10^{37} erg.s^{-1}. Usually the majority of the rotational energy loss is deposited into the magnetised pulsar wind and a negligible portion may go into the electro-magnetic radiation from the pulsar. Even though the pulsar wind is highly magnetised, pulsar wind nebulae show a rather low magnetisation. In order to infer the mean magnetic field of a PWN, different approaches have been attempted [105] :

- A contested method would be to roughly estimate the termination shock radius of the pulsar wind from observations and simulations comparison. This is argued to be done with spatially well resolved non-thermal X-ray observations. The TS radius can be used as an input parameter to a pulsar wind model so as to compute the magnetic field value at the TS and thus extrapolate it to the PWN [53].

- Averaging over the synchrotron emission equipartition of particles and B-fields (Hester 1995[62])

- Deriving it indirectly using the high-energy (GeV) and very-high energy (TeV) observations, in addition to the ones in X-rays. By using the photon energy density ratio of synchrotron and inverse Compton radiations (see Equation 3.14) one may estimate the strength of the magnetic field. This may apply as long as it may the observed synchrotron and IC flux ratio is comparable to the respective luminosity ratio with bolometric corrections.

The inferred mean magnetic-field strengths for the sample of offset nebulae are of the order of a few to a few tens of μG. Based on the PWNe morphologies seen in X-rays, particularly for MSH 15-52 and Vela X, there seem to be indications of non linear distance dependence of the magnetic-field, thus underlining the possibility of non-uniform, relatively strong B-fields in the surrounding medium where the pulsar wind nebula is evolving. The observed asymmetry of these objects may be caused by the effects of particle confinement dictated by more complex magnetic field topologies. Radio polarisation studies have shown that some pulsar wind nebulae have a radial magnetic field, others exhibit a toiroidal structure and a few have more chaotic configurations [61], [10], [117].

In order to study this possible offset cause, it would be required to have very high-resolution X-ray and gamma-ray skymaps, along with a well understanding of the location of emission to be able to estimate the signal extinction due to absorption and other observational conditions such as noise contamination in the field of view, brightness emission and comparable error estimation on flux and position.

6.2.4 Inhomogeneous ambient medium

Another prime actor behind the offset pulsar wind nebulae populations would be the scale of inhomogeneity of the ambient medium. If the density contrast through the length of the system is strong enough (1 to 2 orders of magnitude), the PWN may be offset by an asymmetric crush caused by the shocked ejecta via the reverse shock (RS) propagating towards the centre of the nebula. This will cause a quicker evolution on the higher ambient density immersed side of the nebula, that will no longer be expanding freely in the known as *ejecta-dominated stage*. Subsequently it will interact with the hot shocked incoming particle flow driven by the RS thus triggering an adiabatic evolution (the *Sedov-Taylor stage*) whereas for the lower density surrounded side, its evolution shall continue freely. This will cause a displacement and a strongly asymmetrical evolution.

Chapter 7

Relativistic magneto-hydrodynamic numerical study

Contents

7.1 Simulating pulsar wind nebulae systems

In this chapter I shall relate briefly the work I have conducted during the last year of my PhD with Dr Meliani and my supervisor Dr Gallant, that has build the grounds for future studies regarding the morphology of pulsar wind nebula using relativistic hydrodynamical simulations. Unfortunately, this embarked project has not yet yielded scientifically exploitable results as expected due to the complexity of the task we have tackled. Nevertheless, the current state of the study will allow prospective conclusions hopefully in the near future that could help understand better the evolution of such astrophysical systems and constrain particle transport models.

7.1.1 Physical motivation

In order to study the morphology of pulsar wind nebulae, it is important to consider both the occurring energy injection that deposit the lepton quota in the PWNe, and the surrounding medium in which they are embedded. In conventional evolution scenarii, the input energy originates from the central pulsar of the system and therefore depends on its characteristics, such as its spin period, defining the rotational energy that in tandem with its magnetic field structure will create a pulsar wind (PW) of cold highly magnetised leptons, and its braking behaviour, which dictates the rate of pulsar energy loss and particle injection. The pulsar wind at its termination shock deposits highly energetic relativistic electrons and positrons that agglomerate in a weakly magnetised zone (less than the pulsar wind but more magnetised than the ejecta) and form the pulsar wind nebula. The nebula expands by shocking the ambient ejecta matter. The surrounding medium of the PWN is composed by the progenitor star ejecta layered in unshocked and shocked regions. The supernova explosion initially induces a forward blast wave that will propagate outwardly and shock the interstellar medium (ISM). As a result of this forward shock (FS) and the ISM impediment, a reverse shock wave (RS) will travel inwards to the central system, shocking progressively the interior of the remnant, reaching eventually the pulsar wind nebula. Therefore the ambient medium, including the remnant ejecta region and the interstellar medium, will be determined one hand by the core-collapse supernova energy explosion and ejecta matter bulk and on the other, by the temperature and density structure of the ISM where the supernova happens. A more detail recount of these evolution steps may be found in Section 2.4.

As presented in Section 6.1, several detected pulsar wind nebulae show hints in their morphology of asymmetrical evolution. We take particular interest in two of the most possible drivers behind offset systems, the pulsar kick velocity and the inhomogeneity of the ambient medium. We aim to use simulations to quantify their effect on the pulsar wind nebula morphology and explore prospective constraints on their plausible asymmetric evolution.

In the PWN community, such studies have been conducted by experts using non-relativistic hydrodynamical simulations of individual objects in the physical system [129], [121], [13], [120], [17], [40]. Our goal is to generalise studies that have been performed previously in order to include the full *relativistic* (magneto)-hydrodynamic properties of pulsar wind nebulae. Furthermore, we include in the scope of such study the objective of extrapolating the results applicable to the whole PWN population.

7.1.2 Using adaptive mesh refinement

MPI-AMRVAC is an open-source parallelised code for adaptive grid hydrodynamic and magneto-hydrodynamic simulations. Its name stands for *Multi-Processor Interface - Adaptive Mesh*

Refinement Versatile Advective Code[97], . We have chosen to use this available code because of its adaptive refinement feature which is a key to the multi-scale nature of the evolution of a composite supernova remnant-pulsar wind nebula-pulsar wind system.

We use the upgraded software version *MPI-AMRVAC 2.0*[137] which initially had been created by its developers as a tool to study hyperbolic partial differential equation systems such as the Euler continuity equations or ideal magneto-hydrodynamics with patch-based or hybrid-block-based adaptive mesh refinement(Keppens et al. (2003)[73], van der Holst and Keppens (2007)[127]). The code is written in Fortran 90 using the loop annotation syntax (LASY)[123], plus with Perl annotations, so to be translated by a Perl preprocessor into any dimensional pure Fortran code before compilation, which has been proven to me as a very handy features because the LASY syntax is a sore to the eye for an unfamiliar with this particular syntax user as myself. The developers of the software chose to use the LASY implementation as a way to concise code expressions in multidimensional simulations when allocating variables into arrays.

The code may be used in a Cartesian, polar, cylindrical or spherical geometry applied on an up to three dimensional adaptively refined or coarse meshed grid. This adaption is based on a quadtree-octree block-based hierarchy, with an automated regridding for each of its block. First all blocks are considered at levels between the two extrema values regarding the refinement level input bounds, $AMR_{min,level}$ and $AMR_{max,level}$ and the local error at each grid point of a given block is computed thanks to the local error estimator chosen on a Lohner[83] type scheme. If the local error value exceeds a chosen fluctuation threshold $AMR_{error,thresh}$, the parent block is refined by dividing its size by two on each axis.

7.1.3 Relativistic magneto-hydrodynamics

In order to study in a realistic frame the evolution of the composite pulsar-pulsar wind nebula-supernova remnant systems, we opted to use a (magneto)-hydrodynamic approach. The supernova remnant is evolving as a hydrodynamic fluid while the pulsar wind will require to take into account the strongly magnetised outflow, so as to describe the relativistic effusion of positrons and electrons that shall eventually form the pulsar wind nebula. Our main goal is to study the morphology of pulsar wind nebulae and in particular the asymmetry in respect to the position of the pulsar.

We use in the latest *MPI-AMRVAC* code, a manually implemented relativistic magneto-hydrodynamic module developed by Meliani et al. (2012)[72] in a previous version of the software. This module computes numerically special relativistic magnetohydrodynamics by solving the conservation equation system including the Lorentz factor $\gamma = \left(1 - (\frac{v}{c})^2\right)^{-\frac{1}{2}}$ of the following form :

$$\frac{\partial \Xi}{\partial t} + \nabla . \mathcal{F}(\Xi) = 0 \tag{7.1}$$

where Ξ is the set of conservative variables of the conservation law system, comprised by the mass density ρ, the momentum density ρv along the the number of dimensions of the problem, the total energy density e and the magnetic-field B. The algorithmic details for the numerical solution of the relativistic MHD equations in the *MPI AMRVAC* framework are presented in [128].

Our aim is to use a fully magnetohydrodynamic two-dimensional approach however it is essential to check the validity of our simulations and to test the efficiency of the code by starting with a simpler numerical strategy. Thus we have conducted several configuration tests and physical set-ups with a relativistic (γ ranging up to 10) hydrodynamic solution in one dimension.

We use the same implemented module as the relativistic magnetohydrodynamic case but we set the magnetisation to null. In this dissertation I shall thus present some extremely preliminary and subject to imprecision results obtained when solving the following set of expressions :

$$\frac{\partial}{\partial t}\begin{pmatrix} \gamma\,\rho \\ \gamma^2\,\rho\,(1+\epsilon\ +\frac{p}{\rho})\,\mathbf{v} \\ \gamma^2\,\rho\,(1+\epsilon\ +\frac{p}{\rho})\ -p \end{pmatrix} + \nabla.\begin{pmatrix} \gamma\,\rho\,\mathbf{v} \\ \gamma^2\,\rho\,(1+\epsilon\ +\frac{p}{\rho})\,\mathbf{v}.\mathbf{v}+\mathbb{I}p \\ \gamma^2\,\rho\,(1+\epsilon\ +\frac{p}{\rho})\,\mathbf{v} \end{pmatrix}^T = \begin{pmatrix} \mathbf{0} \\ \mathbf{0} \\ \mathbf{0} \end{pmatrix} \tag{7.2}$$

with $\mathbf{v}$ the velocity vector, the term $(1+\epsilon\ +\frac{p}{\rho})$ being the specific enthalpy related to the specific internal energy ϵ.

These consistency checks have been validated or discarded by cross-examining them with previous studies such as the one dimensional spherical symmetry simulations of van der Swaluw et al. (2001)[129] and Bucciantini al. (2004)[40].

We have separated our code into several sub-modules so as to better handle the different objects we handle in this composite system and to define special boundary conditions that suit the physics for each element of the simulation. The structure of the code consists on loading all different sub-routines by calling them in a single user defined module so as to set-up our simulation framework so to have more freedom in determining the physical source terms for our equations.

7.2 One dimensional study

In our 1D simulations, we set, using the inherit tree nature of the code, a total of 96 cells in blocks, with each block of an 8 cell dimension for a grid with a maximum radius of $6 \cdot 10^{19}$ cm ($\sim$ 19.5 pc). Each refinement ratio between levels is by default set to 2 and we proceed by adapting the regions of each system component (located via appointed tracers) by an adequate interval of allowed refinement levels based on the order of physical variables' local small-scale fluctuations. We opt for this method to make sure that, 1) the pulsar wind and its termination shock are sufficiently resolved in comparison with the rest of the system so that the density and pressure of the relativistic wind is bounding the inside of the PWN without being rendered into too coarse a block by the adaptive nature of the refinement, and 2) the reverse and forward shock waves are resolved as well but not too finely so that the *Rayleigh-Taylor* instabilities at the contact discontinuity between the shocked ejecta and ISM do not dominate the small-scale fluctuations. We define for the pulsar wind and nebula region a minimum of 5 and maximum of 11 levels of refinement, and for the supernova remnant shock region an interval from 1 to 8 refinement levels.

We simulated a supernova by depositing an initial explosion energy of $E_{\rm SN} = 10^{51}$ erg in 5 $M_\odot$ of uniform-density ejecta, and imposing a radial velocity profile with a maximum ejecta velocity of 5700 km.s^{-1}, ensuring that $\sim$ 97% of $E_{\rm SN}$ is in the form of kinetic energy. The initially set ejecta radius corresponds to an evolution time of 80 yr. The pulsar, characterised by a typical spin-down braking index $n = 3$ and an initial spin-down energy loss rate $\dot{E}_0 = 5\ 10^{38}$ erg.s^{-1}, is being switched on 20 yr after the start of the simulation and powers a relativistic wind (of

Lorentz factor γ on the order of 10) with an initially input termination shock radius of $\sim 10^{16}$ cm and pulsar wind nebula size of $\sim 10^{17}$ cm at the moment when it is switched on. We let the system evolve in a homogeneous simulated interstellar medium with density $n_0 = 1.0$ cm^{-3} density and temperature $T = 10^4$ K.

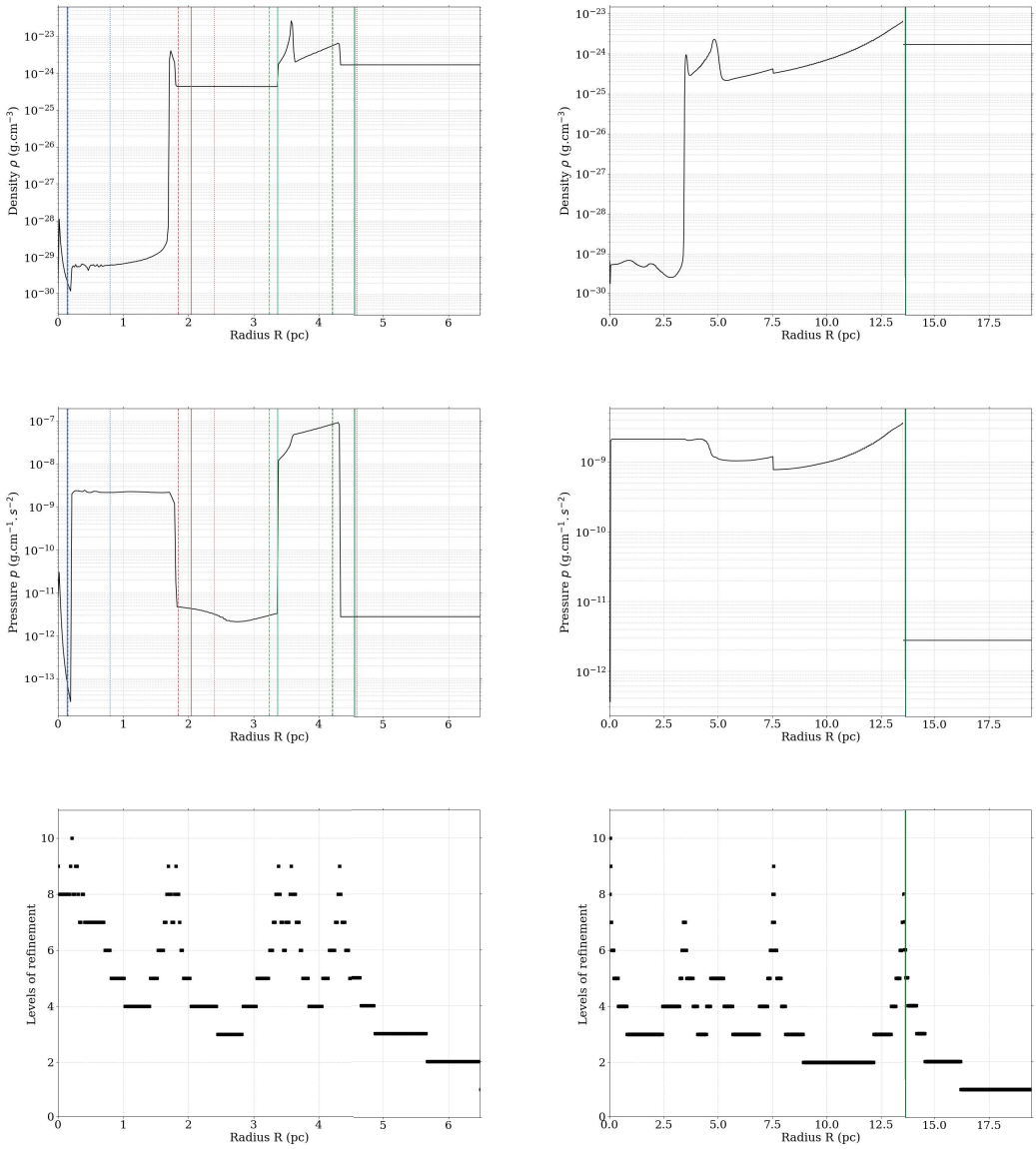

Figure 7.1 – Radial profiles of density, pressure and refinement level from top to bottom, for simulated ages of 1 000 years (*free expansion* stage, on the left panels) and 10 000 years (*Sedov-Taylor* stage, on the right panels) in a relativistic hydrodynamic frame. The evolution of the termination shock, pulsar wind nebula and the supernova remnant's forward and reverse shock waves are in agreement with published non-relativistic [129] and relativistic [40] studies, taking into account the differences in the simulation configuration physical set-ups. The coloured lines for the 1 kyr snapshot represent the analytical expected radii for the pulsar wind termination shock (blue), the pulsar wind nebula (red), the forward (green) and reverse (turquoise) supernova remnant shock waves, during the early free expansion ejecta-dominated phase, just before transitioning to the *Sedov-Taylor* stage (Section 2.4).

7.3 Towards a two dimensional study

We are currently working on simulations in a two-dimension cylindrical framework (r, z, θ) where the system is let to evolve radially with an imposed proper motion in the z axis. We use a 2.5D framework by imposing cylindrical symmetry along the θ axis and chose a large grid size of 1.2 10^{20} cm ($\sim$ 40 pc).

To gain some computational time, we let evolve in a first trial the supernova remnant without the pulsar up to 1000 yr with a required resolution applied on the contact discontinuity but more importantly on the forward and reverse shock-waves. This trial is made without adding the pulsar, which renders the solving to occur quickly. We then use the solution (output grid with the data point) for different time steps as initial conditions to start the full trial where the pulsar is added and an initial imposed radius for its wind is defined over a small fraction of the ejecta within the SNR bubble. After our tests in the 1D approach, we have decided upon introducing the pulsar in the grid box at t= 500 yrs. This simulation time range has proven to be a good compromise between saving some valuable computational time by starting the combined computation at higher ages, while leaving time to the system to shock enough the supernova ejecta so as to ensure a comparable dynamical evolution by the time the system steps into the adiabatic phase in comparison to our trials in the simulated (1D) case. Unfortunately our 2D study is still extremely

preliminary and has not yielded any exploitable results :

- we have not yet completed our simulation pathological behaviour tests to underline possible numerical issues as the case depicted in Figure 7.2
- we need to test different solving flux and time schemes to make sure that we do not have dynamically dominant diffusion along the axes where we impose a reflective boundary condition and to test possible numerically driven advection on the bounds with continuous boundary conditions.
- another crucial and prioritary step would be to find a more efficient way to impose the adaptive criterion on the regions of interest so as to allow the computation to speed up. Unfortunately, so far all tests that we have conducted point to a high level of refinement as a necessity so as to maintain a physical propagation of the shocked pulsar wind without introducing irregularities due to coarsening and re-distribution of the computed data and losing significantly the smoothness of the resolution of the source radii.

To counter the artificial and unphysical deformation of the nebula, we have increased the refinement level resolution. We set a general 3 to 14 levels for the global grid space but impose an 8 to 10 levels of refinement at the reverse and forward shock region of the SNR and an 11 to 15 refinement level as to continue adequately resolving the pulsar wind at its termination shock. This has increased the computational time by a factor of $\sim$ 6 which is raising the necessity to find a better and more viable in the long term numerical strategy.

7.3.1 Pulsar proper motion

We simulate the proper motion of the pulsar by setting it static in our simulation frame and by setting both the interstellar medium and the supernova remnant in motion. Thus, at the early stages of the simulation run, we switch on the pulsar in a moving z-axis frame, which is numerically easier to handle than affecting the proper motion into a non-ab initio set object.

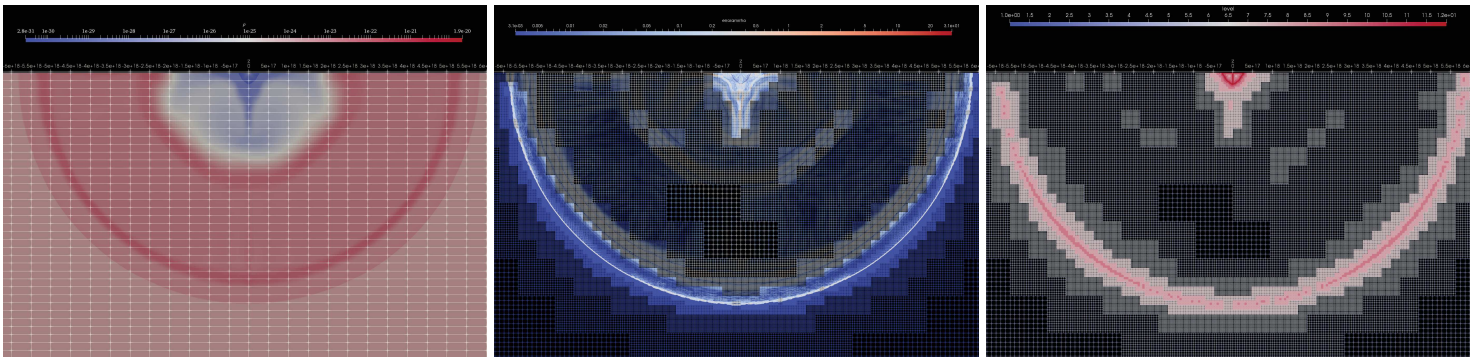

Figure 7.2 – Snapshots of a clearly problematic simulation trial at after a few simulated hundreds of years. On the left the density matter ρ is shown. The pulsar wind and then consequently the pulsar wind nebula are advected along the R axis while the evolution is not symmetric radially as it would be expected for this stage. On the middle, the estimated error fluctuation $AMR_{error,thresh}$ for the ρ variable, as discussed in Section 7.1.2, is shown for each grid block, while the chosen refinement level based on this error value on the map on the right.

Our goal is to reach middle-aged systems and to accurately simulate the beginning of the *Sedov-Taylor* phase as it is the interactions preceding it, id est the reverse shock reaching the pulsar wind nebula boundaries, that could induce a quicker asymmetry along the direction of the pulsar proper motion.

So far we notice a consistent evolution with the expected free expansion analytical solutions but we notice the growing boundary effects forming on the lateral sides of the nebula in contact with the grid edge. Therefore we need to assess in a few simulated centuries how much this effect has dominated the outflow within the nebula.

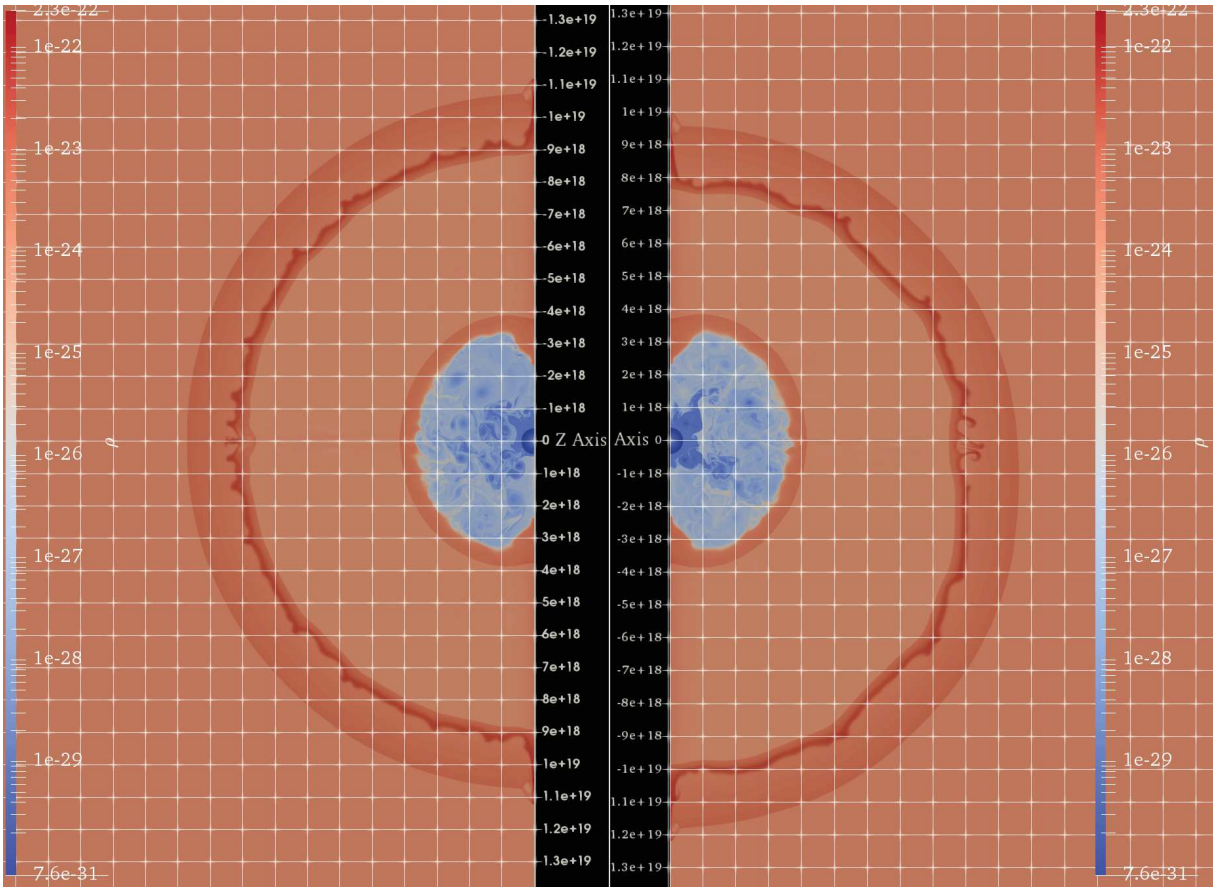

Figure 7.3 – Two snapshots of the simulated matter density ρ in g.cm−3 for a similar physical set-ups, as the one described in Section 7.3 at t∼ 730 yr. The snapshot on the right includes a proper motion of the pulsar of - 500 . **z** km.s^{-1}. The two systems are shown in their pulsar's rest-frame. Numerical border effects on the z axis are beginning to show after 100 - 200 simulated years and are still subject to further investigation.

7.3.2 Inhomogeneous media

We as well separated the grid into two density media, one significantly denser than the other, to simulate the differed and delayed evolution of the joint supernova remnant - embedded pulsar wind nebula system. In future work, we will impose a gradient of density rather than the currently strong contrasted media so as to investigate a more realistic ambient medium.

Motivated by the large scale offsets between the position of the pulsar and centroid of the very-high-energy gamma-ray emission of several pulsar wind nebulae, we have begun a study with relativistic hydrodynamic and magneto-hydrodynamic simulations. We aim to characterise the possible lengths of offsets expected with high pulsar proper velocities and compare them to the ones caused by ambient medium inhomogeneities so as to understand why these observed offsets are a typical feature in the evolution of pulsar wind nebulae.

Part V

Conclusion

Chapter 8

Summary of thesis results and prospects

In this epilogue, I will come to my conclusions by summarising the results found during the course of my PhD thesis studies. Firstly, I shall focus on the phenomenological aspect of my work in the pulsar wind nebula and very-high-energy gamma-ray scientific fields. Furthermore I will outline the modelling and numerical simulation groundwork that I have conducted during the end of my thesis and finally frame them into the context of pulsar wind nebulae studies as prospective constraints for future investigations.

8.1 Observing PWNe

During my thesis I have been invested primarily in the investigation of the very-high-energy emission of the pulsar wind nebula within the composite supernova remnant MSH 15-52 . I have, with my supervisor and collaborators, conducted morphological and spectral analyses in depth for dedicated studies of this source.

Our main motivation to revisit the H.E.S.S. Collaboration (2005) paper[30] has been to disentangle the above TeV gamma-ray emission of the nebula so as to understand the reasons behind its morphology. We have used a larger dataset of HESS-I observations that permitted us to :

- Confirm the reported elongated shape of the nebula[30] by tracing with more precision the extent of the very-high-energy gamma-ray emission of the pulsar wind nebula and confirm, based on a dedicated morphological analysis, that a lone component Gaussian model is not enough to fully account for the spatial distribution of the emission [59].

- Hint on the non-linear variation of the magnetic field within the pulsar wind nebula. We base this statement on the results we obtain when fitting the PWN gamma-ray emission with a synchrotron template map and scale its relative spatial correspondence as a power-law with the distance to the pulsar, in which we fit the index. The obtained index suggests that, assuming a simple radial dependence of the magnetic field is not the case for MSH 15-52 .

- Infer from a physically motivated modelling of the gamma-ray emission, consisting to map the synchrotron radiation thanks to the use of the X-ray template, several possible

scenarii on interpreting the gamma-ray emission extending further from the X-ray one which has been quantified for the first time by us [125] which are :

  - Considering the case that the gamma-ray emission at the outer region of the PWN traces leptons escaping their confinement and propagating into the ejecta. This scenario is not supported by the results of our energy-dependent analyses, where we find a decreasing size of the nebula at higher energies.

  - Pondering on the reported density medium values that range from the south-west region from a low density medium ~ 0.01 cm^{-3}, to a denser up to ~ 5 cm^{-3} at the northern region, which could mean that at the position where we detect the extended gamma-ray emission, the PWN would be expanding freely, while at the north it would be entering its *Sedov-Taylor* phase and interacting with a forthcoming reverse shock crashing at the northern (and denser) side of the system. We measure the centroid of the TeV emission at a distance of ~ 3.8 pc from the position of the pulsar, which has been previously reported as an upper limit. This offset would require a pulsar proper motion of $\sim 3\,000$ km.s^{-1}. Given the pulsar detections announced up until today, there is just a handful of examples to be accounted for having proper velocities greater than 3 000 km.s^{-1}. As we are waiting on announcements of measurement of proper motion for PSR B1509-58, we consider the inhomegeneity of the medium as a possible and viable explanation for the displacement seen in MSH 15-52 .

- Investigated the energy dependence of the morphology and assessed that the VHE gamma-ray emission shrinks at higher energies. The shrinking of the morphology becomes statistically significant above ~ 10 TeV.

- We reported a significant steepening of the spectrum of MSH 15-52 occurring at a compatible energy of ~ 10 TeV as the decreasing of the TeV emission extent is observed.

- Studied the spectral energy distribution of MSH 15-52 using our H.E.S.S. spectral analysis data to model the electron energy spectrum. This encompasses the following features :

  - We used three of the latest modeled interstellar Infra-red radiation fields available to us, as constraints on the photon density and temperature parameters we use to account inverse Compton scattering in our model. Our findings do not point into one of those models in particular, since for the region of MSH 15-52 these ISRF values are compatible to each other in each of the three considered modellings of the photon populations. Our SED fit results are compatible with the expected radiation fields.

– Our best-fit results, based on an exponentially cut-off broken power-law spectral shape assumption, show an electron energy break at ~ 10 TeV, with a slope at lower energies of ~ 2.5 and at energies above a steepening exhibiting a slope of ~ 3.2. The magnetic field value we find, is set at ~ 12 μG, which is still in agreement with the published 17 μG but suggests a slightly weaker mean magnetic-field strength than previously estimated.

– We find that the Far Infra-red radiation field is the dominant target photon field, while we find that the contribution from the Cosmic Microwave Background is not negligible and at energies beyond the spectral steepening, it becomes the dominant target. This feature could explain the spectral steepening of the photon spectrum seen in our H.E.S.S. analysis, as a manifestation of *Klein-Nishina* effects.

– We investigated the electron energy break possibility to be reckoned from synchrotron cooling losses. We find that given the energy ranges of the pulsar wind nebula observed X-ray emission, the cooling scales are comparable to the age of the system, from ~ 6% to ~ 60% of the pulsar's characteristic age but for energies at least an order of magnitude above the fitted spectral break. We deduced that this effect would not dominate the steepening our results indicate at an electron energy of ~ 10 TeV.

8.2 Understanding the PWN morphology

Prompted by the complexity of interpreting our observational results for the morphology of MSH 15-52 , and intrigued by the population study published by H.E.S.S. on very-high-energy pulsar wind nebulae that put forward a significant offset between the pulsar and the TeV centroid in older PWNe, we began a study of the asymmetry drivers using numerical (magneto)-hydrodynamic simulations.

This work is based on the *MPI-AMRVAC* public code, adapted to include relativistic physics. We use an adaptive refinement for our simulation grid so as to deal with the multi-scale nature of the composite system's evolution. We simulate the supernova remnant and create the pulsar wind nebula by introducing the pulsar and the young pulsar wind at early dynamical evolution stages and let the system evolve. We impose great levels of precision on the boundaries of each system component as a measure to reduce numerical instabilities and fluctuations, thus accurately simulating their expansion into space and verging upon realistic physical structures.

Our one dimensional study has yielded results in agreement with previous published hydrodynamical non-relativistic and relativistic simulated cases. Our two dimensional study is still on going. Unfortunately, this high level refinement method we have opted for, is very computationally expensive in time. To this day we have simulated young pulsar wind nebulae, during their ejecta dominated phase. We have been able to test our code's limitation and strengths by converging on physical simulation set-ups that minimise the numerical effects during the free expansion of the PWN.

Our aims in the longer term would be to :

- quantify the required density gradients of an inhomogeneous medium that could lead to a

significant asymmetric evolution and attest if the offset magnitudes are compatible with the ones reported from observations

- estimate how the inhomogeneous medium effect compares to the morphological deformation caused by high pulsar proper motion propagating within the composite system
- combine the two drivers and assess their influence on PWN evolution so as to provide constraints on their observed morphological asymmetry

8.3 Future prospects

In the dawn of the Cherenkov Telescope Array (CTA) era, which is a project in progress, consisting of building the widest array of next generation ground-based Cherenkov telescopes, the current knowledge of physics regarding pulsar wind nebulae would be challenged by future observations. Thanks to its ambitious concept of two vast observatories, one in the northern and one in the southern hemispheres, and to the employment of more than a hundred telescopes constituting the arrays, of small, medium and large size instruments, CTA is expected to reach an exceptional sensitivity in comparison with current state telescopes as shown in Figure 8.1.

The upcoming CTA observatories forecast numerous new detections of sources thanks to achieved better sensitivity, in depth morphology disentanglement of source emission regions thanks to their improved angular resolution and shall cover a wide energy range, from the GeV range up to hundreds of TeV, opening a new window in Astrophysics. These technological advancements will ensure more pulsar wind nebula detections in different environments, providing us with a variety of evolution habitats to study lepton transport and will enable to observe and extract sources from the central and denser regions of the Galactic plane.

I have had a small involvement in the calibration tasks of the H.E.S.S. large Cherenkov telescope and I have grasped the complexity behind the instrument challenges and the reconstruction ramifications of reliably relating the acquired information.

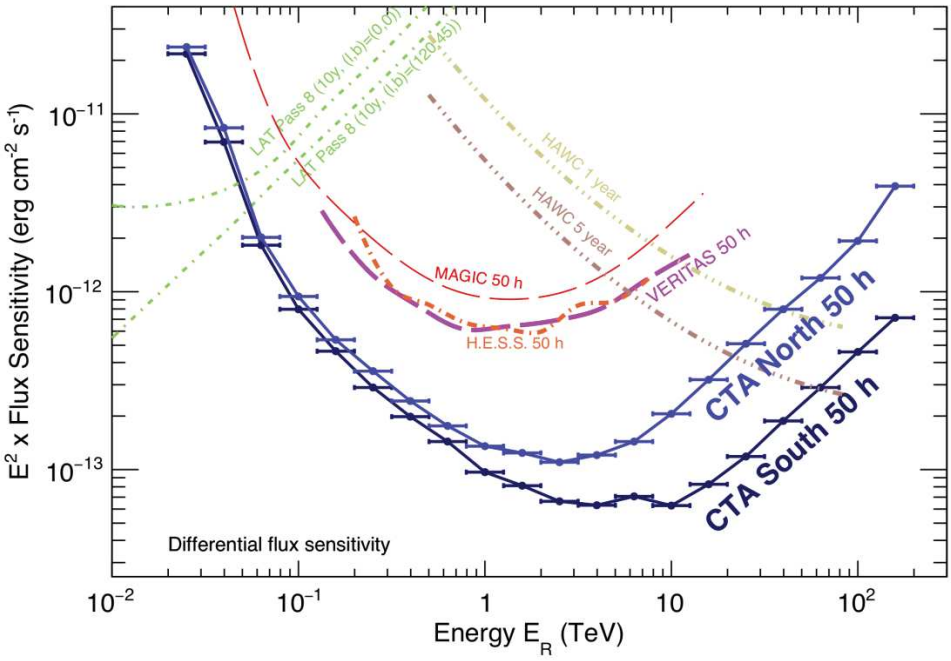

Figure 8.1 – Differential sensitivity for several gamma-ray ground based experiments (and the satellite Fermi-LAT) in comparison with the projected performance of the Cherenkov Telescope Array, in the south and north sites. It depicts the minimum flux per energy bin, required to be able to detect the emission from a point-like source at a 5σ level confidence, during an observation of the indicated duration. Using this indicative comparison between different instrument sensitivities, the CTA observatories are expected to reach unprecedented sensitivity. Figure taken from [35].

As we are waiting for the exciting science that future CTA observations will provide us, it is of the utmost importance to 1) understand the responses and limitations of the observing instruments, 2) consider adapted configurations for the analysis of an astrophysical source and estimate the significance of the extracted information, 3) model the phenomenology using the best physical constraints one may acquire from theoretical approaches. In my thesis work, I have had the opportunity to engage in different approaches that have permitted me to be introduced into the intricacies of observational and theoretical characterisation of pulsar wind nebulae, and to build the foundation for future exciting projects to understand their nature and evolution.

Energy is information.

Bibliography

[1] *Neutron Stars in Supernova Remnants*, volume 271 of *Astronomical Society of the Pacific Conference Series*, Jan 2002. 87

[2] A. A. Abdo, B. T. Allen, T. Aune, D. Berley, C. Chen, G. E. Christopher, T. Deyoung, B. L. Dingus, R. W. Ellsworth, M. M. Gonzalez, J. A. Goodman, E. Hays, C. M. Hoffman, P. H. Hüntemeyer, B. E. Kolterman, J. T. Linnemann, J. E. McEnery, T. Morgan, A. I. Mincer, P. Nemethy, J. Pretz, J. M. Ryan, P. M. Saz Parkinson, A. Shoup, G. Sinnis, A. J. Smith, V. Vasileiou, G. P. Walker, D. A. Williams, and G. B. Yodh. Milagro observations of multi-tev emission from galactic sources in the fermi bright source list. *Astrophysical Journal*, 700(2 PART 2):1–13, 2009. 87, 99

[3] K. Abe, H. Fuke, S. Haino, T. Hams, M. Hasegawa, A. Horikoshi, A. Itazaki, K. C. Kim, T. Kumazawa, A. Kusumoto, M. H. Lee, Y. Makida, S. Matsuda, Y. Matsukawa, K. Matsumoto, J. W. Mitchell, Z. Myers, J. Nishimura, M. Nozaki, R. Orito, J. F. Ormes, N. Picot-Clemente, K. Sakai, M. Sasaki, E. S. Seo, Y. Shikaze, R. Shinoda, R. E. Streitmatter, J. Suzuki, Y. Takasugi, K. Takeuchi, K. Tanaka, N. Thakur, T. Yamagami, A. Yamamoto, T. Yoshida, and K. Yoshimura. Measurements of Cosmic-Ray Proton and Helium Spectra from the BESS-Polar Long-duration Balloon Flights over Antarctica. *The Astrophysical Journal*, 822(2):65, May 2016. 28

[4] H. Akaike. A New Look at the Statistical Model Identification. *IEEE Transactions on Automatic Control*, 19:716–723, Jan 1974. 89

[5] Roberto Aloisio, Veniamin Berezinsky, Pasquale Blasi, Askhat Gazizov, Svetlana Grigorieva, and Bohdan Hnatyk. A dip in the UHECR spectrum and the transition from galactic to extragalactic cosmic rays. *Astroparticle Physics*, 27(1):76–91, Feb 2007. 56

[6] Hongjun An, Kristin K. Madsen, Stephen P. Reynolds, Victoria M. Kaspi, Fiona A. Harrison, Steven E. Boggs, Finn E. Christensen, William W. Craig, Chris L. Fryer, Brian W. Grefenstette, Charles J. Hailey, Kaya Mori, Daniel Stern, and William W. Zhang. High-energy X-ray imaging of the pulsar wind nebula MSH 15-52: Constraints on particle acceleration and transport. *Astrophysical Journal*, 793(2), 2014. 82

[7] Hongjun An, Kristin K. Madsen, Stephen P. Reynolds, Victoria M. Kaspi, Fiona A. Harrison, Steven E. Boggs, Finn E. Christensen, William W. Craig, Chris L. Fryer, Brian W. Grefenstette, Charles J. Hailey, Kaya Mori, Daniel Stern, and William W. Zhang. High-energy X-ray imaging of the pulsar wind nebula MSH 15-52: Constraints on particle acceleration and transport. *Astrophysical Journal*, 793(2), 2014. 107, 110

[8] K. A. Arnaud. XSPEC: The First Ten Years. In G. H. Jacoby and J. Barnes, editors, *Astronomical Data Analysis Software and Systems V*, volume 101 of *Astronomical Society of the Pacific Conference Series*, page 17, 1996. 86

[9] Z. Arzoumanian, D. F. Chernoff, and J. M. Cordes. The Velocity Distribution of Isolated Radio Pulsars. *ApJ*, 568(1):289–301, Mar 2002. 126, 127

[10] Maxim V. Barkov and Maxim Lyutikov. On the nature of radio filaments near the Galactic Centre. *MNRAS*, 489(1):L28–L31, Oct 2019. 128

[11] Gordon Baym, Christopher Pethick, and Peter Sutherland. The Ground State of Matter at High Densities: Equation of State and Stellar Models. *The Astrophysical Journal*, 170:299, Dec 1971. 20

[12] M. S. Bessell. UBVRI photometry II: the Cousins VRI system, its temperature and absolute flux calibration, and relevance for two-dimensional photometry. *Publications of the Astronomical Society of the Pacific*, 91:589–607, Oct 1979. 15

[13] John M Blondin, Roger a Chevalier, and Dargan M Frierson. Pulsar Wind Nebulae in Evolved Supernova Remnants. *The Astrophysical Journal*, 563(2):22, 2001. 132

[14] John M. Blondin, Eric B. Wright, Kazimierz J. Borkowski, and Stephen P. Reynolds. Transition to the Radiative Phase in Supernova Remnants. *The Astrophysical Journal*, 500(1):342–354, Jun 1998. 40

[15] D. L. Book. The sedov self-similar point blast solutions in nonuniform media. *Shock Waves*, 4(1):1–10, Jul 1994. 35

[16] P R Brook, A Karastergiou, and S Johnston. Linking long- and short-term emission variability in pulsars. *Monthly Notices of the Royal Astronomical Society*, 488(4):5702–5712, 07 2019. 22

[17] N. Bucciantini. Theory of pulsar wind nebulae. *AIP Conference Proceedings*, 983:186–194, 2008. 132

[18] D. Caprioli, P. Blasi, and E. Amato. Non-linear diffusive acceleration of heavy nuclei in supernova remnant shocks. *Astroparticle Physics*, 34(6):447–456, Jan 2011. 56

[19] Benoît Cerutti, Alexander Philippov, Kyle Parfrey, and Anatoly Spitkovsky. Particle acceleration in axisymmetric pulsar current sheets. *Monthly Notices of the Royal Astronomical Society*, 448(1):606–619, Mar 2015. 29

[20] R. A. Chevalier. The interaction of supernovae with the interstellar medium. *Annual Review of Astronomy and Astrophysics*, 15:175–196, Jan 1977. 34

[21] R. A. Chevalier and C. Fransson. Pulsar nebulae in supernovae. *The Astrophysical Journal*, 395:540–552, aug 1992. 34

[22] Roger A. Chevalier. Supernova Remnants in Molecular Clouds. *The Astrophysical Journal*, 511(2):798–811, Feb 1999. 55

[23] FERMI Collaboration. Detection of the energetic pulsar PSR B1509-58 and its pulsar wind nebula in MSH 15-52 using the Fermi-large area telescope. *Astrophysical Journal*, 714(1):927–936, 2010. 82, 110

[24] Fermi Collaboration. 2FHL: The Second Catalog of Hard Fermi-LAT Sources. *ApJ*, 222(1):5, Jan 2016. 84, 116

[25] FERMI Collaboration. Search for extended sources in the galactic plane using 6 years of FERMI-Large Area Telescope PASS 8 data above 10 GeV. pages 1–28, 2017. 110

[26] H. E. S. S. Collaboration. The H.E.S.S. Survey of the Inner Galaxy in Very High Energy Gamma Rays. *ApJ*, 636(2):777–797, Jan 2006. 123, 124

[27] H. E. S. S. Collaboration. Discovery of the source HESS J1356-645 associated with the young and energetic PSR J1357-6429. *A&A*, 533:A103, Sep 2011. 123

[28] H. E. S. S. Collaboration. Particle Transport within the Pulsar Wind Nebula HESS J1825-137. 2018. 122

[29] H.E.S.S. Collaboration. Calibration of cameras of the H.E.S.S. detector. *Astroparticle Physics*, 22:109–125, nov 2004. 73, 74

[30] H.E.S.S. Collaboration. Discovery of extended VHE gamma-ray emission from the asymmetric pulsar wind nebula in MSH 15-52 with HESS. *A&A*, 435(1):L17–L20, May 2005. 82, 87, 91, 102, 104, 108, 140

[31] H.E.S.S. Collaboration. H.E.S.S. and Suzaku observations of the Vela X pulsar wind nebula. (arXiv:1905.07975v1 [astro-ph.HE]). *arXiv High Energy Astrophysical Phenomena*, 45, 2019. 124

[32] NuSTAR collaboration. The Nuclear Spectroscopic Telescope Array (NuSTAR) High-energy X-Ray Mission. *ApJ*, 770(2):103, Jun 2013. 102

[33] Suzaku collaboration. The X-Ray Observatory Suzaku. *PASJ*, 59:S1–S7, Jan 2007. 102

[34] E. D. Courant and H. S. Snyder. Theory of the alternating-gradient synchrotron. *Annals of Physics*, 3(1):1–48, Jan 1958. 43

[35] CTA Consortium and Rene A. Ong. The Cherenkov Telescope Array Science Goals and Current Status. In *European Physical Journal Web of Conferences*, volume 209 of *European Physical Journal Web of Conferences*, page 01038, Sep 2019. 144

[36] Ocker C. de Jager and Arache Djannati-Ataï. Implications of HESS Observations of Pulsar Wind Nebulae. In Werner Becker, editor, *Astrophysics and Space Science Library*, volume 357 of *Astrophysics and Space Science Library*, page 451, Jan 2009. 90

[37] Mathieu de Naurois. *Very High Energy astronomy from H.E.S.S. to CTA. Opening of a new astronomical window on the non-thermal Universe*. Habilitation à diriger des recherches, Université Pierre et Marie Curie - Paris VI, 2012. 74, 80, 82

[38] Mathieu de Naurois and Loïc Rolland. A high performance likelihood reconstruction of γ-rays for imaging atmospheric Cherenkov telescopes. *Astroparticle Physics*, 32(5):231–252, Dec 2009. 79

[39] Gerard de Vaucouleurs. Recherches sur les Nebuleuses Extragalactiques. *Annales d'Astrophysique*, 11:247, Jan 1948. 89

[40] L. Del Zanna, E. Amato, and N. Bucciantini. Axially symmetric relativistic MHD simulations of Pulsar Wind Nebulae in Supernova Remnants. *Astronomy and Astrophysics*, 421(3):1063–1073, 2004. 35, 132, 134, 135

[41] T. Delahaye, R. Lineros, F. Donato, N. Fornengo, J. Lavalle, P. Salati, and R. Taillet. Galactic secondary positron flux at the Earth. *Astronomy and Astrophysics*, 501(3):821–833, Jul 2009. 28

[42] Camilia Demidem, Martin Lemoine, and Fabien Casse. Relativistic magnetohydrodynamical simulations of the resonant corrugation of a fast shock front. *Monthly Notices of the Royal Astronomical Society*, 475(2):2713–2723, Apr 2018. 29

[43] MATTIA DI MAURO, SILVIA MANCONI, and FIORENZA DONATO. Detection of a gamma-ray halo around Geminga with the Fermi-LAT and implications for the positron flux. In *AAS/High Energy Astrophysics Division*, AAS/High Energy Astrophysics Division, page 112.35, Mar 2019. 28

[44] A. Donath, C. Deil, M. Paz Arribas, J. King, E. Owen, R. Terrier, I. Reichardt, J. Harris, R. Buehler, and S. Klepser. Gammapy: An open-source Python package for gamma-ray astronomy. In *34th International Cosmic Ray Conference (ICRC2015)*, volume 34 of *International Cosmic Ray Conference*, page 789, Jul 2015. 85

[45] I. Du Plessis, O. C. de Jager, S. Buchner, H. I. Nel, A. R. North, B. C. Raubenheimer, and D. J. van der Walt. The Nonthermal Radio, X-Ray, and TeV Gamma-Ray Spectra of MSH 15-52. *ApJ*, 453:746, Nov 1995. 82

[46] G. M. Dubner, B. M. Gaensler, E. B. Giacani, W. M. Goss, and A. J. Green. The Interstellar Medium around the Supernova Remnant G320.4-1.2. *AJ*, 123(1):337–345, Jan 2002. 82, 102, 105

[47] Claude André Faucher-Giguère and Victoria M. Kaspi. Birth and evolution of isolated radio pulsars. *AIP Conference Proceedings*, 983(1997):607–609, 2008. 26

[48] Fermi-LAT Collaboration. Fermi Large Area Telescope Third Source Catalog. *ApJ*, 218(2):23, Jun 2015. 84, 116

[49] Alexei V. Filippenko. Optical Spectra of Supernovae. *Annual Review of Astronomy and Astrophysics*, 35:309–355, Jan 1997. 17

[50] P. Freeman, S. Doe, and A. Siemiginowska. Sherpa: a mission-independent data analysis application. In J.-L. Starck and F. D. Murtagh, editors, *Astronomical Data Analysis*, volume 4477, pages 76–87, nov 2001. 85

[51] H. T. Freudenreich. A COBE Model of the Galactic Bar and Disk. *The Astrophysical Journal*, 492(2):495–510, Jan 1998. 54

[52] B. M. Gaensler, K. T. S. Brazier, R. N. Manchester, S. Johnston, and A. J. Green. SNR G320.4-01.2 and PSR B1509-58: new radio observations of a complex interacting system. *Monthly Notices of the Royal Astronomical Society*, 305(3):724–736, May 1999. 106, 107

[53] Bryan M. Gaensler and Patrick O. Slane. The Evolution and Structure of Pulsar Wind Nebulae. *Annual Review of Astronomy and Astrophysics*, 44(1):17–47, 2006. 128

[54] Gordon P. Garmire, Mark W. Bautz, Peter G. Ford, John A. Nousek, and Jr. Ricker, George R. Advanced CCD imaging spectrometer (ACIS) instrument on the Chandra X-ray Observatory. In Joachim E. Truemper and Harvey D. Tananbaum, editors, *SPIE*, volume 4851 of *Society of Photo-Optical Instrumentation Engineers (SPIE) Conference Series*, pages 28–44, Mar 2003. 102

[55] G. Giacinti and R. Lopez-Coto. Constraining the Properties of the Interstellar Turbulence around Geminga using HAWC Measurements. In *36th International Cosmic Ray Conference (ICRC2019)*, volume 36 of *International Cosmic Ray Conference*, page 685, Jul 2019. 28

[56] G. Giacinti, A. M. W. Mitchell, R. López-Coto, V. Joshi, R. D. Parsons, and J. A. Hinton. On the TeV Halo Fraction in gamma-ray bright Pulsar Wind Nebulae. pages 1–10, 2019. 105

[57] Claire Guépin, Lucia Rinchiuso, Kumiko Kotera, Emmanuel Moulin, Tanguy Pierog, and Joseph Silk. Pevatron at the Galactic Center: multi-wavelength signatures from millisecond pulsars. *Journal of Cosmology and Astro-Particle Physics*, 2018(7):042, Jul 2018. 27

[58] H. E. S. S. Collaboration. Identification of HESS J1303-631 as a pulsar wind nebula through γ-ray, X-ray, and radio observations. *A&A*, 548:A46, Dec 2012. 122, 123

[59] H. E. S. S. Collaboration. The H.E.S.S. Galactic plane survey. *A&A*, 612:A1, Apr 2018. 82, 84, 85, 96, 102, 115, 140, 154

[60] A. Heger, C. L. Fryer, S. E. Woosley, N. Langer, and D. H. Hartmann. How Massive Single Stars End Their Life. *The Astrophysical Journal*, 591(1):288–300, Jul 2003. 17

[61] J. Jeff Hester, Paul A. Scowen, Ravi Sankrit, Christopher J. Burrows, III Gallagher, John S., Jon A. Holtzman, Alan Watson, John T. Trauger, Gilda E. Ballester, Stefano Casertano, John T. Clarke, David Crisp, Robin W. Evans, Richard E. Griffiths, John G. Hoessel, John Krist, Roger Lynds, Jeremy R. Mould, Jr. O'Neil, Earl J., Karl R. Stapelfeldt, and James A. Westphal. WFPC2 Studies of the Crab Nebula. I. HST and ROSAT Imaging of the Synchrotron Nebula. *ApJ*, 448:240, Jul 1995. 128

[62] Jeff Hester. The Structure, Polarization, and Evolution of the Crab Synchrotron Nebula. HST Proposal, Jul 1995. 128

[63] A. Hewish, S. J. Bell, J. D. H. Pilkington, P. F. Scott, and R. A. Collins. Observation of a Rapidly Pulsating Radio Source. *Nature*, 217(5130):709–713, Feb 1968. 20

[64] W. Hillebrandt, K. Nomoto, and R. G. Wolff. Supernova explosions of massive stars - The mass range 8 to 10 solar masses. *A&A*, 133:175–184, apr 1984. 17

[65] Jr. Iben, Icko. Stellar Evolution. II. The Evolution of a 3 M_{sun} Star from the Main Sequence Through Core Helium Burning. *The Astrophysical Journal*, 142:1447, Nov 1965. 15

[66] Jr. Iben, Icko. Stellar Evolution. III. The Evolution of a 5 M_{sun} Star from the Main Sequence Through Core Helium Burning. *The Astrophysical Journal*, 143:483, Feb 1966. 15

[67] Jr. Iben, Icko. Stellar Evolution.IV. The Evolution of a 9 M_{sun} Star from the Main Sequence Through Core Helium Burning. *The Astrophysical Journal*, 143:505, Feb 1966. 15

[68] F. Jansen, D. Lumb, B. Altieri, J. Clavel, M. Ehle, C. Erd, C. Gabriel, M. Guainazzi, P. Gondoin, R. Much, R. Munoz, M. Santos, N. Schartel, D. Texier, and G. Vacanti. XMM-Newton observatory. I. The spacecraft and operations. *A&A*, 365:L1–L6, Jan 2001. 102

[69] Simon Johnston and A. Karastergiou. Pulsar braking and the P-dot{P} diagram. *Monthly Notices of the Royal Astronomical Society*, 467(3):3493–3499, May 2017. 22

[70] Byung-Il Jun. Interaction of a Pulsar Wind with the Expanding Supernova Remnant. *The Astrophysical Journal*, 499(1):282–293, May 1998. 39

[71] E. Kafexhiu, F. Aharonian, A. M. Taylor, and G. S. Vila. Parametrization of gamma-ray production cross sections for p p interactions in a broad proton energy range from the kinematic threshold to PeV energies. *PRD*, 90(12):123014, dec 2014. 108

[72] R. Keppens, Z. Meliani, A. J. van Marle, P. Delmont, A. Vlasis, and B. van der Holst. Parallel, grid-adaptive approaches for relativistic hydro and magnetohydrodynamics. *Journal of Computational Physics*, 231(3):718–744, Feb 2012. 133

[73] R. Keppens, M. Nool, G. Tóth, and J. P. Goedbloed. Adaptive Mesh Refinement for conservative systems: multi-dimensional efficiency evaluation. *Computer Physics Communications*, 153(3):317–339, Jul 2003. 133

[74] Matthieu Kieffer. *Recherche indirecte de matière noire avec l'expérience H.E.S.S.* Theses, Université Pierre et Marie Curie - Paris VI, September 2015. 69

[75] S. S. Komissarov and Y. E. Lyubarsky. Synchrotron nebulae created by anisotropic magnetized pulsar winds. *Monthly Notices of the Royal Astronomical Society*, 349(3):779–792, 2004. 127

[76] U. S. Kushwara. Ionisation Loss of Electrons at High Energies. In *Cosmic Rays, Elementary Particle Physics and Astrophysics*, pages 664–669, Jan 1966. 65

[77] Jeffrey Lagarias, James A. Reeds, Margaret H. Wright, and Paul Wright. Convergence properties of the nelder-mead simplex algorithm in low dimensions. ., 12 1997. 85

[78] M. I. Large, B. Y. Mills, A. G. Little, D. F. Crawford, and J. M. Sutton. The Molonglo Reference Catalogue of radio sources. *MNRAS*, 194:693–704, Feb 1981. 102

[79] C. J. Leliveld, J. G. Maas, V. R. Bom, and C. W. E. van Eijk. Monte Carlo modeling of coherent scattering: influence of interference. *IEEE Transactions on Nuclear Science*, 43(6):3315–3321, Dec 1996. 65

[80] Martin Lemoine. A corrugated termination shock in pulsar wind nebulae? *Journal of Plasma Physics*, 82(4):635820401, Aug 2016. 29

[81] T. P. Li and Y. Q. Ma. Analysis methods for results in gamma-ray astronomy. *ApJ*, 272:317–324, Sep 1983. 85, 100

[82] Maxim Lyutikov. A high-sigma model of pulsar wind nebulae. *Monthly Notices of the Royal Astronomical Society*, 405(3):1809–1815, Jul 2010. 29

[83] Rainald Löhner. Mesh adaptation in fluid mechanics. *Engineering Fracture Mechanics*, 50(5):819 – 847, 1995. 133

[84] R. N. Manchester, G. B. Hobbs, A. Teoh, and M. Hobbs. The Australia Telescope National Facility Pulsar Catalogue. *The Astronomical Journal*, 129(4):1993–2006, Apr 2005. 23, 24, 26, 107, 118, 126

[85] R. N. Manchester, I. R. Tuohy, and N. Damico. Discovery of radio pulsations from the X-ray pulsar in the supernova remnant G 320.4-1.2. *ApJ*, 262:L31–L33, Nov 1982. 82

[86] V. Marandon, A. Djannati-Atai, R. Terrier, G. Puehlhofer, D. Hauser, S. Schwarzburg, and D. Horns. A closer look at HESS J1837-069 following the pulsar discovery. In Felix A. Aharonian, Werner Hofmann, and Frank Rieger, editors, *American Institute of Physics Conference Series*, volume 1085, pages 320–323, Dec 2008. 123

[87] J. Matthews. A Heitler model of extensive air showers. *Astroparticle Physics*, 22(5-6):387–397, Jan 2005. 64

[88] American Optical. Micromanipulator. *Journal of Scientific Instruments*, 33(2):87–87, Feb 1956. 70

[89] E. Parizot, A. Marcowith, J. Ballet, and Y. A. Gallant. Observational constraints on energetic particle diffusion in young supernovae remnants: amplified magnetic field and maximum energy. *Astronomy and Astrophysics*, 453(2):387–395, Jul 2006. 56

[90] R. D. Parsons and J. A. Hinton. A Monte Carlo template based analysis for air-Cherenkov arrays. *Astroparticle Physics*, 56:26–34, Apr 2014. 80

[91] A. A. Penzias and R. W. Wilson. A Measurement of Excess Antenna Temperature at 4080 Mc/s. *The Astrophysical Journal*, 142:419–421, Jul 1965. 52

[92] J. Pétri and Y. Lyubarsky. Magnetic reconnection at the termination shock in a striped pulsar wind. *Astronomy and Astrophysics*, 473(3):683–700, Oct 2007. 29

[93] Planck Collaboration. Planck 2018 results. I. Overview and the cosmological legacy of Planck. *arXiv e-prints*, page arXiv:1807.06205, Jul 2018. 52

[94] H E S S Galactic Plane, H E S S Collaboration, H Abdalla, A Abramowski, F Aharonian, F Ait Benkhali, A G Akhperjanian, and T Andersson. Astrophysics Special issue The population of TeV pulsar wind nebulae. 2:1–25, 2018. 118, 120, 154

[95] C. C. Popescu, R. Yang, R. J. Tuffs, G. Natale, M. Rushton, and F. Aharonian. A radiation transfer model for the Milky Way: I. Radiation fields and application to high-energy astrophysics. *Monthly Notices of the Royal Astronomical Society*, 470(3):2539–2558, Sep 2017. 53, 54, 106, 121

[96] Troy A. Porter, Guolaugur Jóhannesson, and Igor V. Moskalenko. High-Energy γ-rays from the Milky Way: Three-dimensional spatial models for the cosmic-ray and radiation field densities. *Proceedings of Science*, 846(1):67, 2017. 54, 106, 121

[97] O. Porth, C. Xia, T. Hendrix, S. P. Moschou, and R. Keppens. *MPI-amrvac for solar and astrophysics*, volume 214. 2014. 133

[98] William H. Press, Saul A. Teukolsky, William T. Vetterling, and Brian P. Flannery. *Numerical recipes in C++ : the art of scientific computing*. Cambridge University Press, 2002. 100

[99] Leif Radel. *Simulation Studies of the Cherenkov Light Yield from Relativistic Particles in High Energy Neutrino Telescopes with Geant4.* PhD thesis, Fakultat fur Mathematik, Informatik und Naturwissenschaffen, Rheinish-Westfalischen Tchnischen Hochschule Aachen, 2012. 66

[100] Rayleigh. Investigation of the character of the equilibrium of an incompressible heavy fluid of variable density. *Proceedings of the London Mathematical Society*, s1-14(1):170–177, 1882. 31

[101] Lord Rayleigh. On the Dynamics of Revolving Fluids. *Proceedings of the Royal Society of London Series A*, 93(648):148–154, Mar 1917. 31

[102] M. Renaud, P. Goret, and R. C. G. Chaves. On the nature of HESS J1503-582 revealed by the H.E.S.S. experiment: Coincidence with a FVW? In Felix A. Aharonian, Werner Hofmann, and Frank Rieger, editors, *American Institute of Physics Conference Series*, volume 1085 of *American Institute of Physics Conference Series*, pages 281–284, Dec 2008. 84

[103] Stephen P. Reynolds. Synchrotron-Loss Spectral Breaks in Pulsar-Wind Nebulae and Extragalactic Jets. *ApJ*, 703(1):662–670, Sep 2009. 105

[104] Stephen P. Reynolds and Kazimierz J. Borkowski. A Compact X-Ray Source in the Radio Pulsar-wind Nebula G141.2+5.0. *The Astrophysical Journal*, 816(2):L27, Jan 2016. 46

[105] Stephen P. Reynolds, B. M. Gaensler, and Fabrizio Bocchino. Magnetic fields in supernova remnants and pulsar-wind nebulae. *Space Science Reviews*, 166(1-4):231–261, 2012. 128

[106] G. Richards and VERITAS Collaboration. Recent pulsar results from VERITAS on Geminga and the missing link binary pulsar PSR J1023+0038. In *34th International Cosmic Ray Conference (ICRC2015)*, volume 34 of *International Cosmic Ray Conference*, page 869, Jul 2015. 28

[107] Jane Roberg and L. W. Nordheim. The Angular and Lateral Spread of Cosmic-Ray Showers. *Physical Review*, 75(3):444–457, Feb 1949. 65

[108] T. P. Robitaille, E. Churchwell, R. A. Benjamin, B. A. Whitney, K. Wood, B. L. Babler, and M. R. Meade. A self-consistent model of Galactic stellar and dust infrared emission and the abundance of polycyclic aromatic hydrocarbons. *Astronomy and Astrophysics*, 545:A39, Sep 2012. 54

[109] Bruno Rossi and Kenneth Greisen. Cosmic-Ray Theory. *Reviews of Modern Physics*, 13(4):240–309, Oct 1941. 65

[110] Edwin E. Salpeter. The Luminosity Function and Stellar Evolution. *The Astrophysical Journal*, 121:161, Jan 1955. 15

[111] L. I. Sedov. *Similarity and Dimensional Methods in Mechanics*. ., 1959. 39

[112] J. L. Sérsic. Influence of the atmospheric and instrumental dispersion on the brightness distribution in a galaxy. *Boletin de la Asociacion Argentina de Astronomia La Plata Argentina*, 6:41, 1963. 89

[113] F. Seward, R. Smith, J. Hagler, L. Portolese, T. Gaetz, P. Slane, B. C. Koo, and J. J. Lee. The Chandra Supernova Remnant Catalog. In Fernando Camilo and Bryan M. Gaensler, editors, *Young Neutron Stars and Their Environments*, volume 218 of *IAU Symposium*, page 93, Jan 2004. 86

[114] Lorenzo Sironi and Anatoly Spitkovsky. Relativistic Reconnection: An Efficient Source of Non-thermal Particles. *The Astrophysical Journal*, 783(1):L21, Mar 2014. 29

[115] Stephen J. Smartt. Progenitors of Core-Collapse Supernovae. *Annual Review of Astronomy and Astrophysics*, 47(1):63–106, Sep 2009. 18

[116] Anatoly Spitkovsky. Time-dependent Force-free Pulsar Magnetospheres: Axisymmetric and Oblique Rotators. *The Astrophysical Journal*, 648(1):L51–L54, Sep 2006. 21, 29

[117] Shuta J. Tanaka, Kenji Toma, and Nozomu Tominaga. Confinement of the Crab Nebula with tangled magnetic field by its supernova remnant. *MNRAS*, 478(4):4622–4633, Aug 2018. 128

[118] Geoffrey Ingram Taylor. The instability of liquid surfaces when accelerated in a direction perpendicular to their planes. i. *Proceedings of the Royal Society of London. Series A. Mathematical and Physical Sciences*, 201(1065):192–196, 1950. 31

[119] A. Tchekhovskoy, A. Spitkovsky, and J. G. Li. Time-dependent 3D magnetohydrodynamic pulsar magnetospheres: oblique rotators. *Monthly Notices of the Royal Astronomical Society*, 435:L1–L5, Aug 2013. 29

[120] Tea Temim, Patrick Slane, Christopher Kolb, John Blondin, John P Hughes, and Niccoló Bucciantini. {LATE}-{TIME} {EVOLUTION} {OF} {COMPOSITE} {SUPERNOVA} {REMNANTS}: {DEEPCHANDRAOBSERVATIONS} {AND} {HYDRODYNAMICAL} {MODELING} {OF} A {CRUSHED} {PULSAR} {WIND} {NEBULA} {IN} {SNR} G327.1-1.1. *The Astrophysical Journal*, 808(1):100, 2015. 132

[121] Tea Temim, Patrick Slane, Paul P. Plucinsky, Joseph Gelfand, Daniel Castro, and Christopher Kolb. Proper Motion of the High-Velocity Pulsar in SNR MSH 15-56. 2017. 132

[122] Regis Terrier. Spectral and spatial characteristics of the Kookaburra's northern wing. XMM-Newton Proposal, Oct 2008. 46

[123] Gábor Tóth. The LASY Preprocessor and Its Application to General Multidimensional Codes. *Journal of Computational Physics*, 138(2):981–990, Dec 1997. 133

[124] J. Kelly Truelove and Christopher F. McKee. Evolution of Nonradiative Supernova Remnants. *The Astrophysical Journal Supplement Series*, 120(2):299–326, 1999. 33, 35, 36, 38

[125] M. Tsirou, Y. A. Gallant, R. Terrier, R. Zanin, and H. E. S. S. Collaboration. Study of the Very High Energy emission of the Pulsar Wind Nebula in MSH 15-5 2. In *5th Annual Conference on High Energy Astrophysics in Southern Africa*, page 23, Oct 2017. 141

[126] S. van den Bergh. A systematic search for galactic supernova remnants. *ApJ*, 38:119–128, Oct 1978. 82

[127] B. van der Holst and R. Keppens. Hybrid block-AMR in cartesian and curvilinear coordinates: MHD applications. *Journal of Computational Physics*, 226(1):925–946, Sep 2007. 133

[128] B. van der Holst, R. Keppens, and Z. Meliani. A multidimensional grid-adaptive relativistic magnetofluid code. *Computer Physics Communications*, 179(9):617–627, Nov 2008. 133

[129] E. van der Swaluw, A. Achterberg, Y. A. Gallant, and G. Tóth. Pulsar wind nebulae in supernova remnants. Spherically symmetric hydrodynamical simulations. *Astronomy and Astrophysics*, 380:309–317, Dec 2001. 31, 39, 132, 134, 135

[130] P. A. Čerenkov. Visible Radiation Produced by Electrons Moving in a Medium with Velocities Exceeding that of Light. *Physical Review*, 52(4):378–379, Aug 1937. 66

[131] F. J. Voisin, G. P. Rowell, M. G. Burton, Y. Fukui, H. Sano, F. Aharonian, N. Maxted, C. Braiding, R. Blackwell, and J. Lau. Connecting the ISM to TeV PWNe and PWN candidates. *Publications of the Astronomical Society of Australia*, 2019. 27

[132] S. P. Wakely and D. Horan. TeVCat: An online catalog for Very High Energy Gamma-Ray Astronomy. *International Cosmic Ray Conference*, 3:1341–1344, 2008. 115, 117

[133] Joseph C. Weingartner and B. T. Draine. Dust Grain-Size Distributions and Extinction in the Milky Way, Large Magellanic Cloud, and Small Magellanic Cloud. *The Astrophysical Journal*, 548(1):296–309, Feb 2001. 54

[134] F. Werner, C. Bauer, S. Bernhard, M. Capasso, S. Diebold, F. Eisenkolb, S. Eschbach, D. Florin, C. Föhr, S. Funk, A. Gadola, F. Garrecht, G. Hermann, I. Jung, O. Kalekin, C. Kalkuhl, J. Kasperek, T. Kihm, R. Lahmann, A. Marszalek, M. Pfeifer, G. Principe, G. Pühlhofer, S. Pürckhauer, P. J. Rajda, O. Reimer, A. Santangelo, T. Schanz, T. Schwab, S. Steiner, U. Straumann, C. Tenzer, A. Vollhardt, D. Wolf, K. Zietara, and CTA Consortium. Performance verification of the FlashCam prototype camera for the Cherenkov Telescope Array. *Nuclear Instruments and Methods in Physics Research A*, 876:31–34, Dec 2017. 79

[135] C. Winkler, T. J. L. Courvoisier, G. Di Cocco, N. Gehrels, A. Giménez, S. Grebenev, W. Hermsen, J. M. Mas-Hesse, F. Lebrun, N. Lund, G. G. C. Palumbo, J. Paul, J. P. Roques, H. Schnopper, V. Schönfelder, R. Sunyaev, B. Teegarden, P. Ubertini, G. Vedrenne, and A. J. Dean. The INTEGRAL mission. *A&A*, 411:L1–L6, Nov 2003. 102

[136] S. E. Woosley, A. Heger, and T. A. Weaver. The evolution and explosion of massive stars. *Reviews of Modern Physics*, 74(4):1015–1071, Nov 2002. 17

[137] C. Xia, J. Teunissen, I. El Mellah, E. Chané, and R. Keppens. MPI-AMRVAC 2.0 for Solar and Astrophysical Applications. *The Astrophysical Journal Supplement Series*, 234(2):30, 2018. 133

[138] J. M. Yao, R. N. Manchester, and N. Wang. Determination of the Sun's Offset from the Galactic Plane Using Pulsars. 6(April):1–6, 2017. 107

[139] Y. Yatsu, J. Kataoka, N. Kawai, K. Tamura, and W. Brinkmann. Chandra observation of the interaction between the plasma nebula RCW89 and the pulsar jet of PSR B1509-58. *Advances in Space Research*, 35(6):1066–1069, 2005. 86

[140] V. Zabalza. naima: a python package for inference of relativistic particle energy distributions from observed nonthermal spectra. *Proc. of International Cosmic Ray Conference 2015*, page 922, 2015. 45, 107

[141] Justus Zorn and H. E. S. S. Collaboration. Sensitivity Improvements of Very-High-Energy Gamma-Ray Detection with the Upgraded H.E.S.S. I Cameras using Full Waveform Processing. *Proceedings of Science*, pages 1–11, 2019. 71

Chapter 9

Appendices

In Section 9.2 one may find the H.E.S.S. Galactic Plane Survey [59] maps and the offset population of PWNe showing an offset with the pulsar as reported in [94].

I also add as a reference the available computed by C. Evoli all-particle cosmic-ray spectrum that I borrow in Figure 3.10. I have never met him, but I am very grateful for him sharing his meticulous work with the community. The references of his laborious work and the spectrum graph, may be found on the following website URL : Evoli

9.1 Thesis summary (French version)

As required by the doctorate school I2S rules, I provide a summary of my thesis work in French. It consists of a brief recounting of the methods and main results discussed in the English corpus of the dissertation, but in the beautiful native language of *Baudelaire* instead, and the butchering literary style of a sleep-deprived foreign student.

Voici le résumé en français des activités et des résultats principaux obtenus pendant ma thèse, présentés dans ce manuscrit.

Résumé

Lors de mes travaux de préparation de thèse, mes activités se sont concentrées sur l'étude de nébuleuses de pulsars en rayons gamma, avec une approche phénoménologique et théorique de systèmes astrophysiques de très hautes énergies.

Les nébuleuses de pulsars consistent à des nuages de particules magnétisés se formant autour d'une étoile à neutron à rotation rapide (pulsar). Elles sont composées majoritairement d'électrons et de positrons, qui sont accélérés à des régimes relativistes par l'action du pulsar central, au sein d'un vestige de supernova. De plus, les nébuleuses de pulsars sont la classe de sources galactiques avec le plus grand nombres de détections confirmées dans le domaine des rayons gamma de très hautes énergies cataloguées dans le relevé du plan galactique de H.E.S.S., ce qui les établie en tant qu'excellents laboratoires astrophysiques pour l'étude de processus de rayonnement. De plus, les nébuleuses de pulsars sont des sources potentielles de rayons cosmiques leptoniques et figurent parmi les candidats les plus plausibles pour être à l'origine de l'excès de positons cosmiques mesurés aux hautes énergies.

Pendant ma thèse, je me suis focalisée sur la caractérisation de l'asymétrie de l'émission gamma de très hautes énergies (au-delà de 0.3 TeV) observée par le réseau de télescopes Cherenkov H.E.S.S.. (de l'anglais *High Energy Stereoscopic System*) concernant plusieurs nébuleuses. J'ai analysé, guidée par mon directeur de thèse Dr Y. Gallant et en collaboration avec d'autres membres du groupe H.E.S.S. , des données de la phase I de H.E.S.S. (HESS-I), c'est-à-dire des observations qui précèdent l'ajout d'un cinquième télescope Cherenkov de grande taille (CT5) dans le réseau de quatre télescopes de taille moyenne (CT1). Ces données prises de façon stéréoscopique par les télescopes du réseau, ont été reconstruite en énergie et en direction pour obtenir des cartes du ciel vue en rayons gamma correspondant à l'émission de la source observée. La résolution angulaire de H.E.S.S. ., étant parmi les meilleures des observatoires de rayons gamma au sol utilisant des techniques d'imagerie Cherenkov, actuellement, permet de mener des analyses morphologiques de haute qualité. Ainsi, nous nous sommes focalisés sur la nébuleuse de pulsar dans le vestige de supernova composite MSH 15-*52* , pour mener plusieurs analyses spectrales et morphologiques.

Le vestige de supernova nommé MSH 15-*52* est vue, partiellement dans le domaine radio et montre une morphologie semblable à la forme d'un "tonneau". Seul deux extrémités de sa coquille sont détectées, dont celle située au nord-ouest jointe à la région Hα RCW 89. Au sein du vestige, se trouve le pulsar énergétique B1509-58, âgé de $\sim$ 1560 ans d'après son temps caractéristique, et émettant fortement en radio, rayons X et rayons gamma de hautes énergies. La nébuleuse de pulsar émet aussi en radio et en X, et est aussi connue sous divers surnoms en

tant que la "main cosmique" liés à son apparence réminiscente de la paume et des doigts d'une main humaine.

Pour mieux dépeindre la forme de l'émission vue en gamma de la source MSH 15-52 , nous avons utilisé des observations d'archives *Chandra*, constituant l'émission de la nébuleuse de pulsar en rayon X de 4 à 7 keV afin de tracer spatialement la population d'électrons et de positons émettant dans le domaine des rayons X via rayonnement synchrotron. Nous avons opté pour cet ajustement basé sur les cartes de l'émission synchrotron car elles fournissent l'information spatiale sur le champ magnétique, à condition de tracer l'émission non-thermique vue en rayons X. Cette population de leptons correspond a priori, spatialement à la population qui par diffusion Compton inverse sur des photons ambiants engendrera l'émission observée dans le domaine du TeV.

En seconde approche, nous avons aussi analysé la dépendance en énergie de l'émission gamma en ajustant la forme de l'émission dans plusieurs bandes en énergie, choisies afin d'assurer des échantillons statistiquement adéquats. Nous avons par la suite utilisé nos résultats de nos analyses spectrales et morphologiques afin de modéliser l'émission de la nébuleuse de pulsar MSH 15-52 .

Un de nos résultats consiste à la mise en évidence de la non-linéarité de la dépendance du champ magnétique B dans la nébuleuse avec la distance R, obtenue en introduisant un paramètre dans notre modèle utilisant la carte synchrotron en tant que motif spatial, visant à caractériser cette dépendance en tant que : $B \propto R^{\delta}$. Dans cette approximation, $\delta = -\frac{\alpha}{\beta}$ composé de l'indice β relié aux distributions en loi de puissance des spectres d' électrons et de photons synchrotron, et de l'indice α étant le paramètre ajustable de notre modèle qui relie le flux en rayons gamma produit par Compton inverse Φ_{IC} et le flux de rayons X produit par effet synchrotron Φ_{sync} de sorte que : $\Phi_{IC} \propto \Phi_{sync}^{\alpha}$. Ce paramètre α traduit ainsi la linéarité de la carte du rayonnement synchrotron avec la carte de photons produit par IC. Nous trouvons un indice α d'environ 1.3, ce qui pointe vers la non-linéarité du champ magnétique par rapport à la distance au pulsar. Cependant, notre hypothèse initiale sur l'isotropie du champ magnétique est une hypothèse forte et nous ne pouvons pas en conclure au-delà de stipulation de scénarios considérant un champ magnétique plus faible au sein des régions externes de la nébuleuse de pulsar.

De plus, nous trouvons que le meilleur modèle pour décrire l'émission gamma, comporte à la fois la carte synchrotron utilisant notre approximation sur le champ magnétique mais aussi une composante géométrique supplémentaire. Nous mettons en avant une émission étendue en rayons gamma, comportant $\sim$ 70 % du flux total, située à $\sim$ 9 pc au sud-est de la position du pulsar et non complètement corrélée spatialement avec l'étendue de l'émission en rayons X. Nous stipulons plusieurs scénarios concernant son interprétation en considérant les propriétés du système, liées à l'âge jeune et à la puissance considérable du pulsar, la densité du milieu qui est plus élevée au nord (~ 5 cm^{-3}) à celle estimée au sud (~ 0.01 cm^{-3}) et aux pertes radiatives.

Nous poursuivons avec une analyse poussée pour explorer la dépendance en énergie de l'émission gamma de MSH 15-52 . Nous obtenons que la morphologie de la nébuleuse de pulsar se rétrécit à plus hautes énergies et se concentre vers la position du pulsar. La diminution de l'étendue de l'émission devient statistiquement significative au-delà de $\sim$ 10 TeV.

Notre analyse spectrale a montré que le spectre de l'émission des rayons gamma de très haute

énergie de la source se raidit aux alentours de 10 TeV, ce qui correspondrait au rétrécissement observée au niveau de sa morphologie. Nous avons procédé par l'ajustement de la distribution spectrale d'énergie en utilisant nos données H.E.S.S.. Nous utilisons une supposition sur la forme spectrale décrite par une loi de puissance brisée et exponentiellement coupée. De plus nous adoptons des valeurs de champ de photons émettant dans les infra rouges lointain et proche obtenu par des modèles galactiques d'actualités, et incluons le fond diffus cosmologique dans notre modèle pour déterminer la population de photons cibles dont les électrons libres du milieu sont susceptibles d'entrer en collision avec.

Nous trouvons une brisure du spectre des électrons au niveau d'une dizaine de TeV, et ne trouvons pas d'autre coupure statistiquement significative. Le spectre aux énergies au-dessous de la brisure suit une loi de puissance d'indice ~ 2.5 et au-delà de la cassure une pente de ~ 3.2. Nous considérons dans notre modèle plusieurs processus radiatifs, telle que synchrotron, Compton inverse et une estimation simple d'interactions proton-proton basées sur des valeurs nominales. Les résultats de l'ajustement des données aux modèles prescrivent un champ magnétique moyen de $\sim 12\,\mu$G, qui reste en accord avec la valeur publiée mais qui pointe vers un champ légèrement plus faible qu'estimé principalement, des processus hadroniques négligeables comparés au Compton inverse sur l'infra-rouge lointain mais aussi sur le fond diffus cosmologique.

En particulier, la dominance du dernier aux hautes énergies au-delà de la brisure du spectre des électrons pourrait expliquer la coupure que l'on observe sur le spectre des photons, car le régime *Thompson* ne serait plus d'actualité, et l'effet du régime *Klein-Nishina* serait dominant. Ce résultat suggérerait une explication possible pour le rétrécissement de la morphologie de la nébuleuse dans ce domaine d'énergie.

En estimant les pertes dues au refroidissement synchrotron, nous avons conclu que cet effet ne domine pas et qu'il ne pourrait pas, tenant en compte les valeurs du champ magnétique de la nébuleuse de pulsar expliquer la cassure du spectre des électrons.

Pendant la dernière année de préparation de mon doctorat, j'ai entamé un projet utilisant des simulations numériques. A l'aide de mon directeur de thèse et de notre collaborateur Dr Z. Meliani, nous avons commencé une étude à l'aide de codes (magnéto-)hydrodynamiques pour caractériser l'évolution de la morphologie de certaines nébuleuses de pulsar.

En effet, H.E.S.S. a observé pour un nombre considérable de source fermement identifiées en tant que nébuleuses de pulsar, un décalage spatial significatif entre le centre de l'émission gamma de très haute énergie et la position du pulsar du système. Pour plusieurs de ces objets d'un âge intermédiaire, ce décalage ne peut pas être expliqué que par l'effet du mouvement propre du pulsar, étant la vitesse acquise lors du rebond causé par l'asymétrie de l'explosion à son origine, car ils nécessiteraient des vitesses propres très élevées, qui s'écartent de la moyenne basée sur la population observée de pulsars. Ainsi un autre effet qui pourrait éventuellement entrer en jeu, serait l'inhomogénéité du milieu ambiant. Le but de notre étude serait de quantifier l'influence des ces acteurs sur la déformation de la nébuleuse et d'estimer les décalages obtenus dans nos simulations avec ceux observées par H.E.S.S..

Nous avons simulé l'évolution du système pulsar-nébuleuse-vestige à l'aide du code *MPI-AMRVAC* qui nous permet de bénéficier d'un raffinement adaptatif de la grille de simulation. Nous utilisons la dernière version de ce code public mais ayant implémenté et adapté un module

de magnéto-hydrodynamique relativiste développé par Meliani et al. (2012) pour une ancienne version du code. Le raffinement adaptatif est un trait du code qui est indispensable dans les cas physiques que nous souhaitons simuler car l'évolution de la nébuleuse de pulsar dépend de 1) du vent du pulsar qui va l'approvisionner en particules déposées au choc de terminaison et de 2) de la propagation du choc en retour créer par le choc avant de l'explosion de la supernova progénitrice qui rencontre de la résistance lors de sa propagation vers le milieu interstellaire. Ce choc de retour interagira avec les parois externes de la nébuleuse de pulsar une fois l'ayant atteint et affectera son évolution, qui depuis sa formation était en expansion libre. Par la suite, l'objet débutera une phase adiabatique et en fonction de la géométrie dans laquelle l'interaction choc de retour-nébuleuse aura lieu, cette dernière pourrait continuer son évolution de manière asymétrique. Ce système consiste donc de trois sous-systèmes à très différentes échelles que nous souhaitons résoudre avec grande précision afin de caractériser de façon réaliste les décalages possibles et sa morphologie asymétrique.

Nous avons simulé en 1D avec une approche hydrodynamique des systèmes évoluant jusqu'à 20 000 ans afin de tester la rigueur de notre code et améliorer ses performances. Nous avons comparé nos résultats avec des simulations non-relativistes et relativistes tirées de la littérature et trouvons des évolutions comparables.

Nos productions de simulations en 2D sont en cours et sujettes à plusieurs vérifications, notamment l'endiguement de l'effet d'instabilités créées numériquement. Pour lutter contre cet effet, nous avons augmenté et imposé un raffinement à plusieurs niveaux sur les régions d'intérêt qui délimitent la nébuleuse de pulsar dans le système. Ceci est coûteux numériquement et n'avons, au temps de la rédaction de ce manuscrit, simulé que des systèmes encore jeunes $\sim$ 800 ans où les éjecta du vestige dominent leur évolution dynamique, n'ayant pas encore été perturbés par l'arrivée du choc de retour. Nous simulons des systèmes ayant un pulsar avec un mouvement propre de 500 km.s^{-1} et implémenterons un gradient de densité pour étudier le problème physique du décalage du centre de la nébuleuse.

Ma thèse a consisté à étudier la morphologie de nébuleuses de pulsars dans le cadre de très hautes énergies et à considérer leur évolution vis-à-vis de leur milieu et de leur budget énergétique. Ayant analysé des données H.E.S.S. , nous avons mené des études sur le spectre de l'émission et sur la description de la structure spatiale de MSH 15-52 afin de dépeindre la distribution des leptons et entrevoir le transport de ces particules au sein de la source. Les résultats de nos simulations d'évolution dans un système composite, permettrons de placer des contraintes et des limites sur un phénomène fréquent souligné dans les observations de hautes et de très hautes énergies.

9.2 HGPS significance maps

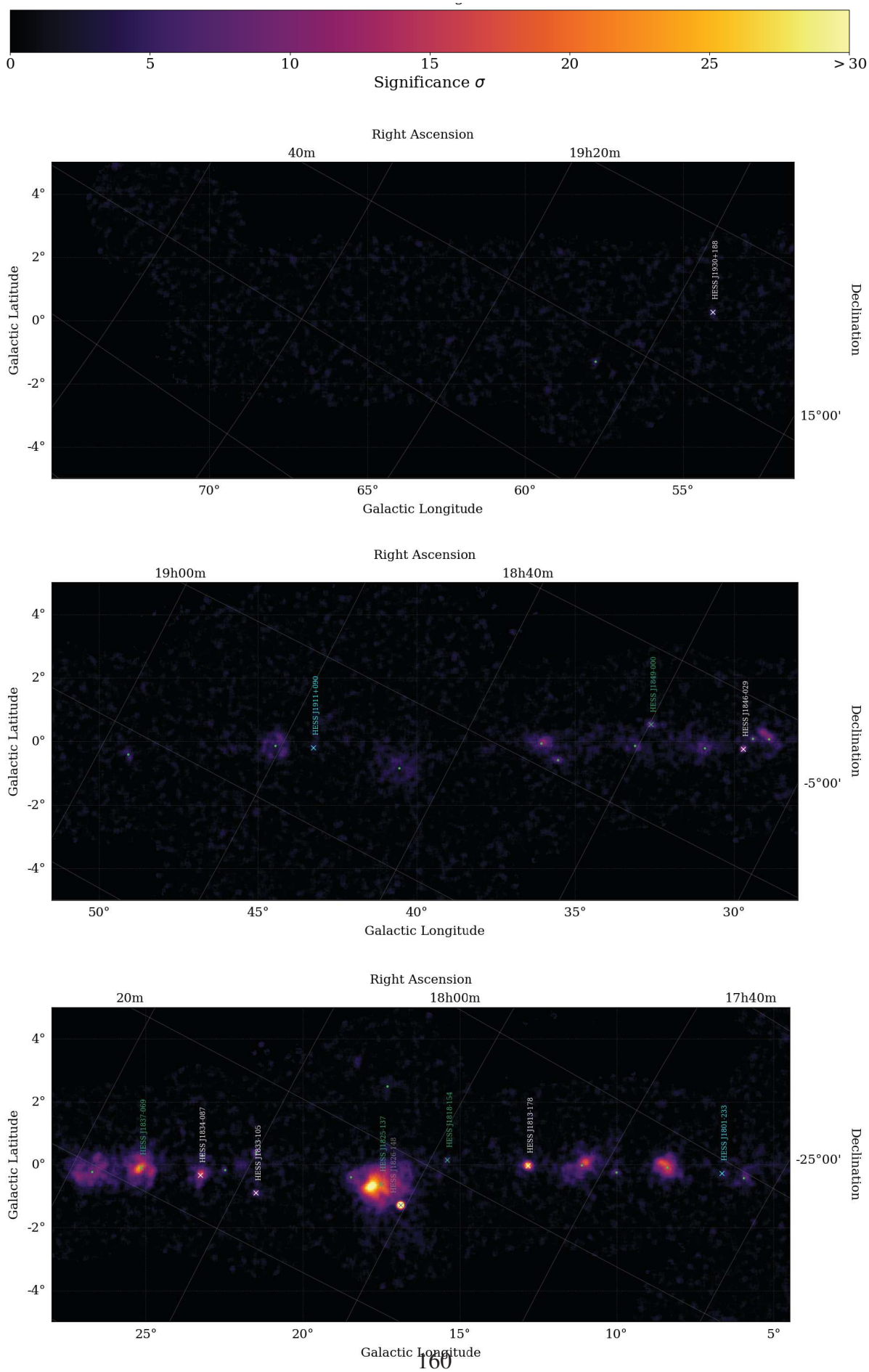

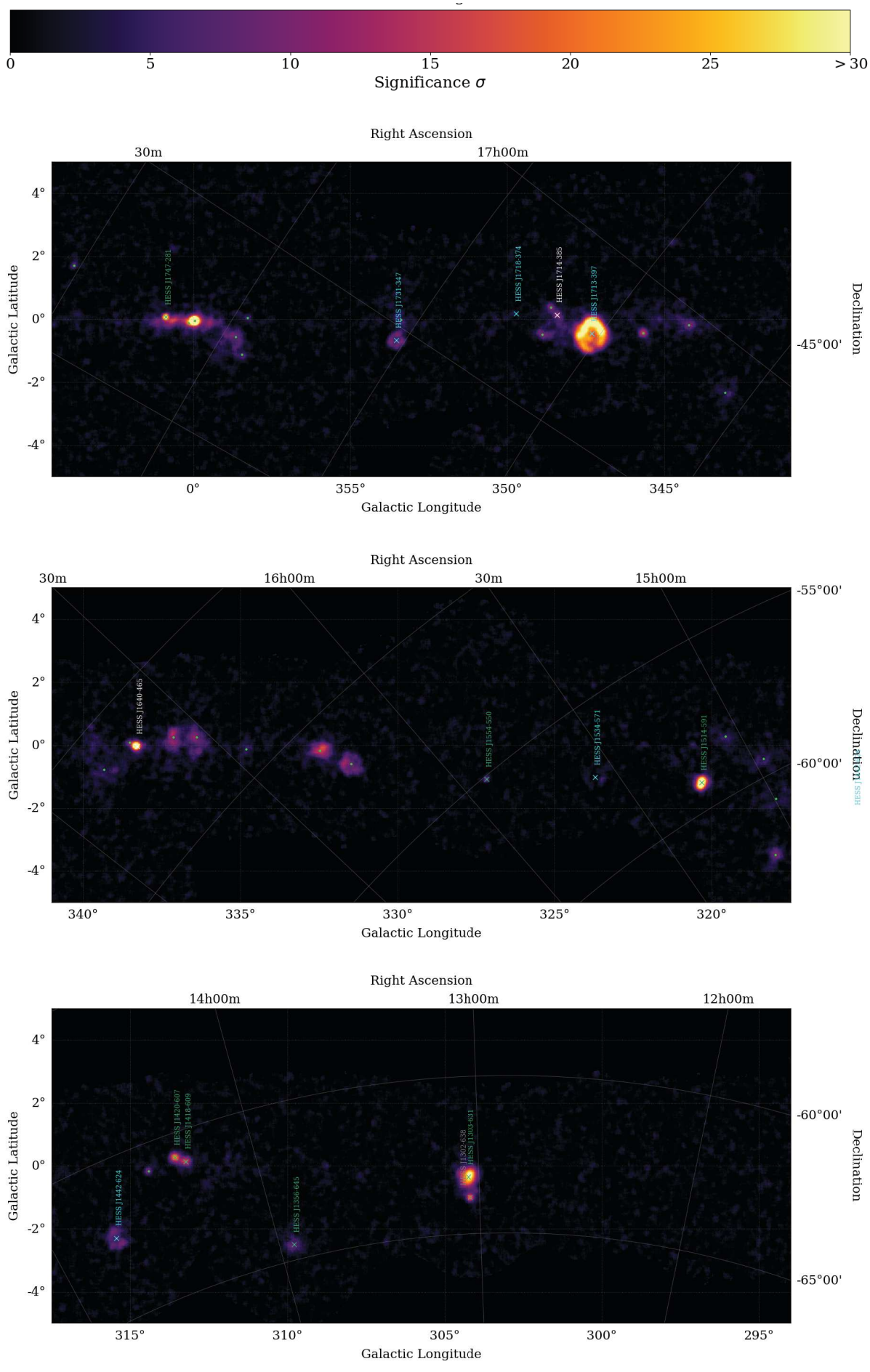
0
5
10
15
20
25
> 30
Significance σ
Right Ascension
30m
17h00m
4°
2°
0°
-2°
-4°
Galactic Latitude
HESS J1747-281
HESS J1731-347
HESS J1718-374
HESS J1714-385
HESS J1713-397
-45°00'
Declination
0°
355°
350°
345°
Galactic Longitude
Right Ascension
30m
16h00m
30m
15h00m
-55°00'
4°
2°
0°
-2°
-4°
Galactic Latitude
HESS J1640-465
HESS J1554-550
HESS J1534-571
HESS J1514-591
-60°00'
Declination
340°
335°
330°
325°
320°
Galactic Longitude
Right Ascension
14h00m
13h00m
12h00m
4°
2°
0°
-2°
-4°
Galactic Latitude
HESS J1420-607
HESS J1418-609
HESS J1442-624
HESS J1356-645
HESS J1302-638
HESS J1303-631
-60°00'
-65°00'
Declination
315°
310°
305°
300°
295°
Galactic Longitude

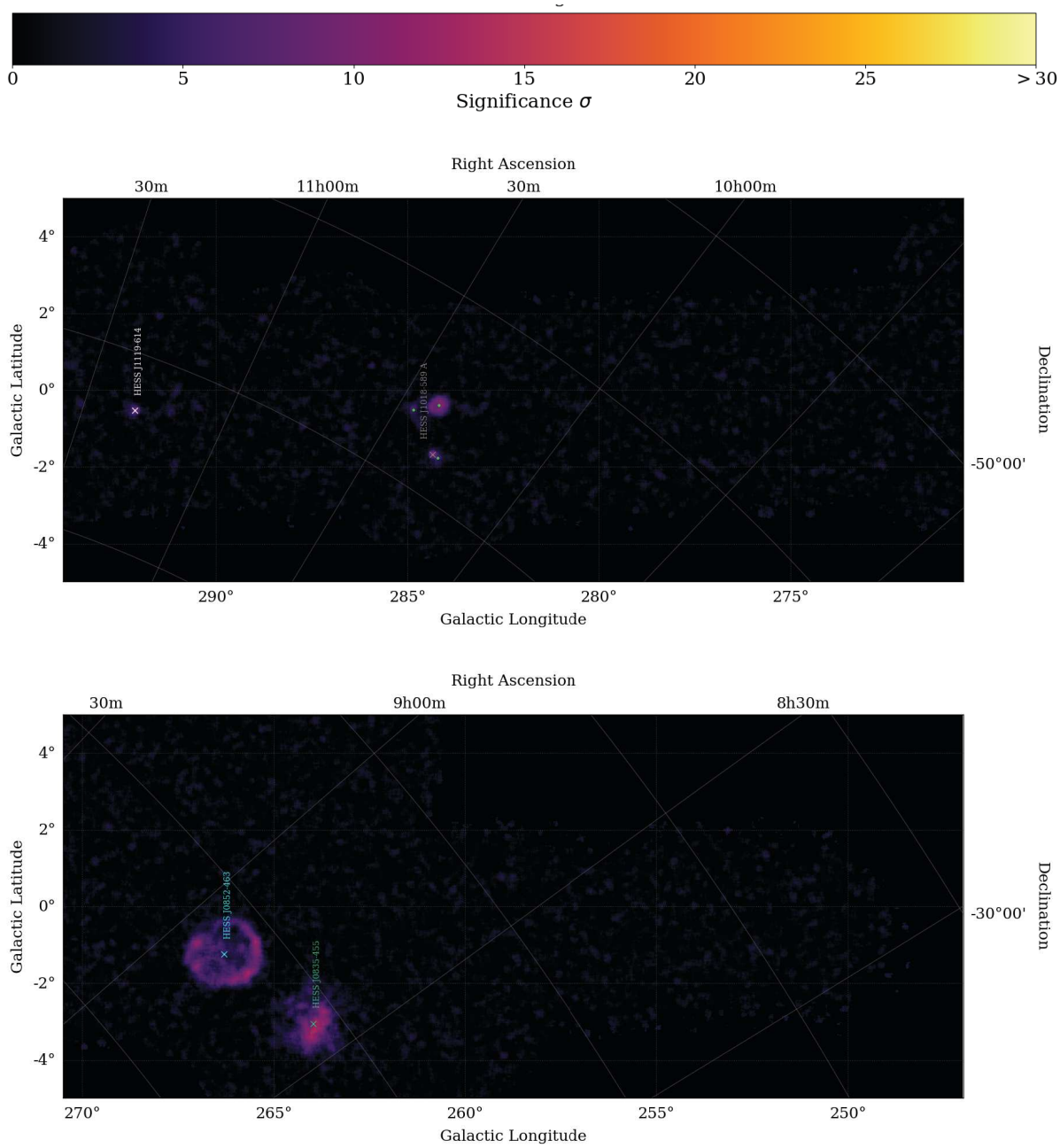

Figure 9.1 – HGPS significance maps for a 0.1 ° correlation radius, showing the published positions of the firmly identified sources with a cross (the length is not indicative of the error on the position). The white crosses point to the sources labelled in the HGPS as PWNe, the green ones for the composite SNR-PWN candidate systems, the cyan ones for the SNRs and the gray ones for the gamma-ray binary systems. The light green dots represent the position of the not firmly identified sources in the survey as well as the ones that have not been associated with any other catalogued emission. The colorbar for the map has been set with a lower limit to $\sigma = 0$ and an upper limit to $\sigma = 30$ for illustration purposes to pop-up the faint extended sources.